

Bergische Universität Wuppertal

Fachbereich Mathematik und Naturwissenschaften

Institute of Mathematical Modelling, Analysis and Computational Mathematics
(IMACM)

Preprint BUW-IMACM 14/28

Andreas Bartel, Carsten Cimala, Markus Clemens, Michael Günther, Jan ter Maten
(eds.)

Program & Book of Abstracts

—

The 10th International Conference on Scientific Computing in Electrical Engineering SCEE 2014

July, 2014

<http://www.math.uni-wuppertal.de>

Program & Book of Abstracts

The 10th International Conference on
**Scientific Computing in
Electrical Engineering
SCEE 2014**

July 22 - July 25, 2014
Wuppertal, Germany



SCEE

SCEE 2014

Program

& Book of Abstracts

The 10th International Conference on

Scientific Computing in
Electrical Engineering
(SCEE 2014)

July 22 – July 25, 2014
Wuppertal, Germany

Image source (front cover, Bildquelle):

Medienzentrum der Stadt Wuppertal, Wuppertal, Germany.

SCEE 2014 Contact:

✉ scee2014@math.uni-wuppertal.de

Preface

The bi-annual conference on Scientific Computing in Electrical Engineering is an excellent environment for scientific exchange also of intersectorial research. It brings together scientists from applied mathematics, electrical engineering, computer sciences as well as scientists from industry. The workshop character of SCEE is an important feature, where all talks are given in the plenary and also posters are presented with an introductory slide. Thus, it builds an fruitful basis for intensive discussions on modeling and numerical simulation in both electric circuits and electromagnetic fields. It makes the conference a unique meeting.

The SCEE started as a national German meeting in Darmstadt (1997) and Berlin (1998). It became international from 2000 on and was held at the following places: Warnemünde, (Germany, 2000), Eindhoven (The Netherlands, 2002), Capo D'Orlando (Italy, 2004), Sinaia (Romania, 2006), Espoo (Finland, 2008), Toulouse (France, 2010), Zurich (Switzerland, 2012).

The 10th edition, the SCEE 2014, is held in Wuppertal from July 22 to July 25, 2014. The venue is the historical city hall of Wuppertal (*Historische Stadthalle Wuppertal*), which is a remarkable place (also member of the Historic Conference Centers of Europe). The SCEE 2014 has five main directions:

- computational electromagnetics (CEM)
- electric circuit and device modeling and simulation (Circ)
- coupled problems (CP)
- model order reduction (MOR)
- mathematical and computational methods (Meth)

The abstracts within this book have successfully passed a review process, which was executed by the Program Committee and the Local Organizing Committee for support. All authors of these accepted contributions are invited to submit full paper. After a peer-review process, the accepted full papers will be published in the Springer Series "Mathematics in Industry".

In addition, the authors of excellent proceedings publications will be invited to submit an extended version. This extended version needs to include further unpublished material to allow for a second publication. These papers will be submitted for a special issue of the open access Springer journal "Mathematics in Industry" with a compulsory, additional review process. However, if the invited publication is accepted, the organizers of the conference will cover the publication fee.

We thank all invited speakers to accept our invitation to Wuppertal. Furthermore, we would like to thank all authors for their contributions; generally the the quality of the abstracts has been quite high. We are also grateful to our sponsors for their material and financial support.

Finally, we cordially welcome all participants to Wuppertal and wish you a fruitful and inspiring meeting.

Wuppertal, July 2014

*Andreas Bartel
Carsten Cimala
Markus Clemens
Michael Günther
Jan ter Maten*

Committees

Local Organizing Committee

Prof. Dr. Michael Günther (Chairman)
Prof. Dr. Markus Clemens (Co-Chairman)
Dr. Andreas Bartel
Dr. Jan ter Maten
Carsten Cimala, M.Sc.

Conference Desk

Christa Kelly
Lara V. Knist, B.A.
Elvira Mertens

Scientific & Program Committee

Prof. Gabriela Ciuprina (Politehnica University of Bucharest, Romania)
Dr. Georg Denk (Infineon, Germany)
Prof. Dr. Michael Günther (University of Wuppertal, Germany)
Prof. Dr. Stéphane Lantéri (INRIA, France)
Dr. Jan ter Maten (University of Wuppertal, Germany)
Dr. Jörg Ostrowski (ABB, Switzerland)
Prof. Dr. Ronan Perrussel (Toulouse, France)
Prof. Dr. Ursula van Rienen (University of Rostock, Germany)
Prof. PhD Vittorio Romano (University of Catania, Italy)
Prof. Dr. Wil Schilders (TU Eindhoven, The Netherlands)
Prof. Dr. Thomas Weiland (TU Darmstadt & CST, Germany)

Sponsors

ABB, Switzerland
CST AG, Darmstadt, Germany
Bergische Universität Wuppertal, Germany

Conference Schedule

Tue. 22.07.	Wed. 22.07.	Thu. 22.07.	Fri. 22.07.
08:00 Registration 09:10 Opening 09:25 Clénet (Inv.) 10:15 Kirsch	09:00 Frommer (Inv.) 09:50 Alotto (Inv.)	09:00 Klagges (Inv.) 09:50 Pistauer (Inv.)	08:30 Rommes (Inv.) 09:20 Feng 09:45 Banagaaya 10:10 Bollhöfer
Coffee Break			
11:10 Casagrande 11:35 Farle 12:00 Banove	11:10 Gruber 11:35 Jerez-Hanckes 12:00 Hollaus	11:10 Bittner 11:35 Romano 12:00 Gausling	11:10 Pulch 11:35 Hess 12:00 Samuel 12:25 Hachtel 12:50 Closing
Lunch			
14:15 Schöps (Inv.) 15:05 Liu 15:30 Tischendorf 15:55 Intro P1 16:20 Poster P1 with Coffee 17:25 Jüttner 17:50 Kerler		14:15 La Magna (Inv.) 15:05 Gangl 15:30 Intro Poster P2 15:55 Poster P2 with Coffee 17:00 Ali 17:25 Jansen	

Poster P1: Tuesday, 15:55 – 17:25

101 Stefano Grivet-Talocia
102 Andrea Cremasco
103 Giovanni De Luca
104 Rakesch Jha
105 Davide Cagnoni
106 Andrea Patanè
107 Frank Gronwald
108 Gabriela Ciuprina
109 Helia Niroomand Rad
110 Romain Thomas
111 Marcus Stiemer
112 Carsten Cimala

Poster P2: Thursday, 15:30 – 17:00

113 Konstantin Porzig
114 Andreas Blaszczyk
115 Michaela Mehlin
116 Ulf Zimmermann
117 Zeger Bontinck
118 Piotr Putek
119 Bastian Bandlow
120 Dawei Zheng
121 Ignacio Garcia de la Vega Chamorro
122 Carlos Jerez-Hanckes
123 Christian Richter
124 Michael Günther

Contents

Session: Tuesday, July 22, 09:25–12:25

Approximation Methods to solve Stochastic Problems in Computational Electromagnetics <i>Stéphane Clénet</i> (invited talk)	1
A Material Averaging Scheme for the Finite Integration Technique Based on Local Field Information <i>Stefan Kirsch, Christoph Classen, Rolf Schuhmann</i>	3
DG Treatment of Sliding Interfaces in 3D Eddy Current Problems <i>Raffael Casagrande, Christoph Winkelmann, Ralf Hiptmair, Jörg Ostrowski</i>	5
A symmetric and low-frequency stable potential formulation for the finite-element simulation of electromagnetic fields <i>Martin Jochum, Ortwin Farle, Romanus Dyzcij-Edlinger</i>	7
Systematic Determination of Eigenfields in Frequency Domain <i>Todorka Banova, Wolfgang Ackermann, Thomas Weiland</i>	9

Session: Tuesday, July 22, 14:15–18:15

Iterative Schemes for Coupled Multiphysical Problems in Electrical Engineering <i>Sebastian Schöps</i> (invited talk)	11
Modeling and Simulation of Inductive Heating involving Mechanical Deformations <i>Qingzhe Liu, Thomas Petzold, Dawid Nadolski, Roland Pulch</i>	13
Jacobian Structure of Coupled Electromagnetic Field and Lumped Circuit Models <i>Wim Schoenmaker, Caren Tischendorf</i>	15
Iterative Software Agent Based Solution of Multiphysics Problems <i>Matthias Jüttner, André Buchau, Alexander Faul, Wolfgang M. Rucker, Peter Göhner</i>	17
Model reduction and dynamic iteration for coupled nonlinear systems <i>Johanna Kerler, Tatjana Stykel</i>	19

Poster Session 1: Tuesday, July 22

Tuning the accuracy of rational macromodels to nominal load conditions <i>Stefano Grivet-Talocia, Andrea Ubolli, Alessandro Chinea, Michelangelo Bandinu</i>	21
Thermal Simulations for Optimization of Dry Transformers <i>Andrea Cremasco, Paolo Di Barba, Bogdan Cranganu-Cretu, Andreas Blaszczyk</i>	23
Accelerating the Transient simulation of Nearly-Periodic Circuits <i>Giovanni De Luca</i>	25
Acceleration of transient simulation of analog and mixed signal circuits in 14nm technology generation <i>Rakesh Jha</i>	27
Coupled Electrothermal Simulation of 3D Semiconductor Devices and Lumped Circuit Elements <i>D. Cagnoni, M. Bellini, M. Restelli, J. Vobecký, C. de Falco</i>	29
Sensitivity Techniques for Effective Optimization of Tandem Thin-Film Silicon Solar Cells <i>A. Patanè, A. Santoro, G. Carapezza, V. Romano, A. La Magna, G. Nicosia</i>	31
An advanced transmitter and receiver modelling scheme for the EMC analysis of smart grid components <i>Frank Gronwald</i>	33
Mixed-domain Macro-Models for RF MEMS Capacitive Switches <i>Gabriela Ciuprina, Daniel Ioan, Dragoş Isvoranu, Ştefan Sorohan, Sorin Lup, Sebastian Kula</i>	35
Modeling and Analysis of the Non-Stationary Maxwell Equations Coupled with the Circuit Equations <i>Helia Niroomand Rad, Andreas Steinbrecher</i>	37
Approximate Linear Solvers for Adaptive Runge-Kutta Methods Applied to the Simulation of Transients in Power Systems <i>Romain Thomas, Domenico Lahaye, Kees Vuik, Lou van der Sluis</i>	39
Computational Electromagnetic Design by Mathematical Optimization <i>Marcus Stiemer, Marco Rozgić, Lars-Ole Fichte, David Sanchez, Sebastian Böhmelt</i>	41
Coupled Two-Step MoM / FITD Method for Calculation of Electrically Large Problems in Urban Areas <i>Carsten Cimala, Oliver Spathmann, Simon Runke, Martin Zang, Markus Clemens</i>	43

Session: Wednesday, July 23, 09:00–12:25

Computing $f(A)\mathbf{b}$ - the Action of a Matrix Function on a Vector <i>Andreas Frommer, Stefan Güttel, Marcel Schweitzer</i> (invited talk)	45
---	----

Parallelization and Sparsification of a Surface-Volume Integral Code for Plasma-Antenna Interaction <i>Davide Melazzi, Piergiorgio Alotto, Vito Lancellotti, Marco Manente, Fabio Freschi, Daniele Pavarin</i> (invited talk)	47
Rectangular Cavity Green's Functions with Ewald Summation Technique and Fast Fourier Transform Acceleration <i>M. E. Gruber, C. Koenen, T. F. Eibert</i>	49
Spectral Multiple Traces Formulation for Heterogeneous Penetrable Objects Scattering <i>Carlos Jerez-Hanckes, José Pinto, Simon Tournier</i>	51
MSFEM to Simulate Eddy Currents in Laminated Iron <i>Karl Hollaus, Joachim Schöberl</i>	53

Session: Thursday, July 24, 09:00–12:25

Simulation of Power Electronics in Automotive Product Development <i>Daniel Klagges, Matthias Richwin</i> (invited talk)	55
High Level Simulation of Cyber-Physical Systems <i>Ralph Weissnegger, Markus Pistauer, Christian Steger</i> (invited talk)	57
Latency exploitation in Wavelet Based Multirate Circuit Simulation <i>Kai Bittner, Hans Georg Brachtendorf</i>	59
Simulation of graphene nanoribbons <i>Giovanni Mascali, Vittorio Romano</i>	61
Analysis of Contraction-Conditions Combined with Uncertainty Quantification in Co-Simulation for Coupled Electrical Circuits <i>Kai Gausling, Andreas Bartel</i>	63

Session: Thursday, July 24, 14:15–17:50

Graphene nano-device design from first principles calculations <i>Ioannis Deretzis, Gaetano Calogero, Giuseppe G.N. Angilella, Antonino La Magna</i> (invited talk)	65
Design Optimization of Electrical Machines Using Sensitivity-Based Topology and Shape Optimization <i>Peter Gangl, Ulrich Langer</i>	67
Some results on the two-temperature energy-transport model for semiconductors <i>Giuseppe Ali, Vittorio Romano</i>	69
Global Solvability of Nonlinear Parabolic PDAEs: A Coupled Systems Approach and its Application to Circuit Simulation <i>Lennart Jansen, Michael Matthes</i>	71

Poster Session 2: Thursday, July 24

Uncertainty Analysis in Transcranial Magnetic Stimulation Using Non-intrusive Polynomial Chaos Expansion <i>Konstantin Porzig, Luca Di Rienzo, Hartmut Brauer, Jens Hauelsen</i>	73
A New Generation of BEM Solvers for Electric Field Computations <i>Thomas Müller, Carsten Trinitis, Andreas Blaszczyk</i>	75
Runge-Kutta type Explicit Local Time-Stepping Methods for Electromagnetics <i>Marcus J. Grote, Michaela Mehlin</i>	77
Numerical Investigation of an Electrostimulative Hip Stem with a Multi-Electrode Setting <i>Ulf Zimmermann, Cathérine Ebner, Rainer Bader, Ursula van Rienen</i>	79
Uncertainty Quantification for Permanent Magnet Synchronous Machines with an Inclined Rotor Shaft <i>Zeger Bontinck, Herbert De Gersem, Sebastian Schöps</i>	81
Robust topology optimization of a Permanent Magnet synchronous machine using level set and stochastic collocation methods <i>Piotr Putek, Kai Gausling, Andreas Bartel, Konstanty M. Gawrylczyk, Jan ter Maten, Roland Pulch, Michael Günther</i>	83
Solution of Nonlinear Eigenmode Formulations for Externally Coupled Cavities <i>Bastian Bandlow, Rolf Schuhmann</i>	85
On several Green's function methods for fast Poisson solver in free space <i>Dawei Zheng, Gisela Pöplau, Ursula van Rienen</i>	87
Turning points in nonlinear circuits <i>Ignacio García de la Vega, Ricardo Rianza</i>	89
Boundary Integral Formulation for the Electrical Response of an Axon to an Extracellular Stimulation <i>Fernando Henríquez, Carlos Jerez-Hanckes, Fernando Altermatt</i>	91
Multi-GPU Acceleration of Algebraic Multigrid Preconditioners <i>Christian Richter, Sebastian Schöps, Markus Clemens</i>	93
Multirate GARK schemes for multiphysics problems <i>Andreas Bartel, Michael Günther, Christoph Hachtel, Adrian Sandu</i>	95

Session: Friday, July 25, 08:30–13:00

Different views on model order reduction for the electronics industry <i>Joost Rommes</i> (invited)	97
An a posteriori error bound for reduced order modeling of micro- and nano-electrical(-mechanical) systems <i>Lihong Feng, Peter Benner, Athanasios C. Antoulas</i>	99

Reduction of index-2 electrical networks using the Implicit-IMOR method <i>N. Banagaaya, G. Ali, W. H. A. Schilders</i>	101
Model Reduction for Maxwell Equations using Subspace Recycling <i>André Bodendiek, Matthias Bollhöfer</i>	103
Reduction of Stochastic Circuit Models for Uncertainty Quantification <i>Roland Pulch</i>	105
Reduced Basis Modeling for Uncertainty Quantification of Electromagnetic Problems in Stochastically Varying Domains <i>Peter Benner, Martin W. Hess</i>	107
Multipoint Model Order Reduction using Reflective Exploration <i>Elizabeth Rita Samuel, Francesco Ferranti, Luc Knockaert, Tom Dhaene</i>	109
Efficient Simulation for Electrical-Thermal Systems via Multirate-MOR <i>Christoph Hachtel, Michael Günther, Andreas Bartel</i>	111

Approximation Methods to solve Stochastic Problems in Computational Electromagnetics

Stéphane Clénet

L2EP, Arts et Métiers ParisTech, 8, Bd Louis XIV, 59046 Lille cedex, France, stephane.clenet@ensam.eu

Summary. To account for uncertainties on model parameters, stochastic models can be used. The model parameters are then random fields or variables. To solve these models several methods are available. In this communication, we will focus on the solution of stochastic problems in computational electromagnetics using approximation methods. Some applications in low frequency will be presented in order to illustrate the possibilities offer by the stochastic approach but also its current limitations.

1 Context

Applying a numerical method (FEM, FIT, ...) to solve the Maxwell equations leads to valuable tools for understanding and predicting the features of electromagnetic devices. With the progress in the fields of numerical analysis, CAD and postprocessor tools, it is now possible to represent and to mesh very complex geometries and also to take into account more realistic material behavior laws with non linearities, hysteresis Besides, computers have nowadays such capabilities that it is customary to solve problems with millions of unknowns. The modeling error due to the assumptions made to build the mathematical model (the set of equations) and the numerical errors due especially to the discretisation (by a Finite Element method for example) can be negligible. Consequently, in some applications, if a gap exists between the measurements, assuming them perfect, and the results given by the numerical model, it comes from deviations on input parameters which are not in the “real world” equal to their prescribed values.

The origins of these deviations are numerous and are related to either a lack of knowledge (epistemic uncertainties) or uncontrolled variations (aleatoric uncertainties). For example, mechanical parts are manufactured with dimensional tolerances whereas some dimensions, such as air gaps in electric machines, are critical as they strongly influence performance. Besides uncertainties in material composition, the material characteristics which change with uncontrolled environmental factors (humidity, pressure, etc.) are also often unknown [1]. Even if the environmental factors are perfectly known, in some situations, the behavior law parameters can't be identified because measurements are not possible under the right experimental conditions. Consequently, to be more realistic, numerical models must now be able to take into account uncertainties. The stochastic approach, which

consists in representing the uncertain parameters as random variables, (the output variables are then also random variables) is one possible way to model and to evaluate the influence of the uncertainties on the parameters. In the 90's, researches on quantification of uncertainties in numerical models using stochastic approaches first began in the field of mechanical and civil engineering [2]. In the 2000's, this approach has met with renewed interest with the development of approximation methods based especially on truncated polynomial chaos that offer a higher convergence rate than the Monte Carlo Simulation Method if the model outputs have smooth variations according to the input random parameters.

In this communication, we will focus on the solution of stochastic problems in computational electromagnetics using approximation methods. Some applications in low frequency will be presented in order to illustrate the possibilities offer by the stochastic approach but also its current limitations.

2 Solution of the Stochastic Problem

In the deterministic case, the use of a numerical method to solve a low frequency electromagnetic problem requires the solution of a linear equation system:

$$\mathbf{S}\mathbf{X} = \mathbf{F} \quad (1)$$

With \mathbf{X} the vector of unknowns, \mathbf{S} the stiffness matrix and \mathbf{F} the source vector. When accounting for the uncertainties using the stochastic approach, the input parameters are then modelled by random variables $\mathbf{p}(\theta)$. The parameters $\mathbf{p}(\theta)$ are related either to the geometry or to the behaviour laws of the materials or to the sources. The output \mathbf{X} of the electromagnetic model (1) becomes then random and verifies the following equation system:

$$\mathbf{S}(\mathbf{p}(\theta))\mathbf{X}(\mathbf{p}(\theta)) = \mathbf{F}(\mathbf{p}(\theta)) \quad (2)$$

Among the different methods available to solve the problem (2), approximation methods are of great interest when the solution is sufficiently regular. Indeed, the speed of convergence is very fast according to sampling techniques like the Monte Carlo Simulation Method. We seek for a solution under the form:

$$\mathbf{X}(\mathbf{p}(\theta)) \approx \sum_{i=0}^P \mathbf{X}_i \Psi_i(\mathbf{p}(\theta)) \quad (3)$$

With \mathbf{X}_i unknown vectors of scalar coefficients and $\Psi_i[\mathbf{p}(\theta)]$ the approximation functions which are often multivariate polynomials such as truncated Polynomial Chaos Expansion (PCE). The vectors \mathbf{X}_i can be determined by solving only one but often huge equation system obtained by applying the Galerkin method, so called intrusive method [2]. Methods (so called non intrusive) of projection, collocation or regression [4] based on the solution of numerous deterministic problems (1) for well suited parameter values ($\mathbf{p}_1, \dots, \mathbf{p}_d$) can be also implemented. The total number of polynomials in the truncated PCE is equal to:

$$P = \frac{(M+p)!}{M!p!} \quad (4)$$

With M the number of random parameters and p the maximum order of the multivariate polynomials Ψ_i . We can see that P increases exponentially with M which is usually so-called the “curse of dimensionality”. In practice, if M is higher than a dozen, the size P of the approximation basis becomes too large to be practically computed. It is then necessary to use adaptive methods, i.e., to build the basis of approximation automatically, according to the model output. Methods have been proposed in the literature to construct approximations called “sparse” approximations, in which the number of terms of the basis is controlled [3–5]. the different types of methods will be presented and compared.

3 Applications

In the field of computational electromagnetics, the development and the application of such models have started in the early 2000’s and know a growing interest in the community [7–9]. To illustrate the stochastic approach, examples of application will be presented.

A Eddy Current-Non Destructive Testing problem where some material characteristics are assumed to be random will be detailed. To solve this problem, the Galerkin method and an Adaptive Projection method are compared [4]. This study shows that the stochastic approach is a powerful tool for improving the accuracy of models by determining the input parameters whose uncertainties strongly influence the quantity of interest. It can also be very helpful to develop indicators based on measurements that are robust, that is to say that these indicators are few influenced by the variability of the input parameters.

The influence of the dimension variability on the performances of an electrical machine is also studied when the number of random parameters is about a dozen [9, 10]. A sparse approximation has been deduced applying a least angle regression [5]. The aim is to propose a methodology based on a stochastic approach to assess the influence of the variability of the

fabrication process on the performances of the electrical machines.

References

1. R. Ramarotafika; A. Benabou, S. Clénet, S, J.C. Mipo. Experimental characterization of the iron losses variability in stators of electrical machines, *IEEE Trans. on Mag.*, Vol. 48, No. 4, pp 1629-1632 (2012).
2. R. Ghanem, P.D. Spanos. *Stochastic Finite Elements: A spectral approach*, Dover, New York, 2003.
3. S. Clénet. *Uncertainty Quantification in Computational Electromagnetics: The Stochastic Approach*, ICS Newsletter, March 2013.
4. K. Beddek, S. Clénet, O. Moreau, V. Costan, Y. Le Menach and A. Benabou. Adaptive Method for Non Intrusive Spectral Projection Application on a Stochastic Eddy Current NDT Problem, *IEEE Trans. on Mag.*, Vol. 48, No. 2, pp 759-752 (2012).
5. G. Blatman and B. Sudret Adaptive sparse polynomial chaos expansion based on least angle regression. *Journal of Computational Physics*, Vol. 230, Issue 6, March 2011, Pages 2345-2367.
6. A. Doostan, A and H. Owhadi. A non-adapted sparse approximation of PDEs with stochastic inputs, *Journal of Computational Physics*, Vol. 230, 2011, pp. 3015-3034.
7. A. Drissaoui, S. Lanteri, P. Lévlque, P. Musy, L. Nicolas, R. Perrussel and D. Voyer. A Stochastic Collocation Method Combined With a Reduced Basis Method to Compute Uncertainties in Numerical Dosimetry, *IEEE Trans. on Mag.*, Vol. 48, No. 2, 2012, pp 563-566.
8. E. Rosseel, H. De Gersem, S. Vandewalle, Spectral Stochastic Simulation of a Ferromagnetic Cylinder Rotating at High Speed *IEEE Trans. on Mag.*, Vol. 47, No. 5, pp 1182-1185, 2011.
9. H. Mac, S. Clénet, S. Zheng, T. Coorevits, J.C. Mipo. On the geometric uncertainties of an electrical machine : stochastic modeling and impact on the performances, *COMPUMAG 13*, Budapest (Hungary), 2013
10. P. Offermann, H. Mac, T. T. Nguyen, S. Clénet, H. De Gersem and K. Hameyer. Uncertainty quantification and sensitivity analysis in electrical machines with stochastically varying machine parameters, *CEFC 14*, Grenoble (France), 2014.

A Material Averaging Scheme for the Finite Integration Technique Based on Local Field Information

Stefan Kirsch, Christoph Classen, and Rolf Schuhmann

Technische Universität Berlin, Fachgebiet Theoretische Elektrotechnik, Einsteinufer 17, 10587 Berlin
 {kirsch, classen, schuhmann}@tet.tu-berlin.de

Summary. In general, the accuracy of mesh based electromagnetic simulations strongly suffers from mesh cells that are cut by material boundaries under an arbitrary angle. The topic of this contribution is a generalized material averaging formula for the Finite Integration Technique that is not deranged by skewed material interfaces. An adapted solver based on this formula will be shown to yield more accurate results compared to a conventional approach.

1 Introduction

In order to simulate the electromagnetic properties of an object, its geometry and material have to be discretized. Commonly, a computational mesh with a finite number of elements (nodes, edges, facets and volumes) is employed for that purpose. The higher the number of elements, the more accurate the object's discrete representation usually gets. Unfortunately, the computational effort also rises with increasing elements. It is therefore desirable to find a discretization, that accurately maps the object's geometry and material to a reasonably coarse mesh.

A possible approach is to use a mesh, whose facets adapt well to material discontinuities. The most popular example of this kind is the tetrahedral mesh. However, its irregular structure makes it hard to handle efficiently. Nevertheless, its low discretization error often makes up for the higher computational effort.

Hexahedral meshes, especially those aligned to a Cartesian coordinate system, offer superior manageability and, in general, yield faster algorithms compared to tetrahedral meshes. Their main disadvantage is the preassigned direction of edges and facets along coordinate lines. Hence, material discontinuities usually cause higher discretizations errors than on a tetrahedral mesh.

Various attempts have been made in order to mitigate this error. For interfaces to perfect electric conductor for example, a technique to retain the numerical method's original convergence rate is well-established [1], [2]. For dielectric interfaces, on the other hand, ongoing research has not yet culminated in a method as efficient and at the same time robust as [1], [2]. The most promising approaches rely on an artificial anisotropic material tensor ([3], [4]). A study on methods based on a priori known field behaviour can be found in [5].

By means of the Finite Integration Technique [6], this contribution's topic is the deduction and application of an alternative approach to achieve good accuracy for skewed dielectric interfaces.

2 Finite Integration Technique

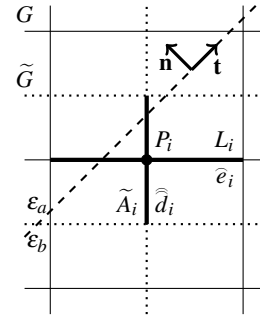


Fig. 1. Portion of a staggered Cartesian grid system (G : primary mesh, \tilde{G} : dual mesh) with material interface (dashed line).

By evaluating the integral form of Maxwell's equations on a staggered grid system consisting of a primary (G) and a dual (\tilde{G}) mesh (cf. Fig. 1), a matrix-vector formulation can be derived:

$$\mathbf{C}\tilde{\mathbf{e}} = -\frac{d}{dt}\tilde{\mathbf{b}}, \quad \tilde{\mathbf{S}}\tilde{\mathbf{d}} = \mathbf{q} \quad (1)$$

$$\tilde{\mathbf{C}}\mathbf{h} = \frac{d}{dt}\tilde{\mathbf{d}} + \mathbf{j}, \quad \mathbf{S}\mathbf{b} = \mathbf{0} \quad (2)$$

For a detailed explanation of the symbols and their relationship cf. [6]. The electric grid voltage vector $\tilde{\mathbf{e}}$ contains the electric field integrated along each primary edge L_i . The corresponding electric grid flux is obtained by integrating the electric displacement \mathbf{D} over the dual facet \tilde{A}_i :

$$\tilde{e}_i = \int_{L_i} \mathbf{E} \cdot d\mathbf{s}, \quad \tilde{d}_i = \iint_{\tilde{A}_i} \mathbf{D} \cdot d\mathbf{A} \quad (3)$$

Similar to the well-known identity $\mathbf{D} = \epsilon\mathbf{E}$, there exists a relationship between electric grid voltages and fluxes, which can be expressed by means of a diagonal matrix \mathbf{M}_ϵ :

$$\widehat{\mathbf{d}} = \mathbf{M}_\varepsilon \widehat{\mathbf{e}} \quad (4)$$

In order to derive a closed form expression for \mathbf{M}_ε , its i th main diagonal entry is evaluated using (3):

$$M_{\varepsilon,i} = \frac{\iint_{\widetilde{A}_i} \mathbf{D} \cdot d\mathbf{A}}{\int_{L_i} \mathbf{E} \cdot d\mathbf{s}} \quad (5)$$

Assuming a material interface, that is strictly parallel or perpendicular to edge L_i , (5) approximates to the following expressions [5]:

$$M_{\varepsilon,i}^{\parallel} = \frac{\widetilde{A}_i \langle \varepsilon \rangle_{\widetilde{A}_i}}{L_i} \quad (6)$$

$$M_{\varepsilon,i}^{\perp} = \frac{\widetilde{A}_i}{L_i \langle \varepsilon^{-1} \rangle_{L_i}} \quad (7)$$

Therein, $\langle \varepsilon \rangle_{\widetilde{A}_i}$ stands for the permittivity's mean value over the dual area \widetilde{A}_i and $\langle \varepsilon^{-1} \rangle_{L_i}$ is the inverse permittivity's mean along the primary edge L_i . Note, that compared to (5), these formulae no longer depend on the electric field or displacement, which enables them to be calculated in preprocessing.

However, very often the assumption of parallel or perpendicular material interfaces can't be met by the mesh. In the following section, a more general approximation to (5) for skewed interfaces is introduced in order to improve accuracy.

3 Generalized Material Averaging

Starting from (5), the electric field \mathbf{E} and displacement \mathbf{D} are decomposed into components tangential (\mathbf{t}) and normal (\mathbf{n}) to the material interface (cf. Fig. 1). Furthermore, the integrations are carried out

- separately for each side of the interface (indices a and b)
- over those components, that are continuous at the interface (\mathbf{E}_t and \mathbf{D}_n)

$$M_{\varepsilon,i} = \frac{\int_{\widetilde{A}_a} (\varepsilon_a \mathbf{E}_t + \mathbf{D}_n) \cdot d\mathbf{A} + \int_{\widetilde{A}_b} (\varepsilon_b \mathbf{E}_t + \mathbf{D}_n) \cdot d\mathbf{A}}{\int_{L_a} \left(\mathbf{E}_t + \frac{1}{\varepsilon_a} \mathbf{D}_n \right) \cdot d\mathbf{s} + \int_{L_b} \left(\mathbf{E}_t + \frac{1}{\varepsilon_b} \mathbf{D}_n \right) \cdot d\mathbf{s}} \quad (8)$$

So far, no approximations are present.

The next step is to assume each integrand being constant over its respective region of integration. This leads to an integral-free formulation of (8). Since, in general, the interface intersects both the primary edge and dual facet, \mathbf{E}_t and \mathbf{D}_n need to be evaluated at up to 4 different locations. Advantageously, the restriction to continuous components reasonably allows for the assumption, that each of them can be replaced by their value at the intersection of edge and facet, denoted by $\mathbf{E}_t|_{P_i}$ and $\mathbf{D}_n|_{P_i}$. The result is the following generalized material averaging formula:

$$M_{\varepsilon,i} \approx \frac{\widetilde{A}_i}{L_i} \frac{\langle \varepsilon \rangle_{\widetilde{A}_i} \mathbf{e}_\xi \cdot \mathbf{E}_t|_{P_i} + \mathbf{e}_\xi \cdot \mathbf{D}_n|_{P_i}}{\mathbf{e}_\xi \cdot \mathbf{E}_t|_{P_i} + \langle \varepsilon^{-1} \rangle_{L_i} \mathbf{e}_\xi \cdot \mathbf{D}_n|_{P_i}} \quad (9)$$

The edge's direction (x , y or z) has to be substituted for ξ .

If the interface is parallel to the ξ -directed edge, the dot product $\mathbf{e}_\xi \cdot \mathbf{D}_n|_{P_i}$ vanishes, $\mathbf{e}_\xi \cdot \mathbf{E}_t|_{P_i}$ cancels out and (6) results. Analogously, (7) follows for a perpendicular interface.

In all other cases, (9) blends facet based averaging ($\langle \varepsilon \rangle_{\widetilde{A}_i}$) with inverse length averaging ($\langle \varepsilon^{-1} \rangle_{L_i}$). Note, that opposed to those methods proposed in [3] and [4], the resulting matrix remains diagonal.

4 Application

In practice, (9) can only be incorporated gradually into existing algorithms, because usually no field information is available a priori.

For an electrostatic example, which is based on iteratively solving a linear system of equations, a modified solver is studied. Initially, the system matrix is built by means of (6) or (7). As soon as the solution is sufficiently accurate, $\mathbf{e}_\xi \cdot \mathbf{D}_n|_{P_i}$ and $\mathbf{e}_\xi \cdot \mathbf{E}_t|_{P_i}$ are estimated where appropriate. Upon updating the system matrix according to (9), the solver is restarted. This procedure can be repeated arbitrarily often. The gain in accuracy is shown to overcompensate the increased computational effort.

References

1. S. Dey and R. Mittra. A locally conformal finite-difference time-domain (FDTD) algorithm for modeling three-dimensional perfectly conducting objects. *IEEE Microwave and Guided Wave Letters*, 7:273–275, 1997.
2. Krietenstein et al. The perfect boundary approximation technique facing the big challenge of high precision field computation. *Proceedings of the XIX International Linear Accelerator Conference (LINAC), Chicago, USA*, 860–862, 1998.
3. A. Farjadpour et al. Improving accuracy by subpixel smoothing in the finite-difference time domain. *Optics Letters*, 31:2972–2974, 2006.
4. C. A. Bauer et al. A second-order 3D electromagnetics algorithm for curved interfaces between anisotropic dielectrics on a Yee mesh. *Journal of Computational Physics*, 230:2060–2075, 2011.
5. C. Classen et al. Local approximation based material averaging approach in the finite integration technique. *IEEE Transactions on Magnetics*, 48:447–450, 2012.
6. T. Weiland. Time domain electromagnetic field computation with finite difference methods. *International Journal of Numerical Modelling: Electronic Networks, Devices and Fields*, 9:295–319, 1996.

DG Treatment of Sliding Interfaces in 3D Eddy Current Problems

Raffael Casagrande¹, Christoph Winkelmann¹, Ralf Hiptmair¹, and Jörg Ostrowski²

¹ ETH Zürich raffael.casagrande@sam.math.ethz.ch,

christoph.winkelmann@sam.math.ethz.ch, hiptmair@sam.math.ethz.ch,

² ABB Switzerland Ltd., Corporate Research joerg.ostrowski@ch.abb.com

Summary. We consider the eddy current model in the presence of rigid moving conductors, a situation commonly encountered in the simulation of electrical machines. Our method exploits the Galilean invariance and uses a Lagrangian description to treat moving parts. The mesh of the dynamic components is moved in every time step which leads to sliding, non-conforming mesh interfaces which are treated in the framework of DG-methods. The resulting system matrix is sparse, symmetric positive semi-definite and is easily solved with iterative methods.

1 Introduction

The Eddy Current model is commonly used for the simulation of various electrical machines. In many cases the design consists of moving, conducting parts which are separated from the static parts by a non-conducting material (e.g. air). Typical applications are electric motors/generators, circuit breakers, railguns or Eddy Current brakes. In order to deal with the moving components, one can define the electro-magnetic fields relative to a laboratory frame and extend Ohm's law by a convective $\sigma \mathbf{v} \times \mathbf{B}$ term (upwinding may be necessary [4]).

However, a more elegant method is obtained by taking a Lagrangian point of view, and attaching the electro-magnetic quantities to the underlying conductor. Because the Eddy Current model is invariant under Galilean transformations [2], there is no need to treat the $\sigma \mathbf{v} \times \mathbf{B}$ term separately (Sect. 3, [3, 6]). This implies the use of separate sub-meshes for the moving and the static parts. Non-conforming interfaces with hanging nodes typically exist between them. Mortar type methods restore the continuity by introducing additional Lagrange multipliers [7]. Alternatively one can consider the problem in mixed form and treat the non-conforming interface with Locally Discontinuous Galerkin techniques [1].

In this work we use a single-variable formulation and handle the hanging nodes with Nitsche's Method [8], also called Symmetric Interior Penalty method (see Sect. 2). The resulting method is easily analyzed in the framework of Discontinuous Galerkin methods and convergence can be proven [3].

2 Non-conforming interfaces

Consider the setting depicted in Fig. 1: There is a conductor Ω_c and two permanent magnets Ω_m which are

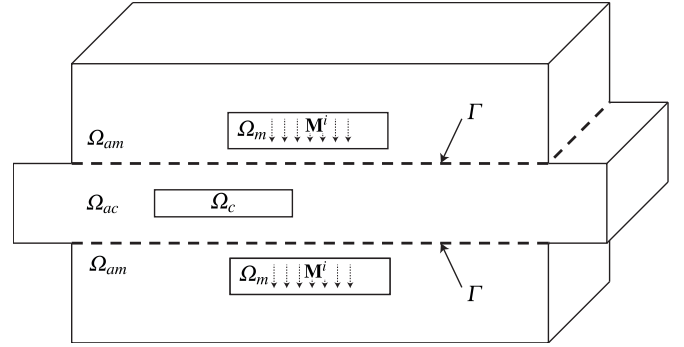


Fig. 1. Cross section of the 3D tube with the airbox and permanent magnet inside.

surrounded by the airbox Ω_{ac} respectively Ω_{am} . We are interested in the magnetic field $\mathbf{B} = \nabla \times \mathbf{A}$ in the domain $\Omega := \Omega_c \cup \Omega_{ac} \cup \Omega_m \cup \Omega_{am}$, and compute it by solving Ampère's Law,

$$\begin{aligned} \nabla \times \left(\frac{1}{\mu} \nabla \times \mathbf{A} \right) &= \nabla \times \mathbf{M}^i, \\ \mathbf{n} \times \mathbf{A} &= 0 \quad \text{on } \partial\Omega. \end{aligned} \quad (1)$$

Herein the material has the constant permeability μ and a magnetization \mathbf{M}^i is prescribed on the permanent magnets ($\text{supp}(\mathbf{M}^i) \subset \Omega_m$). Note that we have deliberately omitted a gauge condition (e.g. $\nabla \cdot \mathbf{A} = 0$) in (1) which would render the solution unique. The advantage is that the resulting system matrix is symmetric positive semi-definite and can be easily solved with the preconditioned conjugate gradient method [5].

For the discretization we require four meshes \mathcal{T}_c , \mathcal{T}_{ac} , \mathcal{T}_m , \mathcal{T}_{am} which are conforming in the respective sub-domains. The global mesh $\mathcal{T} := \mathcal{T}_c \cup \mathcal{T}_{ac} \cup \mathcal{T}_m \cup \mathcal{T}_{am}$ may have *non-conforming* interfaces at $\Gamma := \overline{\Omega_{ac}} \cap \overline{\Omega_{am}}$, but at all other inter-mesh faces the elements have to match.

The discrete solution \mathbf{A}_h is sought in the space

$$W_0^h := \{ \mathbf{A}_h \in R_1(\mathcal{T}_c \cup \mathcal{T}_{ac}) \times R_1(\mathcal{T}_m \cup \mathcal{T}_{am}) \mid \mathbf{n} \times \mathbf{A}_h = 0 \text{ on } \partial\Omega \}, \quad (2)$$

where R_1 is the space of first order edge functions. Note that along Γ the global shape functions are not even *tangentially continuous*, i.e. $W_0^h \not\subset H(\mathbf{curl}; \Omega)$. It is therefore necessary to couple the degrees of freedom across the interface Γ which is realized by penalizing tangential discontinuities. This is incorpo-

rated into the variational formulation which reads as follows (cf. [3]): Find $\mathbf{A}_h \in W_0^h$ such that

$$a_h^{SIP}(\mathbf{A}_h, \mathbf{A}'_h) = (\mathbf{M}^i, \nabla \times \mathbf{A}'_h) \quad (3)$$

for all $\mathbf{A}'_h \in W_0^h$. The bracket (\cdot, \cdot) denotes the usual L_2 inner product and the Symmetric Interior Penalty bilinear form is given by

$$\begin{aligned} a_h^{SIP}(\mathbf{A}_h, \mathbf{A}'_h) &= \int_{\Omega} \left(\frac{1}{\mu} \nabla \times \mathbf{A}_h \right) \cdot (\nabla \times \mathbf{A}'_h) - \\ &\sum_{F \in \mathcal{CT}} \int_F \left\{ \frac{1}{\mu} \nabla \times \mathbf{A}_h \right\} \cdot [\mathbf{A}'_h]_T - \\ &\sum_{F \in \mathcal{CT}} \int_F \left\{ \frac{1}{\mu} \nabla \times \mathbf{A}'_h \right\} \cdot [\mathbf{A}_h]_T + \\ &\sum_{F \in \mathcal{CT}} \frac{\eta}{h_F} \int_F [\mathbf{A}_h]_T \cdot [\mathbf{A}'_h]_T. \end{aligned} \quad (4)$$

Herein $\{\cdot\}$ and $[\cdot]_T$ stand for the vector average, respectively the tangential jump across a face F of the mesh \mathcal{T} and η is the penalty parameter (which must be chosen sufficiently large) [3].

3 Moving frame of reference

In this section we study the evolution of the magnetic field $\mathbf{B} = \nabla \times \mathbf{A}$; We start from the initial situation depicted in Fig. 1 and begin to move the conductor together with its airbox to the right with prescribed velocity $\mathbf{v}_m(t)$. The initial state is thus given by the solution of (3) and the evolution over time is naturally described by the \mathbf{A} -based eddy current model which, expressed in laboratory coordinates \mathbf{x} , reads as

$$\sigma \frac{\partial \mathbf{A}}{\partial t} + \nabla \times \left(\frac{1}{\mu} \nabla \times \mathbf{A} \right) = \nabla \times \mathbf{M}^i + \sigma \mathbf{v} \times (\nabla \times \mathbf{A}). \quad (5)$$

Herein the scalar conductivity σ is zero in $\Omega_{ac}(t) \cup \Omega_{am}$ and positive in $\Omega_m \cup \Omega_c(t)$, and $\mathbf{v}(\mathbf{x}, t)$ is the local velocity field.

Furthermore we introduce the moving coordinate system $\tilde{\mathbf{x}}(\mathbf{x}, t) = \mathbf{x} - \int_0^t \mathbf{v}_m(\tau) d\tau$ such that it follows the moving subdomains $\Omega_c(t) \cup \Omega_{ac}(t)$.

Thanks to the Galilean invariance [2] the eddy current equation (5) takes exactly the same form if it is expressed w.r.t. the local coordinate system $\tilde{\mathbf{x}}$:

$$\begin{aligned} \sigma \frac{\partial \tilde{\mathbf{A}}(\tilde{\mathbf{x}}, t)}{\partial t} + \tilde{\nabla} \times \left(\frac{1}{\mu} \tilde{\nabla} \times \tilde{\mathbf{A}}(\tilde{\mathbf{x}}, t) \right) = \\ \tilde{\nabla} \times \tilde{\mathbf{M}}^i(\tilde{\mathbf{x}}) + \sigma \tilde{\mathbf{v}} \times (\tilde{\nabla} \times \tilde{\mathbf{A}}(\tilde{\mathbf{x}}, t)). \end{aligned} \quad (6)$$

The quantities in the moving frame are related to the quantities in the rest frame by [6]

$$\begin{aligned} \tilde{\mathbf{E}} &= \mathbf{E} + \mathbf{v}_m \times \mathbf{B}, & \tilde{\mathbf{B}} &= \mathbf{B}, & \tilde{\mathbf{M}}^i &= \mathbf{M}^i, \\ \tilde{\mathbf{v}} &= \mathbf{v} - \mathbf{v}_m, & \tilde{t} &= t, & \tilde{\mu} &= \mu, & \tilde{\sigma} &= \sigma, \end{aligned} \quad (7)$$

which is accomplished by the transformation [3]

$$\tilde{\mathbf{A}} = \mathbf{A} - \int_0^t \nabla(\mathbf{v}_m \cdot \mathbf{A}) d\tau. \quad (8)$$

A proof of this will be presented in the full paper.

Note that the convective term in (6), disappears in $\Omega_c(t) \cup \Omega_{ac}(t)$ because $\mathbf{v} = \mathbf{v}_m$. The same holds for the convective term of (5) in $\Omega_m \cup \Omega_{am}$.

Because we work in Lagrangian variables this suggests the following scheme: We discretize the temporal derivative in (6) with the implicit Euler scheme and move the meshes \mathcal{T}_c , \mathcal{T}_{ac} in every time step by $\mathbf{v}_m(t) \Delta t$. The moving and the static subdomains are coupled across the non-conforming interface Γ by penalizing jumps (Sect. 2). We choose to treat the vector average and tangential jumps in (4) in the moving coordinate system $\tilde{\mathbf{x}}$. I.e. we have to transform the values of \mathbf{A} and \mathbf{M}^i in Ω_{am} by (7).

The resulting system matrix is again symmetric positive semi-definite and only the coupling terms between the static and the dynamic part have to be re-assembled in every time step.

It has already been shown by one of the authors that 2D rotating bodies are successfully simulated by a similar method [3]. The presented approach is an extension of this idea to 3D. The results will be presented at the conference.

References

1. P. Alotto, A. Bertoni, I. Perugia and D. Schotzau. Efficient use of the local discontinuous Galerkin method for meshes sliding on a circular boundary. *Magnetics, IEEE Transactions on.*, 38:405-408, 2002.
2. A. Bossavit. On the numerical analysis of eddy-current problems. *Computer Methods in Applied Mechanics and Engineering.*, 27:303-318, 1981.
3. R. Casagrande. Sliding Interface for Eddy Current Simulations. Master's thesis, ETH Zürich, 2013.
4. T. Furukawa, k. Komiya and I. Muta. An upwind Galerkin finite element analysis of linear induction motors. *Magnetics, IEEE Transactions on.*, 26:662-665, 1990.
5. E. Kaasschieter. Preconditioned conjugate gradients for solving singular systems. *Journal of Computational and Applied Mathematics.*, 24:265-275, 1988.
6. S. Kurz, J.Fetzer, G. Lehner and W. Rucker. A novel formulation for 3D eddy current problems with moving bodies using a Lagrangian description and BEM-FEM coupling. *Magnetics, IEEE Transactions on.*, 34:3068-3073, 1998.
7. F. Rapetti, Y. Maday, F. Bouillault, A. Razek. Eddy-current calculations in three-dimensional moving structures. *Magnetics, IEEE Transactions on.*, 38:613-616, 2002.
8. R. Stenberg. Mortaring by a method of JA Nitsche. *Computational mechanics*, 1998.

A symmetric and low-frequency stable potential formulation for the finite-element simulation of electromagnetic fields

Martin Jochum¹, Ortwin Farle¹, and Romanus Dyzcij-Edlinger¹

Chair for Electromagnetic Theory, Saarland University, Germany, m.jochum@lte.uni-saarland.de, o.farle@lte.uni-saarland.de, edlinger@lte.uni-saarland.de

Summary. Static, quasi-static, and transient electromagnetic fields have traditionally been treated by separate numerical methods. By disregarding displacement currents or any time-derivatives at all, the respective formulations achieve minimum complexity and maximum performance. However, there do exist cases, e.g. in mixed-signal analysis or model-order reduction, where it is convenient, or even necessary, to have a single mathematical formulation that covers the whole range from statics to wave propagation. This paper presents a new low-frequency stable formulation of the time-harmonic Maxwell equations, which is suitable for the finite-element analysis of structures that comprise lossy and/or lossless materials. Numerical examples demonstrate the benefits of the suggested approach.

1 Notation

In the following, subscript C and N , respectively, stands for conducting and non-conducting material. Let Ω be a field domain that consists of lossy and lossless regions, Ω_C and Ω_N , which may share a common interface Γ_{NC} . The unit normal vector on Γ_{NC} from Ω_C to Ω_N is denoted by $\hat{\mathbf{n}}_{NC}$. So we have

$$\overline{\Omega_C} \cup \overline{\Omega_N} = \overline{\Omega}, \quad (1)$$

$$\overline{\Omega_C} \cap \overline{\Omega_N} = \Gamma_{NC}, \quad (2)$$

$$\Omega_C \cap \Omega_N = \emptyset. \quad (3)$$

We consider the time-harmonic Maxwell equations in the frequency domain and denote the phasors of the electric field intensity, magnetic flux density, and impressed current density by \mathbf{E} , \mathbf{B} , and \mathbf{J}_i . The wavenumber, characteristic impedance, and light speed of free space are abbreviated by k_0 , η_0 , and c_0 , and the relative magnetic reluctivity, relative electric permittivity, and electric conductivity by ν_r , ϵ_r , and σ .

2 Low-Frequency Instability

The most common finite-element (FE) formulation for wave-propagation problems is in terms of \mathbf{E} . The corresponding partial differential equation (PDE) reads

$$\nabla \times (\nu_r \nabla \times \mathbf{E}) + ik_0 \eta_0 \sigma \mathbf{E} - k_0^2 \epsilon_r \mathbf{E} = -ik_0 \eta_0 \mathbf{J}_i. \quad (4)$$

Applying the divergence operator confirms that, for non-zero wavenumbers, (4) imposes the continuity equation of the electric current density in Ω_C and the

electric flux balance in Ω_N . In (4), however, these conditions are multiplied by k_0 and, thus, vanish in the static limit. As a result, the stability constant worsens as k_0 decays and, finally, at $k_0 = 0$, the formulation becomes ambiguous.

Even though improved methods have been proposed to alleviate the problem [1–4], none is completely satisfactory: [1] does not fully cover the lossy case, [2] lacks unique solutions, [3] utilizes numerical breakdown of the FE matrix factorization, and [4] requires a suitably chosen LF threshold.

3 Low-Frequency Stable Formulation

To prevent the difficulties described in Section 2, we propose a gauged potential formulation which is based on the magnetic vector potential \mathbf{A} as well as the scalar potentials V and Ψ . Specifically, we have

$$\mathbf{B} = \nabla \times \mathbf{A}, \quad (5)$$

$$\mathbf{E} = -\nabla V - ik_0 c_0 (\mathbf{A} + \nabla \Psi). \quad (6)$$

The gauge is imposed by the following measures: In the discretization process, the magnetic vector potential is taken from an FE subspace of non-vanishing curl, which is realized by a tree-cotree splitting [5]. This restriction will be indicated by \mathbf{A}^c . Moreover, we impose the gauge conditions

$$\nabla \cdot [(\eta_0 \sigma + ik_0 \epsilon_r)(\mathbf{A}^c + \nabla \Psi)] = 0 \quad \text{in } \Omega_C, \quad (7)$$

$$\Psi = 0 \quad \text{in } \Omega_N. \quad (8)$$

Equation (8) means that the support of Ψ is restricted to $\overline{\Omega_C}$. As will be detailed in the full paper, the PDE (7) needs to be supplemented by an additional boundary condition on the interface Γ_{NC} :

$$\begin{aligned} & [(\eta_0 c_0 \sigma_C + ik_0 c_0 \epsilon_{r,C})(\mathbf{A}_C^c + \nabla \Psi_C)] \cdot \hat{\mathbf{n}}_{NC} \\ & = [\epsilon_{r,N} (\nabla V_N + ik_0 c_0 \mathbf{A}_N^c)] \cdot \hat{\mathbf{n}}_{NC}. \end{aligned} \quad (9)$$

The proposed formulation always satisfies the whole set of the Maxwell equations and is therefore applicable to the whole range from statics to wave propagation, without any user-defined LF threshold. Moreover, the resulting FE matrices are symmetric and, aside from undamped resonances, the solutions are unique. Compared to the popular field formulation, the price to be paid is an additional scalar potential in the conducting region Ω_C .

4 Numerical Examples

4.1 Partially lossy cavity resonator

To demonstrate the LF stability of the proposed formulation, we consider the half-filled resonator of [6]. Figure 1 presents the condition number of the FE matrix as a function of frequency. In case of the field formulation, it grows strongly with decreasing frequency. The observed saturation in the order of 10^{17} is due to numerical noise; at this point the FE matrix is virtually singular. In contrast, the condition number of the new approach remains almost constant.

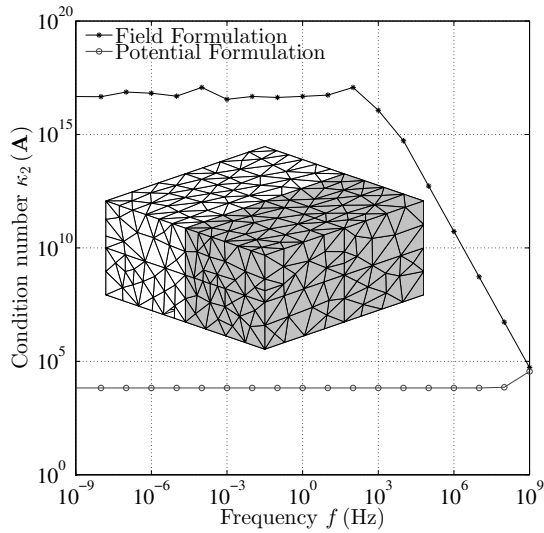


Fig. 1. Condition number of FE matrix versus frequency. Inset shows resonator of dimensions $22.86 \times 2 \cdot 11.43 \times 10.16 \text{ mm}^3$. Materials: $\epsilon_{r,N} = 1$, $\mu_{r,N} = 1$, $\sigma_N = 0 \text{ S/m}$; $\epsilon_{r,C} = 2$, $\mu_{r,C} = 1$, $\sigma_C = 1 \text{ S/m}$.

4.2 RLC circuit

Our goal is to demonstrate qualitatively that the proposed formulation captures resistive, inductive, and capacitive effects correctly over the whole range from statics to the high-frequency regime. For this purpose, we examine a simple voltage-driven RLC series circuit using a wire of finite conductivity. The corresponding FE mesh is given in Fig. 2. The resulting field distributions of \mathbf{E} , \mathbf{B} , and the conduction current density $\mathbf{J}_c = \sigma \mathbf{E}$ are shown in Fig. 3: In the static case, the capacitor imposes an open circuit; both current density and magnetic field vanish. In contrast, at 1 MHz there is significant current flow, and the accompanying magnetic field is particularly strong inside the inductor. Moreover, eddy current effects cause a marked decay in \mathbf{J}_c in the interior of the wire.

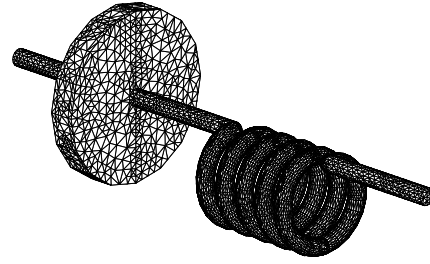


Fig. 2. FE mesh of RLC circuit.

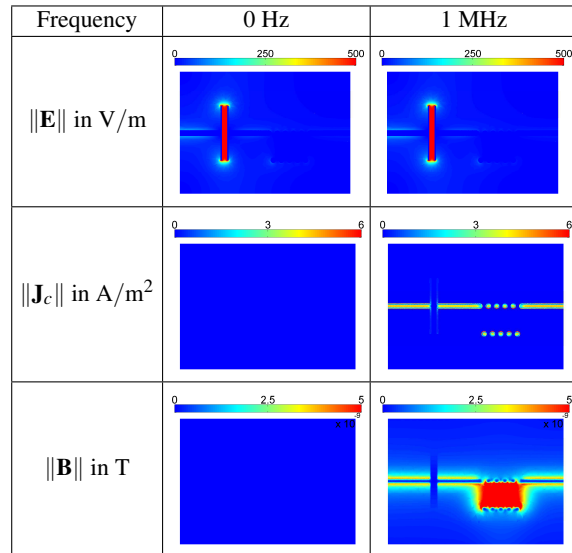


Fig. 3. RLC circuit: field distributions in static and HF case.

References

1. R. Dyczij-Edlinger, G. Peng, J.-F. Lee, *Efficient finite-element solvers for the Maxwell equations in the frequency domain*, *Comput. Methods Appl. Mech. Engrg.*, vol. 169, no.3, pp. 297-309, Feb. 1999.

2. R. Hiptmair, F. Kramer, J. Ostrowski, *A Robust Maxwell Formulation for All Frequencies*, *IEEE Trans. Magn.*, vol. 44, no. 6, pp. 682-685, June 2008.
3. H. Ke, T. H. Hubing, F. Maradei, *Using the LU Recombination Method to Extend the Application of Circuit-Oriented finite-element Methods to Arbitrarily Low Frequencies*, *IEEE Trans. Microwave Theory Techn.*, vol. 58, no. 5, pp. 1189-1195, May 2010.
4. J. Zhu, D. Jiao, *Fast Full-Wave Solution that Eliminates the Low-Frequency Breakdown Problem in a Reduced System of Order One*, *IEEE Trans. Compon. Packag. Manuf. Technol.*, vol. 2, no. 11, pp. 1871-1881, Nov 2012.
5. J. B. Manges, Z. J. Cendes, *A generalized tree-cotree gauge for magnetic field computation*, *IEEE Trans. Magn.*, vol. 31, no. 3, pp. 1342-1347, May 1995.
6. Y. Zhu, A. C. Cangellaris, *Robust finite-element solution of lossy and unbounded electromagnetic eigenvalue problems*, *IEEE Trans. Microwave Theory Techn.*, vol. 50, no. 10, pp. 2331-2338, Oct 2002.

Systematic Determination of Eigenfields in Frequency Domain

Todorka Banova^{1,2}, Wolfgang Ackermann¹, and Thomas Weiland¹

¹ Institut für Theorie Elektromagnetischer Felder (TEMF), Technische Universität Darmstadt, Schlossgartenstr. 8, D-64289 Darmstadt {banova, ackermann, thomas.weiland}@temf.tu-darmstadt.de

² Graduate School of Computational Engineering, Technische Universität Darmstadt, Dolivost. 15, D-64293 Darmstadt

Summary. This paper presents numerical procedures applied to the accurate and robust calculation of thousands of eigenfrequencies for the Dirac billiard resonator. The eigenfield calculations are accomplished in two steps. Initially, the finite integration technique or the finite element method is used, and further, the (B-)Lanczos method with its variations is exploited for the eigen pair determination. The comparison of the numerical results to the experiments confirms the applicability of the approaches and points out the significant reductions of computational costs.

1 Introduction

Over the last years, the increasing number of applications has stimulated the development of new methods and software for the numerical solution of large-scale eigenvalue problems. At the same time, the realistic applications frequently challenge the limit of both computer hardware and numerical algorithms, as one might possibly need large number of eigen pairs for matrices with dimension in excess of several millions. In the present work, the investigations of the properties of a graphene using a microwave photonic crystal (Dirac billiard) [1] also emphasize the necessity for calculation of thousands of interior eigenfrequencies.

Reflecting the fact that an analytical solution for the electromagnetic problem of a Dirac billiard is not available, this work resorts to a numerical solution. Namely, if the finite element method [2] is utilized to solve the electromagnetic problem of a superconducting cavity, the numerical solution of a generalized large-scale eigenvalue problem

$$A \mathbf{x} = \lambda B \mathbf{x} \quad (1)$$

for given real symmetric matrices A and B is considered at the end. Thereon, the algebraic eigenvalue problem is solved with the B-Lanczos solvers [3]. Supposing that the numerical solution of the same problem is treated by the finite integration technique [4], finally it yields to a standard eigenvalue problem

$$A \mathbf{x} = \lambda \mathbf{x} \quad (2)$$

for a given symmetric sparse matrix $A \in \mathbb{R}^{n \times n}$.

Despite the fact that various types of numerical methods for eigenvalue determination (Krylov-Schur, Jacobi-Davidson, Arnoldi) are available in different

software packages, not as many are specifically adapted for computing thousands of eigen pairs. The Lanczos method [5] with its variations is very attractive for the project necessities, as it reduces the original eigenvalue problem to a tridiagonal one. Among the basic implementations of the Lanczos algorithm, a combination with a filtering method is used as a valuable tool to enable the computation of interior eigen pairs. Moreover, the implementations exploit all parallelism from a multithreaded and multiprocess implementation of the used libraries.

2 Eigenvalue Determination in Frequency Domain

Within this work, the excited electromagnetic fields inside closed resonators are considered under the assumption of perfectly electric conducting walls. Prior to frequency-domain simulations, the related geometry is modeled and decomposed into tetrahedral elements with the CST Microwave Studio. Afterward, the corresponding mesh information is passed to the CEM3D solver [2] in order to produce the sparse matrices that are used as input for the eigenmode solvers.

2.1 Lanczos Method with Polynomial Filtering

The Lanczos algorithm with polynomial filtering replaces the matrix-vector product $A \mathbf{v}_j$ in the Lanczos algorithm [3] by $\rho(A) \mathbf{v}_j$, where ρ is a polynomial being determined from the knowledge on the distribution of the sought eigenvalues. The main goal of the polynomial filtering is to enhance the Lanczos projection scheme by processing the vectors \mathbf{v}_j , such that their components in the unwanted parts of the spectrum are relatively reduced to those in the wanted parts. It should be noted that the matrices A and $\rho(A)$ share the same eigenvectors, and the matrix $\rho(A)$ has eigenvalues $\rho(\lambda_1), \dots, \rho(\lambda_n)$, where $\lambda_1, \dots, \lambda_n$ are the eigenvalues of the matrix A .

A fundamental problem lies in computing an appropriate polynomial ρ in order to approximate a step function that covers the interval of the desired eigenvalues $[\xi, \eta]$. If the polynomial $\rho(\lambda)$ is chosen such that $\rho([\xi, \eta])$ is in an extreme region of the spectrum, the eigenvalues of the matrix $\rho(A)$ in $\rho([\xi, \eta])$ will be approximated first. However, a high-degree polynomial approximation to a discontinuous step function

exhibits parasitic oscillations. Therefore, a two-stage process [6] is adapted. First, a smooth function similar to the step function is selected and then a polynomial approximation $\rho(\lambda)$ to this function is applied in the least-squares sense. A variant, known as the filtered conjugate residual polynomial algorithm is proposed in [6]. Here, the functions are expanded in the proper scaled and shifted basis of the Chebyshev polynomials.

3 Application Example: Dirac Billiard

The dedicated eigenmode solvers are implemented in C++ and based on PETSc data structures. Additionally, the PETSc library enables parallel computing by employing the MPI standard for all message-passing communication. Moreover, the implemented solvers employ the Intel MKL 10.2 library with LAPACK¹. In case of the standard eigenvalue problem (2), the algorithm presented in Sect. 2.1 performs repeated computations of matrix-vector products, which are the only large-scale operations included within this approach. On the other hand, the solution of the problem (1) introduces a factorization of the matrix B . The details are omitted and can be found in [3].

The frequency spectrum from 19 GHz to 31 GHz is numerically calculated and then, compared with the measurements². During the measurements, the analyzed structure is cooled down to a temperature of 4.2 K, which is naturally accompanied with a geometrical shrinkage. Thus, the raw measurement data are scaled with a factor that compensates for the difference in the dimensions of the measured and the simulated structure. In the numerical studies, the eigenfrequencies are determined for the cases when the Dirac billiard is discretized with 4,515,840 hexahedrons and 630,348 tetrahedrons by using the Lanczos solver with polynomial filtering and the B-Lanczos solver with shift-and-invert, respectively. Finally, the results for the level-density analysis are compared in Fig. 1 and evidently, the measured spectrum closely resembles those obtained by the numerical simulations. In the considered frequency spectrum, only one band with a Dirac point around 23.5 GHz is present. Below 19 GHz and above 31 GHz band gaps can be noticed.

Table 1. Computational costs.

	Lanczos with polynomial filtering	B-Lanczos with shift-and-invert
Eigenfrequencies	1,656	1,656
Time (days)	0.4	1.6
Memory/eig (MB)	201.3	295.2

¹ The used libraries will be referenced in the full paper.

² The measurements are kindly provided from the Institute for Nuclear Physics at TU Darmstadt.

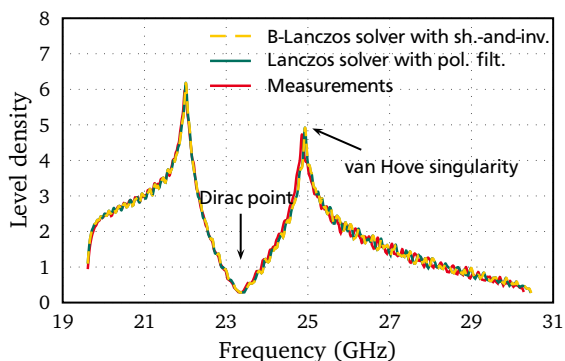


Fig. 1. Level-density analysis for a Dirac billiard.

In terms of computational resources, it was experienced that 15 cluster nodes are suited for problems with more than 10^6 mesh cells when using the Lanczos solver with polynomial filtering. Each node has two six-core Intel Xeon X5650 3.0 GHz processors and 24 GB main memory. On the other side, the B-Lanczos solver with shift-and-invert is run on a powerful computer with 256 GB of RAM memory and two quad-core Intel Xeon E5-2643 processors, clocked at 3.3 GHz. The computational costs for the eigen pair determination are summarized in Table 1.

Acknowledgement. This work was supported by the ‘‘Excellence Initiative’’ of the German Federal and State Governments and the Graduate School of Computational Engineering at TU Darmstadt.

References

1. S. Bittner, B. Dietz, M. Miski-Oglu, and A. Richter. Extremal transmission through a microwave photonic crystal and the observation of edge states in a rectangular Dirac billiard. *Phys. Rev. B*, 85(6), 2012.
2. W. Ackermann, G. Benderskaya, and T. Weiland. State of the art in the simulation of electromagnetic fields based on large scale finite element eigenanalysis. *ICS Newsletter*, 17(2):3–12, 2010.
3. T. Banova, W. Ackermann, and T. Weiland. Accurate determination of thousands of eigenvalues for large-scale eigenvalue problems. *IEEE Trans. Magn.*, 50(2):481–484, 2014.
4. T. Weiland. A discretization method for the solution of Maxwell’s equations for six-component fields. *Electronics and Communication (AEÜ)*, 31(3):116–120, 1977.
5. C. Lanczos. An iteration method for the solution of the eigenvalue problem of linear differential and integral operators. *J. Res. Natl. Bur. Stand.*, 45(4):255–282, 1950.
6. Y. Saad. Filtered conjugate residual-type algorithms with applications. *SIMAX*, 28(3):845–870, 2006.

Iterative Schemes for Coupled Multiphysical Problems in Electrical Engineering

Sebastian Schöps^{1,2}

¹ Technische Universität Darmstadt, Graduate School for Computational Engineering, Dolivostrasse 15, Darmstadt

² Technische Universität Darmstadt, Institut für Theorie Elektromagnetischer Felder, Schlossgartenstrasse 8, Darmstadt
schoeps@gsc.tu-darmstadt.de

Summary. This contribution addresses iterative coupling schemes for coupled model descriptions in computational electromagnetics. Theoretical issues of accuracy, stability and numerical efficiency of the resulting formulations are addressed along with advantages and disadvantages of the various approaches. Three application examples are given: field-circuit coupling, a mechanical-electromagnetic and thermal-electromagnetic problem.

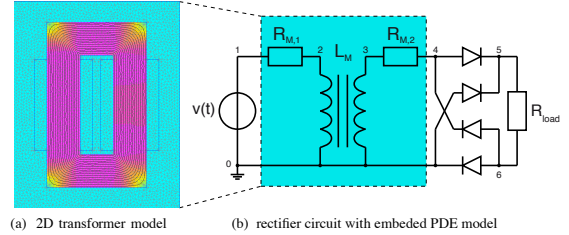


Fig. 1. Simple field-circuit coupled problem.

1 Introduction

Today, due to increased accuracy of modeling and simulation, multiphysical problems become more and more important in many engineering applications. Often a monolithic approach, i.e., the solution of all subproblems at once, is cumbersome or even impossible because incompatible algorithms or software packages are involved. Thus simulation engineers need to couple subproblems in an efficient and stable way, where subdomains are solved separately. This introduces a splitting error, which is mitigated by an iterative procedure.

In this contribution we like to advertise the increased accuracy and stability due to iterative procedures by discussing three examples: field-circuit coupling in Section 1, a mechanical-electromagnetic problem in Section 2 and finally a thermal-electromagnetic problem in Section 3. In the full contribution also implementation issues and the practical relevance of those iteration schemes will be discussed.

2 Field-Circuit Problem

For field-circuit coupled models of electrical energy transducers, two general approaches are well established. A first approach consists of extracting lumped parameters or surrogate models from a field model and inserting these as a netlist into a Spice-like circuit simulator. This is circumvented by monolithic coupling, where field and circuit models are solved together. We propose a particular synthesis: the parameter extraction is applied iteratively on time intervals. The eddy-current field problem on Ω is

$$\sigma \partial_t \mathbf{a}^{(n)} + \nabla \times \left(\mathbf{v}(|\nabla \times \mathbf{a}^{(n)}|) \nabla \times \mathbf{a}^{(n)} \right) = \boldsymbol{\chi} \mathbf{j}^{(n)}$$

where $\mathbf{a}^{(n)}$ is the magnetic vector potential after the n -th iteration (with homogeneous Dirichlet conditions), σ and \mathbf{v} are conductivity and reluctivity, respectively and the winding functions $\boldsymbol{\chi} = [\chi_1, \dots, \chi_k, \dots, \chi_K]^T$ are functions of space that distribute the lumped currents \mathbf{j} in the 3D domain. The circuit coupling is established via integration

$$\partial_t \int_{\Omega} \chi_k \mathbf{a}^{(n)} dx + R_k j_k^{(n)} = v_k^{(n-1)} \quad k = 1, \dots, K$$

to the circuit system of differential algebraic equations

$$\begin{aligned} \mathbf{A}_C \partial_t \mathbf{q}_C (\mathbf{A}_C^T \mathbf{u}^{(n)}, t) + \mathbf{A}_R \mathbf{g}_R (\mathbf{A}_R^T \mathbf{u}, t) + \mathbf{A}_L \mathbf{i}_L^{(n)} \\ + \mathbf{A}_M \mathbf{j}^{(n)} + \mathbf{A}_V \mathbf{i}_V^{(n)} + \mathbf{A}_I \mathbf{i}_s(t) = 0, \\ \partial_t \Phi_L (\mathbf{i}_L^{(n)}, t) - \mathbf{A}_L^T \mathbf{u} = 0, \\ \mathbf{A}_V^T \mathbf{u} - \mathbf{v}_s(t) = 0, \end{aligned}$$

with incidence matrices \mathbf{A}_* where $\mathbf{v}_* = \mathbf{A}_*^T \mathbf{u}$ and constitutive laws for conductances, inductances and capacitances (functions with subscripts R, L and C), independent sources \mathbf{i}_s and \mathbf{v}_s , unknowns are the potentials \mathbf{u} and currents \mathbf{i}_L and \mathbf{i}_V .

In the full paper the convergence, [1, 2], of this iteration scheme and tailored time integration will be discussed. It will be shown that the optimal time integration order depends on the iteration counter n , [6].

3 Field-Mechanical Problem

The Lorentz detuning of an accelerating cavity, which is the change of the resonant frequency due to the mechanical deformation of the cavity wall induced by the

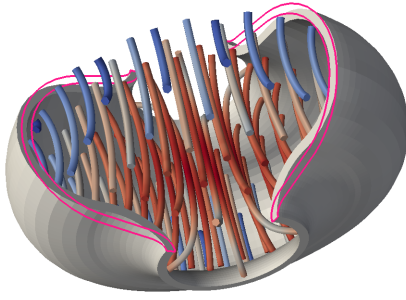


Fig. 2. One cavity cell with field lines and exaggerated deformation, [3]

electromagnetic pressure is a coupled electromagnetic-mechanical problem. In a first step, Maxwell's eigenproblem is solved

$$\nabla \times \left(\frac{1}{\mu_0} \nabla \times \mathbf{e}^{(n)} \right) = \omega_0^2 \varepsilon_0 \mathbf{e}^{(n)} \quad \text{on } \Omega^{(n-1)}$$

where \mathbf{e} is the phasor of the electric field with adequate boundary conditions; μ_0 and ε_0 are the permeability and permittivity of vacuum. From this the magnetic field \mathbf{h} can be obtained. Both fields create a radiation pressure at the boundary of $\Omega^{(n-1)}$

$$p^{(n)} = -\frac{1}{2} \varepsilon_0 e_{\perp}^{(n)} \left(e_{\perp}^{(n)} \right)^* + \frac{1}{2} \mu_0 \mathbf{h}_{\parallel}^{(n)} \left(\mathbf{h}_{\parallel}^{(n)} \right)^*$$

which gives rise to the linear elasticity problem in the wall of the cavity

$$\nabla \cdot \left(2\eta \nabla^{(S)} \mathbf{u} + \lambda \mathbf{I} \nabla \cdot \mathbf{u} \right) = 0$$

for the displacement $\mathbf{u}^{(n)}$ where $p^{(n)}$ is a boundary condition on the inner boundary. We denote by $\nabla^{(S)}$ the symmetric gradient, while η and λ are the Lamé constants. Finally a deformed domain

$$\Omega^{(n)} \equiv \left\{ \mathbf{x} + \mathbf{u}^{(n)}(\mathbf{x}), \mathbf{x} \in \Omega^{(0)} \right\},$$

is derived from the initial domain $\Omega^{(0)}$ and the iteration can be restarted with the computation of an eigenvalue. In the full paper this scheme will be discussed in more details. The focus will be on the spatial discretization with Isogeometric Analyses using Non-Uniform Rational B-Spline (NURBS) and De-Rham-conforming B-Splines [3].

4 Field-Thermal Problem

In the previous sections we have discussed the mutual coupling of transient and frequency-domain to static problems. The third example revisits the well-known iterative coupling of frequency to time domain problems. Again, the electromagnetic field is given by the curl-curl equation, however since we are in frequency domain we can regard displacement currents

$$\varepsilon \omega^2 \mathbf{a}^{(n)} + \sigma(T^{(n-1)}) j \omega \mathbf{a}^{(n)} + \nabla \times (\nu \nabla \times \mathbf{a}^{(n)}) = \chi \mathbf{j}.$$

where \mathbf{a} is now a complex phasor. This is coupled to the heat equation

$$\rho c \partial_t T^{(n)} = \nabla \cdot (k \nabla T^{(n)}) + Q(\mathbf{a}^{(n)}, t)$$

by the Joule losses Q , where k is the heat conductivity, ρ the density and c the specific heat capacity. Besides the electric conductivity σ , all material parameters are constant. The important modelling step is to relax the coupling of both problems by introducing a averaged heat source

$$\bar{Q}^{(n)} := \frac{1}{t_1 - t_0} \int_{t_0}^{t_1} Q(\mathbf{a}^{(n)}(t), t) ds.$$

obtained by converting the vector potential a back to the time domain. Convergence will be discussed in view of the works [4, 5] and the fractional step method, [7].

Acknowledgement. Many people have contributed to this work. The author likes to thank A. Bartel, M. Brunk, M. Clemens, J. Corno, H. De Gersem, C. de Falco, M. Günther, C. Kaufmann and E.J.W. ter Maten. This work is supported by the German BMBF in the context of the SIMUROM project (grant 05M2013), by the ‘Excellence Initiative’ of the German Federal and State Governments and the Graduate School of Computational Engineering at TU Darmstadt.

References

1. A. Bartel, M. Brunk, M. Günther, and S. Schöps. Dynamic iteration for coupled problems of electric circuits and distributed devices. *SIAM J. Sci. Comput.*, 35(2):B315–B335, 2013.
2. A. Bartel, M. Brunk, and S. Schöps. On the convergence rate of dynamic iteration for coupled problems with multiple subsystems. *J. Comput. Appl. Math.*, 262:14–24, 2014.
3. J. Corno, C. de Falco, H. De Gersem, and S. Schöps. Iso-geometric simulation of lorentz detuning in superconducting accelerator cavities. Presented at CEFC 2014. In prep. 2014.
4. C. Kaufmann, M. Günther, D. Klagges, M. Knorrenschild, M. Richwin, S. Schöps, and E.J.W. ter Maten. Efficient frequency-transient co-simulation of coupled heat-electromagnetic problems. *Journal of Mathematics in Industry*, 2014. To be published.
5. C. Kaufmann, M. Günther, D. Klagges, M. Richwin, S. Schöps, and E. J. W. ter Maten. Coupled heat-electromagnetic simulation of inductive charging stations for electric vehicles. In *Progress in Industrial Mathematics at ECMI 2012*, Mathematics in Industry, 2014. Springer. To be published.
6. S. Schöps, A. Bartel, and M. Günther. An optimal p-refinement strategy for dynamic iteration of ordinary and differential-algebraic equations. In *PAMM*, volume 13, pages 549–552, 2013.
7. P. K. Vijalapura, J. Strain, and S. Govindjee. Fractional step methods for index-1 differential-algebraic equations. *J. Comput. Phys.*, 203(1):305–320, 2005.

Modeling and Simulation of Inductive Heating involving Mechanical Deformations

Qingzhe Liu¹, Thomas Petzold², Dawid Nadolski³, and Roland Pulch¹

¹ Institut für Mathematik und Informatik, Ernst Moritz Arndt Universität Greifswald, 17487 Greifswald
liuq, pulchr@uni-greifswald.de

² Weierstraß-Institut, Mohrenstr. 39, 10117 Berlin Thomas.Petzold@wias-berlin.de

³ Stiftung Institut für Werkstofftechnik IWT, Badgasteiner Str. 3, 28359 Bremen nadolski@iwt-bremen.de

Summary. Inductive heating is one of the most important surface hardening procedures for enhancing mechanical properties of components made from steel. In practice there exists a growing demand of pre-experiments for proper adjustment of a set-up for induction hardening of a newly designed component. We report the model and simulation of inductive heating, especially present numerical results of mechanical effects like the residual stress distribution and thermally induced distortions.

1 The model

Inductive heating is one of the most important surface hardening procedures for enhancing mechanical properties of components made from steel. Fig. 1 depicts the inductive heating of a disc from steel. A mathematical treatment of induction hardening has been intensively investigated during the last years, see e.g. [2, 4, 5]. To model the coupled problem of



Fig. 1. Induction heat treatment (by Stiftung Institut für Werkstofftechnik IWT, Bremen)

electro-thermal-stress in the process of inductive heating we first define spatial computational domains. Let $D \subset \mathbb{R}^3$ be a domain which contains the inductor Ω and the workpiece Σ , then we consider the governing equations of the electromagnetic field, the temperature evolution, the mechanical deformations and stresses as well as the steel phase transformations as follows:

$$\begin{aligned} \gamma \partial_t A + \operatorname{curl} \mu^{-1} \operatorname{curl} A - J_{src} &= 0, & \text{in } D \\ \rho c_\epsilon \partial_t \theta - \operatorname{div} \kappa \nabla \theta &= F, & \text{in } \Sigma \\ -\operatorname{div} \sigma &= 0, & \text{in } \Sigma \\ \dot{z} - f(z, \theta, t) &= 0, & \text{in } \Sigma \end{aligned} \quad (1)$$

where the variables (A, θ, σ, z) denote the magnetic vector potential, the temperature, stress tensor and phase fraction, respectively. The material dependent

parameters $(\gamma, \mu, \rho, c_\epsilon, \kappa)$ denote electrical conductivity, magnetic permeability, density of the workpiece, specific heat and heat conductivity. J_{src} denotes the source current density satisfying $-\operatorname{div} J_{src} = 0$, F summarizes the source term caused by Joule heat, mechanical dissipation and latent heat due to phase transitions. Here the vector potential formulation of Maxwell's equations is taken into account, the heating equation has been derived from energy balance, the deformation equation is based on balance of momentum, the governing equations of phase transitions that are caused by the enormous changes of temperature during the heat treatment arise from the Johnson-Mehl-Avrami equation and Schröder's approach, see e.g. [1]. Fig. 2 depicts the interrelations among these physical model components.

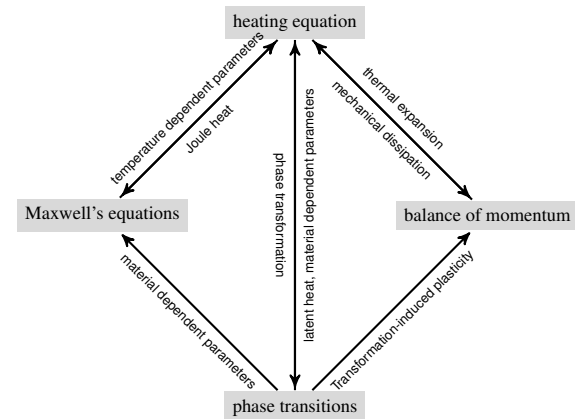


Fig. 2. Electro-thermal-stress coupling

2 Numerical discretization

The workpiece boundary is dissected into a part τ_s which is free from any acting force and a part τ_u where the workpiece is fixed. The method of lines (MOL) is applied for discretization of the equations (1). The first step is to discretize the partial differential equations with respect to space while keeping the time variable continuous. We use curl-conforming finite elements for the vector potential A . For the temperature θ and the phase fraction z we use classical

H^1 -conforming elements while the stress tensor σ is approximated by vector-valued H^1 elements. More precisely, we introduce the spaces as

$$L^2(\Sigma) = \{v : \Sigma \rightarrow \mathbb{R} \mid \int_{\Sigma} |v(x)|^2 dx < \infty\}$$

$$H^1(\Sigma) = \{v : \Sigma \rightarrow \mathbb{R} \mid v \in L^2(\Sigma), \nabla v \in [L^2(\Sigma)]^3\}$$

$$H(\text{curl}, D) = \{v : D \rightarrow \mathbb{R}^3 \mid v \in [L^2(D)]^3, \text{curl } v \in [L^2(D)]^3\}$$

$$X^u(\Sigma) = \{v : \Sigma \rightarrow \mathbb{R}^3 \mid v \in [H^1(\Sigma)]^3, v \cdot n|_{\tau_s} = 0, v|_{\tau_u} = 0\}$$

$$\mathbb{X} = \{v \in H(\text{curl}, D) \mid \text{div } v = 0, v \times n = 0 \text{ on } \partial D\}$$

where n denotes the normal to the boundary.

With these definitions in mind we use a finite element method (FEM) to compute the projection on corresponding finite dimensional subspaces.

3 Simulation and experimental verification

The numerical simulations are carried out on a disc with diameter 47.7 mm made of steel 42CrMo4. From symmetry reasons we restrict ourselves to compute a segment with an angle of $\frac{\pi}{20}$ (cf. Fig. 3). All material parameters associated with 42CrMo4 for the simulations are provided by IWT (Stiftung Institut für Werkstofftechnik, Bremen), and parameters for phase transitions are taken from [3]. All numerical results presented here are accompanied with the thermally induced deformation scaled by 40 to improve their visualizations. According to experimental setting we use a medium frequency MF= 12kHz with power 100kW and current 575A.

In such an induction heating process Fig. 4 shows progressive temperature values for different heating stages. Fig. 5 depicts the comparison between simu-

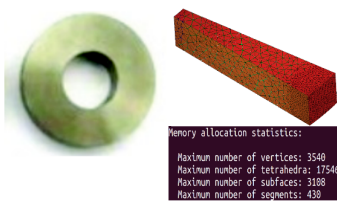


Fig. 3. Disc sample and the reduced computational domain

lated and experimentally measured deformation. The results of axial and tangential residual stresses after cooling are exhibited in Fig. 6.

Acknowledgement. This research is a part of the project MeFreSim (Modeling, Simulation and Optimization of Multi-Frequency Induction Hardening) funded by Bundesministerium für Bildung und Forschung (BMBF).

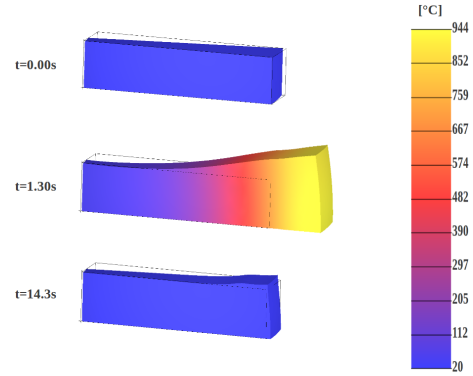


Fig. 4. Temperature evolution at begin of heating ($t = 0.00s$), end of heating ($t = 1.3s$), and end of cooling ($t = 14.3s$)

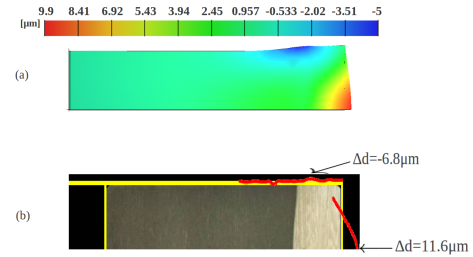


Fig. 5. Size changes of disc diameter ((a): simulated results scaled by 40, (b): experimental measurements depicted by the red contours).

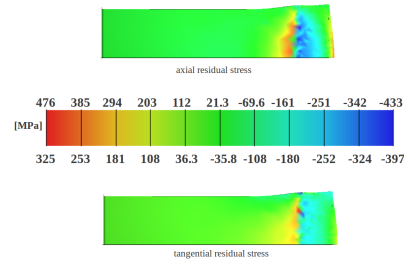


Fig. 6. Axial and tangential residual stresses at the sectional symmetry plane after induction heat treatment

References

1. R. Schröder. *Untersuchung zur Spannungs- und Eigenspannungsbildung beim Abschrecken von Stahlzylindern*. Dissertation (1985), Uni. Karlsruhe.
2. Dietmar Hömberg. *A mathematical model for induction hardening including mechanical effects*. Real World Appl. 5 (2004) 55-90.
3. T. Mioković. *Analyse des Umwandlungsverhaltens bei ein- und mehrfacher Kurzzeithärtung bzw. Laserstrahlhärtung des Stahls 42CrMo4*. Dissertation, Shaker Verlag Aachen, 2005
4. J. M. Urquiza, Q. Liu, and A. Schmidt. *Simulation of quenching involved in induction hardening including mechanical effects*. Comput. Mater. Sci., 79 (2013) 639-649.
5. J. M. Urquiza, Q. Liu, A. Schmidt. *Quenching simulation for the induction hardening process Thermal and mechanical effects*. Berichte aus der Technomathematik, Uni. Bremen, 2013.

Jacobian Structure of Coupled Electromagnetic Field and Lumped Circuit Models

Wim Schoenmaker¹ and Caren Tischendorf²

¹ Magwel NV, Leuven, Belgium wim.schoenmaker@magwel.com

² Humboldt-Universität zu Berlin, Germany caren.tischendorf@math.hu-belin.de

Summary. Motivated by the aim of an efficient coupled electromagnetic field and lumped circuit simulation, we show that one can form the model equations in such a way that the discretized equation system (using FIT method for spatial and BDF method for time discretization) has an exploitable Jacobian structure.

1 Electromagnetic Field Model

The electromagnetic fields can be described by the full-wave Maxwell's equations

$$\begin{aligned}\nabla \cdot \mathbf{D} &= \rho, & \nabla \times \mathbf{E} &= -\partial_t \mathbf{B} \\ \nabla \cdot \mathbf{B} &= 0, & \nabla \times \mathbf{H} &= \mathbf{J} + \partial_t \mathbf{D}\end{aligned}$$

equipped with the material laws

$$\mathbf{D} = \varepsilon \mathbf{E}, \quad \mathbf{H} = \nu \mathbf{B},$$

where \mathbf{D} , \mathbf{E} , \mathbf{B} , \mathbf{H} , \mathbf{J} and ρ are the displacement field, electric field, magnetic induction, magnetic field, free current density and charge density. The material dependent parameters ε and $\mu = 1/\nu$ are the permittivity and the magnetic permeability. The charge ρ and the current density \mathbf{J} can be described by the following model equations:

$$\rho = \begin{cases} 0 & \text{for metal and isolator} \\ q(n - p - N_D) & \text{for semiconductor} \end{cases} \quad (1)$$

and

$$\mathbf{J} = \begin{cases} \sigma \mathbf{E} & \text{for metal} \\ \mathbf{J}_n + \mathbf{J}_p & \text{for semiconductor} \\ 0 & \text{for isolator} \end{cases} \quad (2)$$

with the electron and hole current densities J_n and J_p as well as the electron and hole concentrations n and p satisfying

$$q \partial_t n - \nabla \cdot \mathbf{J}_n + qR(n, p) = 0 \quad (3)$$

$$q \partial_t p + \nabla \cdot \mathbf{J}_p + qR(n, p) = 0 \quad (4)$$

with

$$\mathbf{J}_n = qD_n \nabla n + q\mu_n n \mathbf{E}, \quad \mathbf{J}_p = -qD_p \nabla p + q\mu_p p \mathbf{E}.$$

The material depending parameters N_D , σ , μ_n and μ_p describe the doping concentration, the conductivity, the mobility of electrons and the mobility of holes. The function R gives the recombination rate for electrons and holes. Finally, q is the elementary charge and D_n , D_p are the diffusion coefficients.

Note that the semiconductor current density model reflects the drift-diffusion model [9] and should be extended by an additional current density part caused by the self-induced Lorentz force in case of circuits with fast-transient signals, see [8].

To facilitate the coupling between the electromagnetic field simulation with a lumped circuit simulation, the Maxwell equations are written in potential form using the scalar potential φ and the vector potential \mathbf{A} [1, 2] satisfying

$$\mathbf{B} = \nabla \times \mathbf{A}, \quad \nabla \varphi = -\mathbf{E} - \partial_t \mathbf{A}. \quad (5)$$

The existence of these potentials follows from the Gauß' law $\nabla \cdot \mathbf{B} = 0$ for magnetism and the Maxwell-Faraday law $\nabla \times \mathbf{E} = -\partial_t \mathbf{B}$. For uniqueness of \mathbf{A} and φ , we need a gauge condition. Because of numerical stability reasons [3], we choose the Lorenz gauging

$$\nabla \cdot \mathbf{A} + c \partial_t \varphi = 0 \quad (6)$$

with a suitable constant c . Using (5), the full Maxwell equations reduce to

$$\nabla \cdot (\varepsilon \nabla \varphi + \varepsilon \partial_t \mathbf{A}) = -\rho \quad (7)$$

$$\nabla \times (\nu \nabla \times \mathbf{A}) + \partial_t (\varepsilon \nabla \varphi + \varepsilon \partial_t \mathbf{A}) = \mathbf{J} \quad (8)$$

with ρ and \mathbf{J} given by (1) and (2) in which \mathbf{E} is replaced by $-\nabla \varphi - \partial_t \mathbf{A}$. Finally, a new variable, the pseudo-canonical momentum $\Pi = \partial_t \mathbf{A}$ is introduced to avoid the second-order time derivative [7].

2 Lumped Circuit Equations

For lumped circuit models, the Kirchhoff's laws are satisfied and can be written as

$$\mathbf{A} \mathbf{i} = 0, \quad \mathbf{v} = \mathbf{A}^\top \mathbf{e} \quad (9)$$

with the incidence matrix A mapping branches to nodes of the circuit. The circuit variables are the vector \mathbf{i} of all branch currents, the vector \mathbf{v} of all branch voltages and the vector \mathbf{e} of all nodal potentials. In

contrast to the field variables, the circuit variables depend on time t only. Additionally, we have the constitutive element equations

$$\mathbf{i}_1 = \frac{d}{dt}q(\mathbf{v}_1, t) + g(\mathbf{v}_1, t), \quad \mathbf{v}_2 = \frac{d}{dt}\phi(\mathbf{i}_2, t) + r(\mathbf{i}_2, t)$$

for lumped current and voltage controlling elements, respectively. Notice, all basic types as capacitances, inductances, resistances and sources are covered by a suitable choice of the functions q , g , ϕ and r .

Splitting the branches of the incidence matrix into $A = (A_1, A_2, A_3)$ with respect to the current controlling, voltage controlling and electromagnetic field element models, the circuit equations can be written in the compact form of the Modified Nodal Analysis (MNA) as [6, 7]

$$A_1 \frac{d}{dt}q(A_1^\top \mathbf{e}, t) + A_1 g(A_1^\top \mathbf{e}, t) + A_2 \mathbf{i}_2 + A_3 \mathbf{i}_3 = 0 \quad (10)$$

$$\frac{d}{dt}\phi(\mathbf{i}_2, t) + r(\mathbf{i}_2, t) - A_2^\top \mathbf{e} = 0 \quad (11)$$

together with $\mathbf{v}_3 = A_3^\top \mathbf{e}$.

3 Interface Model

We assume the interface between the electromagnetic field model and the lumped circuit model to be perfectly electric conducting such that $\mathbf{B} \cdot \mathbf{n}_\perp = 0$ and $\mathbf{E} \cdot \mathbf{n}_\parallel = 0$ with \mathbf{n}_\perp and \mathbf{n}_\parallel being the outer unit normal vectors transversal and parallel to the contact boundary. This motivates the boundary conditions [3]

$$(\nabla \times \mathbf{A}) \cdot \mathbf{n}_\perp = 0, \quad (\nabla \phi) \cdot \mathbf{n}_\parallel = 0. \quad (12)$$

Denoting by Γ_k the k -th contact of the electromagnetic field model element with Γ_0 being the reference contact and choosing any position $x^k \in \Gamma_k$, we obtain the coupling equations

$$\mathbf{i}_3^k = \int_{\Gamma_k} [\mathbf{J} - \partial_t(\varepsilon(\nabla \phi + \Pi))] \cdot \mathbf{n}_\perp d\sigma$$

$$\mathbf{v}_3^k = \phi(x^k) - \phi(x^0)$$

that can be bundled as

$$\mathbf{i}_3 = B_J \mathbf{J} + B_\phi \partial_t \phi + B_\Pi \partial_t \Pi, \quad (13)$$

$$A_3^\top \mathbf{e} = R_\phi \phi. \quad (14)$$

with linear boundary operators B_J , B_ϕ , B_Π and R_ϕ .

4 Coupled Model Structure

Discretizing the electromagnetic field model in space by the FIT discretization as described in [2, 3] and using as time discretization the BDF methods for the resulting differential algebraic system as given in [5], we obtain a Jacobian structure of the form

$$J = \begin{pmatrix} J_E & J_{EB} & 0 \\ J_{BE} & I & J_{BC} \\ 0 & J_{CB} & J_C \end{pmatrix}$$

with a diagonally dominant matrix J_E for the electromagnetic and a positive semi-definite matrix J_C for the lumped circuit part, respectively. The field-circuit coupling is contained in J_{EB} , J_{BE} , J_{BC} and J_{CB} . The variable order is ϕ , \mathbf{A} , \mathbf{J} , n , p , \mathbf{i}_3 , \mathbf{e} , \mathbf{i}_2 and the coupled equation system order is (7), (8), (2), (3), (4), (13), (10), (11). Some details about J_C and J_E are given in [3, 4]. The Jacobian blocks can be constructed from the discretized versions of the equations (12), (14), (1), (6) and $\Pi = \partial_t A$. The end result allows the use of efficient *iterative* solvers for the high dimensional (due to 3D discretization) matrix part J_E resolving ϕ , \mathbf{A} , \mathbf{J} , n , p combined with a simple evaluation process for the determination of the coupling current i_3 and a direct solver for the elimination of the circuit variables \mathbf{e} and \mathbf{i}_2 after use of a Schur complement approach.

Acknowledgement. Part of this work was financially supported by the EU funded FP7 ICT projects nanoCOPS GA619166, ICESTARS GA214911 and the German DFG research center MATHEON in Berlin.

References

1. P. Meuris, W. Schoenmaker, and W. Magnus. Strategy for electro-magnetic interconnect modeling. *IEEE Trans. Comput.-Aided Design*, 20(6):753–762, 2001.
2. W. Schoenmaker and P. Meuris. Electromagnetic interconnects and passives modeling: software implementation issues. *IEEE Trans. Comput.-Aided Design*, 21(5):534–543, 2002.
3. S. Baumanns. *Coupled Electromagnetic Field/Circuit Simulation. Modeling and Numerical Analysis*. PhD thesis, Universität zu Köln, Logos Berlin, 2012.
4. A. Bartel, S. Baumanns and S. Schöps. Structural analysis of electrical circuits including magnetoquasistatic devices. *Appl. Num. Math.* 61(12):1257–1270, 2011.
5. R. Lamour, R. März and C. Tischendorf. *Differential-Algebraic Equations: A Projector Based Analysis: A Projector Based Analysis*. Springer, Heidelberg, 2013.
6. D. Estévez Schwarz and C. Tischendorf. Structural analysis for electric circuits and consequences for MNA. *Int. J. of Circuit Theor. Appl.*, 28(2):131–162, 2000.
7. W. Schoenmaker, M. Matthes, B. De Smedt, S. Baumanns, C. Tischendorf and R. Janssen. Large signal simulation of integrated inductors on semi-conducting substrates. *Proceedings of the Design, Automation and Test in Europe Conference (DATE) 2012*, 1221–1226, 2012.
8. W. Schoenmaker, Q. Chen, P. Galy. Computation of Self-Induced Magnetic Field Effects Including the Lorentz Force for Fast-Transient Phenomena in Integrated Circuits. *IEEE Trans. on Computer-Aided Design of Integrated Circuits and Systems*, June 2014, in print.
9. P.A. Markowich. *The Stationary Semiconductor Device Equations*. Springer, Wien, 1986.

Iterative Software Agent Based Solution of Multiphysics Problems

Matthias Jüttner¹, André Buchau¹, Alexander Faul², Wolfgang M. Rucker¹, and Peter Göhner²

¹ University of Stuttgart, Institute for Theory of Electrical Engineering, Pfaffenwaldring 47, 70569 Stuttgart, Germany
matthias.juettner@ite.uni-stuttgart.de, andre.buchau@ite.uni-stuttgart.de,
rucker@ite.uni-stuttgart.de

² University of Stuttgart, Institute of Industrial Automation and Software Engineering, 70569 Stuttgart, Germany
alexander.faul@ias.uni-stuttgart.de, peter.goehner@ias.uni-stuttgart.de

Summary. A novel approach is presented using software agents for an iterative and distributed solution of a coupled electromagnetic wave propagation and heat transfer problem inside a waveguide. Total convergence is reached by combining individual functionalities of different software agents within a multi agent system. Single physics agents cooperatively solve the problem based on specialized, commercial or in-house code. To do so, only an interface for data exchange is required. Here, three software agents are used and described in detail.

1 Introduction

An iterative strategy is a common way to solve multiphysics problems. Therefore, the problem is segregated into multiple single physics problems and solved by exchanging dependent values. These values are extracted from one problem and integrated as boundary conditions or domain sources into loop wise coupled problems. So multiphysics means the coupling of different types of fields. Here, a novel approach for computational electromagnetic is presented using independent modules [2] for solving a coupled electromagnetic wave propagation problem and heat transfer problem inside a waveguide. The independent modules are implemented regarding the design rules of software agents. Software agents are well tested in automation technologies for solving complex problems. They are independent programs with individual functionalities based on agent specific implemented behaviours [1]. Supervising and managing different numerical methods to solve an equation system could be some of these behaviours. So only a management and supervision interface is required to reuse existing numerical code [3]. Each agent can also decide within its individual limits and based on its knowledge to reach its own goals. Due to that, agents choose best available algorithm for solving its problems. This gets interesting in front of increasing numbers of specific solvers, working best under certain conditions. Combining the functionalities of multiple agents within a multi agent system allows each agent to contribute for a global problem. So a system is created where each agent yields its capabilities to solve complex problems with distributed units.

2 Solver Design

Here the solution process of a coupled electromagnetic wave propagation problem and a heat transfer problem is considered. The problem is one out of many to demonstrate the principle of the segregated agent based solution of multiphysics problems. To solve a coupled electromagnetic wave propagation problem and a heat transfer problem three software agents are needed. They run on an Intel(R) Core(TM) i7-2600 with 4 cores max. 3.4GHz, 16GB(1333MHz) RAM and Windows 8.1 Enterprise 64-bit. *Agent a* segregates the multiphysics problem into two single physics problems. It distributes the partial problems to *agent b* and *agent c*. These two agents solve the total problem cooperatively. For the example, *agent b* handles the electromagnetic wave simulation according to (1) and solve it in frequency domain. The temperature problem, shown in (2) is solved by *agent c* for a stationary case. The electric field \mathbf{E} and the temperature T represent the two dependent variables.

$$\nabla \times \mu_r^{-1}(\nabla \times \mathbf{E}) - k_0^2(\epsilon_r - \frac{j\sigma}{\omega\epsilon_0})\mathbf{E} = 0 \quad (1)$$

$$\rho C_p \mathbf{v} \cdot \nabla T = \nabla \cdot (k \nabla T) + Q \quad (2)$$

The coupling is realized by a heat source Q representing the total power dissipation density in *agent c* and the temperature dependent electric conductivity $\sigma(T)$ in *agent b*. The slow heating process [s] compared to the high frequency wave propagation [10GHz] allows to consider the heat source Q as constant over time. After receiving the problem, *agent b* and *agent c* start computing in parallel by ignoring coupling. The uncoupled partial problems can be described for *agent b* as in (3) and for *agent c* as in (4). Here \mathbf{f} is the function to solve, \mathbf{K} the stiffness matrix, \mathbf{u} the solution and \mathbf{b} the load.

$$\mathbf{f}_E = \mathbf{K}_E \mathbf{u}_E - \mathbf{b}_E = 0 \quad (3)$$

$$\mathbf{f}_T = \mathbf{K}_T \mathbf{u}_T - \mathbf{b}_T = 0 \quad (4)$$

As soon as any agent finishes its calculation, all agents working on the problem get informed about the available result. Also derived values from the calculated results are published. Each agent decides whether to request the result or to ignore them and continue calculating. For the example, (2) is solved successfully at

first. Due to the temperature dependent electric conductivity $\sigma(T)$ at *agent b*, its iteratively processed calculation is interrupted. Now the available results are included for the calculation. In that way a unidirectional coupling from *agent c* to *agent b* is automatically created. The updated problem description is given in (5). Now the calculation of *agent b* is continued. The so far iteratively calculated intermediate results are used as initial conditions for further calculations.

$$\mathbf{f}_E = \mathbf{K}_E(\mathbf{u}_T)\mathbf{u}_E - \mathbf{b}_E \quad (5)$$

Until a solution for (5) is found *agent c* is informed about the available result. Now the total power dissipation density of the electromagnetic wave are present and can be integrated as additional heat source Q into (2). The Problem can now be described as in (6).

$$\mathbf{f}_T = \mathbf{K}_T(\mathbf{u}_E)\mathbf{u}_T - \mathbf{b}_T \quad (6)$$

In that way a bidirectional coupling between both agents is provided. Solving (5) and (6) in a loop further precise the result. The loop ends if no changes for the dependent variables or the derived values at a next iteration. For the considered example, Table 1 shows the maximum difference of the exchanged values compared to the previous value. Due to the small changes at the end of the table, the loop ends.

Table 1. Change of exchanged values for multiple iterations

exchanged value:	T	Q	T	Q	T
Maxium Δ :	first	first	25 K	$7.64 \frac{\text{W}}{\text{m}^3}$	$6 \cdot 10^{-6} \text{K}$

Table 2 shows a comparison between the agent based solver system and a segregated solver. Here identic meshes for both agents and a BiConjugate Gradient Stabilized solver (BiCGStab) are used. Similar results are achieved when using a MULTifrontal Massively Parallel sparse direct Solver (MUMPS). The iterative sequence of computed dependent variables are shown in the first column. To compare the results no solver is interrupted. The shown error is computed as maximum node wise difference of the solution vectors.

Table 2. Solver sequence for the waveguide

Agent	Integrate	Calculation	max. Error rel.	Error %
T	none	36 lin. iter.	$5 \cdot 10^{-14}$	$2 \cdot 10^{-14}$
E	new Source(T)	306 lin. iter.	$5 \cdot 10^{-4}$	$6 \cdot 10^{-4}$
T	new Source(Q)	77 lin. iter.	0.71	0.21
E	update(T)	1 lin. iter.	$5 \cdot 10^{-4}$	$7 \cdot 10^{-4}$
T	update(Q)	43 lin. iter.	0.72	0.22

Table 2 also shows, 306 linear iterations were necessary to solve the electric field problem in a sequential process. To show a solution time advantage of the agent based solver, the initially uncoupled problems

are solved in parallel. The computation of *agent b* is interrupted when the result of *agent c* gets available. For example, *agent b* was interrupted after 160 linear iterations. After integrating results of *agent c*, additional 212 iterations were needed to solve 5. It is important to notice, that the remaining 212 iterations do consume less time compared to the common sequential approach with 306 iterations. It is expected to increase this effect more than two agents working at a problem. In this context domain decomposition is also interesting. Figure 1 and Fig. 2 shows the results of the solved waveguide problem for a mode 10 transverse electromagnetic wave (TE10) at 10GHz and a convective heat flux at the boundaries of $1 \frac{\text{W}}{\text{m}^2 \cdot \text{K}}$.

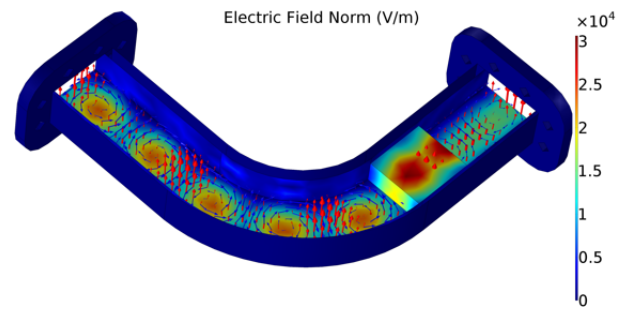


Fig. 1. Visualisation of results from *agent b*.

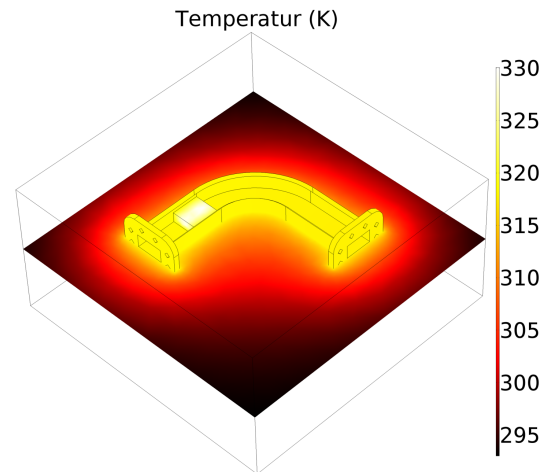


Fig. 2. Visualisation of results from *agent c*.

References

1. F. L. Bellifemine, G. Caire and D. Greenwood, Developing Multi-Agent Systems with JADE, John Wiley & Sons, Chichester, UK, 2007.
2. T.T. Drashansky, A. Joshi and J.R. Rice, SciAgents-an agent based environment for distributed, cooperative scientific computing, *ICTAI'95*, pp 452-459, 1995.
3. M. Jüttner, A. Buchau, M. Rauscher, W. M. Rucker and P. Ghner, Software Agent Based Domain Decomposition Method, *IGTE12*, pp. 89-94, 2013.

Model reduction and dynamic iteration for coupled nonlinear systems

Johanna Kerler¹ and Tatjana Stykel¹

Institute of Mathematics, University of Augsburg, Universitätsstr. 14, 86159 Augsburg, Germany
kerler@math.uni-augsburg.de, stykel@math.uni-augsburg.de

Summary. The dynamical behavior of coupled systems is determined by different interconnected subsystems that are usually governed by entirely different physical laws and often act in different time and space scales. We discuss the simulation of coupled nonlinear systems using dynamic iteration combined with model order reduction. We also study the convergence of this approach and derive error estimates for approximate solutions.

1 Introduction

A wide variety of physical and technical processes can be modeled by coupled systems of differential equations. Application areas of coupled systems include circuit-device simulation and micro-electro-mechanical systems. The dynamical behavior of coupled systems is characterized by different properties of the interacting subsystems that often describe different physical effects in the system. The increasing complexity of mathematical models requires the development of new simulation techniques for large-scale coupled systems.

Dynamic iteration (known also as waveform relaxation), e.g., [1], has proven to be a useful tool for simulation of coupled systems since at every iteration, the decoupled subsystems can be solved separately. Such a modular approach allows us to use different time steps and to employ most appropriate integration methods for the different subsystems. In [4], dynamic iteration was combined with reduced-order models resulting in a DIRM method. This method involves successive simulation of each unreduced subsystem coupled with other reduced-order subsystems. Unfortunately, the convergence analysis carried out in [4] is restricted to coupled linear time-invariant systems with a weak coupling. In this paper, we extend these results to coupled nonlinear systems and present a posteriori error estimation for the DIRM iteration.

2 Dynamic iteration

We consider a coupled system of nonlinear differential equations

$$\begin{aligned} \dot{x}_1 &= f_1(x_1, x_2), & x_1(T_0) &= x_1^0, \\ \dot{x}_2 &= f_2(x_1, x_2), & x_2(T_0) &= x_2^0, \end{aligned} \quad (1)$$

where $x_j : \mathbb{I} \rightarrow \mathbb{R}^{n_j}$, $\mathbb{I} = [T_0, T_e]$ and $f_j : \mathbb{R}^{n_1} \times \mathbb{R}^{n_2} \rightarrow \mathbb{R}^{n_j}$ for $j = 1, 2$. We assume that f_j are continuously differentiable and system (1) is solvable. For a better

readability, we restrict ourselves here to the coupling of two autonomous subsystems, although all results can easily be extended to a more general case.

The dynamic iteration method for the coupled system (1) is formulated as follows. First, the time interval $[T_0, T_e]$ is split into windows $[T_l, T_{l+1}]$ with a time grid $T_0 < T_1 < \dots < T_L = T_e$. Then a k -th iteration in the window $[T_l, T_{l+1}]$ is determined from

$$\begin{aligned} \dot{x}_1^{[k]} &= f_1(X_{11}^{[k]}, X_{12}^{[k]}), & x_1^{[k]}(T_l) &= x_1^{[k-1]}(T_l), \\ \dot{x}_2^{[k]} &= f_2(X_{21}^{[k]}, X_{22}^{[k]}), & x_2^{[k]}(T_l) &= x_2^{[k-1]}(T_l), \end{aligned} \quad (2)$$

where $X_{ij}^{[k]} = \Theta_{ij}^{[0]} x_j^{[k]} + \Theta_{ij}^{[1]} x_j^{[k-1]}$ for $i, j = 1, 2; k = 1, \dots, k_l$, and $x_j^{[0]}$ are obtained by extrapolation of $x_j^{[k_l-1]}$ from $[T_{l-1}, T_l]$ to $[T_l, T_{l+1}]$, respectively the initial data of (1). Choosing

$$\begin{bmatrix} \Theta_{11}^{[0]} & \Theta_{12}^{[0]} \\ \Theta_{21}^{[0]} & \Theta_{22}^{[0]} \end{bmatrix} = \begin{bmatrix} I & 0 \\ 0 & I \end{bmatrix}, \quad \begin{bmatrix} \Theta_{11}^{[1]} & \Theta_{12}^{[1]} \\ \Theta_{21}^{[1]} & \Theta_{22}^{[1]} \end{bmatrix} = \begin{bmatrix} 0 & I \\ I & 0 \end{bmatrix}, \quad (3)$$

we obtain a Jacobi method, whereas

$$\begin{bmatrix} \Theta_{11}^{[0]} & \Theta_{12}^{[0]} \\ \Theta_{21}^{[0]} & \Theta_{22}^{[0]} \end{bmatrix} = \begin{bmatrix} I & 0 \\ I & I \end{bmatrix}, \quad \begin{bmatrix} \Theta_{11}^{[1]} & \Theta_{12}^{[1]} \\ \Theta_{21}^{[1]} & \Theta_{22}^{[1]} \end{bmatrix} = \begin{bmatrix} 0 & I \\ 0 & 0 \end{bmatrix}$$

gives a Gauss-Seidel method. The convergence of the dynamic iteration (2) depends on the window sizes.

2.1 Model order reduction

The goal of model order reduction is to replace a large-scale dynamical system

$$\dot{x} = f(x), \quad x(T_0) = x_0 \quad (4)$$

with $x : \mathbb{I} \rightarrow \mathbb{R}^n$ and $f : \mathbb{R}^n \rightarrow \mathbb{R}^n$ by a reduced-order model

$$\dot{\hat{x}} = \hat{f}(\hat{x}), \quad \hat{x}(T_0) = \hat{x}_0 \quad (5)$$

with $\hat{x} : \mathbb{I} \rightarrow \mathbb{R}^r$, $\hat{f} : \mathbb{R}^r \rightarrow \mathbb{R}^r$ and $r \ll n$ which nearly approximates the dynamical behaviour of (4). A most popular model reduction method for nonlinear systems is proper orthogonal decomposition (POD), e.g., [5]. It is based on determining a snapshot matrix $X = [x(t_1), \dots, x(t_q)]$, $q \leq n$, and computing a singular value decomposition

$$X = [V, V_0] \begin{bmatrix} \Sigma \\ \Sigma_0 \end{bmatrix} [W, W_0]^T,$$

where the matrices $[V, V_0]$ and $[W, W_0]$ are orthogonal, $\Sigma = \text{diag}(\sigma_1, \dots, \sigma_r)$, $\Sigma_0 = \text{diag}(\sigma_{r+1}, \dots, \sigma_q)$ and

$\sigma_1 \leq \dots \leq \sigma_r < \sigma_{r+1} \leq \dots \leq \sigma_q$. Then x is approximated by $V\hat{x}$, where \hat{x} solves the reduced-order model (2.1) with $\hat{f}(\hat{x}) = V^T f(V\hat{x})$ and $\hat{x}_0 = V^T x_0$. Though this system is of low dimension r , the evaluation of the nonlinearity $V^T f(V\hat{x})$ still has a computational complexity of n . To overcome this difficulty, the discrete empirical interpolation method has been developed in [2] which provides an approximate model

$$\dot{\hat{x}} = V^T U (P^T U)^{-1} P^T f(V\hat{x}), \quad \hat{x}(T_0) = \hat{x}_0,$$

where $U \in \mathbb{R}^{n \times m}$ is a POD basis matrix obtained from the snapshot matrix $[f(x(t_1)), \dots, f(x(t_q))]$ and $P = [e_{p_1}, \dots, e_{p_m}] \in \mathbb{R}^{n \times m}$ is a selector matrix constructed from U by a Greedy-algorithm. Here e_{p_j} denotes the p_j -th column of the identity matrix. Note that $P^T f(V\hat{x})$ needs only m function evaluations. For a posteriori error estimates for POD-DEIM reduced models, we refer to [6].

3 Dynamic iteration using reduced-order models

We consider now the DIRM method from [4] for simulation of coupled systems using dynamic iteration combined with POD-DEIM model order reduction. Let $V_j^{[k]}$ and $U_1^{[k]}, U_2^{[k]}$ be the POD basis matrices calculated from the snapshots $\{x_j^{[k-1]}(t_{il})\}_{i=1}^{q_l}$ and

$$\left\{ f_1(x_1^{[k-1]}(t_{il}), V_2^{[k-1]} \hat{x}_2^{[k-1]}(t_{il})) \right\}_{i=1}^{q_l},$$

$$\left\{ f_2(V_1^{[k-1]} \hat{x}_1^{[k-1]}(t_{il}), x_2^{[k-1]}(t_{il})) \right\}_{i=1}^{q_l},$$

respectively, on the time window $[T_l, T_{l+1}]$, and let $P_j^{[k]}$ be the corresponding selector matrices. Then instead of the Jacobi type system (2) with (3), we solve two coupled systems

$$\dot{x}_1^{[k]} = f_1(x_1^{[k]}, V_2^{[k]} \hat{x}_2^{[k]}), \quad x_1^{[k]}(T_l) = x_1^{[k-1]}(T_l), \quad (6)$$

$$\dot{\hat{x}}_2^{[k]} = \hat{f}_2(x_1^{[k]}, \hat{x}_2^{[k]}), \quad \hat{x}_2^{[k]}(T_l) = \hat{x}_2^{[k-1]}(T_l), \quad (7)$$

and

$$\dot{\hat{x}}_1^{[k]} = \hat{f}_1(\hat{x}_1^{[k]}, x_2^{[k]}), \quad \hat{x}_1^{[k]}(T_l) = \hat{x}_1^{[k-1]}(T_l), \quad (8)$$

$$\dot{x}_2^{[k]} = f_2(V_1^{[k]} \hat{x}_1^{[k]}, x_2^{[k]}), \quad x_2^{[k]}(T_l) = x_2^{[k-1]}(T_l), \quad (9)$$

where

$$\hat{f}_1(\hat{x}_1^{[k]}, x_2^{[k]}) = W_1^{[k]} f_1(V_1^{[k]} \hat{x}_1^{[k]}, x_2^{[k]}),$$

$$\hat{f}_2(x_1^{[k]}, \hat{x}_2^{[k]}) = W_2^{[k]} f_2(x_1^{[k]}, V_2^{[k]} \hat{x}_2^{[k]}),$$

and $W_j^{[k]} = (V_j^{[k]})^T U_j^{[k]} ((P_j^{[k]})^T U_j^{[k]})^{-1} (P_j^{[k]})^T$, $j = 1, 2$. Note that if (7) and (8) have low dimensions, then solving systems (6), (7) and (8), (9) is only slightly expensive than that of (2).

In order to analyze the convergence of the DIRM iteration, we have to study the errors caused by approximate initial conditions and model reduction in each window $[T_l, T_{l+1}]$ and the error propagation from

one window to the next one. We can show that the error

$$e(t) = \begin{bmatrix} x_1(t) - x_1^{[k]}(t) \\ x_2(t) - x_2^{[k]}(t) \end{bmatrix}, \quad t \in (T_l, T_{l+1}]$$

in the k -th iteration is estimated as

$$\|e(t)\| \leq \int_{T_l}^t \alpha(s) \exp\left(\int_s^t \beta(\tau) d\tau\right) ds + \|e(T_l)\|,$$

where

$$\beta(t) = \begin{bmatrix} f_1(x_1^{[k]}, x_2^{[k]}) - f_1(x_1^{[k]}, V_2^{[k]} \hat{x}_2^{[k]}) \\ f_2(V_1^{[k]} \hat{x}_1^{[k]}, x_2^{[k]}) - f_2(V_1^{[k]} \hat{x}_1^{[k]}, x_2^{[k]}) \end{bmatrix}$$

measure the error in the nonlinearity and

$$\alpha(t) = L[J_f](x^{[k]}(t))$$

is the logarithmic norm of the Jacobian $J_f(x^{[k]}(t))$ of $f = [f_1^T, f_2^T]^T$ at $x^{[k]}(t) = [(x_1^{[k]})^T(t), (x_2^{[k]})^T(t)]^T$ defined as

$$L[J_f](x^{[k]}(t)) = \frac{1}{2} \lambda_{\max}\left(J_f(x^{[k]}(t)) + J_f^T(x^{[k]}(t))\right).$$

Here, λ_{\max} denotes the largest eigenvalue of the corresponding matrix. The Jacobian logarithmic norm can be computed efficiently by a successive constraint method [3] if we first find a low-dimensional approximation $J_f(x) \approx \sum_{j=1}^{n_J} \theta_j(x) J_j$, where $J_j \in \mathbb{R}^{n \times n}$, $\theta : \mathbb{R}^n \rightarrow \mathbb{R}$ and $n_J \ll n = n_1 + n_2$. Such an approximation can be determined using a matrix DEIM approach [6]. Numerical examples will demonstrate the properties of the presented integration method and error estimations.

References

1. K. Burrage, Z. Jackiewicz, S.P. Nørsett, and R.A. Renault. Preconditioning waveform relaxation iterations for differential systems. *BIT*, 36(1):54-76, 1996.
2. S. Chaturantabut and D.S. Sorensen. Nonlinear model reduction via discrete empirical interpolation. *SIAM J. Sci. Comput.*, 32(5):2737-2764, 2010.
3. D.B.P. Huynh, G. Rozza, S. Sen, and A.T. Patera. A successive constraint linear optimization method for lower bound of parametric coercivity and inf-sup stability constant. *C. R. Acad. Sci. Paris. Ser. I*, 345:473-478, 2007.
4. M. Rathinam and L.R. Petzold. Dynamic iteration using reduced order models: a method for simulation of large scale modular systems. *SIAM J. Numer. Anal.*, 40(4):1446-1474, 2002.
5. S. Volkwein. *Proper Orthogonal Decomposition: Theory and Reduced-Order Modelling*. Lecture Notes, University of Konstanz, 2013.
6. D. Wirtz, D.C. Sorensen, and B. Haasdonk. A posteriori error estimation for DEIM reduced nonlinear dynamical systems. *SIAM J. Sci. Comput.*, 36(2):A311-A338, 2014.

Tuning the accuracy of rational macromodels to nominal load conditions

Stefano Grivet-Talocia¹, Andrea Ubolli¹, Alessandro Chinae², and Michelangelo Bandinu²

¹ Politecnico di Torino, C. Duca degli Abruzzi 24, 10129 Torino, Italy stefano.grivet@polito.it, andrea.ubolli@polito.it

² IdemWorks s.r.l., C. Trento 13, 10129 Torino, Italy a.chinea@idemworks.com, m.bandinu@idemworks.com

Summary. We address the generation of broadband macromodels of complex linear systems via rational curve fitting. We show that standard approaches may not ensure that the macromodel accuracy is preserved in system-level simulations, under loading conditions that are different from the adopted identification settings. Our main contribution is an automated procedure for the definition of a frequency-dependent norm weighting strategy that tunes the macromodel accuracy for a specific nominal termination network, thus improving model robustness under realistic operation.

1 Introduction and problem statement

We consider the situation depicted in Fig. 1. The box on the left represents a complex (large-scale) Linear Time Invariant (LTI) system, that we assume without loss of generality to be known through a set of tabulated frequency samples of its scattering matrix (ω_k, \hat{S}_k) for $k = 1, \dots, K$. The box on the right represents the nominal termination network that is to be connected to the LTI structure during system-level verification via transient numerical simulation. This termination includes at least one transient source $u(t)$ and at least one output variable $y(t)$ of interest.

Our reference application is Power Integrity (PI) verification of electronic structures, for which the LTI system represents the electrical interconnect network that is responsible for power distribution to the chip through package and board, and the termination network includes: a number of transient current sources (the inputs) representing on-chip switching; several decoupling capacitors; and at least one Voltage Regulator Module (VRM) which defines the nominal supply voltage V_{dd} . All these components or subsystems are connected at suitably defined ports of the Power Distribution Network (PDN). The outputs of interest are the transient voltages at all interface ports. The purpose of PI verification is to make sure that the transient voltage fluctuations due to the parasitics of the PDN are kept below a prescribed design threshold.

System-level verification is usually performed via transient simulation within standard circuit solvers of the SPICE class. Due to the complexity of the PDN structure, it is desirable to compute a reduced-order macromodel described by a state-space realization $\{A, B, C, D\}$, whose frequency response $S(j\omega) = D + C(j\omega I - A)^{-1}B$ matches closely the raw available frequency samples. Once synthesized into a SPICE-compatible netlist, this macromodel allows fast tran-

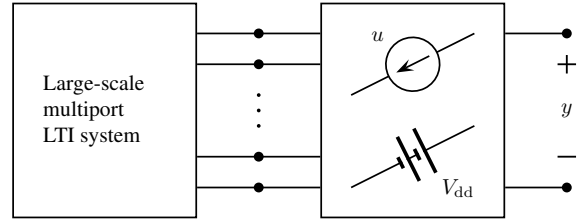


Fig. 1. System configuration under investigation

sient analysis and enables simulation-driven design, verification, and optimization flows.

In this work, we concentrate on a black-box macromodeling procedure, which constructs the macromodel in pole-residue form

$$S(s) = R_0 + \sum_{n=1}^N \frac{R_n}{s - p_n} \quad (1)$$

by optimizing poles p_n , residue matrices R_n and direct coupling R_0 so that the following cost function is minimized

$$E^2 = \sum_{k=1}^K \epsilon_k^2 = \sum_{k=1}^K w_k^2 \|S(j\omega_k) - \hat{S}_k\|_F^2, \quad (2)$$

where $\| \cdot \|_F$ denotes the Frobenius norm and w_k is a suitable frequency-dependent weighting scheme. The standard practice is to set $w_k = 1$. The well-known Vector Fitting (VF) algorithm [1] computes a solution to the above optimization problem through a so-called iterative pole relocation process. The VF algorithm is the de facto standard rational curve fitting tool in signal and power integrity modeling, due to its excellent robustness and scalability properties. Therefore, we will use this scheme as the main identification engine.

Suppose now that the termination network (Fig. 1, right box) is known exactly, and let us consider the frequency samples of the transfer function $H(s)$ between some input u and some output y . The error between the exact transfer function \hat{H}_k evaluated using the raw scattering samples \hat{S}_k and the approximate samples $H(j\omega_k)$ evaluated using the macromodel can be defined as

$$\Delta^2 = \sum_{k=1}^K \delta_k^2 = \sum_{k=1}^K \|H(j\omega_k) - \hat{H}_k\|_F^2 \quad (3)$$

The real objective is to control the target error Δ , since this is the error that is observed when running

a system-level simulation using the macromodel instead of an exact PDN model. The question arises whether we can control Δ by minimizing E . Our main objective is therefore to design optimal weighting coefficients w_k that, when used in the minimization of (2) through VF, will guarantee a small target error $\Delta < \Delta_{\max}$.

2 Formulation

The main idea is to embed the minimization of (2) within an outer loop that optimizes the weights w_k through iterations. Denoting the outer iteration index with μ , we setup the following scheme:

1. set $\mu = 0$ and initialize weights $w_k^0 = 1$ for all k ;
2. compute by VF a macromodel $S^\mu(s)$ by minimizing (2) based on the current weights w_k^μ ;
3. compute the resulting target errors δ_k and Δ based on (3); if $\Delta < \Delta_{\max}$, stop;
4. update the weights as $w_k^{\mu+1} = w_k^\mu \cdot f_k(\delta)$, where δ is a vector collecting all δ_k , and where f_k is a smoothing filter centered at the k -th sample;
5. set $\mu \leftarrow \mu + 1$ and go to step 2.

The above scheme updates the weighting coefficients in step 4, based on the frequency-dependent target error δ_k of the current macromodel. This allows to emphasize those frequencies for which there is a large sensitivity of the target error due to the feedback mechanism induced by the terminations onto the macromodel. The smoothing filter f is used to reduce the influence of noise.

Several improvements are possible and have been successfully implemented and tested. For instance, step 1 can start with an initial set of weights determined by a first-order sensitivity analysis (either numerical or analytical) of the error transformation $\delta_k(\epsilon_k)$, see [2]. Alternatively, an elementwise or matrix-based relative instead of absolute error metric can be used in (2) and (3). This choice depends on the particular application at hand. We finally remark that, once a final set of weights w_k is available, they can be used to define a cost function to be minimized within standard passivity enforcement schemes [3], should the computed macromodel be affected by passivity violations.

3 Results

We demonstrate our proposed scheme on two PDN examples having 18 and 11 ports, respectively. Both cases correspond to industrial chip-package structures and are known through tabulated frequency samples of their scattering matrix, obtained numerically from a full-wave solver. In both cases one of the ports is connected to an ideal voltage source (a VRM model), and the remaining ports are connected to either decoupling capacitor models or to core circuit block models. The target transfer function is represented by the

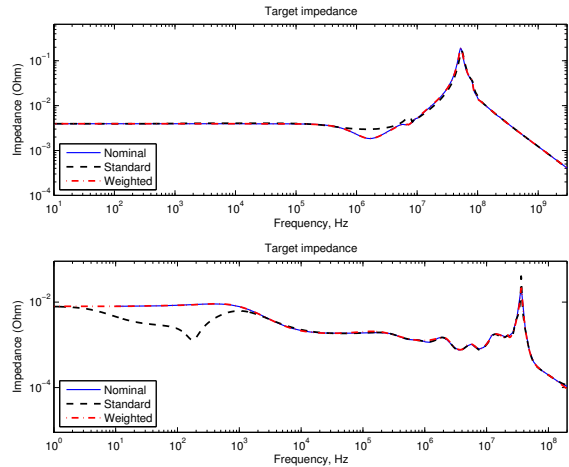


Fig. 2. Comparison between standard and proposed macromodels (see text).

transfer impedance that returns the voltage at a prescribed node resulting from a uniformly distributed current excitation at all device ports.

Figure 2 depicts in top and bottom panels the results obtained from the two cases. The thin solid blue line represents the nominal impedance computed from the raw scattering samples describing the PDN. The black dashed line is the target impedance computed using a standard macromodel, obtained with relative weights without applying the proposed strategy. The red dashed line reports the result of our proposed approach, which is observed to match now very closely the nominal impedance. We remark that these responses are resulting from passive macromodels, as processed by the passivity enforcement scheme of [3].

In summary, we have proposed a black-box macromodeling strategy that optimizes accuracy based on closed-loop nominal operating conditions, and not on standard input-output open-loop representations. The simple proposed approach is able to compensate for the error amplification that occurs when loading the macromodel with termination networks.

References

1. B.Gustavsen and A.Semlyen. Rational approximation of frequency responses by vector fitting. *IEEE Trans. Power Delivery*, 14:1052–1061, 1999.
2. S.Grivet-Talocia, A.Ubolli, M.Bandinu and A. China. An iterative reweighting process for macromodel extraction of power distribution networks. *EPEPS2013, 27–30 October 2013, San Jose (CA), USA*, 125–128.
3. A.Ubolli, S.Grivet-Talocia, M.Bandinu and A. China. Sensitivity-based weighting for passivity enforcement of linear macromodels in power integrity applications. *DATE2014, 24–28 March 2014, Dresden, Germany*.

Thermal Simulations for Optimization of Dry Transformers

Andrea Cremasco¹, Paolo Di Barba¹, Bogdan Cranganu-Cretu², and Andreas Blaszczyk³

¹ University of Pavia, Italy andrea.cremasco01@universitadipavia.it, paolo.dibarba@unipv.it

² ABB Transformers, Switzerland bogdan.cranganu-cretu@ch.abb.com

³ ABB Schweiz AG, Corporate Research, 5405 Baden-Dättwil, Switzerland andreas.blaszczyk@ch.abb.com

Summary. An efficient computational model based on thermodynamic principles is crucial for thermal design and optimization of transformers. In this paper we propose a thermal/pressure network model of a dry transformer with forced and natural cooling encapsulated in enclosure with ventilation grids. The network has been validated by a Computational Fluid Dynamics (CFD) simulation with Fluent and applied to computation of real transformers.

1 Introduction

For air-insulated (dry) transformers, see Fig. 1, the heat generated in the windings is transferred via convection to the bulk air above the winding and then dissipated to the ambient air through the ventilation system including a fan (which can be optionally switched off) and the enclosure inlet/outlet openings. For a numerical simulation of such complex phenomena a very resource demanding CFD analysis is required [1]. Therefore, designers of transformers typically create their own simplified calculation procedures based on rough assessment of heat transfer phenomena and empirical parameters that are valid for specific transformer technology [2]. Such procedures are integrated into transformer design systems and used for optimization. In this paper we propose a new method for the thermal simulation of a dry transformer together with the whole cooling system. It is based on a coupled pressure/thermal network approach [3], which in contrast to simplified engineering methods follows the physical approach validated by CFD computations. The new method offers much better computational performance than the detailed CFD and is extendable to all transformer technologies and cooling configurations.

2 Modeling of network components

The network components represent basic thermodynamic phenomena inside of the transformer and its cooling system. An example of such a component is the cooling duct for which the network model has been developed in [4] and is reused in computations presented in the next section. In this section we focus on investigation of a network component (resistor) representing the convection from a vertical heated (or cooled) wall to the bulk fluid. Fig. 2 shows the

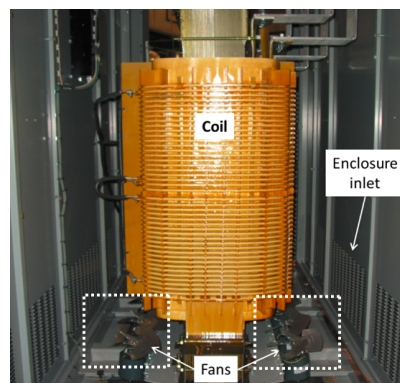


Fig. 1. Dry transformer with forced cooling in enclosure.

results of temperature computation for a cylindrical surface of a transformer coil. The curves 1 and 2 have been computed based on the constant temperature and constant heat flux models, respectively, with laminar and turbulent flow components [5]. The curves 3 and 4 are calculated using a simple model based on the Nusselt number Nu expressed as a function of Rayleigh number Ra : $Nu = c_1 Ra^{n_1}$ with $c_1 = 0.59, n_1 = 0.25$ for laminar flow (curve 3) and $c_1 = 0.1, n_1 = 0.33$ for the turbulent one (curve 4) [6]. It is possible to construct a convection resistor that combines both curves by switching from the laminar to turbulent model after the the limit of $Ra = 10^9$ has been exceeded.

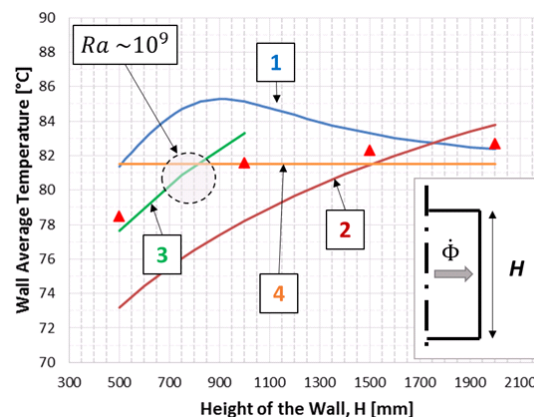


Fig. 2. Convection models for a vertical wall compared with CFD results. Heat flux applied $\phi = 150 W/m^2$.

3 Model of a transformer cooling system

CFD Model. For the CFD analysis we selected an equivalent axisymmetric transformer model consisting of a coil, core leg, fan and enclosure with ventilation openings. The coil includes a low voltage winding divided into 2 radially stacked parts LV1 and LV2, a barrier B and a high voltage winding HV embedded in solid insulation. Cooling ducts between them enable air circulation from the bottom to the top of the coil. The hot air exits the enclosure through the outlet opening. The cold air is entering the enclosure through the inlet opening and is sucked by the fan, which is blowing it towards the bottom of the coil. Fig. 3 shows selected CFD simulation results.

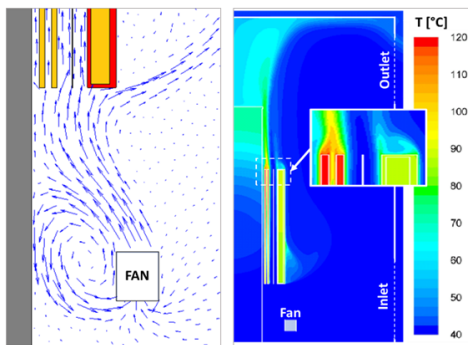


Fig. 3. a) Velocity vector plot at the bottom of the coil, b) Temperature contour plot.

Network model. For exactly the same geometry as used in the CFD analysis we have created an equivalent network model shown in Fig. 4.

Comparison between CFD and network results. The winding temperatures are included in Table 1 while the mass flow rates for the major air streams are shown in Table 2. More comprehensive comparison between network and CFD results will follow in the extended version of the paper.

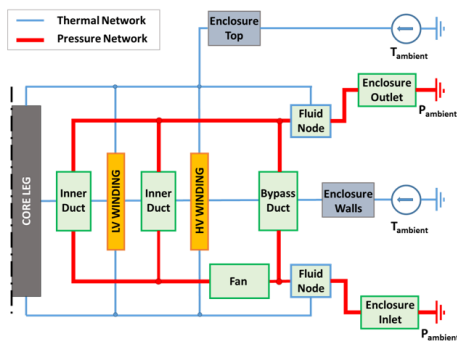


Fig. 4. Network scheme for the transformer in a cooling system with fan and enclosure. Note: this scheme shows the network concept rather than details of the calculated example.

Table 1. Winding average temperatures, in °C.

	LV1	LV2	HV
CFD	107.0	100.9	89.3
Network	108.4	106.7	95.0

Table 2. Mass flow rates, in g/s, for air streams in the transformer model (Fan mass flow rate = 208.6 g/s).

	core-LV1	LV1-LV2	LV2-B	B-HV	Bypass	Outlet
CFD	9.5	9.1	36.0	40.8	143.9	239.2
Network	9.7	9.0	37.1	40.9	142.0	239.0

4 Computation and optimization of real transformers. Outlook

We apply the validated network components to the modeling of real transformers with the full geometrical complexity (non-axisymmetric, 3 phases), with radiation, non-linear material properties and temperature dependency of losses. All these phenomena can be included in the network model without significant computational effort while an acceptable accuracy (5 K standard deviation of temperature from tests results) can be achieved [4]. The results for real transformers with enclosures will be presented in the extended version of this paper.

A parametrized equivalent transformer network model can be incorporated in an optimization loop for rapid design. In this respect, the use of a gradient-free optimization algorithm, though being slower than a gradient-based one, is recommended in order to avoid local minima and also to smooth the dependence on the initial guess. An optimization example will be shown in the extended version.

References

1. J. Smolka , A. J. Nowak, Experimental validation of the coupled fluid flow, heat transfer and electromagnetic numerical model of the medium-power dry-type electrical transformer, International Journal of Thermal Sciences 47 (2008) 1393-1410.
2. M. Bockholt, W. Mönig, B. Weber, B. Patel, B. Cranganu-Cretu, Thermal Design of VSD Dry-Type Transformer, SCEE 2012, Zurich.
3. A. Blaszczyk, R. Flückiger, T. Müller and C.-O. Olsson, Convergence behavior of coupled pressure and thermal networks, SCEE 2012 Zurich, (accepted for publication in COMPEL Journal 2014).
4. E. Morelli, P. Di Barba, B. Cranganu-Cretu, A. Blaszczyk, Network based cooling models for dry transformers, ARWtr Conference, Baiona, Spain, 2013.
5. W. M. Rohsenow, J. P. Hartnett, and Y. I. Cho (Eds.), Handbook of Heat Transfer, Ch. 5, McGraw-Hill, New York, 1998.
6. J. P. Holman, Heat transfer. 8th Edition, McGraw-Hill, 1999.

Accelerating the Transient simulation of Nearly-Periodic Circuits

Giovanni De Luca¹

Department of Mathematics and Computer Science, Eindhoven University of Technology, 5612 AZ Eindhoven, The Netherlands g.de.luca@tue.nl

Summary. Nowadays, faster and smaller electronic devices are more and more required. However, for some circuits the D&V¹ process is still slow. Thus, there is an urgent need for developing new, fast and efficient algorithms in the EDA² industry, targeting the 14nm deep submicron, and even smaller. In this contribution, we describe the problems that affect PLL³ circuits simulation and propose some methodologies to address them, in order to drastically speed up the simulation time of such circuits.

Key words: Electronic Design Automation, Analog and Mixed-Signal, Transient analysis, Nearly-Periodic circuits, Stiff systems, Vector Extrapolation methods, Optimization

1 Introduction

Nowadays, most EDA methods and tools are **inadequate**, since they must account for an enormous number of design considerations (PVT⁴ variation, power consumption, etc.). Advanced numerical techniques are imperative to address present-day challenges (particularly with the move to deep submicron CMOS, going to 14nm) in the electronics industry. In this regard, **Analog and Mixed-Signal (AMS)** content has grown in electronic devices. In fact, nearly 70% of today's designs can be considered mixed signal (think about complex ICs⁵ and PCBs⁶). **The speed limiting factor of a mixed-signal simulation is the analog engine**, since digital simulators are orders of magnitude faster. Designers desperately need a comprehensive transistor-level D&V framework up to the task of analyzing, optimizing and verifying AMS circuits, and well before tape-out.

There are several types of circuits for which most of the Spice and FasterSpice engines have a very long transient simulation time that make their systematic use impracticable in the D&V phase. It is typical to have **weeks of simulation even in multi-threaded mode**, and this is in contrast with the Time-to-Market constraint and the compelling need for faster and smaller electronic devices. To cite a few, Power regulators (DC-DC switching regulators, current regula-

tors) and PLLs fall into this category. Both are negative-feedback control systems, comparing the actual output signal, and producing a control signal based on the difference between the inputs to satisfy desired specifications, and both exhibit a trade-off between stability and speed of the response to changes.

In the next section, we briefly describe the functioning of a PLL and the problems related in its D&V phase, characterized by a **slow transient simulation**; thus, in the following section we propose some methodologies to combat with these problems.

2 Phase-Locked Loop device

2.1 Description of a PLL circuit

The PLL is a control system allowing one oscillator to track with another. It is possible to have a phase offset between input and output, but when locked, the frequencies must exactly track [1]:

$$\phi_{out}(t) = \phi_{in}(t) + const, \quad (1)$$

$$\omega_{out}(t) = n \times \omega_{in}(t), \quad (2)$$

where n is not necessarily an integer.

PLLs are employed in radio, telecommunications, computers and other electronic applications. Among its applications, it can be used as a frequency synthesizer (see figure 1).

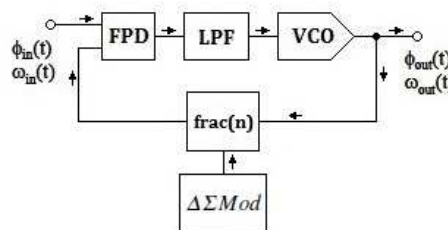


Fig. 1. Simple blocks schematic PLL (frequency synthesizer).

A frequency synthesizer receives as input a signal coming from a crystal oscillator, with phase $\phi_{in}(t)$ and frequency $\omega_{in}(t)$, and compares it by means of

¹ D&V: Design and Verification

² EDA: Electronic Design Automation

³ PLL: Phase-Locked Loop

⁴ PVT: Process, Voltage and Temperature

⁵ IC: Integrated Circuit

⁶ PCB: Printed Circuit Board

a *Frequency/Phase Detector* (FPD) with the outputs $\phi_{out}(t)$ and $\omega_{out}(t)$, through a feedback. Based on the phase error between them, a *bang-bang charge pump* (switching device) translates the error in two signals (UP and DOWN), causing the voltage across the *Loop (pass-band) Filter* (LPF) to increase or decrease. Several considerations can be done about the ability of the LPF to make the feedback control system stable, and on its ability to purge from low and high-frequency noises [1]. The voltage at the output of the LPF is used to tune a *Voltage-Controlled Oscillator* (VCO), generating the desired output signal frequency. The feedback block is the *Fractional-n Divider*, which allows (output) frequency resolution as fractional portion of the reference frequency. One of the reason for this architecture is to improve phase noise [4]. Finally, the $\Delta\Sigma$ *Modulator* block generates the number for the Divider block.

Generally, signals in PLLs are phase-modulated, i.e.:

$$x(t) = A \times \cos[\omega t + \phi_n(t)], \quad (3)$$

where $x(t)$ represents voltages and currents through the device, and $\phi_n(t)$ is the phase that slowly varies from cycle-to-cycle in the loop.

In fact, the difference between consecutive periods of the waveform $x(t)$ is small, and the signal only slightly deviates from a strictly periodic behaviour (i.e., $\phi_i(t)$ is slightly different from $\phi_{i-1}(t)$ during the transient simulation). The signal is then **nearly periodic**.

2.2 Problems

Various aspects cause a slow transient simulation:

- The charge pump *slowly builds* a power signal (in the *ms* range), cycle after cycle, whereas the VCO block produce a *fast signal* (in the *ns* or *ps* range). Because of this, the overall system is **stiff** ($|\Re(\lambda_{max})|/|\Re(\lambda_{min})| \gg 0$). Firstly, we note that we need a reliable transient noise analysis. Secondly, we observe that we encounter very fast varying signals. To deal with this, in normal transient simulation one has to drastically reduce the step size of the integration, in order to produce a *Local Truncation Error* (LTE), caused by approximating differential equations with difference ones, within a certain threshold [2];
- Also, the VCO is a problematic block: not only it is described by nonlinear equations, but also affected by several interferences (power line interference, thermal noise, etc., resulting in the phase noise).

2.3 Methodologies

- To deal with the small time step during transient analysis, we will use **vector extrapolation** techniques to adaptively skip the computation of some

signal's time points (without loss of accuracy): since the slow-varying signals at certain nodes of the circuits will have a larger step size with respect to the fast-varying ones, one can think of speeding up the simulation by skipping the computation of the slow-varying variables (node voltages and branch currents) for some discrete time points, required by the fast-varying signals only, and use **interpolation methods** to reconstruct the solutions of the slow part at those points needed by the fast dynamics.

- Alternatively to the previous single-time dimension method, it will be useful to exploit a **multi-time approach** (from DAE to multi-rate PDAE, as in [5]) to represent and simulate stiff circuits that exhibit multi-time scales, using **envelope** circuit equation formulation to have a two-dimensions (split) signal representation;
- Make use of efficient mathematical methods to describes nonlinear devices (e.g., the VCO which is also affected by high-frequency noise), such as the **Perturbation Projection Vector** (PPV) for oscillators [3], which helps using a linearized model of the VCO that can further speedup the simulation.
- Since time performance is a key requisite of the algorithm (stability and accuracy are obvious), it has to be implemented with a **multi-threaded** programming language (such as *Pthread*), to exploit the powerful of multi-core computers.

References

1. B. Razavi *Design of Analog CMOS Integrated Circuits*. McGraw-Hill, Inc., New York, 2001.
2. F.N. Najm *Circuit Simulation*. Wiley, Toronto, 2010.
3. D. Harutyunyan and J. Rommes *Simulation of Coupled Oscillators Using Nonlinear Phase Macromodels and Model Order Reduction*. In: *Model Reduction for Circuit Simulation*, Vol. 74, pp. 163-175, Springer, 2011. <http://alexandria.tue.nl/repository/books/641933.pdf>
4. C. Barrett *Fractional/Integer-N PLL Basics*. Texas Instruments, Texas, 1999. <http://www.ti.com/lit/an/swra029/swra029.pdf>.
5. K. Bittner, H.G. Brachtendorf *Adaptive Multi-Rate Wavelet Method for Circuit Simulation*. *Radioengineering* 2014, issue 1, pp. 300-307. http://www.radioeng.cz/fulltexts/2014/14_01_0300_0307.pdf.

Acceleration of transient simulation of analog and mixed signal circuits in 14nm technology generation

Rakesh Jha¹

Department of Mathematics and Computer Science, Eindhoven University of Technology (Technische Universiteit Eindhoven) 5612 AZ Eindhoven, The Netherlands r.jha@tue.nl

Summary. As per Moore’s law, the number of transistors on chip doubles every 18 months, with decrease in feature sizes of transistors in successive generations. Parasitic effects, like capacitances and leakage currents, of different transistors and interconnects are becoming more and more dominant. Coupled with increasing chip density it is becoming increasingly difficult to simulate these circuits with desired accuracy and speed. We aim to work on acceleration of transient simulation of AMS¹ circuits for 14nm deep sub micron designs.

1 Introduction

The need for faster and accurate EDA² tools for simulation of AMS circuits has been evolving with each new technology generation. In each new technology generation we have smaller transistors and greater chip density³. It makes the parasitic effects in the transistors and parasitic effects of interconnects more pronounced. Simulation time is also increased with greater chip density. These in turn pose a more stringent process, voltage, temperature, power consumption and yield requirements.

Nearly 70% of today’s design is mixed signal and it is the analog engine of AMS simulators, which is a bottleneck in simulation speed. In order to address the current challenges (for 14nm), advanced numerical techniques are needed.

Our aim is to accelerate transient simulation of AMS circuits. Enhancement in the performance of existing simulators and parallelization of simulation algorithms, with improved scalability, are targeted. The idea of parallelization to achieve faster simulation is not entirely new. The approach has regained interest recently because of easy availabilities and excellent price-performance ratio of CMP⁴s, and the increasingly complex IC⁵ designs, which is making even the best serial solvers inadequate in terms of simulation speed [1].

2 Acceleration of Circuit Simulation

2.1 Background of Circuit Simulation

In time domain any electronic circuit can be expressed as a set of DAE⁶s.

$$\frac{d}{dt}q(x(t), u(t)) + f(x(t), u(t)) = 0 \quad (1)$$

where $x(t) \in R^N$ is the vector of unknown node voltages and branch currents, $u(t) \in R^N$ is the input excitation vector, $f(x(t), u(t)) \in R^N$ is the vector of resistive currents and $q(x(t), u(t)) \in R^N$ is the vector of charges or fluxes. Transient simulation involves solving for values of $x(t)$ at different values of time $t \in (t_0, t_f)$. It is an IVP⁷ where $x(t_0) = x_0$. Often x_0 is obtained from the DC analysis. DAEs are discretized using numerical integration techniques and non-linear equations are linearized using Newton’s method. Finally, the linearized set of equations are solved using linear solvers [2] [1]. The steps in transient simulation are shown in Fig. 1. The sparse nature of the system matrix is exploited for better performance by using algorithms like KLU [6].

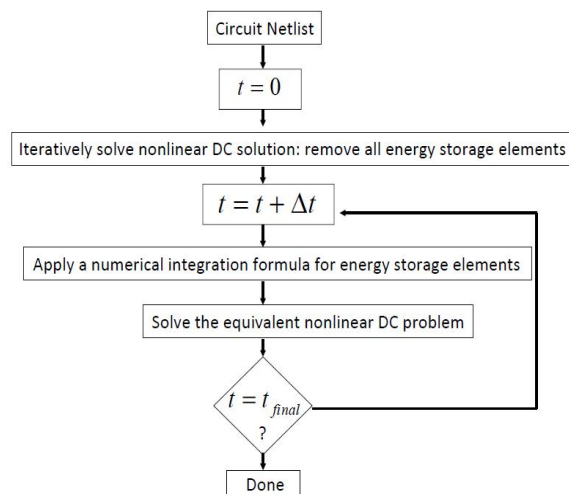


Fig. 1. General flow of transient simulation [1].

¹ Analog and Mixed Signal

² Electronic Design Automation

³ Chip density is the number of transistors in a unit area of chip.

⁴ Chip Multi Processors or Multi-Core processors

⁵ Integrated Circuit

⁶ Differential Algebraic Equation

⁷ Initial Value Problem

2.2 Parallelization

Parallelization can be at all the different steps of transient simulation shown in Fig. 1. Device evaluations and solution of linearized equations are the most time consuming and have been targets of earlier parallelization efforts. Parallelization of device evaluations is quite straightforward [1]. Solution of a large system of linear equations is more complicated. Circuit partitioning is an important technique for solving a large set of equations faster. Parallelism may also be explored in the time domain by computing the circuit response at several time points instantaneously [3].

2.3 Circuit Partitioning

Using circuit partitioning techniques, circuits can be partitioned recursively into sub-circuits [5]. The partitioning can be done in a nested manner. The idea of circuit partitioning is shown in Fig. 2.

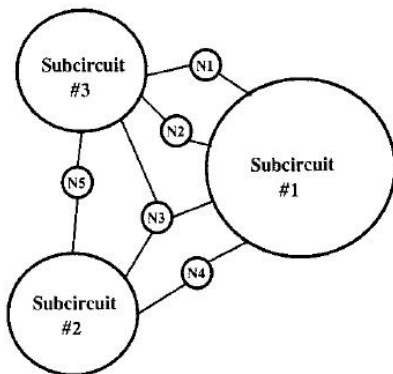


Fig. 2. Circuits partitioning through node tearing [4]. N1, N2, N3, N4 and N5 are interconnect nodes between different sub-circuits.

2.4 Problem

Existing simulators with serial and parallel solvers are becoming inadequate with growing size and complexity of IC designs. A part of the problem is in improving the performance of different simulation steps of serial solvers. Another problem is in finding good algorithms for partitioning and task scheduling, which would keep the overheads of parallelization low and remain scalable. The existing parallel direct matrix solvers are not highly scalable. Parasitic coupling between different circuit nodes in 14nm would not be negligible [1]. Non-negligible parasitics would require that the device model used in simulators account for the parasitics as well. The application of relaxation methods, which hold promise for large circuits, would be difficult because of the coupling. Relaxation methods exploit unidirectionality of signal propagation to achieve fast convergence. Contribution of parasitics would reduce the sparsity of the Jacobian.

In circuit partitioning the interconnects between different sub-circuits present a serial bottleneck. Achieving a suitable level of granularity and load balance is a challenging task, which is essential to obtain efficient resource utilization. In addition different sub-circuits converge at different rates. Using same time steps for all the sub circuits, therefore, leads to inefficient resource utilization.

2.5 Methodologies

Some of the ways in which the problem can be approached are:

- Improvements in the partitioning algorithm and scheduling of tasks on different cores can be made.
- Application of mixed granularity to achieve better load balance.
- General purpose parallel matrix solvers, involving task graphs and supernodes, can be adapted for circuit simulation.
- Use of relaxation methods with parallel Schwarz preconditioners.
- Adoption of partial LU factorization and partial forward substitution.
- Parallelization of LU factorization and solves for the different sub-circuits in hierarchical solvers.
- Application of latency and multi-rate techniques to different levels of hierarchy, in time integration and newton's iterations.
- Reduction of computations by non-linear model order reduction and through development of non-linear macro models.

References

1. P. Li. *Parallel Circuit Simulation: A Historical Perspective and Recent Developments*. Foundations and Trends in Electronic Design Automation, Vol. 5, No. 4, 2011.
2. F.N. Najm. *Circuit Simulation*. ISBN 978-0-470-53871-5, Wiley, New Jersey, 2010.
3. W. Dong, P.Li and X. Ye. Wavepipe: Parallel transient simulation of analog and digital circuits on multi-core shared memory machines. *ACM/IEEE Design Automation Conference (DAC 2008)*, pp. 238-243, June, 2008.
4. P.F. Cox, R.G. Burch, D.E. Hocevar, P. Yang and B.D. Epler. Direct circuit simulation algorithms for parallel processing. *IEEE transactions on COmputer-Aided Design of Integrated Circuits and Systems*, vol. 132, no. 6, pp. 714-725, June 1991.
5. M. Vlach. LU decomposition and forward-backward substitution of recursive bordered block diagonal matrices. *IEEE proceedings G, Electronic Circuits and Systems*, vol. 132, no. 1, pp. 24-3, February 1985.
6. T.A. Davis, E.P. Natarajan Sparse matrix methods for circuit simulation problems. *Proceedings of Scientific Computing in Electrical Engineering SCEE 2010*, pp. 3-14, *Mathematics in Industry*, Vol. 16, ISBN 978-3-642-22452-2, Springer 2012.

Coupled Electrothermal Simulation of 3D Semiconductor Devices and Lumped Circuit Elements

D. Cagnoni¹, M. Bellini², M. Restelli³, J. Vobecký⁴, and C. de Falco^{1,5}

¹ MOX Politecnico di Milano, Milano, Italy carlo.defalco@polimi.it, davide.cagnoni@polimi.it

² ABB Corporate Research, Dättwil, Switzerland marco.bellini@ch.abb.com

³ NMPP - Numerische Methoden in der Plasmaphysik, Max-Planck-Institut für Plasmaphysik, Garching, Germany
marco.restelli@polimi.it

⁴ ABB Switzerland Ltd, Semiconductors, Lenzburg, Switzerland jan.vobecky@ch.abb.com

⁵ CEN, Centro Europeo di Nanomedicina, Milano, Italy

Summary. The numerical simulation of large area semiconductor devices for power electronics applications, such as Phase Control Thyristors (PCTs) or Bimode Insulated Gate Transistor (BIGTs) requires full-scale 3D simulations. Furthermore the lack of efficient and accurate lumped element models for complex power devices, demands for mixed mode simulation of distributed devices coupled to external controlling circuits. Here we propose a strategy for the coupled electrothermal simulation of 3D semiconductor-oxide devices and lumped circuit elements, with particular emphasis on the performance of iterative solution strategies for nonlinear equations.

1 Introduction

Advanced power semiconductor devices are characterized by complex 3D geometries and therefore can be studied accurately only with 3D simulations.

Commercial 3D TCAD simulators, are mainly focused on the numerical modeling of CMOS devices rather than on providing the computational efficiency required for the simulation of large devices with complex geometries. For this reason MOX and ABB initiated a collaboration aimed at studying algorithms for large scale simulation of power electronics devices, and developed an experimental TCAD simulator based on the in-house finite element libraries LDGH and BIM++, already in use at MOX.

2 Coupled mathematical model

Let Ω be the device domain, $\bar{\Gamma}^N$ be the insulated device boundary, and $\bar{\Gamma}_i^D$ represent each of the \mathcal{N}_c contacts of the device. Let Ω_{Si} and Ω_{SiO_2} be the silicon and silicon-oxide regions respectively. A general assumption is made that voltage over a contact surface is uniform: the voltages F_i , with $i = 1 : \mathcal{N}_c$, are added to the system as additional variables. We suppose for the sake of simplicity that each contact is connected to one of the \mathcal{N}_c pins of the connected circuit, whose voltage is represented as one of the \mathcal{N}_f circuit state variables.

The model reads:

$$\begin{aligned} -\nabla \cdot (\varepsilon \nabla \phi) + q(n - p - D) &= 0 \\ \frac{\partial n}{\partial t} + \nabla \cdot J_n + RG(n, p, \nabla \phi) &= 0 \\ \frac{\partial p}{\partial t} + \nabla \cdot J_p + RG(n, p, \nabla \phi) &= 0 \end{aligned}$$

in the silicon domain Ω_{Si} , where ϕ is the electric potential, ε is the material absolute permittivity, n and p are the electron and hole number densities, q is the elementary charge, D is the doping density, t is time, $RG(n, p, \phi)$ is the recombination-generation rate, $J_n = -(\mu_n V_{th} \nabla n - \mu_n n \nabla(\phi + \phi_{BGN}))$ and $J_p = -(\mu_p V_{th} \nabla p + \mu_p p \nabla(\phi - \phi_{BGN}))$ are the electron and hole fluxes, μ_n and μ_p are the (variable) electron and hole mobilities, V_{th} is the thermal voltage, and ϕ_{BGN} is the half-bandgap voltage variation due to doping effects. In the oxide domain Ω_{SiO_2} , the equations reduce to:

$$-\nabla \cdot (\varepsilon \nabla \phi) = 0, \quad n = p = 0.$$

The conditions on the boundaries read:

$$D + p - n = 0 \quad n = n_i \exp\left(\frac{F_i - \phi}{V_{th}}\right) \quad p = n_i \exp\left(\frac{\phi - F_i}{V_{th}}\right)$$

on $\Gamma_i^D \cap \overline{\Omega_{Si}}$, $\forall i = 1 : \mathcal{N}_c$,

$$\nabla \phi \cdot \mathbf{v}^N = 0 \quad J_n \cdot \mathbf{v}^N = 0 \quad J_p \cdot \mathbf{v}^N = 0$$

on $\Gamma^N \cap \overline{\Omega_{Si}}$,

$$\phi - F_i = \Phi_{bi} \quad n = p = 0$$

on $\Gamma_i^D \cap \overline{\Omega_{SiO_2}}$, $\forall i = 1 : \mathcal{N}_c$, and

$$\nabla \phi \cdot \mathbf{v}^N = 0 \quad n = p = 0$$

on $\Gamma^N \cap \overline{\Omega_{SiO_2}}$, \mathbf{v}^N and \mathbf{v}_i^D being the outward normal versors on Γ^N and Γ_i^D , respectively. The device-circuit coupling reads

$$A \frac{d}{dt} x + Bx + C + rI = 0$$

with $x_j = F_i$, $r_{j,k} \in \{0, 1\} \iff (\mathcal{M}_{cont.}(k) = \Gamma_i^D) \wedge (\mathcal{M}_{pins}(k) = j)$, where x_j are the electrical and thermal degrees of freedom describing the circuit state, according to the models of [4–6], A , B are the matrices and C the source term of the descriptor system for

the circuit, and I is the vector of the currents outflowing the device contacts, defined as:

$$I_k = \int_{\Gamma_i^D} \mathcal{M}_{\text{pins}}(k) \left(-\frac{d}{dt} (\epsilon \nabla \phi) + q(J_p - J_n) \right) \cdot \nu_i^D d\Gamma,$$

The maps $\mathcal{M}_{\text{cont}}$ and $\mathcal{M}_{\text{pins}}$, defined from $\{1, 2, \dots, \mathcal{N}_c\}$ onto the set of contacts $\{\Gamma_i^D\}_i$ and the circuit variables indexes $\{1, 2, \dots, \mathcal{N}_f\}$ respectively, represent the device-circuit connections, r being a tensor coupling the k -th current with the j -th circuit equation, according to both the map $\mathcal{M}_{\text{pins}}$ and the kind of control to be imposed.

3 Device Structure

As a benchmark test case, we consider the power diode studied in [7]. Such diodes are irradiated with 1–5 MeV electrons at a dose between 5 and 20 kGy and 5–12 MeVHe at doses ranging between 10^{10} – 10^{11} cm^{-2} and annealed at a temperature below 300 °C. In these conditions the dominant deep levels are the vacancy-oxygen pair (V-O) at \simeq EC – 0.16 eV and the divacancy (V-V) at \simeq EC – 0.42 eV.

As a result, an accurate model of the recombination-generation centers in the semiconductor, is necessary to precisely reproduce the reverse recovery characteristics of the diode. Since the inclusion of the complete trap models is computationally expensive and degrades convergence, an effective carrier lifetime profile was computed via a commercial simulator ([8]) and introduced with a conventional SRH type recombination model.

The schematic of testing circuit used for reverse recovery measurements is shown in Fig. 1. The exact value of the inductance LS used in the test is finetuned to match the di/dt of the measurements. The measured reverse recovery current at temperatures of 80 °C, 125 °C, and 140 °C is shown in Fig. 2.

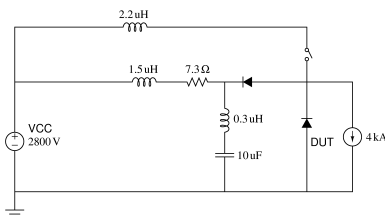


Fig. 1. Schematic structure of the simulated circuit.

References

1. G. Ali, A. Bartel, M. Günther, and C. Tischendorf. Elliptic partial differential-algebraic multiphysics models in electrical network design. *Mathematical Models and Methods in Applied Sciences*, 13(09):1261–1278, 2003.

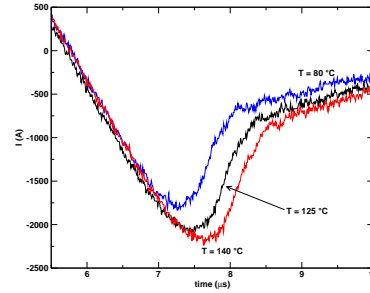


Fig. 2. Reverse recovery characteristics at 80 °C, 125 °C, and 140 °C.

2. Amestoy P., Duff I., L'Excellent J.-Y., and J. Koster. Mumps: A general purpose distributed memory sparse solver. In *Applied Parallel Computing. New Paradigms for HPC in Industry and Academia*, volume 1947 of *Lecture Notes in Computer Science*, pages pp. 121–130. Springer Berlin–Heidelberg, 2001.
3. Brown P.N. and Saad Y. Hybrid krylov methods for nonlinear systems of equations. *SIAM J. Sci. and Stat. Comput.*, 11:pp. 450–481, 1990.
4. G. Ali, A. Bartel, M. Culpò, and C. de Falco. Analysis of a PDE thermal element model for electrothermal circuit simulation. In *Proceedings of Scientific Computing in Electrical Engineering (SCEE) 2008*, volume 14 of *Mathematics in Industry*, pages 273–280. Springer-Verlag, 2010.
5. M. Culpò and C. de Falco. Dynamical iteration schemes for coupled simulation in nanoelectronics. In *Proceedings of the 79th GAMM meeting*, volume 8 of *Proc. Appl. Math. Mech. (PAMM)*, pages 10065–10068. WILEY-VCH Verlag GmbH & Co. KGaA, Weinheim, 2008.
6. M. Culpò, C. de Falco, G. Denk, and S. Voigtmann. Automatic thermal network extraction and multiscale electro-thermal simulation. In Janne Roos and Luis R.J. Costa, editors, *Scientific Computing in Electrical Engineering SCEE 2008*, volume 14 of *Mathematics in Industry*, pages 281–288. Springer-Verlag, 2009.
7. M. Bellini and J. Vobecký. TCAD simulations of irradiated power diodes over a wide temperature range. *Simulation of Semiconductor Processes and Devices (SISPAD), 2011 International Conference on*, pages 183–186. IEEE, 2011.
8. Sentaurus Device User Guide, Version D-2010.03, Synopsys, 2010.

Acknowledgements

Carlo de Falco's work was partially funded by the "Start-up Packages and PhD Program project", co-funded by Regione Lombardia through the "Fondo per lo sviluppo e la coesione 2007-2013", formerly FAS program.

Sensitivity Techniques for Effective Optimization of Tandem Thin-Film Silicon Solar Cells

A. Patanè¹, A. Santoro¹, G. Carapezza¹, V. Romano¹, A. La Magna², and G. Nicosia¹

¹ Dept. of Mathematics & Computer Science - University of Catania, Italy

² IMM - CNR, Italy

Summary. The aim of our research work is to analyse tandem thin-film Silicon solar cells, optimizing the optical efficiency vs cost trade-off. The model used to compute cells quantum efficiency is composed of i) a Maxwell simulation, which captures light scattering through nano-textured interfaces, and ii) a photonic Monte Carlo approach to statistically evaluate coherent and scattered photon absorption in within the cell layers. The model is undergone to the Morris screening method and its Sobol indexes are calculated, in order to have both a qualitative and quantitative Sensitivity Analysis measure. Sensitivity Analysis results are hence used to efficiently optimize the model, reducing its order: ad hoc Single Objective Optimization Algorithm (MCS) is applied only on the most sensitive parameters to fully maximize the Quantum efficiency and ad hoc derivative-free Multi Objective Evolutionary Algorithm (NSGA-II) is used (again considering only the most sensitive parameters) in order to balance efficiency and cost. Optimal designs robustness is evaluated throughout the computation of three different statistical indexes: Local (which gives information about single parameter variations effect on a given design), Global (which evaluate the effect on a given designs when all parameters are varying) and Glocal (which compute the largest *stable* neighborhood of a given design). At last, notable points set are analysed by a data-based Identifiability Analysis algorithm (MOTA), to infer functional relationships between the parameters considered. The results obtained (up to a 5.88% total absorption improvement) widely demonstrate the solidity and the strength of our approach balancing optimality and computational efficiency.

An advanced transmitter and receiver modelling scheme for the EMC analysis of smart grid components

Frank Gronwald

Hamburg University of Technology, Institute of Electromagnetic Theory, 21079 Hamburg, gronwald@tuhh.de

Summary. The comprehensive EMC analysis of smart grids includes, as fundamental basis, the physical layer of signal transmission. In this contribution it is pointed out that also the data link layer should be included into the analysis. As a consequence, traditional transmitter and receiver EMC models need to be combined with the concepts of modern communication theory. As an example, the performance of a generic OFDM data link under the influence of external interference is studied.

1 Introduction

Modern communication systems have become an essential part of today's power supply networks that often are referred to as *smart grids* [1]. The merging of communication systems and power supply networks, however, also has led to considerable problems concerning their Electromagnetic Compatibility (EMC) [2, 3]. Corresponding analysis methods and countermeasures require concepts that are beyond analog data transmission and additionally require digital signal processing [4]. These concepts do not appear in classical EMC models, such as the ones outlined in [5, 6], and the question appears how to include them in an EMC analysis. Referring to the International Standards Organization / Open System Interconnection (ISO/OSI) layer model, as illustrated in Fig. 1, this implies to investigate whether besides the physical layer 1 also the data link layer 2 can be included in an EMC analysis. Generally, this encompasses transmitter, propagation, and receiver models. The propagation models typically are described by transmission line or electromagnetic theory and the inclusion of digital signal processing mainly requires appropriate and advanced transmitter and receiver models.

2 Traditional and advanced transmitter and receiver models

The notion of traditional transmitter and receiver models is not well-defined. In view of the EMC of smart grids there are established models which take into account properties such as the spectral content of a signal, the type of modulation used, the signal to noise ratio, and the receiver bandwidth and sensitivity, e.g. [8]. In these models the different stages of data transmission are analog and, in the linear case, can

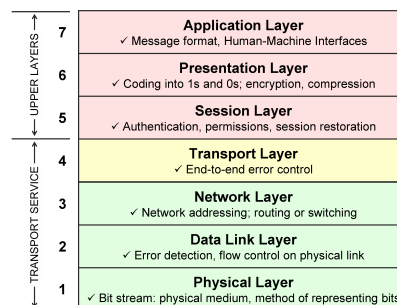


Fig. 1. ISO/OSI layers which characterize digital communication systems by a hierarchical layer model [7]. The usual EMC analysis concerns the physical layer 1 which, in particular, contains the physical wired or wireless data connections. The data link layer 2 already involves advanced methods of digital signal processing and includes error detection and the digital elimination of unwanted signals, as possibly produced by EMI sources.

be modelled by means of transfer functions. To also include digital signal processing they have to be supplemented by operations such as analog-digital conversion, digital modulation, synchronization, and error detection.

As an example for a digital transmitter and receiver configuration, in Fig. 2 a generic model of an Orthogonal Frequency Division Multiplexing (OFDM) data link is shown. On the transmitter side, initial data words are mapped on a complex Quadrature Amplitude Modulation (QAM) plane and eventually modulated, digitally upconverted, and finally converted to the analog domain. On the receiver side, the incoming signal is converted back to the digital domain, digitally down-converted, demodulated and finally demapped on a complex QAM plane.

The single steps that are necessary to perform the transmission can, in principle, be done analytically by hand. However, it is more feasible to model and implement the data transmission within a software environment such as MATLAB/SIMULINK [9]. It is then possible to also add disturbing signals to the propagation channel and to investigate their influence on the received data words. In Fig. 3 the influence of some specific interferences are shown and illustrated.

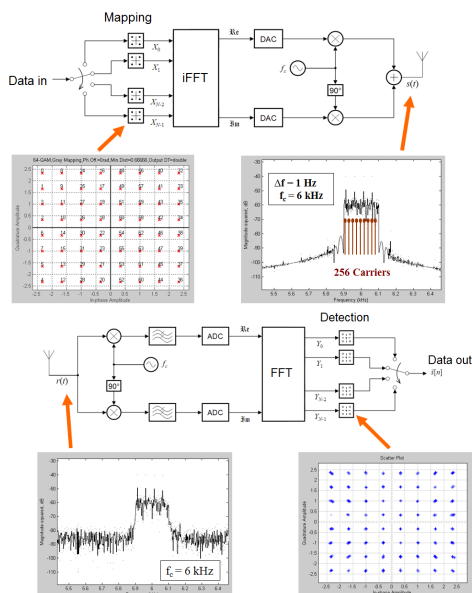


Fig. 2. Transmitter and receiver configuration of a generic OFDM data link.

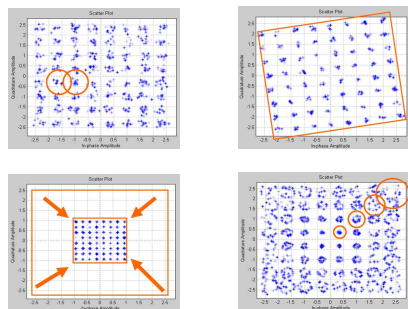


Fig. 3. Resulting data word sets, obtained under the influence of, from left to right: (i) noise, (ii) phase shift, (iii) damping, and (iv) multipath effects. It is noted that the data link model does not include synchronization and error correction.

3 Example: Symbol error rate of a generic OFDM data link for smart grid power line communication

A transmitter and receiver configuration as shown above can be used, for example along the lines of [10–12], to study the symbol error rate (SER) in dependency of various disturbances. For a generic OFDM data link a number of parameters have to be set. These concern the different simulation blocks where modulation/demodulation, up-/down-conversion, and DA-/AD-conversion take place. For a fixed setting, Fig. 4 shows the SER in dependency of different parameters of a damped sinusoidal pulse which affects the propagation paths. The SER increases with increasing pulse amplitude and peaks at a pulse carrier frequency of about 1 MHz which corresponds to a passband frequency of the transmitter. Also other observables and dependencies can be analyzed in this framework.

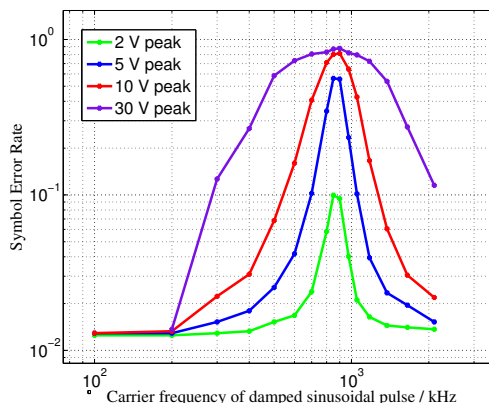


Fig. 4. Illustration of a Symbol Error Rate in dependency of specific damped sinusoidal pulses that separately act as disturbances. The Symbol Error Rate refers to a generic OFDM data link.

References

1. Strzelecki, R. and Benysek, G. (eds.): *Power Electronics in Smart Electrical Energy Networks*, (Springer, London, 2008).
2. Smolenski, R.: *Conducted Electromagnetic Interference (EMI) in Smart Grids*, (Springer, London, 2012).
3. CENELEC SC 205A: “Study Report on Electromagnetic Interference between Electrical Equipment/Systems in the Frequency Range below 150 kHz”, ed. 2, SC 205A/Sec0339/R (April 2013).
4. Proakis, J.G. and Manolakis, D.G.: *Digital Signal Processing*, 4th ed., (Prentice Hall, New Jersey, 2006).
5. Tesche, F.M., Ianoz, M.V., and Karlsson, T.: *EMC Analysis Methods and Computational Methods*, (John Wiley & Sons, New York, 1997).
6. Paul, C.R.: *Introduction to Electromagnetic Compatibility*, 2nd ed., (John Wiley & Sons, New York, 2006).
7. Cisco Networking: “What is OSI Model & the Overall Explanation of ISO 7 Layers”, <http://www.cisco1900router.com>, retrieved in February 2014.
8. Duff, W. and White, D.R.J.: *EMI Prediction and Analysis Techniques – A Handbook Series on Electromagnetic Interference and Compatibility*, vol. 5, (Don White Consultants Inc., Maryland, 1972).
9. MATLAB and SIMULINK, The MathWorks, Inc., Natick, Massachusetts, United States.
10. Matsumoto, Y., Shimizu, T., Murakimi, T., Fujii, K., and Sugiura: “Impact of Frequency-Modulated Harmonic Noises from PCs on OFDM-based WLAN Systems”, *IEEE Trans. on Electromagn. Compat.*, vol. 49, no. 2, (May 2007), pp. 455–462.
11. Matsumoto, Y., Murakimi, T., Fujii, K., and Sugiura: “Impact of Electromagnetic Noise from PCs on Performance of Multiband-OFDM UWB Systems”, *IEEE Transactions on Consumer Electronics*, vol. 56, no. 2, (May 2010), pp. 348–352.
12. Schwarz, M. and Gronwald, F.: “EMI analysis of a generic power line communication OFDM data link”, in *EMC Europe 2011*, York, England, (September 2011), 625–628.

Mixed-domain Macro-Models for RF MEMS Capacitive Switches

Gabriela Ciuprina¹, Daniel Ioan¹, Dragoş Isvoranu¹, Ştefan Sorohan¹, Sorin Lup¹, and Sebastian Kula²

¹ Politehnica University of Bucharest, Spl. Independenţei 313, 060042, Bucharest, Romania
 gabriela.ciuprina@upb.ro, daniel.ioan@upb.ro, dragos.isvoranu@upb.ro,
 sorohanstefan@resist.pub.ro, sorin@lmn.pub.ro

² Kazimierz Wielki University, Bydgoszcz, Poland skula@ukw.edu.pl

Summary. A method to extract macromodels for RF MEMS switches is proposed. The macromodels include both the coupled structural-electric behaviour of the switch as well as its RF behaviour. The device with distributed parameters is subject to several analyses from which the parameters of the macromodel are extracted, by model reduction. Finally, all parameters are combined in a Spice circuit model, which is controlled by the MEMS actuation voltage and is excited with the RF signal.

1 Context

RF MEMS switches are devices containing electrostatic actuated movable parts with two stable states (up and down), used to allow or block the paths of RF signals in various applications. They are based on micromachining technologies, being more suitable than solid electronic switching devices [1]. A typical capacitive RF switch contains an elastic bridge over a coplanar waveguide line (Fig. 1). The capacitance between the grounded bridge and the signal line, isolated with a dielectric layer is strongly dependent on the bridge position. The design of this

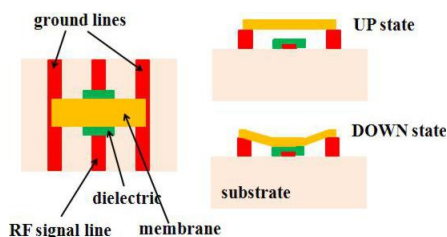


Fig. 1. Typical capacitive RF switch.

device focuses not only on the RF performances (S parameters at the RF terminals) in its stable states, but also on relevant quantities (pull-in/out voltages at the actuation terminals, commutation time between the stable states) related to its switching from one stable state to the other. The investigation of the latter aspects needs multiphysics simulations since several physical effects (mechanical motion, air damping, electrostatic actuation) come together. Even since the early development of these devices, the computational challenges identified, are the multiphysics level modelling, required for the estimation of the switching properties, and the nonlinear macromodelling or

the nonlinear order reduction, which is very important for the designers who need dynamical device-level models. The effective macromodels should be accurate enough and have few degrees of freedom, and they have to be correlated to design parameters such as dimensions and material properties, with the aim of being embedded in system-level models [2]. The multiphysics modeling is still a difficult challenge [3].

A common approach is to use separate macromodels for the physical domains involved, depending on the investigated properties. The RF macromodels, consist of short sections of transmission lines and R, L, C elements (Fig. 2), and they are used to model the S-parameters of the switch in its stable states. The values of the capacitance are different for the down and up states. They are computed with simple formulas based on an uniform electrostatic field assumption as in [4], whereas R and L are computed from down-state simulations with an EM field solver and fitting of the obtained S parameters.

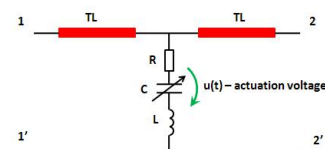


Fig. 2. Typical RF macromodel.

Circuit macromodels are also proposed for the multiphysics domain, as in [5], where large signal dynamic circuit simulation models for MEMS devices using controlled current sources are proposed and implemented in APLAC. The importance of device level models is that they can be combined and integrated into existing design environments [6]. Aspects related to the mixed-domain electromechanical and electromagnetic simulation of RF-MEMS devices and network are reported in [7]. Combined techniques that derive both lumped and distributed components are used to obtain a fully coupled model described in a hardware description language. A MEMS component model library is offered by this team at <http://rfmems.sourceforge.net/>.

2 Mixed Domain Macro-Models

The device with distributed parameters is subject to several field analyses from which the parameters of the macromodel are extracted, by model reduction. From the RF characteristics in several positions (Fig. 3), including up/down stable states, the TL parameters and the longitudinal R, L values of the switch are extracted with a procedure we previously proposed for passive components. From the coupled structural-electrostatic-fluidic numeric (FEM) analysis the lumped parameters of the switch are extracted (Fig. 4 and Fig. 5). Finally, all parameters are combined in a Spice circuit model, which is controlled by the MEMS actuation voltage and is excited with the RF signal (Fig. 6). This circuit describes the reduced (1D) equation of the mechanical movement: $m d^2 z/dt^2 + k z + b dz/dt = F_{es}(u, z)$, where the forces are described by behavioural current source. They include the electric force $F_{es}(u, z)$ that depends on the actuation voltage u and the capacitance of the switch which is dependent on the displacement z , as well as the damping force that depends on the bridge velocity $v = dz/dt$ with a global damping coefficient b , the elastic forces that depend on the displacement z and on an equivalent global elastic coefficients k . The "current" flowing through the mass capacitance m is in fact the inertial force $m dv/dt$.

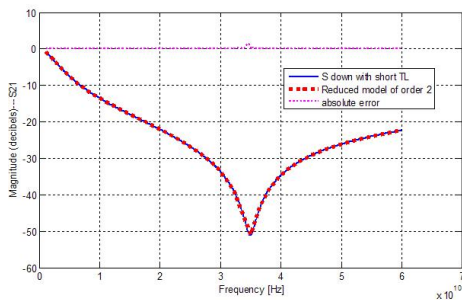


Fig. 3. RF characteristics. Reduced models of very low order are needed for the RF domain

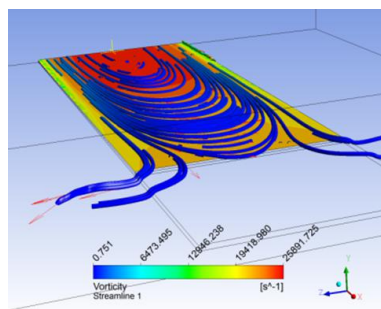


Fig. 4. Fluid flow lines around the bridge.

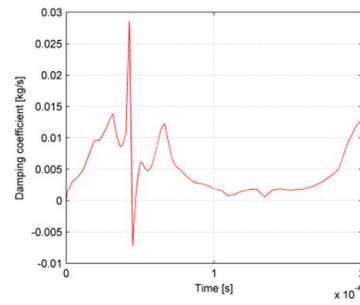


Fig. 5. Damping parameter extracted from the multiphysics simulation.

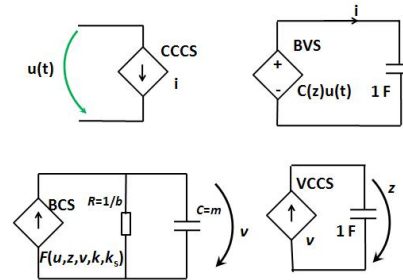


Fig. 6. Multiphysics macromodel described as a circuit (CCCS/VCCS = current/voltage controlled current source; BCS/BVS = behavioural current/voltage source). This schematic replaces the parametric capacitor in Fig. 2.

Acknowledgement. The financial support of the Romanian Government program PN-II-PT-PCCA-2011-3, ANCS, CNDI UEFISCDI, grant no. 5/2012 is acknowledged.

References

1. G.M. Rebeiz, *RF MEMS: Theory, Design, and Technology*. John Wiley & Sons, 2003.
2. S.D. Senturia, N. Aluru and J. White. Simulating the Behavior of MEMS Devices: Computational Methods and Needs. *IEEE Computational Science and Engineering*, 16(10):30–43, 1997.
3. S. Hannot. Modeling Strategies for ElectroMechanical Microsystems with Uncertainty Quantification. Ph.D. thesis, Delft University of Technology, 2010.
4. J. Muldavin and G. Rebeiz. High-Isolation CPW MEMS Shunt Switches Part 1: Modeling. *IEEE Transactions on Microwave Theory and Techniques*, 48(6):1045–1052, 2000.
5. T. Veijola. Nonlinear Circuit Simulation of MEMS Components: Controlled Current Source Approach. *ECCTD01 - European Conference on Circuit Theory and Design, August 28-31, 2001, Espoo, Finland*, III:377–380, 2001.
6. M. Shafique, K. Virk, A. Menon and J. Madsen. System-Level Modeling and Simulation of MEMS-based Sensors. *9th International Multitopic Conference, IEEE INMIC 2005*, 1–6, 2005.
7. J. Iannacci. Mixed-Domain Fast Simulation of RF and Microwave MEMS-based Complex Networks within Standard IC Development Frameworks. *www.intechopen.com*, 2001.

Modeling and Analysis of the Non-Stationary Maxwell Equations Coupled with The Circuit Equations

Helia Niroomand Rad and Andreas Steinbrecher

Institut für Mathematik, Technische Universität Berlin, Straße des 17. Juni 136, 10623 Berlin, Germany
nirooman@math.tu-berlin.de, steinbrecher@math.tu-berlin.de

Summary. Modeling the parasitic noise between electrical devices which are sitting in the neighboring area in electromagnetic systems, the so-called crosstalk phenomenon, may lead to differential-algebraic equations (DAEs) obtained by bilateral coupling of two subsystems of differential equations.

In this article, modeling of the crosstalk phenomenon based on the bilateral coupling and analysis of the obtained coupled system in terms of its index where the index is the differentiation index are considered .

1 Introduction

In the field of chip design, modeling, simulation and control of the reliability issues such as crosstalk phenomenon is of the great interest. The crosstalk phenomenon can be modeled by the bilateral coupling of two subsystems of the *improved Maxwell system*, obtained by the Maxwell equations, and the *Modified Nodal Analysis system*, derived by the circuit equations. Considering the suitable coupling relations, we obtain the coupled system of partial differential-algebraic equations (PDAEs).

The semi-discretization of the partial differential equations contained in the PDAEs in space by finite element method yields a large DAE system with higher differentiation index compared to the index of the Modified Nodal Analysis system due to the coupling relations. In fact, it can be shown that the underlying equations of the Modified Nodal Analysis system is a DAE system where the associated index doesn't exceed 2 under some conditions on the topological structure of the integrated devices in the electrical circuit. Structural complexity of a DAE system is presented by its index, and therefore index analysis for the purpose of time integration is necessary.

2 Modeling

Improved Maxwell system

For the vector fields magnetic flux density B , electric field E and the magnetic field H defined by

$$B, E, H : \Omega \times \mathbb{I} \rightarrow \mathbb{R}^3$$

the improved set of Maxwell system read as

$$\begin{aligned} \nabla \cdot B &= 0, & \text{in } \Omega \times \mathbb{I} \\ \nabla \times E &= -\partial_t B, & \text{in } \Omega \times \mathbb{I} \\ \nabla \times H &= \partial_t(\varepsilon_0 E + P) + \sigma E + J_a, & \text{in } \Omega \times \mathbb{I} \\ \nabla \cdot (\varepsilon_0 E + P) &= \rho, & \text{in } \Omega \times \mathbb{I} \\ \nabla \cdot (\sigma E + J_a) &= -\partial_t \rho, & \text{in } \Omega \times \mathbb{I} \end{aligned}$$

where $\Omega \subseteq \mathbb{R}^3$ is assumed to be bounded and Lipschitz domain, and \mathbb{I} is a closed interval of \mathbb{R} . Therein, the polarization current density and the electric charge density are denoted by P and ρ , respectively. Furthermore, ε_0 is the vacuum permittivity, σ is the electrical conductivity, and J_a is the applied current density.

Modified Nodal Analysis system

The dynamical behavior of the electrical circuits consisting of linear electrical devices such as the capacitor with the capacitance C , the inductor with the inductance L and the resistor with the resistance R is described by the Modified Nodal Analysis system

$$\begin{aligned} & \begin{bmatrix} A_C C A_C^T & 0 & 0 & 0 \\ 0 & L & 0 & 0 \\ 0 & 0 & 0 & 0 \\ 0 & 0 & 0 & 0 \end{bmatrix} \begin{bmatrix} \dot{\eta} \\ i_L \\ i_{CV} \\ i_V \end{bmatrix} \\ &= \begin{bmatrix} -A_R G A_R^T & -A_L & -A_{CV} & -A_V \\ A_L^T & 0 & 0 & 0 \\ A_{CV}^T & 0 & 0 & 0 \\ A_V^T & 0 & 0 & 0 \end{bmatrix} \begin{bmatrix} \eta \\ u_L \\ i_{CV} \\ i_V \end{bmatrix} \\ &+ \begin{bmatrix} -A_{CC} & -A_I & 0 & 0 \\ 0 & 0 & 0 & 0 \\ 0 & 0 & -I & 0 \\ 0 & 0 & 0 & -I \end{bmatrix} \begin{bmatrix} i_{CC} \\ u_I \\ u_{CV} \\ u_V \end{bmatrix} \end{aligned}$$

where A_{CC} and A_{CV} denote the associated incident matrices to the controlled current sources and to the controlled voltage sources respectively, and η denotes the nodal potential of the electrical circuit. In addition, the corresponding incidence matrices to the devices are denoted by A_i where $i \in \{C, L, R, V\}$.

3 Index analysis

We are interested in the structural properties of the coupled system in terms of its index which are important for the purpose of numerical integration. In principle, high index may lead to the not reliable results

while simulation. For instance, it may lead to instabilities and inconsistencies in the numerical treatment. Therefore, it is essential to determine the index of the obtained coupled system before time integration.

The corresponding differential-algebraic equations to the coupled system is of the type of quasi-linear DAEs with high index due to the hidden constraints established by the coupling relations. In this article, the index of this quasi-linear DAEs is analyzed and some requirements for the smoothness is also considered.

Acknowledgement. This work has been supported by European Research Council through Advanced Grant *MODSIM-CONMP*.

References

1. A. Steinbrecher and T. Stykel Model order reduction of nonlinear circuit equations, *Int. J. Circ. Theor. App.*, 2013
2. A. Steinbrecher Numerical solution of Quasi-Linear Differential-Algebraic Equations and industrial simulation of multibody systems, PhD thesis, Technical University Berlin, 2006

Approximate Linear Solvers for Adaptive Runge-Kutta Methods Applied to the Simulation of Transients in Power Systems

Romain Thomas¹, Domenico Lahaye², Kees Vuik², and Lou van der Sluis¹

¹ Power Systems Department, Delft University of Technology, Delft, The Netherlands R.Thomas@tudelft.nl, L.vanderSluis@tudelft.nl

² Delft Institute of Applied Mathematics, Delft University of Technology, Delft, The Netherlands D.J.P.Lahaye@tudelft.nl, C.Vuik@tudelft.nl

Summary. Changing the topology of a power system during operation typically causes temporary high-frequency oscillations. These transients can be described by a system of linear ordinary differential equations that can be integrated in time by a semi-explicit Runge-Kutta method. This Runge-Kutta method is implicit and consequently requires a linear solver. In this work, several transients are computed for different stiffnesses and problem sizes in order to show the impact of different linear solvers in terms of computation time. This study suggests that the computing time is faster with one iteration of iLU(l) with $l = 20$ as a basic iterative method.

1 Introduction

A transient appears when the topology of a power system changes. The transient is the transition between two steady states and this transition is generally composed of high-frequency oscillations [1]. Numerical integration methods of stiff equations for large system of differential equations require an important computation time.

The system of equations to integrate is a linear system of ordinary differential equations (ODEs). The system of ODEs are obtained from the block modelling method [2]. The principle of this method is to connect different ODEs which represent the different elements of a power system in a large system of ODEs.

Runge-Kutta method are used in different scientific domains [3]. We are interested in the adaptive fourth order Runge-Kutta which is semi-explicit (diagonally implicit numerical integration method) and is able to control the time step [4]. This method needs a linear solver [5] (implicit method). However, the linear solver requires a large amount of computation time. For this reason, in order to reduce the computation time, we have investigated different linear solvers which could be used with the time integration method.

To study the different linear solvers used with the Adaptive Runge-Kutta 4 (ARK4), the software PETSc is used [6]. This mathematical tool is developed for large-scale applications. It implements various algorithms for system of linear and non-linear equations allowing to experiment with various options such as ordering methods, fill in, residual error, ...

Several test cases with diverse proprieties (size and eigenvalues) are used to study the different linear solvers. From these test cases, it is shown that one iteration of iLU(l) with $l = 20$ as basic iterative method (BIM) works efficiently for any size of system of ODEs and for large eigenvalue problems.

The abstract is organized as follows. Section 2 presents the different test cases. Section 3 is a small reminder about semi-explicit Runge-Kutta method. Section 4 shows the different solvers used in the paper. Numerical results are shown in section 5. Finally, section 6 draws the conclusion.

2 Test cases

The block modelling method [2] is used to obtain a linear system of ODEs. The main idea of the method is to connect a multitude of small systems of ODEs which represent some components of the power system inside of a large system of ODEs. This method gives the following formulation:

$$\dot{\mathbf{x}} = \mathbf{A}\mathbf{x} + \mathbf{B}\mathbf{u}(t) \quad (1)$$

where $\mathbf{A} \in \mathbb{R}^{n \times n}$, $\mathbf{B} \in \mathbb{R}^{n \times n_g}$, $\mathbf{x} \in \mathbb{R}^n$ and $\mathbf{u}(t) \in \mathbb{R}^{n_g}$, n is the number of differential variables (currents through inductances and voltages across capacitances) and n_g is the number of sources.

We consider six test cases. The four first test cases (TC 1 to 4) have different sizes from the less to the most import number of differential variables (98, 1034, 4195 and 20999). Finally we consider two test cases (TC 5 and 6) with a number differential variables of 1050 and 104640. The difference is that the stiffness is more important for the test case 5 and 6 than for the test case 1 to 4.

3 Runge-Kutta methods

The Runge-Kutta method used in this paper is the Adaptive Runge-Kutta 4 (ARK4) and the Butcher tableau [7] of this method is given in [4]. This method has six stages ($s = 6$), is a four order method ($p = 4$) and has the ability to control the time step. The time stepping control used is shown in [3]. The system of

linear equations to solve due to the ARK4 algorithm is:

$$(I - \bar{A}_{ii}\Delta t A)\mathbf{k}_i = A \left(\mathbf{u}_n + \Delta t \sum_{j=1}^{i-1} \bar{A}_{ij}\mathbf{k}_j \right) + B\mathbf{u}(t_n + c_i\Delta t) \quad (2)$$

where \bar{A} and c_i come from the Butcher tableau [4] and $1 \leq i \leq s$

4 Linear solver

In order to solve the Equation (2), a linear solver is necessary. In this work, we compare the following linear solvers: one iteration of GMRES with iLU as pre-conditioner, one iteration of GMRES with iLU(l) as pre-conditioner, one iteration of iLU as BIM and one iteration of iLU(l) as BIM where $l = 20$. Moreover, re-ordering method is used to reduce fill in.

At each time step of a numerical integration method a local truncation error is made. The basic idea is to approximate the linear solver. By using an approximation of the linear solver, we guess that the computation time would be smaller than with an exact linear solver. Moreover, the increase of the local truncation error due to the approximation of the linear solver will be negligible.

5 Results

The following table (Table 1) shows the computation time of the simulation of the different test cases (TC 1 to TC 6). The tolerance of the numerical integration method is 0.0001, the simulation time is 0.05s and the initial condition is $\mathbf{x}_0 = 0$.

Table 1. CPU time in second

	GMRES+iLU	GMRES+iLU(20)	iLU	iLU(20)
TC 1	5.3	5.3	4.5	4.5
TC 2	14.7	14.2	10.1	10.4
TC 3	48.1	46.9	30.7	32.3
TC 4	284.7	286.0	201.4	210.9
TC 5	<300	13.3	<300	9.9
TC 6	<1000	629.5	<1000	348

From Table 1, we can see that one iteration of iLU(20) as BIM is faster for large eigenvalue problems. Furthermore, the solution found by iLU(20) is accurate. However, one iteration of iLU(20) as BIM is slower than one iteration of iLU as BIM method for small eigenvalues problems. However, at the beginning of a simulation, usually, eigenvalues are unknown.

6 Conclusion

In this work, we have studied approximate linear solvers with an adaptive Runge-Kutta method (ARK4) for the computation of transients in power systems. From the different test cases, we can state that one iteration of iLU as BIM is sufficient with the ARK4 and is faster than GMRES with iLU as pre-conditioner if the matrix A is well conditioned. However, when the eigenvalues of the matrix A become large, iLU(l) is more efficient. For this reason, by using all time iLU(l) as BIM with for example $l = 20$ is important. This strategy takes into account the values of the eigenvalues of the matrix A especially if the matrix A is badly conditioned. Of course, if the eigenvalues of the matrix A are known, it is possible to choose iLU or iLU(l) with an appropriate l . Further work needs to be investigated to understand these results.

References

1. L. van der Sluis Transients in Power Systems, Wiley, 2001.
2. R.Thomas, D. Lahaye, K. Vuik and L. van der Sluis, New Transient Modelling Approach of Power Systems for Adaptive Time-Stepping Algorithm, In preparation, 2014.
3. W. Hundsdorfer and J. Verwer, Numerical Solution of Time-Dependent Advection-Diffusion-Reaction Equations, Springer, New York, 2003.
4. C. A. Kennedy and M. H. Carpenter, Additive Runge-Kutta schemes for Convection-Diffusion-Reaction equations, *Applied Numerical Mathematics*, 44:139–181, 2003.
5. Y. Saad, Iterative Methods for Sparse Linear Systems, PWS Publishing Company, 1996.
6. S. Balay , K. Buschelman , V. Eijkhout , W. D. Gropp , D. Kaushik , M. G. Knepley , L. Curfman McInnes , B. F. Smith and H. Zhang, PETSc Users Manual, 2010, [online] Available: <http://www.mcs.anl.gov/petsc/>
7. J. Butcher, BIT Numerical Mathematics, *Applied Numerical Mathematics*, 16:237–240, 1976.

Computational Electromagnetic Design by Mathematical Optimization

Marcus Stiemer¹, Marco Rozgić¹, Lars-Ole Fichte¹, David Sanchez¹, and Sebastian Böhmelt¹

Helmut Schmidt University / University of the Federal Armed Forces Hamburg, Holstenhofweg 85, 22034 Hamburg
 m.stiemer@hsu-hh.de, marco.rozgić@hsu-hh.de, lars-ole.fichte@hsu-hh.de,
 david.sanchez@hsu-hh.de, boehmels@hsu-hh.de

Summary. A general framework for the computational identification of design and process parameters in electrical engineering is presented and applied to eddy current and wave problems. The method is based on an appropriate discretization of a mathematical process model, e.g., by finite elements. The discretized relations are employed as constraints in a rigorous mathematical optimization program.

1 Optimization of Technical Processes

We present a method for the numerical identification of suitable design and process parameters of electromagnetic devices. The main purpose of this work is to make this method applicable for engineering problems. The abstract framework and its numerical treatment are described in Section 1. In Section 2 it is applied to two design problems: an electromagnetic-mechanical process and the optimization of a reverberation chamber's ergodicity.

1.1 Abstract Formulation

Let $\Omega \subset \mathbb{R}^3$ be a domain and $P \subset \mathbb{R}^N$ a set of vectors, each modelling a list of N real parameters for an electrotechnical process in Ω . The space of square-integrable vector fields defined in Ω with values in \mathbb{R}^3 is denoted L^2 , and V is a Sobolev space of vector fields on Ω with dual Sobolev space $V' \supset L^2 \supset V$ with respect to the scalar product in L^2 . Further, let $\Lambda_{\mathbf{p}}$ be a linear operator $\Lambda_{\mathbf{p}} : V \rightarrow V'$ with additional regularity properties (see below) and $\mathbf{f}_{\mathbf{p}} \in V'$, both smoothly depending on \mathbf{p} , i.e., the partial derivatives in the sense of Banach-space valued functions with respect to the components of \mathbf{p} up to order 2 exist and are all continuous. Finally, let $\Phi : V \rightarrow \mathbb{R}$ be a functional, which is bounded from below. We are looking for a vector field $\mathbf{u}_{\min} \in V$ such that

$$\Phi(\mathbf{u}_{\min}) = \min_{\mathbf{p} \in P, \mathbf{u}_{\mathbf{p}} \in V} \Phi(\mathbf{u}_{\mathbf{p}}), \quad \text{s.t. } \Lambda_{\mathbf{p}} \mathbf{u}_{\mathbf{p}} = \mathbf{f}_{\mathbf{p}}. \quad (1)$$

Applied to an electrotechnical problem, $\mathbf{u} \in V$ will represent a magnetic vector-potential or another electromagnetic field and $\Lambda_{\mathbf{p}} \mathbf{u} = \mathbf{f}_{\mathbf{p}}$ the weak form of the model equations, whose coefficients, e.g., electrical conductivity κ , permittivity ε , and permeability μ , depend on the design parameter \mathbf{p} , and whose right hand side $\mathbf{f}_{\mathbf{p}}$ represents a source term, e.g., an imposed current density.

1.2 Numerical Solution Procedure

There are two ways to solve (1): *first discretize then optimize* and *first optimize then discretize*, e.g. [1]. The second method requires the formulation of an optimization method in the scope of functional spaces. The derived relations characterizing a minimum configuration are then discretized and finally solved numerically. In the first method, which will be employed here, the optimization procedure is applied to the discretized model equations. This has the advantage of obtaining a standard optimization problem after discretization. However, without further algorithmic control, it is not clear, if local or global minima of the discrete optimization problem are close to minima of the continuous one. To obtain an algorithm whose convergence can be granted, we intend to adapt the discretization of (1) to the current state of the optimization problem, controlled, e.g., by the duality gap. To this end we work with a family of discretizations $\Lambda_{\mathbf{p}}^{\delta} : V^{\delta} \rightarrow V^{\delta'}$ with finite dimensional vector spaces $V^{\delta} \subset V$ and $\mathbf{f}_{\mathbf{p}}^{\delta} \in V^{\delta'}$, controlled via the real parameter $\delta > 0$. Both V^{δ} and $V^{\delta'}$ are isomorphic to the same space \mathbb{R}^n with $n = n(\delta)$. We further claim $\mathbf{u}^{\delta} \rightarrow \mathbf{u}$ in V for $\delta \rightarrow 0$ uniformly with respect to \mathbf{p} , where \mathbf{u}^{δ} denotes the solution of the discretized problems $\Lambda_{\mathbf{p}}^{\delta} \mathbf{u}^{\delta} = \mathbf{f}_{\mathbf{p}}^{\delta}$, $\mathbf{u}^{\delta} \in V^{\delta}$, and \mathbf{u} the solution of the continuous problem. In practical problems the latter will usually be a consequence of standard finite element convergence theory. In this case, δ is typically related to the maximum element size in a quasi-conformal meshing of Ω .

In the *first discretize then optimize* approach, we replace any quantity in (1) by its discretized counterpart obtaining a standard optimization problem with a few number of parameters p_1, \dots, p_N , a large set of *state variables* $\mathbf{u}^{\delta} = (u_1^{\delta}, \dots, u_n^{\delta})^{\top}$, a functional $\Phi(u_1^{\delta}, \dots, u_n^{\delta})$ in the state variables, which is chosen as simple as possible, e.g., as a quadratic function, and a large number of constraints linear in the state variables and usually non-linear in the parameters:

$$\Phi(\mathbf{u}_{\min}^{\delta}) = \min_{\mathbf{p} \in P, \mathbf{u}_{\mathbf{p}}^{\delta} \in V^{\delta}} \Phi(\mathbf{u}_{\mathbf{p}}^{\delta}), \quad \text{s.t. } \Lambda_{\mathbf{p}}^{\delta} \mathbf{u}_{\mathbf{p}}^{\delta} = \mathbf{f}_{\mathbf{p}}^{\delta}. \quad (2)$$

For any discretization parameter δ , this problem can be solved with standard methods in mathematical optimization – we particularly apply an efficient interior point method according to [3]. Remarkably, for solv-

ing (2), an explicit solution of $\Lambda_{\mathbf{p}}^{\delta} \mathbf{u}_{\mathbf{p}}^{\delta} = \mathbf{f}_{\mathbf{p}}^{\delta}$ is not required.

2 Examples from Electrical Engineering

We next apply the general framework described above first to a magnetic force optimization and then to a wave problem.

2.1 Design of Magneto-Mechanical Processes

Coupled electromagnetic-mechanical devices are usually difficult to design if no experience from foregoing versions is available. Hence, application of formal optimization methods may be useful. For this type of problems, the involved electromagnetic fields can usually be computed in magneto-quasistatic approximation, i.e., the eddy current equation

$$\nabla \times \left(\frac{1}{\mu} \nabla \times \mathbf{A} \right) + \kappa_{\mathbf{p}} \frac{\partial \mathbf{A}}{\partial t} = -\kappa_{\mathbf{p}} \nabla \varphi_{\mathbf{p}} \quad (3)$$

is relevant for the magnetic vector potential \mathbf{A} defined in a domain Ω containing the tool coil S and the good conduction material T to be formed. If a Coulomb gauge $\nabla \cdot \mathbf{A} = 0$ is imposed, $\varphi_{\mathbf{p}}$ fulfills $\Delta \varphi_{\mathbf{p}} = 0$ in $S_{\mathbf{p}}$ with boundary conditions accounting for the imposed voltage $U_{\mathbf{p}}(t)$ applied between the connection surfaces. The parameter vector \mathbf{p} comprises geometric properties of the tool coil modelled via the spatial distribution of the conductivity $\kappa_{\mathbf{p}}$ and the area $S_{\mathbf{p}}$, where $\varphi_{\mathbf{p}} \neq 0$. Additional parameters arise from the total discharging current $I_{\mathbf{p}}(t)$ the tool coil is supplied with. The target function Φ may, e.g., be modeled via an optimum Lorentz force distribution $\mathbf{f}_{\text{ideal}}$:

$$\Phi(\mathbf{A}_{\mathbf{p}}) = \int_T \left| \kappa_{\mathbf{p}} \frac{\partial \mathbf{A}_{\mathbf{p}}}{\partial t} \times (\nabla \times \mathbf{A}_{\mathbf{p}}) - \mathbf{f}_{\text{ideal}} \right|^2 dV. \quad (4)$$

Further equations for the mechanical system can additionally be considered. Then the deviation from a prescribed shape of the electromagnetically deformed body can be chosen as target function. In an axisymmetric context, a Coulomb gauge is trivially fulfilled and standard piecewise linear finite elements suffice. Otherwise, Nédélec finite elements are an appropriate choice (see below). In addition to metal forming, also electromagnetic acceleration can be treated with small modifications within this framework.

2.2 Shape Optimization of Cavity Resonators

Testing the reaction of a technical or biological system to an electromagnetic field requires to generate a field of defined magnitude, direction and polarization. This often limits the possibility to reproduce electromagnetic compatibility tests or tests of biological material, particularly at high frequencies. To avoid this delicate problem, a reverberation chamber, i.e., a cavity resonator with variable geometry, can be employed

to produce a series of field distributions at a certain frequency whose average is in all respects equally distributed, e.g., [2]. To reach this goal, the chamber is equipped with a mode stirrer. For a sufficiently large number of stirrer positions the chamber is excited at a frequency ω in a range where the eigenfrequencies of the resonator are that close to each other that the resulting resonance curves overlap, so that several eigenmodes are excited at the single frequency ω . The device under test is exposed to the different emerging standing waves. If the chamber is sufficiently ergodic the average of these electromagnetic fields are nearly equidistributed. Assuming constant permeability μ and omitting losses, the linear operator defining the constraints in (1) is deduced from the Helmholtz equation for the amplitude \mathbf{E}_k of a time harmonic electrical field generated in the reverberation chamber with stirrer at the k th position ($1 \leq k \leq K$) excited via an adequate boundary condition on $\Gamma \subset \partial\Omega$ at the frequency ω :

$$\begin{aligned} \frac{1}{\mu} \Delta \mathbf{E}_k + \omega^2 \varepsilon \mathbf{E}_k &= \mathbf{0}, & \nabla \cdot (\varepsilon \mathbf{E}_k) &= 0, & \text{in } \Omega, \\ \mathbf{n} \times \mathbf{E}_k &= \mathbf{0} & \text{on } \partial\Omega \setminus \Gamma. \end{aligned} \quad (5)$$

To obtain $\Lambda_{\mathbf{p}}$, this problem is transferred in its weak form. As state variables the whole list $\mathbf{u} = (\mathbf{E})_k$ of electrical fields computed for different stirrer positions is considered. As indicator for the ergodicity of the chamber the functional

$$\Phi(\mathbf{u}_{\mathbf{p}}) = \int_{Q_{k,\mathbf{p}}} \left\| \frac{1}{K} \sum_k \nabla \mathbf{E}_{k,\mathbf{p}} \right\|^2 dV \quad (6)$$

is defined, where $Q_{k,\mathbf{p}} \subset \Omega$ denotes the resonating volume for the k th stirrer position depending on the design parameter vector \mathbf{p} , and $\|\cdot\|$ is an adequate matrix norm. By a conforming discretization with Nédélec elements, (5) is transformed in a system of linear equations providing the constraints in (2).

Acknowledgement. This work is based on results of the project PAK343 funded by the German Research Foundation DFG. The authors thank for the financial support.

References

1. M. Hinze, F. Tröltzsch. Discrete concepts versus error analysis in PDE-constrained optimization. *Gamm-Mitt.* 33(2):148–162, 2010.
2. H. G. Krauthäuser. Grundlagen und Anwendungen von Modenverwirbelungskammern. Habilitationsschrift, Otto-von-Guericke-Universität Magdeburg, Magdeburg, 2007.
3. A. Wächter and L. T. Biegler. On the implementation of an interior-point filter line-search algorithm for large-scale nonlinear programming. *Mathematical Programming* 106:25–57, 2006.

Coupled Two-Step MoM / FITD Method for Calculation of Electrically Large Problems in Urban Areas

Carsten Cimala, Oliver Spathmann, Simon Runke, Martin Zang, and Markus Clemens

Bergische Universität Wuppertal, Chair of Electromagnetic Theory, Rainer-Gruenter-Str. 21, 42119 Wuppertal, Germany.
eMail cimala@uni-wuppertal.de

Summary. In this abstract electromagnetic compatibility (EMC) simulations in complex scenarios of urban areas are considered. Here, a coupled MoM / FITD method is presented that evaluates the calculations of the electric field distribution at an electronic device in an office with an exemplary ground floor of a building.

1 Introduction

Since EMC simulations in complex scenarios may include large distances and also require a sufficiently high resolution of the discrete problems, the numerical solution of these simulations become more challenging to compute. Geometrically large scenarios to analyze [1]-[2] protection measures against intentional electromagnetic interference (IEMI) of critical infrastructure (CI) can incorporate detailed geometries like laptops or any other critical object [3]. While commercial hardware and simulation software technologies are available for this task, careful choice of the numerical techniques must be taken into account to make use of the specific strengths and limitations of each method available.

The Finite Integration Time Domain (FITD) technique [4] can be used for full wave electromagnetic field simulations which tend to be numerical expensive for larger distances but it typically yields sufficiently accurate results for in-homogeneous dielectric material distribution. The Method of Moment approach states an established simulation technique based on the combined field integral equation and calculates surface currents on illuminated perfect electric conductive surfaces. It is well suited for antenna problems and electrically large problems but the applicability for simulations featuring lossy dielectric objects is reduced. In order to combine these advantages, an iterative coupling may become mandatory [5]. For EMC related large scale problems, however, a two-step MoM/FITD method [6]-[7] may yield sufficient accuracy.

The coupling of these techniques with Huygens' surfaces as an interface in between is used to compute a large scale problem but also leads to an inherent numerical uncertainty. This combination of methods has shown to be a feasible approach [7] and in this paper, the first results for the implemented coupling are initially examined by comparison to a monolithic FITD

simulation using multi GPU accelerated high performance computing.

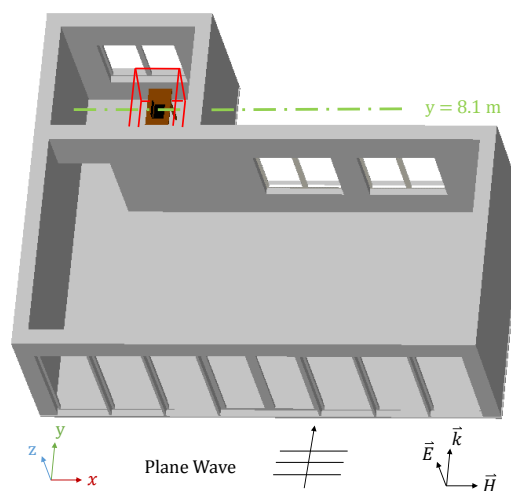


Fig. 1. Perspective view on the simulation model, indicated plane wave excitation and the office area in red

2 The MoM-FITD Method

The aim of the coupling approach is to get a credible representation of the field distribution based on Huygens' surfaces featuring the field equivalence principle [8]-[11] in a distinct area to expose yet unknown devices under test (DUT) to a specific em-field for further emc analysis.

Therefore a first simulation step is performed by using the combined field integral equation technique and is evaluated on a closed cuboid surface around a target area. The extracted field representation is used as a near field source in a second step for numerical simulation of a smaller yet more complex area with the Finite Integration Technique (FIT) to include detailed objects and lossy dielectrics.

3 Numerical Test Example

For the simulation of the electric field distribution in a typical office building exposed to an external field source a building with a base area of about 63 m^2 is

modeled (Fig. 1) using perfectly electric conducting (PEC) walls. The office is represented by a wooden desk ($\epsilon_r = 2.5$; $\sigma = 0.004 \text{ S/m}$; 1 m height and 4 cm thickness) and a laptop (PTFE $\epsilon_r = 2.5$; $\sigma = 0 \text{ S/m}$; 2 cm thickness).

The excitation is modeled as a plane wave propagating through the front apertures which is linearly polarized perpendicular to the ground plane and has an amplitude of 1 V/m . The boundaries are perfect matched layers (also known as absorbing boundary conditions) in 0.5 m distance, except for the basement where an electric boundary condition ($E_{tan} = 0$) is applied.

The reference FITD simulation is compared to the two-step approach using MoM simulation results of the metallic structures and a subsequent FITD simulation. This second step (FITD) now includes the office area where a near field source approximates the former recorded field distribution on the Huygens' surfaces. An excerpt of the electric field distribution for $y = 8.1 \text{ m}$ in a vertical cross-section through the model is shown in Fig. 2 and additionally the uncertainty introduced by the coupling method as absolute error.

The qualitative good agreement of the absolute error in Fig. 2 is further examined on a quantitative basis in Fig. 3. The peak electric field strength along an evaluation line through the area of interest, desk and laptop respectively, shows an error of $< 5\%$ ($\text{Error} / \% = 100(|E_{Ref} - E_{Coupling}| / |E_{Ref}|)$) in the area of interest and therefore is considered to be sufficiently accurate.

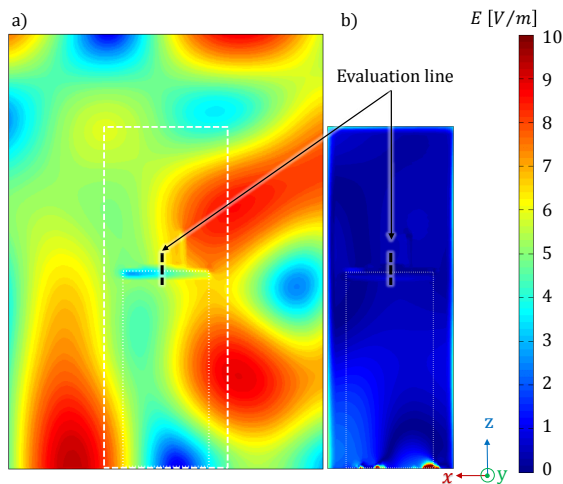


Fig. 2. Peak electric field distribution for a) $y = 8.1 \text{ m}$ in the office area and b) error introduced by coupling and implementation of the method as absolute error

References

1. W. Radasky and R. Hoad. Application of IEC SC 77C standards for protecting commercial buildings from the effects of intentional electromagnetic interference

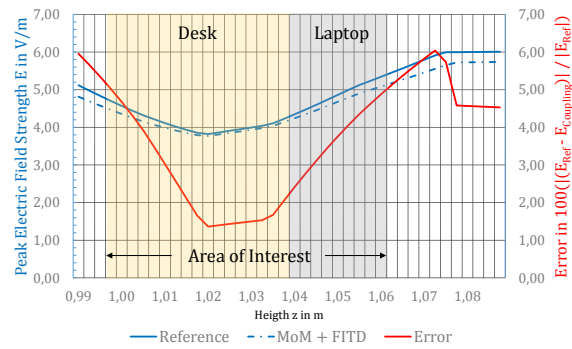


Fig. 3. Electric field strength in V/m at evaluation line (Fig. 2) (blue continuous line: Reference FITD simulation; blue dotted line: MoM + FITD Method; red: $\text{Error} / \% = 100(|E_{Ref} - E_{Coupling}| / |E_{Ref}|)$)

(IEMI) EMC, Organized Session 21T3: IEMI, Kyoto, Japan, 2009.

2. ITU. ITU-T K.81, Series K: Protection against interference, High-power electromag. immunity guide for telecomm. systems, Geneva, Switzerland, 2009.
3. S. Runke, V. Hansen, J. Streckert and M. Clemens. A coupled multi-method approach for the numerical sim. of intentional electromag. interference into critical infrastructure *IEEE ICEAA 2013*, pp. 875-879, Torino, Italy, September 2013.
4. T. Weiland. Time Domain Electromagnetic Field Computation with Finite Difference Methods. *Int. J. Num. Mod.: ENDF*, 9, 1996, pp. 259-319.
5. M. Mangoud, R. Abd-Alhameed, p. Excell. *Numerical Electromagnetics for Personal Dosimetry of Cellular Phones*, LAP Lambert, Saarbrücken 2010
6. C. Cimala, M. Clemens, V. Hansen, O. Spathmann, J. Streckert and T. Timm. High Resolution Numerical Electromagnetic Dosimetry Simulations Using a Coupled Two-Step MoM/FITD Approach. *IEEE Transactions on Magnetics (CEFC 2013)*, Oita, 2013, 49(5):1633-1636.
7. M. Clemens, C. Cimala, S. Runke, J. Streckert and M. Zang. The Coupled MoM/FITD Approach for Electrically Large Problems in Numerical EMC Testing. *Ninth International Conference on the Computation in Electromagnetics (CEM 2014)*, London, 2014.
8. A.E.H. Love. The Integration of Equations of Propagation of Electric Waves. *Phil Trans. Roy. Soc. London, Ser. A*, 197, 1901, pp. 1-45.
9. S.A. Schelkunoff. Some Equivalence Theorems of Electromagnetics and Their Application to Radiation Problems. *Bell System Tech. J.*, 15, 1936, pp. 92-112.
10. S.A. Schelkunoff. Kirchoff's Formula, its Vector Analogue and Other Field Equivalence Theorems. *Comm. in Pure and Applied Math.*, 4, 1951, pp. 43-59.
11. S.R. Rengarajan and Y. Rahmat-Samii. The Field Equivalence Principle: illustration of the Establishment of the Non-Intuitive Null Fields *IEEE Antennas and Propagation Magazine*, Vol. 42, No. 4, Aug' 2000.

Computing $f(A)\mathbf{b}$ - the Action of a Matrix Function on a Vector

Andreas Frommer¹, Stefan Güttel², and Marcel Schweitzer¹

¹ Bergische Universität Wuppertal, Fachbereich Mathematik und Naturwissenschaften, 42097 Wuppertal, Germany
frommer@math.uni-wuppertal.de, schweitzer@math.uni-wuppertal.de

² School of Mathematics, The University of Manchester, M139PL Manchester, UK
stefan.guettel@manchester.ac.uk

Summary. We consider Krylov subspace techniques to iteratively compute $f(A)\mathbf{b}$, where A is a (large) square matrix, \mathbf{b} a vector and f a function. We will focus on efficient and stable restart procedures as well as results on convergence and error estimates. Particular emphasis will be given to the case where f is from the class of Stieltjes functions, which include the fractional power functions with exponents from $(-1, 0)$.

1 The Arnoldi Approximation

The computation of $f(A)\mathbf{b}$, the action of a matrix function $f(A) \in \mathbb{C}^{N \times N}$ on a vector $\mathbf{b} \in \mathbb{C}^N$, is an important task in many areas of science and engineering. Examples include the matrix exponential function $f(z) = e^z$, which is at the heart of exponential integrators for the solution of differential equations, the logarithm $f(z) = \log(z)$ used, e.g. in Markov model analysis and identification problems for linear continuous-time multivariable systems, fractional powers $f(z) = z^\alpha$ in fractional differential equations and the sign function $f(z) = \text{sign}(z)$ which is often related to spectral projectors and also appears in lattice quantum chromodynamics.

In many of these applications, the matrix A is sparse and large so that the explicit computation of the generally dense matrix $f(A)$ by direct methods is infeasible. Instead, one seeks to directly approximate the vector $f(A)\mathbf{b}$ by iterative methods. By far the most important class of iterative methods for this purpose are *Krylov subspace methods*. These methods extract their approximations to $f(A)\mathbf{b}$ from Krylov subspaces $\mathcal{K}_m(A, \mathbf{b}) = \text{span}\{\mathbf{b}, A\mathbf{b}, \dots, A^{m-1}\mathbf{b}\}$. Assume that we are given an *Arnoldi decomposition*

$$AV_m = V_m H_m + h_{m+1,m} \mathbf{v}_{m+1} \hat{\mathbf{e}}_m^T,$$

where the columns of $V_m = [\mathbf{v}_1 | \mathbf{v}_2 | \dots | \mathbf{v}_m] \in \mathbb{C}^{N \times m}$ are an orthonormal basis of $\mathcal{K}_m(A, \mathbf{b})$ obtained from m steps of the Arnoldi orthogonalization process, $H_m \in \mathbb{C}^{m \times m}$ is an upper Hessenberg matrix, and $\hat{\mathbf{e}}_m \in \mathbb{R}^m$ corresponds to the m -th canonical unit vector. Then a popular approach for approximating $f(A)\mathbf{b}$ is the *Arnoldi approximation*

$$\mathbf{f}_m = V_m f(H_m) V_m^H \mathbf{b} = \|\mathbf{b}\| V_m f(H_m) \hat{\mathbf{e}}_1. \quad (1)$$

One way to interpret the Arnoldi approximation is that we obtain \mathbf{f}_m as $p_{m-1}(A)\mathbf{b}$, where p_{m-1} is the

polynomial of degree $m-1$ which interpolates f on the Ritz values of A w.r.t $\mathcal{K}_m(A, \mathbf{b})$, i.e. the eigenvalues of H_m .

2 Restarts

One of the main computational problems associated with the Arnoldi approximation (1) is that the full Arnoldi basis V_m needs to be stored, even when A is Hermitian. This storage requirement may limit the number of iterations m that can be performed in practice, and thus the accuracy that can be achieved for large problems. A further limiting factor is the growing orthogonalization cost of computing V_m in the non-Hermitian case and the cost of evaluating $f(H_m)$ for larger values of m .

In computational practice one is therefore interested in ways to *restart*, similar to what is often done for the solution of (non-Hermitian) linear systems of equations (the case $f(z) = z^{-1}$). This was already investigated several times [1–4, 8], but none of the restarting approaches for general matrix functions was completely satisfactory until now. All of these variants solved the storage problem for the Arnoldi basis, but still had to deal with growing cost per restart cycle [3], were numerically unstable [8], or required an accurate rational approximation $r(z) \approx f(z)$ for all z in some spectral region of A [2]. Instead of relying on an error representation involving *divided differences* (see [3, 8]), we propose here a novel algorithm based on an *integral representation* of the error. This results in a numerically stable restart procedure.

The crucial result for this restart procedure is formulated in the following theorem, see [5].

Theorem 1. *Let $\Omega \subset \mathbb{C}$ be a region and let $f : \Omega \rightarrow \mathbb{C}$ be analytic with the integral representation*

$$f(z) = \int_{\Gamma} \frac{g(t)}{t-z} dt, \quad z \in \Omega,$$

with a path $\Gamma \subset \mathbb{C} \setminus \Omega$ and a function $g : \Gamma \rightarrow \mathbb{C}$. Let $A \in \mathbb{C}^{N \times N}$ with $\text{spec}(A) \subset \Omega$ and $\mathbf{b} \in \mathbb{C}^N$ be given. Denote by \mathbf{f}_m the m -th Arnoldi approximation (1) to $f(A)\mathbf{b}$ with $\text{spec}(H_m) = \{\theta_1, \dots, \theta_m\} \subset \Omega$. Then, provided that the integral on the right hand side in (2) with $w_m(t) = (t - \theta_1) \dots (t - \theta_m)$ exists, we have

$$\begin{aligned} f(A)\mathbf{b} - \mathbf{f}_m &= \gamma_m \int_{\Gamma} \frac{g(t)}{w_m(t)} (tI - A)^{-1} \mathbf{v}_{m+1} dt \quad (2) \\ &=: e_m(A) \mathbf{v}_{m+1}, \end{aligned}$$

where $\gamma_m = \prod_{i=1}^m h_{i+1,i}$.

Theorem 1 shows that the error of the Arnoldi approximation \mathbf{f}_m to $f(A)\mathbf{b}$ can again be interpreted as an error matrix function $e_m(A)$ applied to a vector, \mathbf{v}_{m+1} . The error function is now represented via an integral instead of divided differences, and this new representation can be used in a restart algorithm, in which the occurring integrals have to be approximated via numerical integration. A MATLAB implementation is publically available, see [6]

3 Convergence Results

As is known from Krylov subspace methods for linear systems, restarts may slow down or even completely destroy convergence of the method to the solution. It is therefore of paramount importance to obtain convergence results for the restarted Arnoldi method for matrix functions. We here focus on the class of Stieltjes functions.

Definition 1. A Stieltjes function f is a function $f: \mathbb{C} - (-\infty, 0] \rightarrow \mathbb{C}$ with

$$f(z) = \int_0^{\infty} \frac{1}{t+z} d\mu, \quad (3)$$

where the integral in (3) is to be understood as a Riemann-Stieltjes integral with respect to a function $\mu(t)$ which is monotonically increasing and positive on $[0, \infty)$ and satisfies the condition

$$\int_0^{\infty} \frac{1}{t+1} d\mu < \infty.$$

The class of Stieltjes functions includes the functions $z^{-\alpha}$ for $\alpha \in (0, 1)$ and $\frac{\log(1+z)}{z}$.

The following two results are shown in [7].

Theorem 1. Let f be a Stieltjes function and A be Hermitian and positive definite. Moreover, let κ denote the condition number of A , $c = (\sqrt{\kappa} - 1)/(\sqrt{\kappa} + 1)$ and let m be the restart length. Finally, let $\mathbf{f}_m^{(k)}$ be the approximation to $f(A)\mathbf{b}$ obtained after k restarts of length m . Then

$$\|f(A)\mathbf{b} - \mathbf{f}_m^{(k)}\|_A \leq C \alpha_m^k,$$

where $\alpha_m = \frac{2}{\cosh(m \ln c)}$ and $C > 0$.

If A is not Hermitian and positive definite, there are examples where the approximation sequence of the restarted method diverges, even when f is a Stieltjes function and A is positive real, meaning that its field of values lies in the left half plane. Convergence can be restored, though, if one modifies the Arnoldi approximation.

Theorem 2. Let f be a Stieltjes function and A be positive real. Modify the Arnoldi approximations in such a way that instead of interpolating in the Ritz values we now interpolate in the harmonic Ritz values. Then $\lim_{k \rightarrow \infty} \|f(A)\mathbf{b} - \mathbf{f}_m^{(k)}\|_2 = 0$.

References

1. M. Afanasjew, M. Eiermann, O. G. Ernst, and S. Güttel, A generalization of the steepest descent method for matrix functions, *Electron. Trans. Numer. Anal.* 28 (2008), pp. 206–222.
2. ———, Implementation of a restarted Krylov subspace method for the evaluation of matrix functions, *Linear Algebra Appl.* 429 (2008), pp. 229–314.
3. M. Eiermann and O. G. Ernst, A restarted Krylov subspace method for the evaluation of matrix functions, *SIAM J. Numer. Anal.* 44 (2006), pp. 2481–2504.
4. M. Eiermann, O. G. Ernst, and S. Güttel, Deflated restarting for matrix functions, *SIAM J. Matrix Anal. Appl.* 32 (2011), pp. 621–641.
5. A. Frommer, S. Güttel, and M. Schweitzer, Efficient and stable Arnoldi restarts for matrix functions based on quadrature, *SIAM J. Matrix Anal. Appl.* to appear.
6. A. Frommer, S. Güttel, and M. Schweitzer, FUNM-QUAD: An implementation of a stable quadrature based restarted Arnoldi method for matrix functions, IMACM-Preprint 14/04 (2014), www.imacm.uni-wuppertal.de/research/preprints/2014.html
7. A. Frommer, S. Güttel, and M. Schweitzer, Convergence of the restarted Arnoldi method for Stieltjes functions, in preparation.
8. M. Ilić, I. W. Turner, and D. P. Simpson, A restarted Lanczos approximation to functions of a symmetric matrix, *IMA J. Numer. Anal.* 30 (2010), pp. 1044–1061.

Parallelization and Sparsification of a Surface-Volume Integral Code for Plasma-Antenna Interaction

Davide Melazzi¹, Piergiorgio Alotto², Vito Lancellotti³,
Marco Manente⁴, Fabio Freschi⁵, and Daniele Pavarin²

¹ University of Padova, CISAS “G.Colombo”, Padova, Italy davide.melazzi@unipd.it,

² University of Padova, Dept. of Industrial Eng., Padova, Italy name.surname@unipd.it

³ TU Eindhoven, Dept. of Electrical Eng, Eindhoven, Netherlands v.lancellotti@tue.nl

⁴ T4i S.r.l, Padova, Italy marco.manente@unipd.it

⁵ Polytechnic of Torino, Energy Department, Torino, Italy fabio.freschi@polito.it

Summary. The ADAMANT (Advanced coDe for Anisotropic Media and ANTennas) code has been developed with the aim of computing the power injected into the plasma by RF antennas, especially in the case of thrusters for space applications. The code implements the numerical solution of coupled surface-volume integral equations by the Method of Moments, which lends itself to parallel execution. The parallelization and sparsification of the assembling phase are discussed, and results concerning the speed-up and memory use obtained for different test cases are presented.

1 Formulation and Numerical Approach

The typical problem includes a metallic RF antenna that surrounds a cylindrical plasma column; we assume all metallic parts to be perfectly electric conductors (PEC). By invoking the surface and the volume equivalence principle [1], we substitute the antenna with an equivalent electric surface current density \mathbf{J}_A , and the plasma with a volume polarization current $\mathbf{J}_P = j\omega(\bar{\mathbf{I}} - \bar{\boldsymbol{\epsilon}}_r^{-1}) \cdot \mathbf{D}_P = j\omega\bar{\boldsymbol{\alpha}} \cdot \mathbf{D}_P$; here, $\bar{\boldsymbol{\epsilon}}_r$ denotes the permittivity of the plasma relative to vacuum. A time dependence in the form $\exp(j\omega t)$ for fields and sources is assumed and suppressed throughout. We formulate the problem as a surface integral equation on the antenna surface S_A , and a volume integral equation within the plasma region V_P

$$\mathbf{E}_A^i(\mathbf{r}) - j\omega\mu_0\bar{\mathbf{G}}(\mathbf{r}) * \mathbf{J}_A(\mathbf{r}) + \omega^2\mu_0\bar{\mathbf{G}}(\mathbf{r}) * [\bar{\boldsymbol{\alpha}}(\mathbf{r}) \cdot \mathbf{D}_P(\mathbf{r})] \Big|_{\tan} = 0, \quad \mathbf{r} \in S_A, \quad (1)$$

$$\bar{\boldsymbol{\epsilon}}_r^{-1} \cdot \mathbf{D}_P(\mathbf{r}) = -j\omega\epsilon_0\mu_0\bar{\mathbf{G}}(\mathbf{r}) * \mathbf{J}_A(\mathbf{r}) + k_0^2\bar{\mathbf{G}}(\mathbf{r}) * [\bar{\boldsymbol{\alpha}}(\mathbf{r}) \cdot \mathbf{D}_P(\mathbf{r})], \quad \mathbf{r} \in V_P, \quad (2)$$

where $\bar{\mathbf{G}}(\mathbf{r})$ is the dyadic Green’s function, ‘*’ indicates the 3-D spatial convolution and scalar product, while \mathbf{E}_A^i , and \mathbf{E}_P^i are the impressed electric fields on the antenna surface S_A , and in the plasma volume V_P , respectively. The antenna conductors are modeled with a 3-D triangular mesh and the plasma with a tetrahedral mesh. Linear vector divergence-conforming surface (volume) basis functions are associated with

the inner edges (all the facets) of the triangular (tetrahedral) mesh, in order to expand \mathbf{J}_A (\mathbf{D}_P). Besides, we employ the notion of voltage gap to model the excitation of the antenna; as a result, $\mathbf{E}_A^i(\mathbf{r})$ is non-zero only at the antenna ports, whereas $\mathbf{E}_P^i(\mathbf{r})$ is zero and drops out of (2).

The plasma is assumed to be cold, collisional, and magnetized by an external magnetostatic field \mathbf{B}_0 parallel to the axis of the cylinder so that in a system of Cartesian coordinates with $\mathbf{B}_0 = B_0\hat{\mathbf{z}}$, $\bar{\boldsymbol{\epsilon}}_r$ is :

$$\bar{\boldsymbol{\epsilon}}_r = \begin{bmatrix} S & jD & 0 \\ -jD & S & 0 \\ 0 & 0 & P \end{bmatrix}, \quad (3)$$

where S, D and P are function of the plasma frequency $\omega_{p\alpha} \equiv \sqrt{n_\alpha q_\alpha^2 / \epsilon_0 m_\alpha}$, the gyrofrequency $\omega_{c\alpha} \equiv q_\alpha B_0 / m_\alpha$, the collision frequency ν_α ; the superscript α refers to the index of the plasma species. Besides, as $\bar{\boldsymbol{\epsilon}}_r$ is considered as a function of position, profiles of plasma density, magnetic field, electron temperature, and neutral pressure can be modelled.

The simulation strategy based on equations (1), (2) together with the MoM solution in the form of Galerkin has been implemented in ADAMANT [2].

2 Parallelization and sparsification

In ADAMANT, the weak form corresponding to (1), (2) is the algebraic system

$$\begin{bmatrix} [Z_{AA}] & [Z_{AP}] \\ [Z_{PA}] & [Z_{PP}] \end{bmatrix} \begin{bmatrix} Z_0 [J_A] \\ [D_P] / \epsilon_0 \end{bmatrix} = - \begin{bmatrix} [V_G] \\ [0] \end{bmatrix}, \quad (4)$$

where the intrinsic impedance of free space $Z_0 \equiv (\mu_0 / \epsilon_0)^{1/2}$ and ϵ_0 have been factored out and paired with the vectors of unknown coefficients to improve the conditioning of the matrix. With these assumptions $Z_0 [J_A]$ and $[D_P] / \epsilon_0$ have the physical dimensions of an electric field. The column vectors $[J_A]$ and $[D_P]$ contain the expansion coefficients of \mathbf{J}_A and \mathbf{J}_P , respectively. The system matrix is naturally partitioned into four blocks, where the off-diagonal submatrices $[Z_{AP}]$ and $[Z_{PA}]$ are related to the EM interaction between the antenna surface and the plasma volume; $[Z_{AA}]$ is a surface contribution, while $[Z_{PP}]$ is a

volume contribution, related to the antenna current J_A and plasma current J_P , respectively, radiating in free space.

Since the numerical solution through the MoM leads to large dense matrices, both matrix filling and inversion time can be reduced by parallelization. However, the computational time required for the construction of the four blocks can be larger than the inversion time. Additionally, the assembling time of the $[Z_{PP}]$ sub-matrix is the most important contribution in the overall time to compute the system matrix. This is due to (i) the adoption of the volume-integral-equation formulation in the plasma region, and (ii) to the very nature of the problems we deal with, in which the plasma region is substantially larger than the volume occupied by the metallic parts.

Furthermore, realistic problems not only call for parallelization to reduce computational times, but may quickly exceed the memory capacity even of very large machines since the matrices are fully populated. To be able to solve realistic problems it is necessary to compress these matrices with suitable techniques. Among others, the Fast Multiple Method (FMM) [3] is maybe the most popular for both low and high frequency problems. One more recent approach for integral operators with asymptotically smooth kernels, is based on the adaptive cross approximation (ACA) coupled with hierarchical matrix (\mathcal{H} -matrix) arithmetics [4].

In contrast with the FMM, where the kernel is approximated by a sum of spherical multipole functions, ACA generates low-rank approximations of far-field blocks from the entries of the original matrix. From an implementation viewpoint, ACA can directly use the computational routines of the existing code without any major change. The specific implementation within ADAMANT has been achieved through the *hlibpro* library [5].

3 Results

We have considered a test case with 72 and 924 sub-sectional basis functions on the antenna and in the plasma regions, respectively. We have analyzed the code scalability with respect to the number of threads. In Fig. 1, we report the speedup related to the overall time of the system matrix assembling, and the code performs in accordance with Amdahl's law [6]:

$$T_{elapsd}(P) = \left(\frac{f}{P} + 1 - f + O_P P \right) T_{serial} \quad (5)$$

where P is the number of threads and f is the fraction of parallelized code. It can be seen that the speedup is almost optimal since $f = 0.984$ and the speedup saturation is entirely due to the communication overhead O_P caused by different processes which access the shared memory area containing the full matrices.

As far as sparsification is concerned, Table 1 shows the level of compression that can be achieved for $[Z_{AA}]$

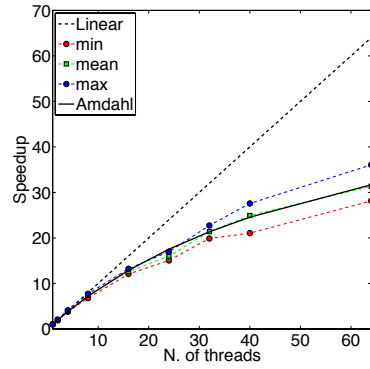


Fig. 1. Speedup obtained with OpenMP compared with Amdahl's law for the assembling phase of the system matrix.

in the case of two typical triangular meshes with 3000 and 9000 basis functions which would result in full matrices of 111.32 MB and 1302.48 MB of memory, respectively.

Table 1. \mathcal{H} -matrix compression

Unknowns	ϵ	MB	% Compression ratio	$ Z_{antenna} [\Omega]$
3000	E-10	85.78	77.03	0.569
3000	E-6	56.88	51.10	0.569
3000	E-4	42.11	38.10	0.557
3000	E-3	34.22	30.74	0.627
9000	E-10	614.19	47.16	0.585
9000	E-6	357.77	27.96	0.585
9000	E-4	233.84	17.94	0.586

References

1. E. J. Rothwell and M. J. Cloud, *Electromagnetics*, London, CRC Press, 2001.
2. D. Melazzi, V. Lancellotti, "ADAMANT: A Surface and Volume Integral-Equation Solver for the Analysis and Design of Helicon Plasma Sources," *Comp. Phys. Comm.* (2014), <http://dx.doi.org/10.1016/j.cpc.2014.03.019>
3. L. Greengard and V. Rokhlin, "A fast algorithm for particle simulations," *Journal of Computational Physics*, vol. 73, no. 1, pp. 325–348, 1987.
4. S. Börm, L. Grasedyck and W. Hackbusch, "Introduction to Hierarchical Matrices with Applications," *Engineering Analysis with Boundary Elements*, vol. 27, no. 5, pp. 405–422, 2003.
5. R. Kriemann, "Paralle \mathcal{H} -Matrix arithmetics on shared memory systems," *Computing*, vol. 74, pp. 273–297, 2005.
6. B. Chapman, G. Jost and R. Van der Pas, *Using OpenMP*, ser. Scientific and Engineering Computation. MIT Press, 2007.

Rectangular Cavity Green's Functions with Ewald Summation Technique and Fast Fourier Transform Acceleration

M. E. Gruber¹, C. Koenen¹, and T. F. Eibert¹

Lehrstuhl für Hochfrequenztechnik, TU München, Arcistr. 23, 80333 München michael.gruber@tum.de, c.koenen@tum.de, eibert@tum.de

Summary. An inverse fast Fourier transform (IFFT) accelerated Ewald summation technique is presented. The Green's function of the rectangular cavity is reformulated and sampled on a uniform grid such that the IFFT can be applied. Values in between the grid are interpolated using Lagrange polynomials. The IFFT accelerated approach achieves a speed-up of up to four orders of magnitude versus the standard Ewald summation.

1 Introduction

The Green's function of the rectangular cavity is utilized in boundary integral (BI) formulations to model microwave resonators [Borji and Safavi-Naeini(2004)] and reverberation chambers [Gronwald(2005), Carlberg et al.(2005)Carlberg, Kildal, and Carlsson]. The use of the cavity Green's function instead of the free-space Green's function in the BI formulation supersedes the discretization of the cavity walls. Depending on the number and the size of the objects within the cavity, the number of unknowns is considerably reduced. Most researchers accelerated the evaluation of the cavity Green's function with the Ewald summation technique [Ewald(1921)] which splits the Green's function into two exponentially convergent series: the spatial and the spectral series. Still, compared to the free-space Green's function, the cavity Green's function remains computationally expensive. Hence, most previous work was restricted to small one-dimensional objects, such as dipole antennas [Gronwald(2005), Carlberg et al.(2005)Carlberg, Kildal, and Carlsson].

To avoid the computationally intensive evaluation of the cavity Green's function, Borji et al. [Borji and Safavi-Naeini(2004)] proposed a best polynomial approximation: the costly cavity Green's function is required only once to generate the polynomial coefficients. Couplings between observation and source points are calculated with the cheaper polynomial approximation. In the low frequency regime the best polynomial approximation achieved a speed-up of about one order of magnitude. However, in the over-moded frequency range the number of necessary terms in the spectral series grows cubically with frequency. The cubic frequency dependence of the Ewald summation technique and the higher polynomial order deteriorate the efficiency of the best polynomial approximation.

To overcome the bad frequency complexity of the Ewald summation technique, it is accelerated by an

inverse fast Fourier transform (IFFT) in this work. The computationally dominant spectral series, which naturally depends on observation and source point (i.e., it is a six-variable function), is rewritten as a sum of eight three-variable functions. The three-variable function is computed with the IFFT on a uniform grid. Values in between the grid are computed using Lagrange polynomial interpolation. Results show that the proposed approach accelerates the computation of the cavity Green's function by up to four orders of magnitude.

2 Inverse Fast Fourier Transform Accelerated Ewald Summation

Consider a rectangular cavity of size $a \times b \times c$ with perfectly electrically conducting walls. The Green's function of the rectangular cavity of the magnetic vector potential has the form [Borji and Safavi-Naeini(2004)]

$$\bar{\mathbf{G}}^A = G_{xx}^A \hat{\mathbf{x}}\hat{\mathbf{x}} + G_{yy}^A \hat{\mathbf{y}}\hat{\mathbf{y}} + G_{zz}^A \hat{\mathbf{z}}\hat{\mathbf{z}}. \quad (1)$$

The Ewald summation technique decomposes the cavity Green's function into a spatial and a spectral series [Park et al.(1998)Park, Park, and Nam]. In the over-moded frequency range the spectral series dominates the overall computational burden as the number of necessary terms in the spectral series increases cubically with frequency. According to [Park et al.(1998)Park, Park, and Nam], the spectral series has the form

$$\bar{\mathbf{G}}_{\text{spec}}^A(\mathbf{r}, \mathbf{r}') = \mu \sum_{m,n,p=0}^{\infty} H_{mnp} \left[\phi_x(\mathbf{r}) \phi_x(\mathbf{r}') \hat{\mathbf{x}}\hat{\mathbf{x}} + \phi_y(\mathbf{r}) \phi_y(\mathbf{r}') \hat{\mathbf{y}}\hat{\mathbf{y}} + \phi_z(\mathbf{r}) \phi_z(\mathbf{r}') \hat{\mathbf{z}}\hat{\mathbf{z}} \right] \quad (2)$$

where \mathbf{r} and \mathbf{r}' are the observation and the source point, respectively, m, n, p are the indices of the respective cavity mode, and ϕ_x, ϕ_y, ϕ_z are the eigenfunctions of the rectangular cavity. The function

$$H_{mnp} = \frac{\exp\left(-\frac{k_x^2 + k_y^2 + k_z^2 - k^2}{4E^2}\right)}{k_x^2 + k_y^2 + k_z^2 - k^2} \quad (3)$$

where k_x, k_y, k_z are the wavenumbers in the respective direction, k is the wavenumber of the material in the cavity, and E is the splitting parameter of the

Ewald summation technique [Park et al.(1998)Park, Park, and Nam].

In the form of (2) the spectral series depends on \mathbf{r} and \mathbf{r}' (i.e., it is a six-variable function). Sampling a six-variable function causes a prohibitively high memory consumption. Using the exponential form of sine and cosine, the spectral series becomes

$$\bar{\mathbf{G}}_{\text{spec}}^A(\mathbf{r}, \mathbf{r}') = \frac{\mu}{8abc} \sum_{q=0}^7 Q(x_q, y_q, z_q) (A_{q,x} \hat{\mathbf{x}} + A_{q,y} \hat{\mathbf{y}} + A_{q,z} \hat{\mathbf{z}}) \quad (4)$$

where $A_{q,x} = \pm 1$, $A_{q,y} = \pm 1$, $A_{q,z} = \pm 1$,

$$Q(x_q, y_q, z_q) = \sum_{m,n,p=-\infty}^{\infty} H_{mnp} e^{jk_x x_q} e^{jk_y y_q} e^{jk_z z_q}, \quad (5)$$

$x_q = x \pm x'$, $y_q = y \pm y'$, and $z_q = z \pm z'$ [Park et al.(1998)Park, Park, and Nam]. When x_q , y_q , and z_q are sampled equispaced, $Q(x_q, y_q, z_q)$ is the IFFT of H_{mnp} . Points at arbitrary positions in between the regular grid are interpolated using Lagrange polynomials.

3 Results

An ideal reverberation chamber of size $5.1 \text{ m} \times 2.5 \text{ m} \times 2.9 \text{ m}$ is considered. The resonance frequency of the fundamental mode is 59.5 MHz. The Q -array is sampled with 15 samples per wavelength. The sampling rate and a Lagrange polynomial order of four yield an accuracy of at least 10^{-4} for the cavity Green's function. Table 1 shows the average computation times of the standard Ewald and the IFFT accelerated Ewald summation for one billion Green's function computations. The times needed by the Lagrange interpolation and the sampling of the Q -array are displayed. The computation time of the standard Ewald summation grows cubically with frequency while the time of the Lagrange interpolation is almost constant. The time of the IFFT is negligible for a large number of Green's function computations. Thus, the IFFT acceleration performs best at high frequencies: at 1600 MHz the speed-up is approximately four orders of magnitude.

Table 1. Average computation times of the IFFT accelerated Ewald summation and the standard Ewald summation for one billion samples.

f (MHz)	Ewald	IFFT Lagrange	
	t_{Ewald} (s)	t_{Lagrange} (s)	$t_{Q\text{-array}}$ (s)
200	$0.7 \cdot 10^6$	$16.1 \cdot 10^3$	0.06
400	$4.6 \cdot 10^6$	$17.7 \cdot 10^3$	0.48
800	$34.2 \cdot 10^6$	$20.0 \cdot 10^3$	3.51
1600	$246.4 \cdot 10^6$	$24.3 \cdot 10^3$	31.30

As an application example, a w-shaped stirrer is placed in the considered reverberation chamber. The

scenario is modeled using the IFFT accelerated cavity Green's function in a boundary integral formulation. Figure 1 shows the surface current density on the stirrer at 800 MHz. The simulation needed roughly 800 million Green's function computations and took about 2.5 h on a single core PC. For comparison, a multilevel fast multipole method (MLFMM) accelerated BI method with the free-space Green's function [Eibert(2005)] needed about 15 h. Thus, the IFFT accelerated Ewald summation technique proves not only to efficiently compute the cavity Green's function, but is also relevant for numerical application.

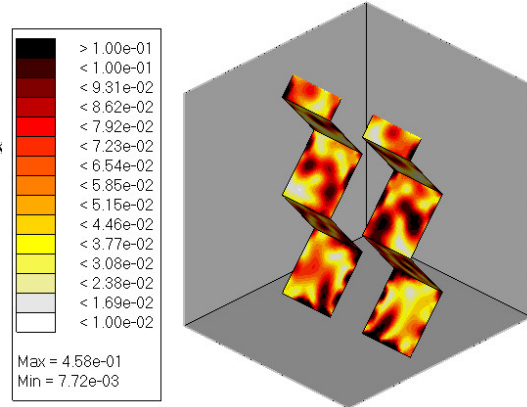


Fig. 1. Absolute value of the surface current density on the w-shaped stirrer at 800 MHz in Am^{-1} .

References

- Borji and Safavi-Naeini(2004). A. Borji and S. Safavi-Naeini. Rapid calculation of the Green's function in a rectangular enclosure with application to conductor loaded cavity resonators. *IEEE Transactions on Microwave Theory and Techniques*, 52(7):1724–1731, 2004.
- Carlberg et al.(2005)Carlberg, Kildal, and Carlsson. U. Carlberg, P-S Kildal, and J. Carlsson. Study of antennas in reverberation chamber using method of moments with cavity Green's function calculated by Ewald summation. *IEEE Transactions on Electromagnetic Compatibility*, 47(4):805–814, 2005.
- Eibert(2005). T.F Eibert. A diagonalized multilevel fast multipole method with spherical harmonics expansion of the k-space integrals. *IEEE Transactions on Antennas and Propagation*, 53(2):814–817, 2005.
- Ewald(1921). P. P. Ewald. Die Berechnung optischer und elektrostatischer Gitterpotentiale. *Annalen der Physik*, 369(3):253–287, 1921.
- Gronwald(2005). F. Gronwald. Calculation of mutual antenna coupling within rectangular enclosures. *IEEE Transactions on Electromagnetic Compatibility*, 47(4): 1021–1025, 2005.
- Park et al.(1998)Park, Park, and Nam. Myun-Joo Park, Jongkuk Park, and Sangwook Nam. Efficient calculation of the Green's function for the rectangular cavity. *IEEE Microwave and Guided Wave Letters*, 8(3):124–126, 1998.

Spectral Multiple Traces Formulation for Heterogeneous Penetrable Objects Scattering

Carlos Jerez-Hanckes, José Pinto, and Simon Tournier

School of Engineering, Pontificia Universidad Católica de Chile, Av. Vicuña Mackenna 4680, Macul, Santiago, Chile
 cjerez@ing.puc.cl, jspinto@uc.cl, simon.tournier@gmail.com

Summary. We are interested in solving Helmholtz and Maxwell transmission problems for heterogeneous penetrable scatterers. Contrary to most common approaches based on integral boundary operators, one can derive a formulation named *Multiple Traces Formulation* (MTF) (Hiptmair & Jerez-Hanckes [2]) by imposing local Dirichlet and Neumann traces per subdomain. The MTF is shown to be a Fredholm first-kind system of integral equations free from spurious resonances, easy to construct with standard codes, entirely parallelizable and, though ill-conditioned, it is amenable to preconditioning via diagonal or Calderón-type techniques. We present new results for higher frequencies via conforming spectral discretizations.

1 Introduction

Consider the simple geometry shown in Fig. 1 where $\Omega := \bar{\Omega}_1 \cup \bar{\Omega}_2$ is a heterogeneous scatterer, composed of two bounded subdomains Ω_1, Ω_2 . The exterior domain is denoted by $\Omega_0 := \mathbb{R}^d \setminus \bar{\Omega}$ and interfaces by $\Gamma_{ij} := \partial\Omega_i \cap \partial\Omega_j$. For an exciting plane wave u^{inc} , we seek u representing the field scattered in Ω_0 and total fields in Ω which satisfy homogeneous Helmholtz equations, with constant wavenumbers $\kappa_i \in \mathbb{C} \setminus \mathbb{R}_-$ in each subdomain $\Omega_i, i = 0, 1, 2$. Standard Dirichlet and Neumann transmission conditions have to be fulfilled across each Γ_{ij} . With this, the local MTF hinges on the following ideas:

1. Every pair of interior Dirichlet and Neumann traces defined on subdomains $\Omega_i, \lambda^i := (\lambda_D^i, \lambda_N^i)$ are unknowns;
2. Transmission conditions across each interface Γ_{ij} are enforced weakly via local restriction and normal orientation operators;
3. Integral representations in each subdomain are used to set up Calderón identities over boundaries $\partial\Omega_i$, such that

$$\begin{aligned} \lambda^i &= \left(\frac{1}{2} \text{Id} + A_i \right) \lambda^i \\ &= \begin{pmatrix} \frac{1}{2} \text{Id} - K_i & V_i \\ W_i & \frac{1}{2} \text{Id} + K_i' \end{pmatrix} \begin{pmatrix} \lambda_D^i \\ \lambda_N^i \end{pmatrix}, \end{aligned}$$

where A_i contains the standard weakly singular, double layer, adjoint double layer and hypersingular integral operators, denoted V_i, K_i, K_i' and W_i , respectively, over $\partial\Omega_i$ for a wavenumber κ_i .

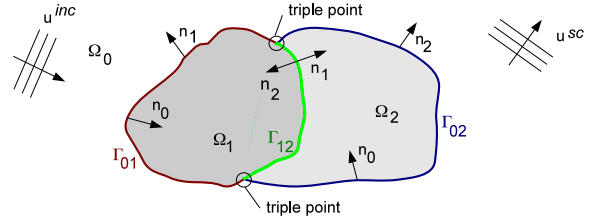


Fig. 1. Simple model geometry. Observe normal definitions.

In order to enforce transmission conditions using interior traces, with their opposite normals, we make use of *restriction-orientation-and-extension operators*, \tilde{X}_{ij} . With the above, the variational form of the MTF system is

$$\left\langle M \begin{pmatrix} \lambda_0 \\ \lambda_1 \\ \lambda_2 \end{pmatrix}, \begin{pmatrix} \varphi^0 \\ \varphi^1 \\ \varphi^2 \end{pmatrix} \right\rangle_{\times} = \left\langle \begin{pmatrix} \mathbf{g}^0 \\ \mathbf{g}^1 \\ \mathbf{g}^2 \end{pmatrix}, \begin{pmatrix} \varphi^0 \\ \varphi^1 \\ \varphi^2 \end{pmatrix} \right\rangle_{\times} \quad (1)$$

where $\langle \lambda^i, \varphi^j \rangle_{\times} = \langle \lambda_D^i, \varphi_N^j \rangle + \langle \lambda_N^i, \varphi_D^j \rangle$ and

$$M := \begin{pmatrix} A_0 & -\frac{1}{2} \tilde{X}_{01} & -\frac{1}{2} \tilde{X}_{02} \\ -\frac{1}{2} \tilde{X}_{10} & A_1 & -\frac{1}{2} \tilde{X}_{12} \\ -\frac{1}{2} \tilde{X}_{20} & -\frac{1}{2} \tilde{X}_{21} & A_2 \end{pmatrix}. \quad (2)$$

The MTF is amenable to parallelization but requires local test functions to have restrictions to interfaces Γ_{ij} lying in $\tilde{H}^{1/2}(\Gamma_{ij}) \times \tilde{H}^{-1/2}(\Gamma_{ij})$. In practical terms, this means that Dirichlet traces have to become zero at triple points for 2D or at triple edges in the case of 3D, while for Neumann data standard bases can be used. Physically, triple points are responsible for the need of such \sim -spaces.

Theorem 1 (Existence and Uniqueness [2]). *The local MTF system has a unique solution for all \mathbf{g} in $H^{1/2}(\partial\Omega_i) \times H^{-1/2}(\partial\Omega_i)$.*

2 Numerical Approximation via Spectral bases

Existing numerical experiments for the MTF are based on mesh refinements using low-order elements, i.e. Dirichlet traces are represented by p.w.-linear functions while Neumann ones via p.w.-constants [1, 2].

Results reveal the expected increasing ill-conditioning of the matrices for decreasing h and show the very positive counter-effects of diagonal and Calderón type preconditioning. Still, such low-orders approximations remain unsuitable for mid-to-high frequencies. Hence, the interest in spectral elements.

In what follows, we prove the amenability of the MTF for spectral elements in 2D under the simple case of a circle of unitary radius divided in two halves left (Ω_1) and right (Ω_2). Reference approximations are mapped through parametrizations of the boundaries and interfaces –circles for the subdomain boundaries $\partial\Omega_i$ and segments $[-1, 1]$ for the interfaces Γ_{ij} .

2.1 Trial spaces

To approximate standard spaces $H^{\pm 1/2}(\partial\Omega_i)$, we use Fourier polynomials of the form:

$$\hat{\chi}_m(\theta) := e^{im\theta}, \quad \theta \in (0, 2\pi), \quad m \in \mathbb{Z}, \quad (3)$$

for both Dirichlet and Neumann unknowns λ_i , so that $\lambda_i = (\sum_m \lambda_d^m \chi_m^i, \sum_m \lambda_n^m \chi_m^i)$, where χ_m is defined as $\hat{\chi}_m$ mapped onto the actual subdomain boundary.

2.2 Test spaces

We use weighted Tchebyshev polynomials of the first and second kind, denoted by U_l and T_l , respectively, defined over $[-1, 1]$, as these bases are shown to be dense in the required functional spaces $\tilde{H}^{\pm 1/2}([-1, 1])$, accordingly [3]. Thus, reference approximation bases

$$\hat{q}_l^+(x) := w(x)U_l(x), \quad \hat{q}_l^-(x) := w^{-1}(x)T_l(x), \quad (4)$$

with $w = \sqrt{1-x^2}$ and $l = 0, \dots, L_i$, L_i being the maximum degree of polynomials used in subdomains $\partial\Omega_i$ are mapped at each interface Γ_{ij} , so that for each $i = 0, 1, 2$

$$\varphi_i = (q_{ij,l}^-, q_{ij,l}^+) \quad \text{for } j \in \{0, 1, 2\}, j \neq i. \quad (5)$$

Consequently, the structure of test bases depends on the number of interfaces and number of Fourier bases to describe λ_i . In the case of 3 subdomains in which every subdomain intersect another in a non empty set, we have that there are $2 \times 2(L_i + 1)$ possibilities for φ_i . In order to achieve square matrices per subdomain we impose

$$L_i = M_i \quad \forall i = 0, 1, 2, \quad (6)$$

and for numerical purposes we set all equal for each i . This observation also justifies an even total number of degrees of freedom for the trial spaces.

2.3 Computational Results

Computational experiments were programmed in MATLAB. Duality products and integration is done semi-analytically when possible. Figure 2 presents the exterior Dirichlet trace λ_D^0 for $N = 2$ using same $k_1 = k_2$ are shown in. Error convergences are obtained against reference solutions due to Mie series.

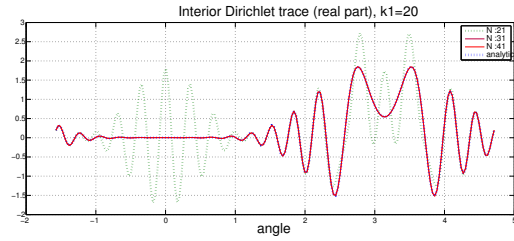


Fig. 2. Dirichlet trace approximation for different harmonics used. Parameters used $k_1 = k_2 = 20$, $k_0 = 1$.

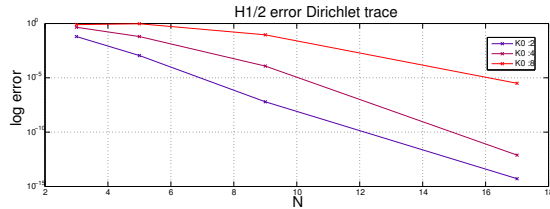


Fig. 3. Error convergence for Dirichlet data for $k_1 = k_2 = 1$ and different k_0 .

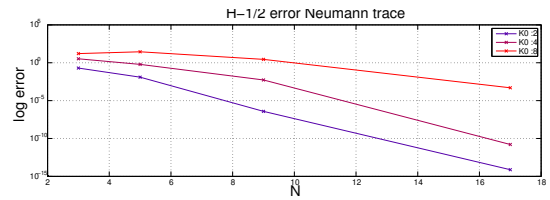


Fig. 4. Error convergence for Neumann data for $k_1 = k_2 = 1$ and different k_0 .

Acknowledgement. This work has been partially supported by Project Fondecyt Iniciación 11121166 and Conicyt ACT 1118 ANANUM.

References

1. X. Claeys, R. Hiptmair, C. Jerez-Hanckes, and S. Pintarelli. Novel Multi-Trace Boundary Integral Equations for Transmission Boundary Value Problems, *SAM Report*, 5, 2014.
2. R. Hiptmair and C. Jerez-Hanckes, Multiple traces boundary integral formulation for Helmholtz transmission problems, *Adv. Comput. Math.*, 37:39–91, 2012.
3. C. Jerez-Hanckes and J.-C. Nédélec, Explicit variational forms for the inverses of integral logarithmic operators over an interval, *SIAM J. Math. Anal.* 44:2666–2694, 2012. (to be submitted).

MSFEM to Simulate Eddy Currents in Laminated Iron

Karl Hollaus¹ and Joachim Schöberl¹

Vienna University of Technology, Institute for Analysis and Scientific Computing, Wiedner Hauptstrasse 8-10 A-1040 Vienna, Austria karl.hollaus@tuwien.ac.at, joachim.schoeberl@tuwien.ac.at

Summary. The simulation of eddy currents in laminated nonlinear iron cores by the finite element method is of great interest in the design of electrical devices. The dimensions of the iron core and the thickness of the laminates are very different. Thus, finite element models considering each laminate require many finite elements leading to extremely large systems of equations. A multi-scale finite element method has been developed to cope with this problem. Numerical simulations in 2D demonstrate an excellent accuracy and very low computational costs.

1 Introduction

The simulation of the eddy current losses in laminated iron cores is still a challenging task [1]. Brute force methods apply for instance an anisotropic conductivity [2]. These solutions are frequently corrected in a second step [3]. The method proposed in [4] imposes the magnetic properties in a weak sense using skin effect sub-basis functions. The multi-scale finite element method (MSFEM) in [5,6] is extended by higher order micro-shape functions in this work.

2 Standard Eddy Current Problem

2.1 Boundary Value Problem

In the standard eddy current problem each laminate is resolved by finite elements. The eddy current problem to be solved is sketched in Fig. 1. It consists of a conducting domain (iron) Ω_c and air Ω_0 , i.e., $\Omega = \Omega_c \cup \Omega_0$ with the boundary $\Gamma = \Gamma_D \cup \Gamma_N$. The material parameters are the magnetic permeability $\mu(A)$ and the electric conductivity σ , respectively. The eddy current problem with the magnetic vector potential A in the time domain reads as

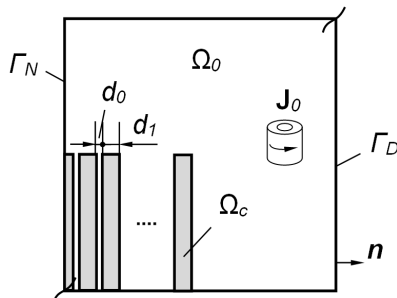


Fig. 1. Standard boundary value problem.

$$\mathbf{curl} \frac{1}{\mu(A)} \mathbf{curl} A + \sigma \frac{\partial}{\partial t} A = \mathbf{J}_0 \text{ in } \Omega \subset \mathbb{R}^3, \quad (1)$$

$$A \times \mathbf{n} = \alpha \text{ on } \Gamma_D, \quad (2)$$

$$\frac{1}{\mu(A)} \mathbf{curl} A \times \mathbf{n} = \mathbf{K} \text{ on } \Gamma_N, \quad (3)$$

where \mathbf{J}_0 in (1) stands for an impressed current density, α in (2) represents a magnetic flux and \mathbf{K} in (3) describes a surface current density.

2.2 Weak Form

Equations (1) to (3) lead to the following weak form for the finite element method (FEM). Find $A_h \in \mathcal{V}_\alpha := \{A_h \in \mathcal{V}_h : A_h \times \mathbf{n} = \alpha_h \text{ on } \Gamma\}$, such that

$$\int_{\Omega} \frac{1}{\mu(A_h)} \mathbf{curl} A_h \cdot \mathbf{curl} v_h d\Omega + \frac{\partial}{\partial t} \int_{\Omega} \sigma A_h \cdot \mathbf{v}_h d\Omega = (4) \int_{\Omega} \mathbf{J}_0 \cdot \mathbf{v}_h + \int_{\Gamma_N} \mathbf{K} \cdot \mathbf{v}_h$$

for all $v_h \in \mathcal{V}_0 := \{v_h \in \mathcal{V}_h : v_h \times \mathbf{n} = \mathbf{0} \text{ on } \Gamma_D\}$, where \mathcal{V}_h is a finite element subspace of $H(\mathbf{curl}, \Omega)$.

3 Multi-Scale Finite Element Method MSFEM

3.1 Multi-Scale Method

Standard FEM provides accurate approximations as long as the unknown solution is smooth. To avoid large equation systems for equations with rough coefficients the standard polynomial basis is augmented by special functions including a priori information into the ansatz space

$$u^h(x) = \sum_i^n \sum_j^m u_{ij} \varphi_i(x) \psi_j(x) = \sum_i^n \sum_j^m u_{ij} \phi_{ij}(x), \quad (5)$$

where n is the number of standard polynomials φ_i , m the number of special functions ψ_j and u_{ij} are the coefficients of the approximated solution u^h . The special functions representing a local basis approximate well the solution locally [7]. Based on (5) a MSFEM for the eddy current problem with laminated iron has been constructed. The MSFEM and the used local basis are presented below.

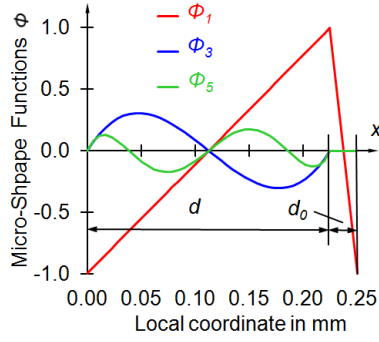


Fig. 2. Micro-shape functions.

3.2 Micro-Shape Function Basis for MSFEM

The micro-shape functions considering the periodic structure of a laminated stack are shown in Fig. 2. The tooth-shaped function ϕ_1 is continuous and piecewise linear. The thicknesses of iron layers and air gaps are d and d_0 , respectively. The feasibility considering only ϕ_1 with respect to the penetration depth have been shown in [6, 8]. Gauss-Lobatto shape functions were selected for the higher order micro-shape functions. Fig. 2 shows them transformed into the interval $[0, d]$. The higher order micro-shape functions ϕ_3 and ϕ_5 represent bubble functions and are equal to zero in the air gap. Thus, $\{\phi_1, \phi_3, \phi_5\}$ span a subspace of the periodic and continuous functions $H_{per}^1(\Omega)$.

3.3 Multi-Scale Approach

Standard polynomial basis functions [9] are augmented by the micro-shape functions leading to the multi-scale approach

$$\tilde{\mathbf{A}} = \mathbf{A}_0 + \sum_{i \in \{1,3,5\}} \left(\phi_i(0, A_{i,2}, A_{i,3})^T + \nabla(\phi_i w_i) \right) \quad (6)$$

where the lamination is perpendicular to the x -direction. The mean value \mathbf{A}_0 considers the smooth variation of the macro-structure, the scalar functions $A_{i,2h}, A_{i,3h}, w_i$ with ϕ_i , respectively, take into account of the periodic micro-structure of the laminated iron. The main magnetic flux density is an even function across a laminate. Consequently, the variation of \mathbf{A} is an odd function. Thus, it suffices to consider only odd micro-shape functions in approach (4). An extension of (6) to higher order again is straightforward.

3.4 Weak Form of MSFEM

Replacing \mathbf{A} in (1) to (3) by (6) leads to the weak form: Find $(A_{0h}, A_{i,2h}, A_{i,3h}, w_{i,h}) \in V_\alpha := \{(A_{0h}, A_{i,2h}, A_{i,3h}, w_{i,h}) : A_{0h} \in \mathcal{U}_h, (A_{i,2h}, A_{i,3h}) \in \mathcal{V}_h, (w_{i,h}) \in \mathcal{W}_h \text{ and } A_{0h} \times \mathbf{n} = \alpha_h \text{ on } \Gamma\}$, such that

$$\int_{\Omega} \frac{1}{\mu(\tilde{\mathbf{A}}_h)} \mathbf{curl} \tilde{\mathbf{A}}_h \cdot \mathbf{curl} \tilde{\mathbf{v}}_h d\Omega + \sigma \frac{\partial}{\partial t} \int_{\Omega} \sigma \tilde{\mathbf{A}}_h \cdot \tilde{\mathbf{v}}_h d\Omega = (7) \int_{\Omega} \mathbf{J}_0 \cdot \tilde{\mathbf{v}}_h + \int_{\Gamma_N} \mathbf{K} \cdot \tilde{\mathbf{v}}_h$$

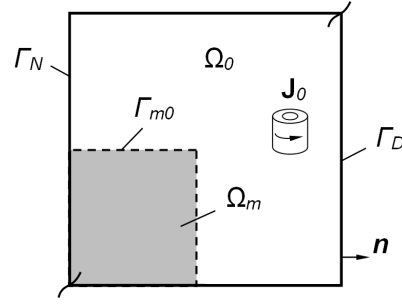


Fig. 3. Multi-scale boundary value problem.

for all $(\mathbf{v}_{0h}, v_{i,2h}, v_{i,3h}, q_{i,h}) \in V_0 := \{(\mathbf{v}_{0h}, v_{i,2h}, v_{i,3h}, q_{i,h}) : \mathbf{v}_{0h} \in \mathcal{U}_h, (v_{i,2h}, v_{i,3h}) \in \mathcal{V}_h, (q_{i,h}) \in \mathcal{W}_h \text{ and } \mathbf{v}_{0h} \times \mathbf{n} = \mathbf{0} \text{ on } \Gamma_D\}$, where \mathcal{U}_h is a finite element subspace of $H(\mathbf{curl}, \Omega)$, \mathcal{V}_h of $L_2(\Omega_m)$ and \mathcal{W}_h of $H^1(\Omega_m)$, respectively, and $\{\phi_1, \phi_3, \phi_5\}$ is a subspace of $H_{per}^1(\Omega_m)$. The subdomain Ω_m comprises the iron laminates and the air gaps in between as indicated in Fig. 3. Natural boundary conditions hold on the interface Γ_{m0} . The main magnetic flux was studied in 2D in [8]. Here, the magnetic stray flux is also taken into account in 3D. The orientation of the lamination can vary arbitrarily in space [5].

References

1. H. De Gerssem, S. Vanaverbeke, and G. Samaey, "Three-dimensional - two-dimensional coupled model for eddy currents in laminated iron cores," *IEEE Trans. Magn.*, vol. 48, no. 2, pp. 815–818, 2012.
2. V. C. Silva, G. Meunier, and A. Foggia, "A 3d finite-element computation of eddy currents and losses in laminated iron cores allowing for electric and magnetic anisotropy," *IEEE Trans. Magn.*, vol. 31, no. 3, pp. 2139–2141, May 1995.
3. O. Bír6, K. Preis, and I. Tigar, "A FEM method for eddy current analysis in laminated media," *COMPEL*, vol. 24, no. 1, pp. 241–248, 2005.
4. P. Dular, J. Gyselinck, and L. Krähenbühl, "A time-domain finite element homogenization technique for lamination stacks using skin effect sub-basis functions," *COMPEL*, vol. 25, no. 1, pp. 6–16, 2006.
5. K. Hollaus, M. Huber, J. Schöberl, and P. Hamberger, "A Linear FEM Benchmark for the Homogenization of the Eddy Currents in Laminated Media in 3D," *IFAC*, vol. 7, no. 1, pp. 1190–1194, 2012.
6. K. Hollaus, A. Hannukainen, and J. Schöberl, "Two-scale homogenization of the nonlinear eddy current problem with FEM," *IEEE Trans. Magn.*, vol. 50, no. 2, pp. 413–416, Feb 2014.
7. I. Babuska and J. M. Melenk, "The partition of unity method," *Int. J. Numer. Meth. Engng.*, vol. 40, pp. 727–758, 1997.
8. K. Hollaus and J. Schöberl, "Multi-scale fem for the eddy current problem in laminated media," *IEEE Trans. Magn.*, 2014, submitted.
9. J. Schöberl and S. Zaglmayr, "High order Nédélec elements with local complete sequence properties," *COMPEL*, vol. 24, no. 2, pp. 374–384, 2005.

Simulation of Power Electronics in Automotive Product Development

Daniel Klagges and Matthias Richwin

Leopold Kostal GmbH & Co. KG, Hauert 11, 44227 Dortmund, Germany

Summary. Automotive product development comes with high requirements for reliability, functionality, package space, temperature stability, mechanical resilience, electromagnetic compatibility and cost efficiency. To meet these requirements, simulations have become an indispensable part of the development and production process. Electric vehicles provide further challenges to automotive electronics engineering, due to their high power and energy densities. In this talk, the application of simulation techniques to the automotive development process is presented with the example of an electric vehicles board net, high power, DC-DC converter. One main challenge in the design process turns out to be the magnetic interferences of the high current and high frequency parts. To capture their behavior, a coupled electromagnetic simulation of all involved components is necessary. The nonlinear properties of the semiconductor power switches further require a harmonic balance approach. It is shown that the used simulation model allows an insight into the system behavior, which would not be possible with a separate simulation of the single components, or a purely linear model. The gathered information can be used to prevent design flaws and optimize the system behavior. Finally an outlook is given how the electromagnetic model can be expanded to a multiphysics model, including the devices environment.

High Level Simulation of Cyber-Physical Systems

Ralph Weissnegger¹, Markus Pistauer¹, and Christian Steger²

¹ CISC Semiconductor GmbH, Klagenfurt, Austria r.weissnegger@cisc.at, m.pistauer@cisc.at

² Graz University of Technology, Austria, steger@tugraz.at

Summary. This abstract presents the simulation based design and verification of Cyber-Physical Systems (CPS) from a system point of view.

1 Abstract

The rapidly developing application of Cyber-Physical Systems (CPS) in our daily life is driven by a closer integration of computational systems (the cloud) and local devices like sensors and actors networked with each other. This results in a novel class of applications that can execute complex system tasks flexibly autonomously and even allow optional individual user interaction. The design and development of such systems requires a large range of expertise and technological components, spanning from heterogeneous sensor elements and communication systems over scalable data processing systems to physical objects involving also humans as users.

The electrical architecture of a vehicle can be seen as such, although in the past this was not the case. Recent trends in the in-vehicle electrical/electronic architectures brought a rapid shift towards multicore, heterogeneous, networked and reconfigurable systems. This makes the design of such systems extremely complex and imposes a large effort for designers (hard- and software) to design their applications. The next generation of such systems should be able to allow applications to run in parallel on different parts (electronic control units (ECU) and/or processors, DSPs within a multicore architecture of a single ECU) of the system such as Multimedia, Human Machine Interface (HMI) like car infotainment or nomadic device (Tablet, Smart Phone) ad-hoc interconnect, Navigation, Advanced Driver Assistance Systems (ADAS) and many more. This has been acknowledged also on a European Industry Level [1] [2].

Beside performance, power consumption and of course safety relevant aspects have to be considered as well once a certain Automotive Safety Integrity Level (ASIL) needs to be applied.

To guarantee the safety of these systems, they have to follow standards like the ISO 26262 [3]. The ISO 26262 standard is an adaption of the functional safety standard IEC 61508 for automotive electric/electronic systems. Today, the compliance of the standard is op-

tional but is more often required from the automotive-companies and their partners. To be ISO 26262 conform it's important to proof the whole system towards its safety goals, not a set of specialized parts. As a result of the foregoing, such a CPS realized in cars demands very fast executable specifications to validate the system concepts and proof the system with particular emphasis on safety relevant criteria.

System level modeling is nowadays a commonly used methodology in design and verification of complex embedded real-time systems to reduce engineering risks through an early, fast and flexible method to detect design flaws. Designs can be verified and simulated long before committing to its implementation. But most of the engineers involved in these tasks apply EDA tools like e.g. Matlab/Simulink [4]. This approach is direct and effective. On the other hand most details of the realized system, code generation for the target hardware platform, parameter descriptions etc. are linked with a dedicated hardware implementation and unlinked with the global system requirements.

As a consequence a paradigm shift will be necessary to further abstract the system modeling languages applied to simulation and verification of CPS. A Unified Modeling Language (UML [5]) is a language that might be considered for modeling of application models.

Further the language SysML [6] can be considered as extension/subset of UML to better address the consideration of requirements and the description of system parameters.

Another approach is MARTE [7] as domain-specific modeling language intended for model-based design and analysis of realtime and embedded software of cyber-physical systems. MARTE is an extension to UML, providing additional parameters for real-time systems, which are missing in UML. Non-functional properties are very important to evaluate the functional safety of the system. With MARTE it is possible to map functional (structural and behavioral) and non-functional (power, thermal, time) properties to models. With MARTE Allocation it is possible to associate the functional application elements with the available resources (execution platform). For interoperability with other tools and the use of standardized

IP-models, the open standard IP-XACT [8] can be used.

1.1 Model-to-text transformation

For the simulation of system-models based on MARTE, the high level language code is generated through a model-to-text transformation process. One of the languages used for this approach is SystemC [9]. SystemC is gaining increasing attention because of its great flexibility in describing the components at different levels of abstraction, from system and transaction level down to RTL level. Even extensions to describe analog and mixed signal systems are available. A second important SystemC extension is SystemC-TLM to describe transaction driven systems. This allows a faster modeling and simulation time while developing phase, to detect HW/SW integration issues. Another language used in this approach is Matlab. Matlab/Simulink is well established in simulation of systems in different domains and used by many other tool vendors but shall not be used in the future for system level descriptions.

1.2 Simulation based verification

To test the system towards their safety goals, testbenches are automatically generated from the safety functions defined in the ISO 26262 process. An automatic stimulus generator and a protocol checker are used to verify the system. The testbenches support transaction level modeling and are written in UVM [10] (Universal Verification Methodology).

Acknowledgement. The approach presented above is experimented in the Catrene (OpenES) research program supported by the FFG (Austrian Research Promotion Agency) in cooperation with the technical University of Graz.

References

1. ECSEL. *2014 ECSEL Multi Annual Strategic Research and Innovation Agenda (MASRIA)*. http://www.smart-systems-integration.org/public/documents/publications/2014_ecsel_masria_partc.pdf.
2. Gartner. *Gartner Says the Internet of Things Installed Base Will Grow to 26 Billion Units By 2020*. <http://www.gartner.com/newsroom/id/2636073>.
3. ISO 26262. *ISO 26262-1:2011(en), Road vehicles Functional safety Part 1: Vocabulary*. <https://www.iso.org/obp/ui/>, Publication date 2011-11-14.
4. MathWorks. *Matlab R2014a Documentation*. <http://www.mathworks.de/de/help/simulink/>.
5. OMG. *Unified Modeling Language, Version 2.5*. September 2013, OMG Document Number: ptc/2013-09-05.
6. OMG. *System Modeling Language, Version 1.3*. June 2012, OMG Document Number: formal/2012-06-01.

7. OMG. *UML Profile for MARTE: Modeling and Analysis of Real-Time Embedded Systems, Version 1.1*. June 2011, OMG Document Number: formal/2011-06-02.
8. IEEE. *IEEE Standard for IP-Xact, Standard Structure for Packaging, Integrating, and Reusing IP within Tool Flows, Version 1.1*. February 2010, IEEE, 3 Park Avenue New York, NY 10016-5997, USA.
9. Accellera. *SystemC 2.3.1 (Includes TLM)*. <http://www.accellera.org/downloads/standards/systemc/>.
10. Accellera. *Universal Verification Methodology (UVM) 1.1 Class Reference*. June 2011, Accellera Organization 1370 Trancas Street 163 Napa, CA 94558 USA.

Latency exploitation in Wavelet Based Multirate Circuit Simulation

Kai Bittner¹ and Hans Georg Brachtendorf¹

University of Applied Sciences Upper Austria, Softwarepark 11, 4232 Hagenberg, Austria
Kai.Bittner@fh-hagenberg.at, Hans-Georg.Brachtendorf@fh-hagenberg.at

Summary. We present a further improvement of the wavelet multirate circuit simulation. In the new algorithm we use different grids for the approximation of the solution on different circuit parts. In particular, for circuits with latencies the grids can be much sparser, which results in the reduction of the overall problem size and leads to a faster simulation.

1 The multi-rate circuit simulation problem

We consider circuit equations in the charge/flux oriented modified nodal analysis (MNA) formulation, which yields a mathematical model in the form of a system of differential-algebraic equations (DAEs):

$$\frac{d}{dt}q(x(t)) + g(x(t)) = s(t). \quad (1)$$

To separate different time scales the problem is reformulated as a multi-rate PDAE, i.e.,

$$\left(\frac{\partial}{\partial \tau} + \omega(\tau) \frac{\partial}{\partial t}\right)q(\hat{x}(\tau, t)) + g(\hat{x}(\tau, t)) = \hat{s}(\tau, t) \quad (2)$$

with mixed initial-boundary conditions $x(0, t) = X_0(t)$ and $x(\tau, t) = x(\tau, t + P)$. A solution of the original circuit equations can be found along certain characteristic lines [3]

Discretization with respect to τ (Rothe method) using a linear multi step method results in a periodic boundary value problem in t of the form

$$\omega_k \frac{d}{dt}q_k(X_k(t)) + f_k(X_k, t) = 0, \quad (3)$$

$$X_k(t) = X_k(t + P),$$

where $X_k(t)$ is the approximation of $\hat{x}(\tau_k, t)$ for the k -th time step τ_k (cf. [1, 3]). The periodic boundary value problem (3) can be solved by several methods, as Shooting, Finite Differences, Harmonic Balance, etc. Here, we consider the spline wavelet based method introduced by the authors in [1]. One problem of traditional methods is that all signals in the circuit are discretized over the same grid. This can pose a problem if different signal shapes are present in the circuit, which may be approximated more efficient if individual grids are used for each of the signals. As an example we consider a chain of 5 frequency dividers (as part of a PLL). In each step the frequency is reduced by a factor 2 as one can see in Fig. 1. Obviously, for the low frequency signals towards the end of the divider chain a much sparser grid would be sufficient for an accurate representation, in comparison to the high frequency input signal.

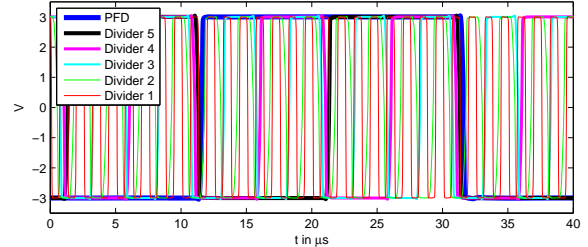


Fig. 1. Several signals in a frequency divider chain as part of a PLL.

2 Division into subcircuits and connections

Although the representation of each signal over its own individual grid seems to give maximal flexibility, this approach leads to several problems, which makes the simulation inefficient. Therefore, we consider groups of signals with similar shape appearing in a part of the circuit. The circuit is divided into N subcircuits which are connected at common nodes. Two facilitate different expansions of signals on the subcircuits we replace each common node by a pair of nodes connected by a perfect conductor. Namely, we introduce the “connection” $C_{\mu, \nu}^{k, \ell}$, if the μ -th node of subcircuit is identified with the ν -th node in subcircuit ℓ , as one can see in Fig. 2. Thus, we have the current through the connection $C_{\mu, \nu}^{k, \ell}$, as additional unknowns i_{μ}^k and i_{ν}^{ℓ} for each of the two involved subcircuits, as well as the equations

$$u_{\mu}^k(t) - u_{\nu}^{\ell}(t) = 0 \quad \text{and} \quad i_{\mu}^{k(t)} - i_{\nu}^{\ell}(t) = 0. \quad (4)$$

in addition to the circuit equations

$$\frac{d}{dt}q^k(x^k(t)) + g^k(x^k(t), t) = 0, \quad k = 1, \dots, N \quad (5)$$

of the N subcircuits.

Using the Rothe’s method on the multirate PDAE’s will yield a system of DAE’s as introduced in (5) and (4). Therefore we consider the solution of the periodic problem for the above DAE’s.

3 Spline Galerkin discretization and wavelet based adaptivity

Our goal is to approximate the solution of the equations (4) and (5) by spline functions as it was done

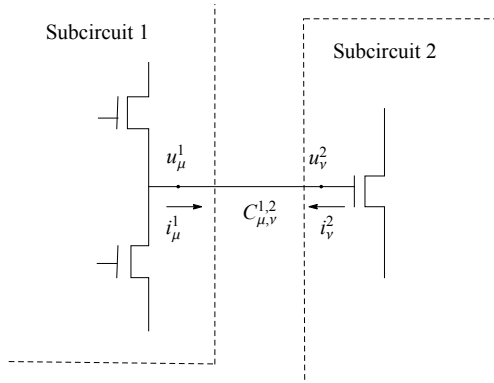


Fig. 2. Splitting of a circuit into subcircuits with connections.

in [1]. However, we use a different spline representations $x^i(t) = \sum_{k=1}^{n_i} c_k^i \phi_k^i(t)$, $i = 1, \dots, N$, for each of the subcircuits. A Petrov-Galerkin discretization yields the nonlinear system of equations

$$\int_{\tau_{\ell-1}^i}^{\tau_{\ell}^i} \frac{d}{dt} q^i(x^i(t)) + g^i(x^i(t), t) dt = 0, \quad \ell = 1, \dots, n_i,$$

for each subcircuit and

$$\int_{\tau_{\ell-1}^i}^{\tau_{\ell}^i} u_{\mu}^i(t) - u_{\nu}^j(t) dt = 0, \quad \ell = 1, \dots, n_i \quad (6)$$

$$\int_{\tau_{\ell-1}^j}^{\tau_{\ell}^j} i_{\mu}^i(t) + i_{\nu}^j(t) dt = 0, \quad \ell = 1, \dots, n_j \quad (7)$$

for each connection $C_{\mu,\nu}^{i,j}$ between subcircuits. The splitting points τ_{ℓ}^i are chosen in close relation to the spline grid.

The wavelet based coarsening and refinement methods described in [1, 2] are used to generate adaptive grids for an efficient signal representation.

4 Numerical test

Fig. 3 shows the spline grid generated for the classical algorithm using the same grid for all signals. We have plotted the grid points t_i against their index i , which allows to recognize the local density of the grid.

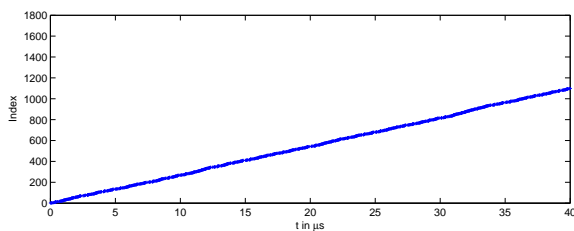


Fig. 3. Grid of the single grid method.

The grids used in our new multiple grid method can be seen in Fig. 4. Obviously, one gets much better

adapted, smaller grids for the lower frequency signals. This leads to a reduction of the total number of equations from roughly 130,000 to 85,000. The number of nonzeros in the Jacobian for Newton's method is reduced from 5,000,000 to 2,500,000. Consequently the time for assembling resp. solving the linear system was reduced from 4s to 2s resp. 8s to 4s.

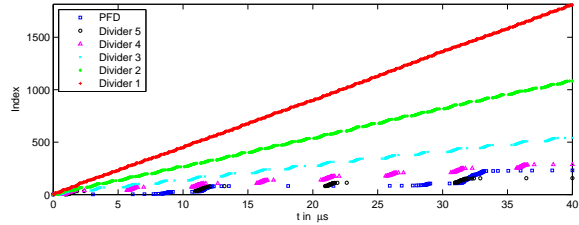


Fig. 4. Several signals in a frequency divider chain as part of a PLL.

A further effect is that the larger the nonlinear system is harder to solve by Newton's method, which results in more Newton iterations as well as shorter envelope time steps. Thus, an envelope simulation with a frequency modulated signal over 0.3s worked well for the multiple grid method and was done in 37min. A similar simulation by the single grid method needed almost 5 hours.

Acknowledgement. This work has been partly supported by the ENIAC research project ARTEMOS under grant 829397 and the FWF under grant P22549.

References

1. K. Bittner and H.-G. Brachtendorf. Adaptive multi-rate wavelet method for circuit simulation. *Radioengineering*, accepted.
2. K. Bittner and H.-G. Brachtendorf. Fast algorithms for grid adaptation using non-uniform biorthogonal spline wavelets. *SIAM J. Scient. Computing*, submitted.
3. K. Bittner and H.-G. Brachtendorf. Optimal frequency sweep method in multi-rate circuit simulation. *COMPEL*, 33(3), to appear.

Simulation of graphene nanoribbons

Giovanni Mascali¹ and Vittorio Romano²

¹ Dipartimento di Matematica, Università della Calabria and INFN-Gruppo c. Cosenza, Italy g.mascali@unical.it,

² Dipartimento di Matematica e Informatica, Università di Catania, Italy romano@dmi.unict.it

Summary. Numerical simulations of graphene nanoribbons are presented. The model has been obtained from the hierarchy of the moment systems associated to the transport equations and the needed closure relations have been achieved by resorting to the maximum entropy principle. Comparisons with Monte Carlo data are included.

1 The model

Monte Carlo investigations of electron transport in suspended graphene monolayers are available in the literature [1] along with direct solutions of the Boltzmann equations [2]. However the computational complexity makes it desirable to have simpler mesoscopic models, like hydrodynamical models, more suitable for computer-aided-design purposes.

The aim of this paper is to formulate a hydrodynamical model for charge transport in graphene nanoribbons based on the maximum entropy principle [3]. The charge carriers are divided into electrons and holes. The evolution equations for macroscopic variables like density, energy, velocity and energy-flux are obtained by taking the moments of the transport equations. All the main scattering mechanisms are included: both acoustic phonons and optical phonon interactions. Degeneracy is also taken into account. The model has been formulated in a planar geometry, which is the natural one for graphene nano ribbons.

Graphene is a gapless semiconductor made of a single layer sheet of carbon atoms arranged into a honeycomb hexagonal lattice. It has, with good approximation, a conical band structure. The electron energy in graphene depends on a wave vector \mathbf{k} belonging to a bidimensional Brillouin zone which has an hexagonal shape. The most part of electrons are in the valleys around the vertices of the Brillouin zone, called Dirac points or K and K' points. We treat the K -valley and the K' -valley as a single equivalent valley. With a very good approximation [4] a linear dispersion relation holds for the energy bands ε_α around the equivalent Dirac points, that is $\varepsilon_\alpha = \alpha \hbar v_F k$, where the index $\alpha = 1$ in the conduction or π^* band (positive energy) and $\alpha = -1$ in the valence or π band (negative energy). v_F is the (constant) Fermi velocity, \hbar the reduced Planck constant and k is the modulus of the wave vector. For consistency k will be allowed to vary in all \mathbb{R}^2 . A reference frame centered in the K or the K' -point will be used.

In a semiclassical kinetic setting, the charge transport in graphene is described by two Boltzmann equa-

tions, one for electrons in the valence (π) band and the other for electrons in the conduction (π^*) band

$$\frac{\partial f^A}{\partial t} + \mathbf{v}^A \cdot \nabla_{\mathbf{r}} f^A + \frac{e}{\hbar} \mathbf{E} \cdot \nabla_{\mathbf{k}} f^A = \mathcal{C}^A, \quad A = \pi, \pi^*, \quad (1)$$

$f^A(\mathbf{r}, \mathbf{k}, t)$ representing the distribution function of charge carriers in the A -band at position \mathbf{r} , time t and wave-vector \mathbf{k} . $\nabla_{\mathbf{r}}$ and $\nabla_{\mathbf{k}}$ are the gradients with respect to the position and wave vector respectively, e is the elementary (negative) charge while the microscopic group velocity \mathbf{v} is related to the energy band by $\mathbf{v} = \frac{1}{\hbar} \nabla_{\mathbf{k}} \varepsilon_\alpha = \alpha v_F \frac{\mathbf{k}}{k}$. \mathbf{E} is the electric field obtained by the Poisson equation which must be coupled with the above system. \mathcal{C}^A is the collision term representing the interactions of electrons with acoustic and optical phonons. Optical phonon scatterings can be intra-band, that leave the electron in the same band, or inter-band pushing the electron from an initial band to the other one. In particular the scattering with optical phonons of K type can push electrons from a valley to a neighbor one (inter-valley scattering). However we will consider the several K -valleys as equivalent.

The collision term is given by the sum of the contributions of the several types of scatterings. The generic term due to a single scattering between a state \mathbf{k} in the A -band and a state \mathbf{k}' in the B -band reads (omitting the dependence on space and time for the sake of simplicity)

$$\mathcal{C}^A(\mathbf{k}) = \frac{2}{(2\pi)^2} \int_{\mathbb{R}^2} [w(\mathbf{k}', \mathbf{k}) f^B(\mathbf{k}') (1 - f^A(\mathbf{k})) - w(\mathbf{k}, \mathbf{k}') f^A(\mathbf{k}) (1 - f^B(\mathbf{k}'))] d^2 \mathbf{k}',$$

where $w(\mathbf{k}', \mathbf{k})$ is the transition rate [5, 6].

For the acoustic phonons, the elastic approximation is used. As regards the optical phonons, the longitudinal optical (LO), the transversal optical (TO) and the K phonons are included.

Since the relaxation time necessary for the decaying of optical phonons into acoustic ones is much longer than the electron relaxation time, phonons are out of equilibrium. Therefore also the phonon transport equations are taken into account.

2 Moment equations

Macroscopic quantities can be defined as moments of the distribution function with respect to some suitable weight functions, assuming a sufficient regularity

for the existence of the involved integral. In particular we propose a set of moment equations comprising for each band the balance equations for average densities ρ_A , velocities V_A , energies W_A and energy fluxes S_A defined as

$$\rho_A = \frac{2}{(2\pi)^2} \int_{\mathbb{R}^2} f^A(\mathbf{r}, \mathbf{k}, t) d^2\mathbf{k}, \quad (2)$$

$$\rho_A \mathbf{V}_A = \frac{2}{(2\pi)^2} \int_{\mathbb{R}^2} f^A(\mathbf{r}, \mathbf{k}, t) \mathbf{v} d^2\mathbf{k}, \quad (3)$$

$$\rho_A W_A = \frac{2}{(2\pi)^2} \int_{\mathbb{R}^2} f^A(\mathbf{r}, \mathbf{k}, t) \varepsilon d^2\mathbf{k}, \quad (4)$$

$$\rho_A \mathbf{S}_A = \frac{2}{(2\pi)^2} \int_{\mathbb{R}^2} f^A(\mathbf{r}, \mathbf{k}, t) \varepsilon \mathbf{v} d^2\mathbf{k}, \quad (5)$$

where $A = e$ stands for electron variables and $A = h$ stands for hole variables. We remark that the velocity of both electrons and holes is given by $\mathbf{v} = \hbar v_F \frac{\mathbf{k}}{\hbar}$. By integrating the Boltzmann equation with respect to \mathbf{k} , after multiplication by the weight, one has the balance equations for the above defined macroscopic quantities ($A = e, h$)

$$\begin{aligned} \frac{\partial}{\partial t} \rho_A + \nabla_{\mathbf{r}} \cdot (\rho_A \mathbf{V}_A) &= \rho_A C_{\rho_A} \\ \frac{\partial}{\partial t} (\rho_A \mathbf{V}_A) + \nabla_{\mathbf{r}} \cdot (\rho_A \mathbf{F}_A^{(0)}) - \alpha e \rho_A \mathbf{G}^{(0)} \cdot \mathbf{E} &= \rho_A C_{\mathbf{V}_A} \\ \frac{\partial}{\partial t} (\rho_A W_A) + \nabla_{\mathbf{r}} \cdot (\rho_A \mathbf{S}_A) - \alpha e \rho_A \mathbf{E} \cdot \mathbf{V}_A &= \rho_A C_{W_A} \\ \frac{\partial}{\partial t} (\rho_A \mathbf{S}_A) + \nabla_{\mathbf{r}} \cdot (\rho_A \mathbf{F}_A^{(1)}) - \alpha e \rho_A \mathbf{G}^{(1)} \cdot \mathbf{E} &= \rho_A C_{\mathbf{S}_A}, \end{aligned}$$

$\alpha = +1$ for the electrons and $\alpha = -1$ for the holes.

Similar equations hold for the phonon subsystem.

We note that, besides the average densities, velocities, energies and energy fluxes, additional quantities appears (omitting for the sake of brevity the dependence on space and time)

$$\begin{aligned} \rho_A C_{\rho_A} &= \frac{2}{(2\pi)^2} \int_{\mathbb{R}^2} \mathcal{C}^A(\mathbf{k}) d^2\mathbf{k}, \\ \rho_A C_{\mathbf{V}_A} &= \frac{2}{(2\pi)^2} \int_{\mathbb{R}^2} \mathbf{v} \mathcal{C}^A(\mathbf{k}) d^2\mathbf{k}, \\ \rho_A C_{W_A} &= \frac{2}{(2\pi)^2} \int_{\mathbb{R}^2} \varepsilon \mathcal{C}^A(\mathbf{k}) d^2\mathbf{k}, \\ \rho_A C_{\mathbf{S}_A} &= \frac{2}{(2\pi)^2} \int_{\mathbb{R}^2} \varepsilon \mathbf{v} \mathcal{C}^A(\mathbf{k}) d^2\mathbf{k}, \\ \rho_A \begin{pmatrix} \mathbf{F}_A^{(0)} \\ \mathbf{F}_A^{(1)} \end{pmatrix} &= \frac{2}{(2\pi)^2} \int_{\mathbb{R}^2} \begin{pmatrix} 1 \\ \varepsilon \end{pmatrix} \mathbf{v} \otimes \mathbf{v} f_A(\mathbf{r}, \mathbf{k}, t) d^2\mathbf{k}, \\ \rho_A \begin{pmatrix} \mathbf{G}_A^{(0)} \\ \mathbf{G}_A^{(1)} \end{pmatrix} &= \frac{2}{\hbar (2\pi)^2} \int_{\mathbb{R}^2} f_A(\mathbf{r}, \mathbf{k}, t) \nabla_{\mathbf{k}} \begin{pmatrix} \mathbf{v} \\ \varepsilon \mathbf{v} \end{pmatrix} d^2\mathbf{k}, \end{aligned}$$

that must be expressed as functions of the basic variables ρ_A , \mathbf{V}_A , W_A , \mathbf{S}_A (closure problem). A similar question arises for the average phonon quantities.

3 Closure relations

A well theoretically motivated way to get the desired closure relations is to resort to the maximum entropy principle [3] for estimating the distributions f^e, f^h, f^{ph} of electrons, holes and phonons. The details will be given in the complete paper. Here we present some preliminary results with phonons at thermal equilibrium at the temperature T_L of the lattice. The typical saturation and overshoot phenomena are captured as shown in Fig. 1 where the average electron velocity is shown in the case of a doping density of 10^{12} cm^{-2} and electric fields of 1kV/cm, 5 kV/cm, 10 kV/cm, 20 kV/cm.

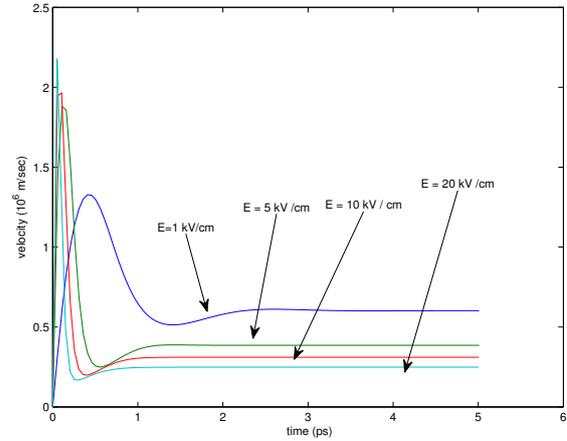


Fig. 1. Average electron velocity in the case of a doping density of 10^{12} cm^{-2} and electric fields of 1kV/cm, 5 kV/cm, 10 kV/cm, 20 kV/cm .

References

1. T. Fang, A. Konar, H. Xing and D. Jena. High-field transport in two-dimensional graphene. *Phys. Rev. B*, 84: 125450, 2011.
2. P. Lichtenberger, O. Morandi, and F. Schürerer. *Physical Review B* 84: 045406, 2011.
3. E. T. Jaynes. *Phys. Rev. B* 106: 620–630, 1957.
4. A. H. Castro Neto, F. Guinea, N. M. R. Peres, K. S. Novoselov, A. K. Geim, *Rev. of Mod. Phys.*, 81(2009) 109.
5. S. Piscanec, M. Lazzeri, J. Robertson, A. C. Ferrari and F. Mauri. *Phys. Rev. B* 75: 035427, 2007.
6. A. Tomadin, D. Brida, G. Cerullo, A. C. Ferrari, and M. Polini. *Phys. Rev. B* 88: 035430, 2013.

Analysis of Contraction-Conditions Combined with Uncertainty Quantification in Co-Simulation for Coupled Electrical Circuits

Kai Gausling and Andreas Bartel

Bergische Universität Wuppertal, Applied Mathematics and Numerical Analysis
gausling@math.uni-wuppertal.de, bartel@math.uni-wuppertal.de

Summary. Co-simulation is an important approach for coupled systems in time domain analysis. Applied to coupled differential algebraic equations, convergence can only be guaranteed if certain contraction properties are given. This paper takes a closer look at the coupling structure of electrical circuits where no contraction would be inferred (via the known theory). By a detailed analysis, we can prove convergence for certain examples. Furthermore we investigate an example of co-simulation with uncertain parameters using uncertainty quantification.

1 Introduction

If the monolithic description of a complex system is not realisable and/or suitable software tools for the subsystems are available, then co-simulation is relevant choice. In the case of coupled ordinary differential equations (ODEs), convergence of the co-simulation can be achieved always. But the situation is different for coupled differential algebraic equations (DAEs). Here convergence can only be guaranteed if certain contraction properties are fulfilled. Then convergence means that in an iteration process the distance to the analytic solution eventually decreases to zero. Thus the subsystems are solved multiple times. In our simulations, the data transfer between the subsystems is realised by a so-called Gauß-Seidel type of iteration scheme. Furthermore, in co-simulation applications it matters in which sequence these subsystems are solved (see e.g. [1]).

2 DAE-DAE Coupling

We assume that we are able to split our whole system into r subsystems. Then the i -th subsystem is given by an initial value problem of differential algebraic equations (for $i = 1, \dots, r$)

$$\begin{aligned} \dot{\mathbf{y}}_i &= \mathbf{f}_i(\mathbf{y}, \mathbf{z}), \quad \mathbf{y}_i(0) = \mathbf{y}_{i,0}, \quad \text{with } \mathbf{y}^T = [\mathbf{y}_1^T, \dots, \mathbf{y}_r^T], \\ 0 &= \mathbf{g}_i(\mathbf{y}, \mathbf{z}), \quad \text{with } \mathbf{z}^T = [\mathbf{z}_1^T, \dots, \mathbf{z}_r^T], \end{aligned} \quad (1)$$

for the unknowns $[\mathbf{y}^T, \mathbf{z}^T]$. All subsystems must fulfill the index-1 assumption, i.e., we require that the Jacobian $\partial \mathbf{g}_i / \partial \mathbf{z}_i$ is not singular. Furthermore the overall system shall be of index-1, such that we have the global the differential part $\mathbf{f}^T = [\mathbf{f}_1^T, \dots, \mathbf{f}_r^T]$ and algebraic part $\mathbf{g}^T = [\mathbf{g}_1^T, \dots, \mathbf{g}_r^T]$. Using splitting functions \mathbf{G}, \mathbf{F} , the co-simulation scheme is encoded. For

further details see [3, 4]. To analyse the iteration, we start from two waveforms $\mathbf{X}, \tilde{\mathbf{X}}$ on the n th time window $[t_n, t_{n+1}]$ and perform k iterations. The difference is measured by $\Delta_n^{(k)}(t) := \mathbf{X}_n^{(k)}(t) - \tilde{\mathbf{X}}_n^{(k)}(t)$, $\delta_n^{(k)} := \|\Delta_n^{(k)}\|_{2,\infty}$. Then, the standard recursion estimation for contraction reads (see [2])

$$\begin{bmatrix} \delta_{\mathbf{y},n}^{(k)} \\ \delta_{\mathbf{z},n}^{(k)} \end{bmatrix} \leq \mathbf{K} \begin{bmatrix} \delta_{\mathbf{y},n}^{(k-1)} \\ \delta_{\mathbf{z},n}^{(k-1)} \end{bmatrix} := \begin{bmatrix} CH_n & CH_n \\ C & CH_n + \alpha_n \end{bmatrix} \begin{bmatrix} \delta_{\mathbf{y},n}^{(k-1)} \\ \delta_{\mathbf{z},n}^{(k-1)} \end{bmatrix}, \quad (2)$$

with $\alpha_n := (1 + Cd) \|\mathbf{G}_{\mathbf{z}^{(k)}}^{-1} \mathbf{G}_{\mathbf{z}^{(k-1)}}\|_{2,\infty} + Cd$ ($C > 1$, $d > 0$) and $\mathbf{G}_{\mathbf{z}^{(k)}}, \mathbf{G}_{\mathbf{z}^{(k-1)}}$ denote partials Jacobians of \mathbf{G} . A sufficient condition for contraction of (2) (i.e., spectral radius $\rho(\mathbf{K}) < 1$) is $\|\mathbf{G}_{\mathbf{z}^{(k)}}^{-1} \mathbf{G}_{\mathbf{z}^{(k-1)}}\| < 1$ (see [1, 2]). Hence it matters whether there are old algebraic constraints depends on old algebraic iterates. The objective should be to design the coupling interface in such a way to keep the contraction factor α_n as small as possible.

3 Information Loss During Lumping

Let $\mathbf{K}_e \in \mathbb{R}^{n_y + n_z \times n_y + n_z}$ denote the fine structure, exact recursion matrix:

$$\begin{bmatrix} \Delta_{\mathbf{y},n}^{(k)} \\ \Delta_{\mathbf{z},n}^{(k)} \end{bmatrix} = \mathbf{K}_e \begin{bmatrix} \Delta_{\mathbf{y},n}^{(k-1)} \\ \Delta_{\mathbf{z},n}^{(k-1)} \end{bmatrix} := \begin{bmatrix} \mathcal{A} & \mathcal{B} \\ \mathcal{C} & \mathcal{D} \end{bmatrix} \begin{bmatrix} \Delta_{\mathbf{y},n}^{(k-1)} \\ \Delta_{\mathbf{z},n}^{(k-1)} \end{bmatrix}. \quad (3)$$

Applying the maximum norm of each submatrix, we obtain an estimation where the information on contraction may be disappeared, i.e., $\rho(\mathbf{K}_e) < 1$ is transformed into $\rho(\mathbf{K}) \geq 1$. In the general case, e.g. of nonlinear networks, the calculation of the explicit recursion matrix will not be a very easy task. Therefore an important question to be answered is, whether we can derive information about stability and contraction directly from the network structure.

We partition a 2-Level RLC-Circuit into two subsystems ($r = 2$), see Fig. 1. For the co-simulation interface we apply source coupling, which implies that we use an voltage source and current source to couple these two systems. Both systems fulfill the index-1 assumption. The Gauss-Seidel-type iteration scheme is applied to (1) with constant extrapolation for the initial guess. Explicit calculation of the contraction condition gives for the two settings:

$$\text{Sub.1 first: } \|\mathbf{G}_{\mathbf{z}^{(k)}}^{-1} \mathbf{G}_{\mathbf{z}^{(k-1)}}\|_2 = R_2 \cdot \sqrt{2} \quad (R_2 > 0), \quad (4a)$$

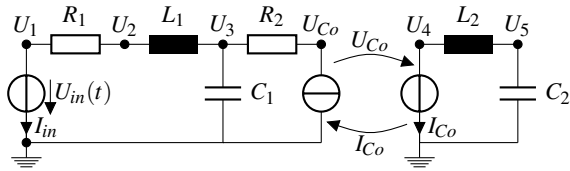


Fig. 1. 2-Level RLC co-simulation model. For the network components, we choose: $R_1 = R_2 = 10\text{k}\Omega$, $L_1 = L_2 = 1\text{mH}$, $C_1 = C_2 = 1\text{nF}$, $U_{in}(t) = 1\text{V}\cos(2\pi \cdot 5\text{kHz} \cdot t)$. Left subsystem 1, right subsystem 2.

$$\text{Sub.2 first: } \|\mathbf{G}_{z^{(k)}}^{-1} \mathbf{G}_{z^{(k-1)}}\|_2 = 1. \quad (4b)$$

Convergence rate and contraction of the 2-Level RLC co-simulation model is shown in Fig. 2. Notice that

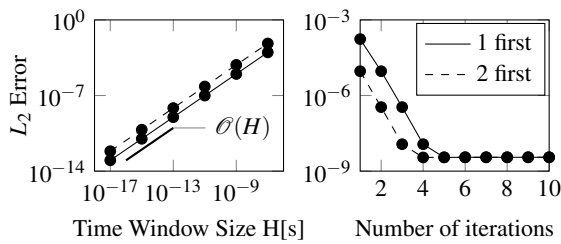


Fig. 2. (Left) Convergence of the 2-Level RLC-Circuit co-simulation model for different time step sizes H with one iteration per time window after $t_0 = 0.4$ ms. (Right) Error of the network components in dependence of the iteration steps k on the time window $[t_0, t_0 + H]$, $H = 0.1$ ms.

in both cases (4a) for $R \gg 1$ and (4b) the contraction condition is not fulfilled. In contrast, for both cases we find window sizes $H < H_{\max}$ where the error decrease for increasing iteration k . Using (3) we can prove convergence for this network.

4 Uncertainty Quantification Combined with Co-simulation

Another very important field concerns the parameter uncertainty in applications. In practice components will have variations around a nominal values, which could change the circuit properties. Uncertainty quantification tries to determine how likely certain outcomes are if some aspects of the system are not exactly known.

We define the resistors R_1 , R_2 from Fig. 1 with nominal value $\langle R_i \rangle$ with a variation of 10% ($\delta R_i = 0.1$):

$$R_i = \langle R_i \rangle \cdot (1 + \delta R_i \cdot Z), \quad (5)$$

where Z is a uniformly distributed random variable on $[-1, 1]$. To determine evolution of uncertainty, generalized polynomial chaos (gPC) method is used. The sensitivity of R_2 for different iteration steps k is shown in Fig. 3. It becomes apparent that we get good approach of the sensitivity already for a small number of iteration steps k .

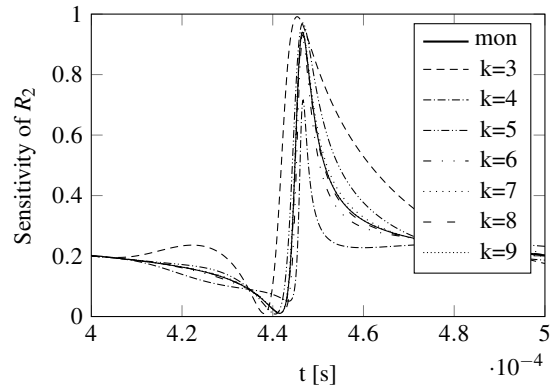


Fig. 3. Sensitivity of the resistor R_2 after $t_0 = 0.4$ ms on one time window $[t_0, t_0 + H]$, $H = 0.1$ ms for different iteration steps $k = 3, \dots, 9$ in comparison with the monolithic solution.

5 Conclusions

Formulating the explicit recursion matrix, we demonstrated stability and contraction cannot be always detected by using the standard theory of co-simulation. It is a future aim to investigate stability and contraction derived directly from the network structure.

Additionally we started combining uncertainty quantification with co-simulation and will analyse the influence on the contraction properties.

References

1. Arnold, M., Günther, M.: *Preconditioned Dynamic Iteration for Coupled Differential-Algebraic Systems*. In: BIT, vol. 41, pp. 1–25 (2001)
2. Bartel, A., Brunk, M., Günther, M. and Schöps, S.: *Dynamic Iteration for Coupled Problems of Electric Circuits and Distributed Devices*. SIAM J. Sci. Comput., vol. 35, No. 2, pp. B315–B335 (2013).
3. Bartel, A., Brunk, M., Schöps, S.: *On the convergence rate of dynamic iteration for coupled problems with multiple subsystems*. J. Comput. Appl. Math., vol. 262, pp. 14–24 (2014)
4. Schöps, S.: *Multiscale Modeling and Multirate Time-integration of Field/circuit Coupled Problems*. Ph.D. thesis, Bergische Universität Wuppertal (2011)

Graphene nano-device design from first principles calculations

Ioannis Deretzis¹, Gaetano Calogero², Giuseppe G.N. Angilella², and Antonino La Magna¹

¹ CNR Istituto per la Microelettronica e Microsistemi, Z.I. VIII Strada 5 I 95121 Catania Italy

² Department of Physics, Università degli studi di Catania, via. S. Sofia 54, I 95100 Catania Italy
antonino.lamagna@imm.cnr.it

Summary. The correlation between the electronic structure and electronic transport properties of doped and defected graphene systems in the quantum coherent regime is presented and discussed. The calibration of effective Hamiltonians using *ab initio* methods and transport calculations based on the Non-Equilibrium Green Function formalism allow for the accurate simulation of the device features in realistic configurations.

1 Introduction

The continuous development of the nano-electronics is ruled by the scaling law of the critical sizes of active device regions. Although the length of the CMOS's channel L_{ch} is the most cited parameter, its width W_{ch} and height H_{ch} also follow this aggressive scaling. In particular, when L_{ch} will achieve the deep *sub-10nm* range, channels with H_{ch} in atomic range have to be fabricated. In this sense, the use of two dimensional 2D materials is imposed by the future trend of nano-electronics and the recent explosive development of graphene knowledge and technology is a lucky coincidence.

Graphene-based nano-structures expose an one-atom-thick surface and as a consequence their properties are deeply subjected to the interaction with the surrounding environment. This interaction is bound to induce various levels of disorder in these materials giving rise to important alterations in their conductance characteristics. The theoretical understanding of disorder on the conductance features of these systems and in general the study of coherent transport represents a fundamental background for the development of graphene-based nano-electronics. Moreover, the transport study in this case is tightly related to electronic structure calculations starting from the correct atomic configuration of the system, since even a single atom alteration could drastically impact the transport features. This issue complements the studies on diffusive transport and it is crucial for predicting the electrical characteristics in the case of nano-device configurations: i.e. when the device length scale is lower than the characteristic lengths of inelastic interactions that give rise to a diffusive behavior or the dephasing of the electron wave functions.

Here we discuss the correlation between the electronic structure and electronic transport properties of

doped and defected graphene systems in the quantum coherent regime.

2 Methods

Without lack of generality, we consider the generalized transport problem of a two-terminal geometry. Assuming that a matrix representation of the Hamiltonian can be obtained using a suitable base. We can write the Hamiltonian of the entire system as:

$$H = \begin{pmatrix} H_L & -\tau_L & 0 \\ -\tau_L^\dagger & H_0 & -\tau_R^\dagger \\ 0 & -\tau_R & H_R \end{pmatrix} \quad (1)$$

Here, H_0 is the device Hamiltonian and $H_{L,R}$ are the bulk contact Hamiltonians, while $\tau_{L,R}$ describe the coupling between the contacts and the device. The matrix Green function \mathcal{G} can be defined by the solutions to the following equation

$$(EI - H)\mathcal{G}(E) = I \quad (2)$$

where E is the energy and I is the unitary matrix (for an orthonormal basis set). The generally infinite problem in eq. 2 can be mapped in a finite one, if we now define the *self-energies* of the two contacts as $\Sigma_L = \tau_L^\dagger g_L \tau_L$, $\Sigma_R = \tau_R^\dagger g_R \tau_R$, where $g_{L,R}$ are the Green functions of the left and right contact respectively. The problem here is the transformation of these two (∞, N) matrices into (N, N) ones. Such a procedure is feasible analytically or numerically since it takes advantage of the semi-infinite lattice symmetry of the two leads. Conceptually one can think of $\Sigma_{L,R}$ as matrices that by being added to the bare device Hamiltonian result in an effective Hamiltonian that accounts also for the exact effect of the leads. This concept is very powerful and can be extended to other types of interaction that take place in the device channel during conduction (e.g. el-ph interactions). The final version of the Green's function matrix of the device that takes also account for the interaction with the two contacts via the two self-energy terms is:

$$\mathcal{G} = (EI - H_0 - \Sigma_L - \Sigma_R)^{-1} \quad (3)$$

Using the Green function we can calculate the quantity of interest. The density matrix is:

$$\rho = \frac{1}{2\pi} \int_{-\infty}^{\infty} (f_L \mathcal{G} \Gamma_L \mathcal{G}^\dagger + f_R \mathcal{G} \Gamma_R \mathcal{G}^\dagger) dE, \quad (4)$$

where $f_{L,(R)}$ is the Fermi-Dirac function of the left (right) contact and $\Gamma = \iota(\Sigma - \Sigma^\dagger)$. The total current is

$$I = I_{inR} - I_{outR} = \frac{e}{h} \int_{-\infty}^{\infty} \text{Trace}(\Gamma_R \mathcal{G} \Gamma_L \mathcal{G}^\dagger) (f_L - f_R) dE \quad (5)$$

where the transmission probability is:

$$T(E) = \text{Trace}(\Gamma_L \mathcal{G} \Gamma_R \mathcal{G}^\dagger) \quad (6)$$

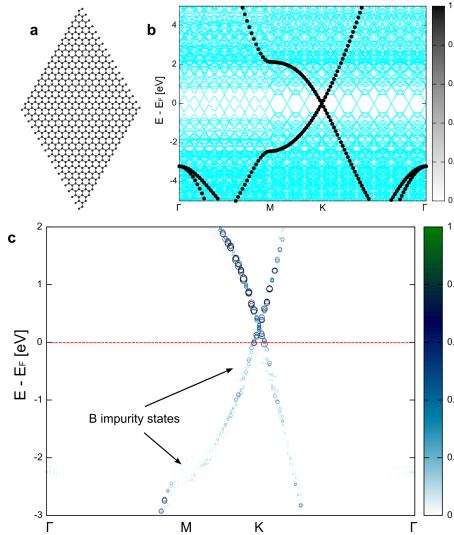


Fig. 1. (a) Structure of a 18×18 graphene supercell. (b) Folded (lines) and unfolded (points) band structure of a (18×18) graphene supercell in its primitive Brillouin zone. (c) Effective band structure obtained for C-orbital contributions for a (18×18) graphene supercell having a concentration of 0.62% of B impurities in a graphitic configuration.

3 Results

The derivation of a suitable electron Hamiltonian is the prerequisite of any coherent transport calculation. The application of a first principles approach is feasible only for very small systems. However we can use *ab initio* calculations to calibrate effective Hamiltonians in the class of the tight-binding models [1–5]. Defective systems have to be studied in super cells and unfolding procedure is necessary for the proper use of the results. Original unfolding techniques [6] are extensively applied to the calibration procedure identifying the alterations with respect to the ideal band structures and the residual graphene-character of the bands in non ideal systems (see fig. 1 for an example).

By varying both the width and the length of two-terminal devices from the nano- to the micro-scale, we study localization phenomena, the formation of pseudo-gaps, transport length scales and conductance characteristics for numerous defect/impurity concentrations (see fig. 2 for an example). When the lateral

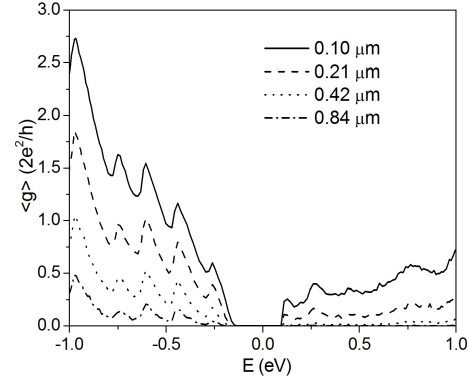


Fig. 2. Average conductance $\langle g \rangle$ as a function of the energy E , for an N-doped $N=45$ aGNR of different lengths. Plotted values represent statistical averages over more than 500 equivalent replicas of the system.

confinement is strong (i.e. in the case of graphene nanoribbons), we show that localization due to scattering is strongly energy dependent, and this fact leads to the appearance of conductance quasi-gaps in the spectral region of the resonance states. Moreover, conductance fluctuations are very large in the quasi-gap regions, indicating significant electrical disorder. We then focus on the conductance variations when gradually passing from the quasi-1D limit (graphene nanoribbons) to the 2D case (graphene). The evaluation of the weights of the phase breaking scattering processes (e.g. electron-phonon scattering) and the phase coherent interactions with defects and impurities in the transport behavior of these systems demonstrate that the latter are dominant in constrained graphene systems.

References

1. A. La Magna, I. Deretzis, G. Forte and R. Pucci. *Phys. Rev. B* 78, 153405 (2008).
2. A. La Magna, I. Deretzis, G. Forte and R. Pucci. *Phys. Rev. B* 80, 195413 (2009).
3. I. Deretzis, G. Fiori, G. Iannaccone and A. La Magna. *Phys. Rev. B* 81, 085427 (2010).
4. I. Deretzis, G. Fiori, G. Iannaccone and A. La Magna. *Phys. Rev. B* 82, 161413 (2010).
5. I. Deretzis and A. La Magna. *Eur. Phys. J. B* 81, 15 (2011).
6. I. Deretzis and A. La Magna. *Phys. Rev. B* 89, 115408 (2014).

Design Optimization of Electrical Machines Using Sensitivity-Based Topology and Shape Optimization

Peter Gangl¹ and Ulrich Langer²

¹ Doctoral Program “Computational Mathematics”, Johannes Kepler University Linz, Austria

peter.gangl@dk-compmath.jku.at,

² Institute of Computational Mathematics, Johannes Kepler University Linz, Austria

ulanger@numa.uni-linz.ac.at

Summary. We aim at finding optimal designs for electric motors. On the one hand, we use a sensitivity-based topology optimization method where material is removed at the most favorable positions. On the other hand, we use a shape optimization technique where an interface is moved along a vector field that assures a decrease of the objective functional. Coupling of topology and shape optimization leads to a powerful design tool.

1 Problem Description

When designing electrical machines it is a crucial task to determine a design that is optimal with respect to some goal. As a model problem we consider an interior permanent magnet (IPM) brushless electric motor consisting of a rotor (inner part) and a stator (outer part), which are separated by a small air gap. Both parts have an iron core, the rotor contains permanent magnets which are magnetized in the indicated directions (see Figure 1). The coil areas are on the inner part of the stator. In general, inducing current in the coils will cause the rotor to rotate due to the interaction between the electric field and the magnetic field generated by the magnets.

In our special application, we aim at minimizing the total harmonic distortion (THD) such that the resulting motor rotates as smoothly as possible. For this purpose, we are only interested in the magnetic flux density \mathbf{B} for one fixed rotor position without any current induced. The task is to find the material distribution in the design areas that drives the radial component of the magnetic flux density \mathbf{B} along a circle Γ_0 in the air gap as close as possible to a prescribed sine curve \mathbf{B}_r^d (see Figure 2). The underlying PDE (2) is the equation of 2D magnetostatics. The optimization problem looks as follows:

$$\min_{\Omega_{iron}} \mathcal{J}(u) := \|\mathbf{B}_r(u) - \mathbf{B}_r^d\|_{L^2(\Gamma_0)}^2 \quad (1)$$

$$\text{s.t.} \begin{cases} -\operatorname{div} (v(|\nabla u|)\nabla u - M^\perp) = J & \text{in } \Omega \\ u = 0 & \text{on } \partial\Omega \end{cases} \quad (2)$$

Here, the state variable u is the z -component of the vector potential of the magnetic flux density, $\mathbf{B}(u) = \operatorname{curl}((0, 0, u)^T)$. Further, $M^\perp = (-M_2, M_1)^T$ and J denote the perpendicular of the permanent magnetization and the current density, which vanish outside the

permanent magnets and the coils, respectively. Since, in our special application, we do not consider any current, we set $J = 0$. The coefficient function v represents the magnetic reluctivity which is a nonlinear function \hat{v} of the magnetic field in the presence of ferromagnetic material (e.g. iron) and a constant v_0 else,

$$v(|\nabla u|) = \chi_{\Omega_{iron}} \hat{v}(|\nabla u|) + \chi_{\Omega_{air}} v_0. \quad (3)$$

In a simplified linear setting we replace the nonlinear function \hat{v} by a constant v_1 and (2) becomes a linear PDE with the coefficient function

$$v = \chi_{\Omega_{iron}} v_1 + \chi_{\Omega_{air}} v_0. \quad (4)$$

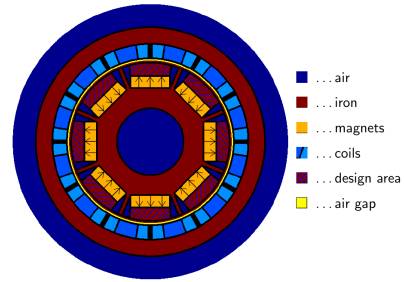


Fig. 1. Electric motor with different components

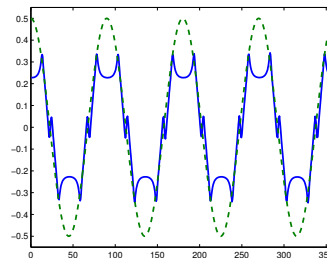


Fig. 2. Radial component of magnetic flux density \mathbf{B} along circle Γ_0 in air gap for initial design as depicted in Fig. 1 (blue curve) and desired curve \mathbf{B}_r^d (dashed green curve)

2 Topology Optimization Using Topological Sensitivities

We apply a sensitivity-based topology optimization method, the so-called ON/OFF method proposed by M. Ohtake, Y. Okamoto and N. Takahashi in 2005 [2], to problem (1) - (2) and show its connection to the mathematical concept of the topological derivative.

2.1 Topological Derivative

The topological derivative (or topological gradient) of a domain-dependent functional $\mathcal{J} = \mathcal{J}(\Omega)$ is the sensitivity of \mathcal{J} with respect to the introduction of a small hole $\omega_\varepsilon = x_0 + \varepsilon D$ of radius ε around a point x_0 in the domain. Here, D is a fixed bounded domain containing the origin with connected and piecewise C^1 boundary and specifies the shape of the perturbation (e.g. unit disk). Denoting the original domain by Ω and the perturbed domain by $\Omega_\varepsilon = \Omega \setminus \overline{\omega_\varepsilon}$, the topological derivative of \mathcal{J} at a spatial point x_0 is defined as the quantity $G(x_0)$ satisfying the topological asymptotic expansion

$$\mathcal{J}(\Omega_\varepsilon) - \mathcal{J}(\Omega) = f(\varepsilon) G(x_0) + o(f(\varepsilon))$$

for some positive function f with $\lim_{\varepsilon \rightarrow 0} f(\varepsilon) [1]$.

We derive the topological derivative for problem (1) - (2) under the simplifying assumption of a linear state equation (4).

2.2 ON/OFF Method

The ON/OFF method was designed for the optimization of electrical machines. It searches for the optimal distribution of iron and air in a design area. The method is based on the fact that the difference between iron and air is only reflected in the magnetic reluctivity ν in (2) which is a constant $\nu = \nu_0$ in the air subdomain and a nonlinear function $\hat{\nu}$ in the iron subdomain, see (3), where the values attained in the iron are much smaller compared to the reluctivity of air, $\hat{\nu}(|\nabla u|) \ll \nu_0$. After discretization of the computational domain, the method uses information on the sensitivity of the objective functional \mathcal{J} with respect to a local perturbation of the magnetic reluctivity in every single element of the mesh in the design area. If this sensitivity,

$$\frac{d\mathcal{J}}{d\nu_k}, \quad (5)$$

in element k is negative then increasing the magnetic reluctivity in the element would lead to a decrease of the objective function. This is realized by setting the element to air (OFF) as $\hat{\nu}(|\nabla u|) \ll \nu_0$. On the other hand, if the sensitivity is positive then a smaller reluctivity value is favorable which is realized by switching the element to iron (ON).

We compute the sensitivities (5) and show the connection to the topological derivative in the case of

a linear state equation. The generalization of (5) to the case of a nonlinear state equation is straightforward whereas the computation of the topological derivative for that case is an open problem. We show numerical results obtained by applying the following algorithm to problem (1) - (2) with the nonlinear material coefficient (3).

Algorithm (ON/OFF method):

Initialize all elements in design area with iron

While not converged **do**

- Solve (2) for u
- Compute sensitivities (5) for each element in design area
- Determine element with most negative sensitivity and introduce hole of certain radius around it

3 Shape Optimization

We address the optimization problem (1) - (2) by shape optimization where the interface between the iron and air subdomain in the design area is moved in such a way that the objective functional decreases.

Velocity Method

In the velocity method for shape optimization, one computes a vector field \mathbf{V} in such a way that moving the geometry along \mathbf{V} results in a decrease of the objective functional. For a vector field \mathbf{V} and a real number $t \geq 0$ let $\Omega_t = \Omega + t\mathbf{V}$.

Definition 1. *The Eulerian semi-derivative (or shape derivative) of a domain-dependent functional \mathcal{J} in direction of a smooth vector field \mathbf{V} is defined as*

$$d\mathcal{J}(\Omega; \mathbf{V}) := \lim_{t \rightarrow 0} \frac{\mathcal{J}(\Omega_t) - \mathcal{J}(\Omega)}{t}.$$

A common procedure to find a descent direction \mathbf{V} is to define a positive definite bilinear form $b(\cdot, \cdot)$ and to compute \mathbf{V} as the solution to a variational problem

$$b(\mathbf{V}, \mathbf{W}) = -d\mathcal{J}(\Omega; \mathbf{W}) \quad \forall \mathbf{W}$$

with properly chosen spaces for \mathbf{V} and \mathbf{W} . We compute the Eulerian semi-derivative for problem (1) - (2) and show numerical results.

References

1. S. Amstutz. Sensitivity analysis with respect to a local perturbation of the material property *Asymptot. Anal.*, 49:87–108, 2006.
2. M. Ohtake, Y. Okamoto, N. Takahashi. Magnetic shield design of perpendicular magnetic recording head by using topology optimization technique. *IEEE Trans. Magn.*, 41(5):1788–1791, 2005.

Some results on the two-temperature energy-transport model for semiconductors

Giuseppe Ali^{1,2} and Vittorio Romano³

¹ Università della Calabria, via Pietro Bucci, 30/B 87036 - Arcavacata di Rende (CS) Italy
giuseppe.ali@unical.it,

² INFN-Gruppo c. Cosenza, Arcavacata di Rende (Cosenza), Italy

³ Università degli Studi di Catania, viale Andrea Doria, 6 95125 - Catania Italy romano@dmi.unict.it

Summary. We consider a two-temperature energy-transport model for semiconductors, with electron temperature and lattice temperature as independent variables. For the steady-state case, we prove an existence and uniqueness result.

1 Introduction

The energy-transport model for semiconductors was first introduced by Stratton [1], in 1962. The first mathematical results had to wait 35 years after the presentation of the model, and are due to Degond, Génieys and Jüngel [2, 3]. They consider a general parabolic-elliptic system, arising in irreversible thermodynamics with thermal and electrical effects, which includes as a special case the energy-transport model. This general model is studied in a bounded multidimensional domain, with physics-based mixed Dirichlet-Neumann boundary conditions, under the restrictive hypothesis of uniform parabolicity and existence of a strictly positive energy.

A few years later, Chen, Hsiao and Li consider the same model, with unphysical no-flow boundary conditions, proving a stability theorem for small initial perturbations, without the last two restrictive assumptions [4].

An improvement on this result is due to Nishibata and Suzuki, who in a recent publication [5], for a one-dimensional energy-transport model, are able to prove existence and uniqueness, under physical boundary conditions, without assuming uniform parabolicity and existence of a strictly positive energy.

In this work we extend Nishibata and Suzuki's results to a two-energy energy-transport model for semiconductor. The inclusion of the lattice temperature as an additional unknown is demanded for an accurate description of heat effects in semiconductors.

2 Main result

We consider an energy-transport model for semiconductors for the following unknowns: the electron number density n , the electron temperature T , the lattice temperature θ , and the electric potential ϕ . In the steady-state one-dimensional case, after scaling, the system can be written as follows:

$$J_x = 0, \quad (1)$$

$$J = n\phi_x - (nT)_x, \quad (2)$$

$$\left(\frac{5}{2}TJ - \kappa T_x\right)_x = J\phi_x - \frac{3}{2\tau}n(T - \theta), \quad (3)$$

$$(-\kappa_L\theta_x)_x = \frac{3}{2\tau}n(T - \theta) - \frac{1}{\tau_L}(\theta - 1), \quad (4)$$

$$\phi_{xx} = n - D, \quad (5)$$

with $x \in (0, 1)$. Here, J is the current density, κ and κ_L the electron and phonon thermal conductivities, respectively, τ and τ_L the electron and phonon energy relaxation times, $D(x)$ the doping profile. We assume the following physics-based boundary conditions:

$$n(0) = n_l, \quad n(1) = n_r, \quad (6)$$

$$T(0) = \theta(0), \quad T(1) = \theta(1), \quad (7)$$

$$\kappa_L\theta_x(0) = \frac{1}{R}(\theta(0) - 1),$$

$$-\kappa_L\theta_x(1) = \frac{1}{R}(\theta(1) - 1), \quad (8)$$

$$\phi(0) = 0, \quad \phi(1) = \phi_r. \quad (9)$$

For the above problem we establish a first existence and uniqueness result, under the assumption of smallness of the relaxation times τ , τ_L , and of the parameter $\delta := |n_r - n_l| + |\phi_r|$, related to the boundary conditions.

References

1. R. Stratton. Diffusion of hot and cold electrons in semiconductor barriers. *Phys. Rev.*, 126, 1962.
2. P. Degond, S. Génieys, and A. Jüngel. A system of parabolic equations in nonequilibrium thermodynamics including thermal and electrical effects. *Journal de Mathématiques Pures et Appliquées*, 76:991–1015, 1997.
3. P. Degond, S. Génieys, and A. Jüngel. A steady-state system in non-equilibrium thermodynamics including thermal and electrical effects. *Mathematical Methods in the Applied Sciences*, 21:1399–1413, 1998.
4. L. Chen, L. Hsiao, and Y. Li. Large time behavior and energy relaxation time limit of the solutions to an energy transport model in semiconductors. *Journal of Mathematical Analysis and Applications*, 312:596–619, 2005.

5. S. Nishibata, and M. Suzuki. *Hierarchy of semiconductor equations: relaxation limits with initial layers for large initial data*. *Mathematical Society of Japan Memoirs: Volume 26*. World Scientific, 2011.

Global Solvability of Nonlinear Parabolic PDAEs: A Coupled Systems Approach and its Application to Circuit Simulation

Lennart Jansen¹ and Michael Matthes

Humboldt-University of Berlin, Rudower Chaussee 25 lejansen@math.hu-berlin.de

Summary. Applications like electrical circuits including electromagnetic devices, semiconductor devices or thermal elements give rise to a mix of PDEs and DAEs. Such a mix is called a partial differential-algebraic equation (PDAE). We investigate a prototype for nonlinear parabolic coupled PDAE systems. The objective is to prove the global existence and uniqueness of a solution for this prototype class. Regarding the applications we consider the simulation of electric circuits including thermal resistors.

1 Introduction

Numerous mathematical models in science and engineering give rise to systems comprising partial differential equations (PDEs) and differential-algebraic equations (DAEs). These systems are called partial differential-algebraic equations (PDAEs) and occur frequently in application areas such as electric circuit simulation, flexible multibody systems, gas or water distribution network simulation or chemical engineering, see [1–3]. In literature the research is mainly focused on the space-discretized system while we investigate the non-discretized system. We will use the term abstract differential-algebraic equation (ADAE) for the non-discretized system. The definition and determination of indexes for linear ADAEs has received attention in recent literature, see [2–6]. ADAEs are also treated with respect to existence under the term degenerate differential equations mainly for the linear case, see [7], but also for certain classes of nonlinear ADAEs, see [8, 9]. However, the theoretical treatment of nonlinear ADAEs and their numerical treatment is still at an initial stage. We are interested in a systematic treatment of nonlinear ADAEs. We formulate a parabolic prototype of an ADAE and address the following questions.

What conditions must be met for an ADAE to be globally solvable? When is the solution unique and which applications fulfill these conditions?

2 A Parabolic Prototype

We consider the following parabolic prototype of a coupled system. Let $\mathcal{I} := [t_0, T]$ be an interval and $V \subseteq H \subseteq V^*$ be an evolution triple. Consider the sys-

$$m'(x(t), t) + f(x(t), y(t), u(t), t) = 0, \quad (1a)$$

$$g(x(t), y(t), t) = 0, \quad (1b)$$

$$u'(t) + \mathcal{B}(u(t)) + \mathcal{R}(u(t), x(t), y(t), t) = 0, \quad (1c)$$

$$x(t_0) = x_0, \quad u(t_0) = u_0 \quad (1d)$$

with functions $m : \mathbb{R}^{n_x} \times \mathcal{I} \rightarrow \mathbb{R}^{n_x}$, $f : \mathbb{R}^{n_x+n_y} \times H \times \mathcal{I} \rightarrow \mathbb{R}^{n_x}$, $g : \mathbb{R}^{n_x+n_y} \times \mathcal{I} \rightarrow \mathbb{R}^{n_y}$ and operators $\mathcal{B} : V \rightarrow V^*$ and $\mathcal{R} : V \times \mathbb{R}^{n_x+n_y} \times \mathcal{I} \rightarrow V^*$. The unknowns are $x(t) \in \mathbb{R}^{n_x}$, $y(t) \in \mathbb{R}^{n_y}$ and $u(t) \in V$ for $t \in \mathcal{I}$. We also use the convention to write $z(t) = (x(t), y(t))$, $n_z = n_x + n_y$. The initial values $x_0 \in \mathbb{R}^{n_x}$ and $u_0 \in H$ are given. Note that equations (1a), (1b) represent a semi-linear (finite dimensional) DAE with a non-linear derivative-term whereas (1c) is an (infinite dimensional) evolution equation involving a generalized derivative where a solution u will be in the space

$$W_2^1(\mathcal{I}; V, H) = \{u \in L_2(\mathcal{I}, V) \mid u' \in L_2(\mathcal{I}, V^*)\}.$$

$L_2(\mathcal{I}, V)$ is the space of square integrable functions on \mathcal{I} with values in the Banach space V . The coupling of these two systems is realized by letting f depend on u and \mathcal{R} depend on z .

3 Global Solvability and Uniqueness

We will investigate (1) regarding its global unique solvability. First we assemble the following assumptions.

Assumption 1

Let the following assumptions hold for system (1):

1. $m \in C^1(\mathbb{R}^{n_x} \times \mathcal{I} \rightarrow \mathbb{R}^{n_x})$ is strongly monotone w.r.t. $x \in \mathbb{R}^{n_x}$.
2. $f \in C(\mathbb{R}^{n_z} \times H \times \mathcal{I}, \mathbb{R}^{n_x})$ is Lipschitz continuous w.r.t. z and u .
3. $g \in C(\mathbb{R}^{n_z} \times \mathcal{I}, \mathbb{R}^{n_y})$ is strongly monotone w.r.t. $y \in \mathbb{R}^{n_y}$ and Lipschitz continuous w.r.t. x .
4. $\mathcal{B} : V \rightarrow V^*$ is Lipschitz continuous and strongly monotone.
5. $\mathcal{R} \in C(V \times \mathbb{R}^{n_z} \times \mathcal{I}, V^*)$ is monotone w.r.t. u and Lipschitz continuous w.r.t. z . Furthermore there are $c_{\mathcal{R},1}, c_{\mathcal{R},2} > 0$ such that

$$\|\mathcal{R}(u, 0, t)\|_{V^*} \leq c_{\mathcal{R},1} \|u\|_V + c_{\mathcal{R},2} \quad \forall u \in V.$$

Here we call a map $f : V \times M \rightarrow W$ Lipschitz continuous on V if there is $L > 0$ such that

$$\|f(v, z) - f(\bar{v}, z)\|_W \leq L \|v - \bar{v}\|_V$$

for all $v, \bar{v} \in V, z \in M$ with $M \subseteq X$ being a subset of the Banach space X . Furthermore we say that f is strongly monotone on V if $W = V^*$ and if there is $\mu > 0$ such that

$$\langle f(v, z) - f(\bar{v}, z), v - \bar{v} \rangle_V \geq \mu \|v - \bar{v}\|_V^2$$

for all $v, \bar{v} \in V, z \in M$. If $\mu = 0$ we call f monotone on V . Note here that L and μ do not depend on $z \in M$. With the help of Assumption 1 we are able to formulate the following theorem.

Theorem 2. *Let Assumption 1 be fulfilled. Then (1) has a unique solution $(z, u) \in C(\mathcal{I}, \mathbb{R}^{n_z} \times H)$ with $x \in C^1(\mathcal{I}, \mathbb{R}^{n_x})$ and $u \in W_2^1(\mathcal{I}; V, H)$.*

We prove the global unique solvability as follows. First, we show the uniqueness of a possible solution to (1). Then we prove a priori estimates for the Galerkin solutions and prove the unique solvability of the Galerkin equations which are given as follows:

$$m'(x_n(t), t) + f(x_n(t), y_n(t), u_n(t), t) = 0, \quad (2a)$$

$$g(x_n(t), y_n(t), t) = 0, \quad (2b)$$

$$\langle u_n'(t), v_i \rangle_V + \langle \mathcal{B}(u_n(t)), v_i \rangle_V + \langle \mathcal{R}(u_n(t), x_n(t), y_n(t), t), v_i \rangle_V = 0, \quad (2c)$$

$$x_n(t_0) = x_0, \quad u_n(t_0) = u_{n0}, \quad (2d)$$

for $i = 1, \dots, n$. The operator equation (2c) is formulated on the finite dimensional subspace $V_n \subseteq V$. So $u_n(t)$ is in V_n which also influences the finite dimensional variable z through the coupling. Hence $z_n = (x_n, y_n)$, too, depends on the Galerkin step n . Finally, we will be able to prove the convergence of the Galerkin solutions and thereby we prove the solvability of (1) by showing that the limit of the Galerkin solutions is the solution of (1).

4 Application to Circuit Simulation

In the classical formulation of the Modified Nodal Analysis equations, cf. [10], heating effects of certain circuit elements are not included. Nevertheless it is well known that resistors, for example, may depend significantly on their temperature. Due to miniaturization in chip design heating effects become ever more important. Accordingly, the influence of heating effects on the circuit's behavior has to be simulated as well. In [11] a first coupled thermal-electric model was described which adds thermal effects to the circuit by means of an additional 1D heat equation. Furthermore, comprehensive information on various heating models for resistors and diodes is given. This approach has been extended to coupled systems involving semiconductors, cf. [12], and 2D/3D heat diffusion effects, cf. [13].

We consider electric circuits including standard elements like capacitors, resistors, inductors and independent sources and also thermally active resistors. For the resulting system we prove the global unique solvability by transforming it into the form of the prototype (1) and applying Theorem 2.

Acknowledgement. The Deutsche Forschungsgemeinschaft supported the authors through the Project "Numerische Analysis Abstrakter Differential-Algebraischer Gleichungen". The authors thank C. Tischendorf for setting the project up.

References

1. B. Simeon. Numerische Simulation gekoppelter Systeme von partiellen und differential-algebraischen Gleichungen in der Mehrkörperdynamik. *AVDI-Verlag, Düsseldorf, Habilitation.*, 2000.
2. C. Tischendorf. Coupled Systems of Differential Algebraic and Partial Differential Equations in Circuit and Device Simulation. *Humboldt University Berlin, Habilitation.*, 2004.
3. S.L. Campbell and W. Marszalek. The index of an infinite dimensional implicit system. *Mathematical and Computer Modelling of Dynamical Systems.*, 5:18–42, 1996.
4. T. Reis. Systems Theoretic Aspects of PDAEs and Applications to Electrical Circuits. *Technische Universität Kaiserslautern, Dissertation.*, 2006.
5. W. Lucht and K. Strehmel and C. Eichler-Liebenow. Indexes and Special Discretization Methods for Linear Partial Differential Algebraic Equations. *BIT Numerical Mathematics.*, 39:484–512, 1999.
6. R. Lamour and R. März and C. Tischendorf. PDAEs and Further Mixed Systems as Abstract Differential Algebraic Systems. *Humboldt University Berlin, Preprint.*, 2001.
7. A. Favini and A. Yagi. Degenerate differential equations in Banach spaces. *Marcel Dekker, New York.*, 1999.
8. A. Favini and A.G. Rutkas. Existence and uniqueness of solutions of some abstract degenerate nonlinear equations. *Differential and Integral Equations.*, 12:373–394, 1999.
9. A.G. Rutkas and I.G. Khudoshin. Global solvability of one degenerate semilinear differential operator equation. *Nonlinear Oscillations.*, 7:403–417, 2004.
10. C.A. Desoer and E.S. Kuh. Basic Circuit Theory. *International student edition, McGraw-Hill.*, 1984.
11. A. Bartel. Partial Differential-Algebraic Models in Chip Design - Thermal and Semiconductor Problems. *Fortschritt-Berichte VDI.*, 2004.
12. M. Brunk and A. Jüngel. Self-heating in a coupled thermo-electric circuit-device model. *Journal of Computational Electronics.*, 10:163–178, 2011.
13. M. Culpo. Numerical Algorithms for System Level Electro-Thermal Simulation. *Bergische Universität Wuppertal, Dissertation.*, 2009.

Uncertainty Analysis in Transcranial Magnetic Stimulation Using Non-intrusive Polynomial Chaos Expansion

Konstantin Porzig¹, Luca Di Rienzo², Hartmut Brauer¹, and Jens Haueisen³

¹ Department of Advanced Electromagnetics, Technische Universitaet Ilmenau, 98693 Ilmenau, Germany
konstantin.porzig@tu-ilmenau.de, hartmut.brauer@tu-ilmenau.de

² Dipartimento di Elettronica, Informazione e Bioingegneria, Politecnico di Milano, 20133 Milan, Italy
luca.dirienzo@polimi.it

³ Institute of Biomedical Engineering and Informatics, Technische Universitaet Ilmenau, 98693 Ilmenau, Germany
jens.haueisen@tu-ilmenau.de

Summary. We investigate the influence of the uncertainty in the knowledge of the electrical conductivity of biological tissues on the induced electric field during transcranial magnetic stimulation. Three different tissues, namely cerebrospinal fluid, grey matter, and white matter, are modeled as random variables. The investigations were performed on a simplified model of a cortical sulcus. The results quantify the major influence of uncertainty in TMS.

1 Introduction

Transcranial magnetic stimulation (TMS) is a non-invasive technique to stimulate cortical regions of the human brain by the principle of electromagnetic induction [1]. In biphasic stimulation, a time changing current with sinusoidal waveform is driven through an excitation coil. As a consequence, an electric field is induced inside the human brain due to Faraday's law. Due to the complex geometry of the human brain, numerical techniques such as the finite element method (FEM) have to be applied in order to compute the spatial distribution of the induced electric field [2]. However, this implies the exact knowledge of the corresponding electrical conductivity. That is almost not possible due to the difficulty of obtaining accurate data measured *in vivo* as well as due to the variability between subjects. Hence, available data shows a wide spread and exact predictions seem to be impossible. For that reason, an analysis regarding the uncertainty of the induced electric field in TMS appears imperative. Sampling methods such as Monte Carlo approaches (MC) are not applicable due to their disadvantage of slow convergence and the need of a high amount of sampling points ($10^4 - 10^6$). For that reason, we propose to apply a generalized polynomial chaos expansion (gPC) based on spectral projection.

2 Deterministic FEM model

A simplified FEM model of a cortical sulcus, similar to the one in [6], is adopted. A commercial figure-of-8 coil¹ acts as excitation coil, assuming a cur-

¹ 2nd Generation Double 70mm - 3191-00 (Magstim Company Ltd, Whitland, United Kingdom)

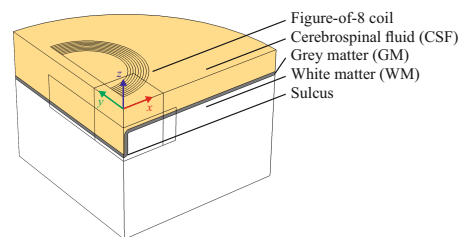


Fig. 1. Quarter-model of the investigated cortical sulcus.

rent amplitude of 5488 A and a frequency of excitation of 2.9 kHz. The coil is positioned such that the normal component of the induced current density is maximum i.e. the long axis of the coil is parallel to the artificial sulcus. Due to the validity of the quasi-static approximation in TMS, the magnetic field produced by the coil is calculated in advance by means of the magnetic vector potential \mathbf{A} . The induced electric field is given by $\mathbf{E} = -j\omega\mathbf{A} - \nabla\varphi$. Commercial FEM software is used to determine the scalar electric potential φ [7]. The FEM model shown in Fig. 1 makes use of two symmetry planes to further reduce computational cost.

3 Polynomial Chaos Expansion

Considering the available data for cerebrospinal fluid (CSF), grey matter (GM), and white matter (WM), a wide spread of the electrical conductivity can be observed [2–4]. Since the statistical properties of the tissues are not known, they are modeled as independent and uniform distributed random variables with the following limits: $1.4341 \leq \sigma_{CSF} \leq 1.9487$ S/m, $0.1224 \leq \sigma_{GM} \leq 0.5106$ S/m, and $0.0957 \leq \sigma_{WM} \leq 0.1663$ S/m. They are combined in a three-variate random vector $\boldsymbol{\xi}$ located in the probability space (\mathcal{E}, Σ, P) . The event space \mathcal{E} contains all possible events, Σ is a σ -algebra which is a subset of \mathcal{E} , and P is a measure for the probability of occurrence. Based on this, the gPC for uniform distributed random variables is defined by a truncated expansion of Legendre polynomials $\psi_n(\boldsymbol{\xi})$ weighted by the gPC coefficients \hat{u}_k [5]:

$$E(\mathbf{r}, \boldsymbol{\xi}) = \sum_{k=0}^{\infty} \hat{u}_k(\mathbf{r}) \psi_k(\boldsymbol{\xi}) \approx \sum_{k=0}^{N_c-1} \hat{u}_k(\mathbf{r}) \psi_k(\boldsymbol{\xi}). \quad (1)$$

In the present framework, the output $E(\mathbf{r}, \boldsymbol{\xi})$ is the magnitude of the induced electric field at a certain point \mathbf{r} . The gPC-coefficients are determined by means of a regression approach by solving the least squares problem $\Psi \hat{\mathbf{u}}(\mathbf{r}) = \mathbf{s}(\mathbf{r})$, where Ψ denotes the gPC-matrix and $\mathbf{s}(\mathbf{r})$ the solution vector determined by the forward simulations.

4 Numerical Results

The results are obtained using an order $p = 7$ expansion. Considering $N = 3$ random variables, this results in $N_c = \binom{N+p}{N} = 120$ gPC-coefficients. In order to provide a certain amount of oversampling, a tensor Gauss-Legendre grid with $7^3 = 343$ points is used. Figure 2 shows the mean of the induced electric field and the standard deviation in the xz -plane at $y = 0$. Furthermore, the probability density function (PDF) at point $(x, z) = (2.8, -31.1)$ mm located close to the sulcus, in the center of GM, is presented. The PDF is obtained by direct MC-sampling with 10^4 points and by sampling the gPC expansion $E(\mathbf{r}, \boldsymbol{\xi})$ from (1) with 10^5 points. The mean of the induced electric field shows high values in the region of the gyri crown. The standard deviation is highest at locations where the normal component of the induced current density is maximum. This behaviour was especially observed in GM. The standard deviation is in the range of 20-40% of the mean induced electric field in this region. The obtained PDFs show good agreement and indicate values between 30-160 V/m. Both PDFs are clearly non-symmetric, which indicates a non-negligible third moment (skewness).

5 Conclusion

The results indicate how drastically the electric field is influenced by the uncertainty of the input parameters. Besides geometrical variations between patients, the uncertainty of electrical conductivity could explain the variability between clinical TMS studies. In the full paper we are going to compare quadrature and collocation approaches [5] with the results obtained by regression. In addition, the spatial distribution of the global sensitivity coefficients of all three tissues will be presented. Finally, we will study the convergence characteristics with respect to the order of expansion as well as the associated simulation time.

Acknowledgement. The present work is supported by the Deutsche Forschungsgemeinschaft (DFG) in the framework of the Research Training Group 1567 at the Technische Universität Ilmenau, Germany.

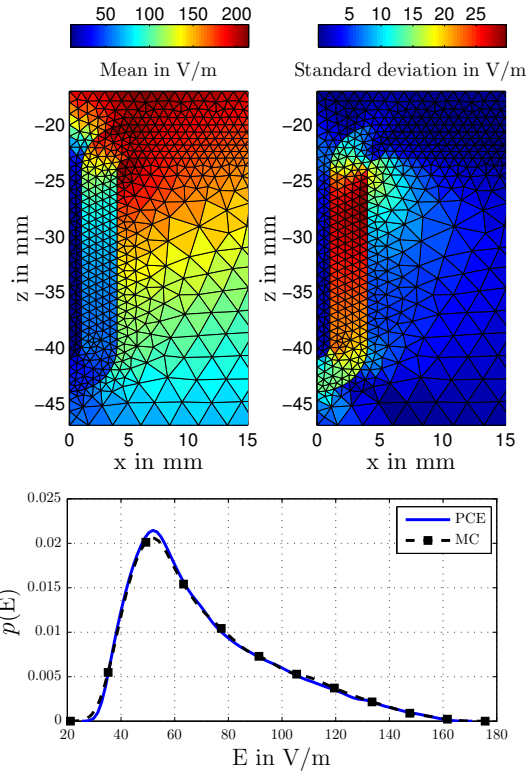


Fig. 2. Mean, standard deviation and PDFs of the induced electric field at point $(x, z) = (2.8, -31.1)$ at $y = 0$.

References

1. A.T. Barker and R. Jalinous. Non-invasive magnetic stimulation of human motor cortex. *Lancet*, 1106:1107–8437, 1985.
2. A. Thielscher, A. Opitz and M. Windhoff. Impact of the gyral geometry on the electric field induced by transcranial magnetic stimulation. *NeuroImage*, 234:243–54, 2011.
3. S. Gabriel, R.W. Lau and C. Gabriel. The dielectric properties of biological tissues: III. Parametric models for the dielectric spectrum of tissues. *Physics in Medicine and Biology*, 2271:2293–41, 1996.
4. J. Latikka, T. Kuurne and H. Eskola. Conductivity of living intracranial tissues. *Physics in Medicine and Biology*, 1611:1616–46, 2001.
5. D. Xiu. *Numerical methods for stochastic computations: A spectral method approach*. Princeton University Press, Princeton (New Jersey), 2010.
6. R. Salvador, S. Silva, P.J. Basser and P.C. Miranda. Determining which mechanisms lead to activation in the motor cortex: A modeling study of transcranial magnetic stimulation using realistic stimulus waveforms and sulcal geometry. *Clinical Neurophysiology*, 748:758–122, 2011.
7. COMSOL Multiphysics®. 2014. Version 4.4. COMSOL, Inc., Burlington, MA, USA.

A New Generation of BEM Solvers for Electric Field Computations

Thomas Müller¹, Carsten Trinitis¹, and Andreas Blaszczyk²

¹ Technische Universität München, Fakultät für Informatik, I10 (LRR), Boltzmannstr. 3, 85748 Garching, Germany
t.mueller@tum.de, carsten.trinitis@tum.de

² ABB Schweiz AG, Corporate Research, 5405 Baden-Dättwil, Switzerland andreas.blaszczyk@ch.abb.com

Summary. BEM¹ is an efficient simulation technique in industrial environments. In contrast to early BEM implementations based on fully populated matrices the novel techniques like FEM² or ACA³ succeed in reducing memory consumption but require more complex parallelization schemes, which generally do not scale properly. In this paper, we compare four different BEM implementations and propose a localized matrix compression technique which reduces memory consumption but at the same time maintains the straightforward parallelization scheme.

1 Introduction

Electrostatic simulation of power devices is used to ensure sufficient safety margins without the need to perform expensive tests with prototypes during initial development and allows the engineer to assess and, if necessary, improve critical parts of the device.

Fig. 1 shows the results of a BEM based simulation performed for a switchgear component where colors represent electric field strength, increasing from blue to red. Such simulation models can nowadays be created in a very user friendly manner using CAD systems. Through this, the model created by the designer can be taken as is and easily be discretized directly inside the CAD system. As a consequence, the overall time for obtaining the electric field distribution as depicted in Fig. 1 from a raw CAD model could be reduced to the order of tens of minutes. Therefore, the remaining bottleneck is the BEM solver computation time, which can become very long for large dimensions.

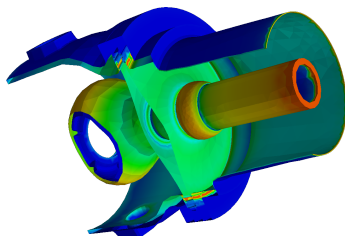


Fig. 1. Visualization of Gas Insulated Switchgear (GIS) Component, Matrix Dimension ≈ 150.000

¹ Boundary Element Method

² Fast Multipole Method

³ Adaptive Cross Approximation

2 Simulation Solvers

Based on recent cooperation projects between industry and academia [5], the following BEM implementations have been investigated:

Polopt0: Developed by ABB and implementing BEM in a straightforward manner using a fully populated matrix. Its MPI based version distributes individual rows of the fully populated matrix and processes them in parallel. Exact details are presented in [1].

Polopt3: Developed by ABB as successor to polopt0 and also parallelized using MPI. It implements the *Fast Multipole Method* (FMM) based on the work published in [4].

BETLdielectric: Based on the BETL [2] framework initiated at ABB. It is currently being developed and maintained by ETH Zürich. *Adaptive Cross Approximation* (ACA) is used to avoid storing a fully populated matrix. A parallel implementation of ACA [6] which is based on shared memory only has been used for our investigations.

gobem: Developed at the Department for Numerical Mathematics of TU Graz and, like polopt3, implementing a Fast Multipole Method. It primarily focuses on the accuracy of the solution rather than on high performance [3] and uses a combination of both MPI and shared memory for parallelization.

2.1 Runtime Performance

Fig. 2 shows the runtime in minutes the individual solvers took to simulate the GIS component on a single node with up to 32 Intel Westmere CPU cores. The number of cores for the fastest parallel runtimes are given in parentheses, respectively.

When using up to 32 cores, the straightforward parallelization of *polopt0* results in a speedup of more than 25, *BETLdielectric* and *gobem* achieve a factor of about 11. *Polopt3* achieves its best runtime using 8 cores and barely halves its sequential runtime. Above 8 cores, *polopt3* starts to slow down again. This demonstrates the advantage of the straightforward parallelization of the *polopt0* solver.

2.2 Memory Requirements

Fig. 3 shows the memory consumption of the individual solvers during simulation of the GIS component. The fully populated matrix constructed and stored in

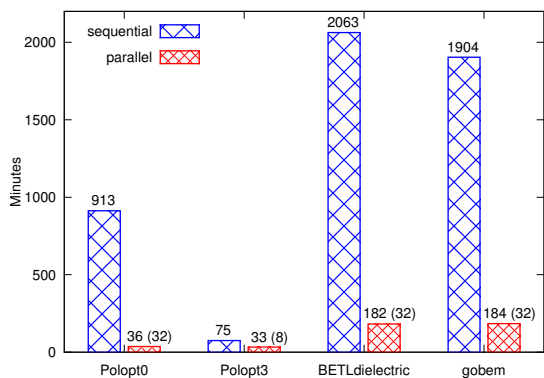


Fig. 2. Runtime for Simulation of GIS Component

polopt0 results in the highest memory consumption of all four solvers. Both *BETLdielectric* as well as *gobem* significantly reduce the amount of memory required for the simulation, while *polopt3*'s memory consumption is about a third less than *polopt0*'s.

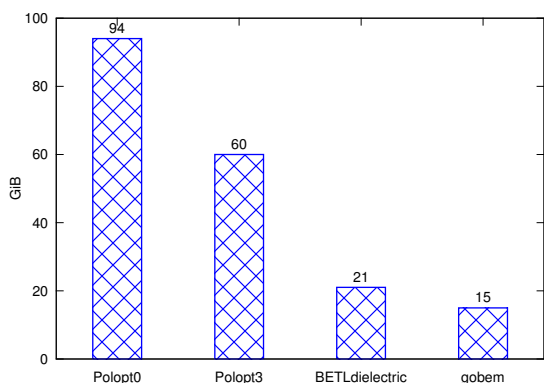


Fig. 3. Memory Requirements for GIS Component

3 Matrix Compression

Due to the fully populated matrix used in *polopt0*, memory consumption is $O(n^2)$ with n being the number of unknowns in the model. Therefore, reducing the amount of memory required for simulation is critical to be able to simulate increasingly complex models.

However, while the other solvers reduce the memory requirements, their parallel speedup is not competitive to *polopt0*. Moreover, *BETLdielectric* and *gobem* can currently not be used on a large number of cluster nodes due to their parallelization structure.

As of now, *polopt3*, *BETLdielectric*, and *gobem* are not suitable for the simulation of models that are noticeably larger than the exemplary model in Fig. 1 as this would require using a high number of cluster nodes and/or improved speedup.

We can significantly reduce memory consumption through a localized data compression technique whilst maintaining the parallelization scheme of *polopt0*

as explained in [1]. It is possible to store the individual matrix rows in a compressed format and only decompress them on-the-fly when necessary. Compression is done by combining consecutive values within a specified range and only store a single average value.

In case of the exemplary GIS component, this reduces overall memory consumption to about 60 GiB, which is comparable to *polopt3* but maintains the beneficial properties of the original parallelization, especially with respect to speedup and uniform distribution of memory across cluster nodes.

The runtime overhead of compression and decompression is not significant (less than 5% in our example). More detailed characteristics of memory consumption, performance and influence on accuracy will be presented in the extended version of this paper.

4 Conclusion

The new generation of BEM solvers shows significant improvement in memory consumption and partially in runtime performance. However, their parallel performance does not yet allow to efficiently use them on massively parallel computer architectures and solve very large industrial models. Further research in this area is required. Currently, matrix compression based on the algebraic approach presented in section 3 can mitigate the current memory limitations for industrial applications.

References

1. A. Blaszczyk, Z. Andjelic, P. Levin, and A. Ustundag. Parallel computation of electric fields in a heterogeneous workstation cluster. In B. Hertzberger and G. Serazzi, editors, *High-Performance Computing and Networking*, volume 919 of *LNCS*, pp. 606–611. Springer, 1995.
2. R. Hiptmair and L. Kielhorn. BETL – a generic boundary element template library. Research Report 2012-36, SAM - Seminar for Applied Mathematics; ETH Zürich, November 2012.
3. D. Amann, A. Blaszczyk, G. Of, and O. Steinbach. Simulation of floating potentials in industrial applications by boundary element methods. *Berichte aus dem Institut für Numerische Mathematik 2013/3*, Technische Universität Graz, 2013.
4. C. Lage. *Softwareentwicklung zur Randelementmethode: Analyse und Entwurf effizienter Techniken*. PhD thesis, Christian-Albrechts-Universität zu Kiel, 1995.
5. EU FP7 Marie Curie IAPP Project CASOPT, *Controlled Component- and Assembly Level Optimization of Industrial Devices*. ABB Corporate Research, TU Graz, TU München, University of Cambridge, 2009-2013.
6. M. Bebendorf *Hierarchical Matrices*, volume 63 of *Lecture Notes in Computational Science and Engineering*. Springer, 2008.

Runge-Kutta type Explicit Local Time-Stepping Methods for Electromagnetics

Marcus J. Grote and Michaela Mehlin

Institute of Mathematics, University of Basel, Rheinsprung 21, 4051 Basel, Switzerland marcus.grote@unibas.ch, michaela.mehlin@unibas.ch

Summary. Starting from explicit Runge-Kutta (RK) methods, we propose high order explicit local time-stepping (LTS) methods for the simulation of electromagnetic wave phenomena. By using smaller time steps precisely where smaller elements in the mesh are located, these LTS methods overcome the bottleneck in explicit time integration caused by local mesh refinement, without sacrificing the explicitness, accuracy or efficiency of the original RK method.

1 Introduction

The evolution of a time-dependent electromagnetic field $\mathbf{E}(\mathbf{x}, t)$, $\mathbf{H}(\mathbf{x}, t)$ propagating through a linear isotropic medium is governed by Maxwell equations:

$$\varepsilon \mathbf{E}_t = \nabla \times \mathbf{H} - \sigma \mathbf{E} + \mathbf{j}, \quad (1)$$

$$\mu \mathbf{H}_t = \nabla \times \mathbf{E}. \quad (2)$$

Here $\mu(\mathbf{x})$, $\varepsilon(\mathbf{x})$ and $\sigma(\mathbf{x})$ are positive, bounded, scalar functions of position denoting the relative magnetic permeability, the relative electric permittivity and the conductivity of the medium, respectively, while the source term \mathbf{j} corresponds to the applied current density. We discretize (1)-(2) in space by using standard edge finite elements (FE) with mass lumping or a discontinuous Galerkin (DG) FE discretization, while leaving time continuous. Either discretization leads to a system of ordinary differential equations

$$\mathbf{y}'(t) = \mathbf{B}\mathbf{y}(t) + \mathbf{F}(t), \quad (3)$$

where the matrix \mathbf{B} involves the inverse, \mathbf{M}^{-1} , of the mass matrix \mathbf{M} . Since \mathbf{M} is essentially diagonal, its inverse is explicitly known, and so is \mathbf{B} .

Standard explicit numerical methods for the time integration of (3) include explicit Runge-Kutta (RK) and also Adams-Bashforth (AB) methods, whose time-step, Δt , is dictated by the smallest elements in the mesh. When mesh refinement is restricted to a small region, using the small time-step Δt on the entire computational domain is generally too high a price to pay. In [1, 3, 4], multi-step based LTS methods were proposed, which alleviate the geometry induced stability restriction by using smaller time-steps, but only where the smallest elements in the mesh are located.

2 Runge-Kutta based LTS

Here we present explicit LTS methods of arbitrarily high accuracy based either on explicit classical or low-storage RK schemes [2]. In contrast to AB methods, RK methods are one-step methods; hence, they do not require a starting procedure and easily accommodate adaptivity in time.

Starting from (3), we first split the vectors \mathbf{y} and \mathbf{F} as

$$\mathbf{y}(t) = (\mathbf{I} - \mathbf{P})\mathbf{y}(t) + \mathbf{P}\mathbf{y}(t) = \mathbf{y}^{[c]}(t) + \mathbf{y}^{[f]}(t), \quad (4)$$

$$\mathbf{F}(t) = (\mathbf{I} - \mathbf{P})\mathbf{F}(t) + \mathbf{P}\mathbf{F}(t) = \mathbf{F}^{[c]}(t) + \mathbf{F}^{[f]}(t). \quad (5)$$

Here the entries of the diagonal matrix \mathbf{P} , equal to zero or one, identify the unknowns associated with the locally refined regions, $\mathbf{y}^{[f]}$.

Hence the exact solution of (3) is given by

$$\begin{aligned} \mathbf{y}(t_n + \xi \Delta t) = & \mathbf{y}(t_n) + \int_{t_n}^{t_n + \xi \Delta t} \mathbf{B}\mathbf{y}^{[c]}(t) + \mathbf{F}^{[c]}(t) dt \\ & + \int_{t_n}^{t_n + \xi \Delta t} \mathbf{B}\mathbf{y}^{[f]}(t) + \mathbf{F}^{[f]}(t) dt. \end{aligned} \quad (6)$$

To derive an LTS method that overcomes the stringent stability conditions dictated by the smallest elements in the mesh, we shall treat the fine elements differently from the remaining coarser elements. In doing so, we approximate the first integral in (6) by a sufficiently accurate quadrature formula, where the (unknown) values of $\mathbf{y}^{[c]}$ at the quadrature points are approximated by Taylor expansion. Differentiation of the resulting expression then leads to a modified differential equation, which is solved numerically from t_n to $t_n + \Delta t$ by using a RK method with local time-step $\Delta \tau = \Delta t/p$; here, p denotes the coarse to fine aspect ratio. The resulting LTS-RK scheme has the same high rate of convergence as the original corresponding RK method.

To illustrate the usefulness of LTS-RK methods we present numerical results in one and two dimensions. We first consider the one-dimensional model problem (1) and (2) with constant material properties $\mu = \varepsilon = 1$ and $\sigma = 0.1$ on the interval $\Omega = [0, 6]$. The initial conditions and source term yield the exact solutions

$$E(x, t) = -\cos(t) \sin(\pi x), \quad (7)$$

$$H(x, t) = -\pi \cos(t) \cos(\pi x). \quad (8)$$

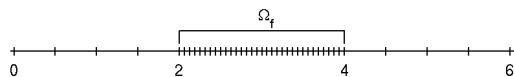


Fig. 1. One-dimensional example: computational domain $\Omega = [0, 6]$ with refined region $\Omega_f = [2, 4]$.

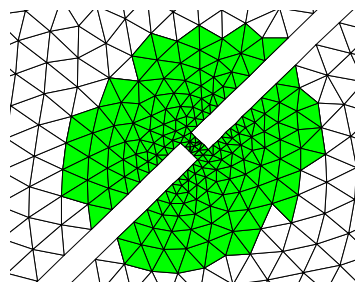


Fig. 3. Zoom on refined part of the mesh.

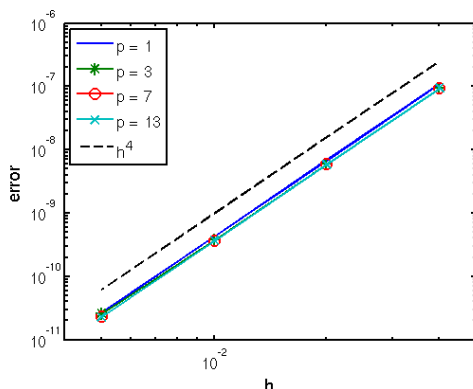


Fig. 2. LTS-RK4(p) error vs. $h = h^{\text{coarse}}$ for nodal DG \mathcal{P}^3 -elements with $p = 1, 3, 7, 13$.

Next we divide Ω into three equal parts. The left and the right intervals, $[0, 2]$ and $[4, 6]$, respectively, are discretized with an equidistant mesh of size h^{coarse} , whereas on the interval $[2, 4]$ the mesh size is chosen as $h^{\text{fine}} = h^{\text{coarse}}/p$. Hence, the two outer intervals correspond to the coarse region and the inner interval to the refined region, see Fig. 1.

We discretize (1)-(2) in space using nodal DG \mathcal{P}^3 -elements on a sequence of increasingly finer meshes. For every time-step Δt , we shall take $p \geq 2$ local steps of size $\Delta \tau = \Delta t/p$ in the refined region, with the fourth-order time-stepping scheme LTS-RK4(p). As we systematically reduce the global mesh size h^{coarse} , while simultaneously reducing Δt , we monitor in Fig. 2 the L^2 space-time error in the numerical solution $\|E(\cdot, T) - E_{h, \Delta t}(\cdot, T)\|_{L^2(\Omega)}$ at the final time $T = 1$. Regardless of the rate of local refinement p , we obtain optimal global convergence of order 4.

In Fig. 4, a vertical Gaussian pulse initiates two plane waves (with Gaussian amplitude) propagating in opposite directions. As the right-moving wave proceeds, it impinges upon the obstacle; then, a fraction of the wave penetrates the gap and generates a circular wave, which further interacts with the propagating wave field. Since the typical mesh size inside the refined region is about $p = 7$ times smaller than in the surrounding coarser region, the LTS-RK method takes $p = 7$ local steps of size $\Delta \tau = \Delta t/p$ inside the refined region, shown in Fig. 3.

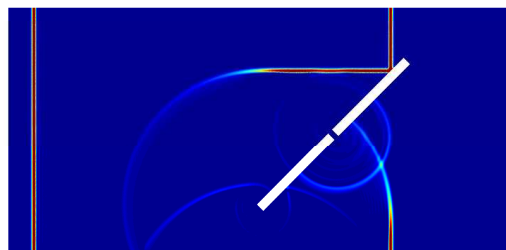


Fig. 4. A Gaussian plane wave impinging upon a narrow gap at time $t = 0.7$.

References

1. J. Diaz and M.J. Grote. Energy conserving explicit local time-stepping for second-order wave equations. *SIAM J. Sci. Comput.*, **31** (2009), 1985–2014.
2. M.J. Grote, M. Mehlin and T. Mitkova. Runge-Kutta Based Explicit Local Time-Stepping Methods for Wave Propagation. *submitted for publication*.
3. M.J. Grote and T. Mitkova. Explicit local time-stepping for Maxwell’s equations. *J. Comput. Appl. Math.*, **234** (2010), 3283–3302.
4. M.J. Grote and T. Mitkova. High-order explicit local time-stepping methods for damped wave equations. *J. Comput. Appl. Math.*, **239** (2013), 270–289.

Numerical Investigation of an Electrostimulative Hip Stem with a Multi-Electrode Setting

Ulf Zimmermann¹, Cathérine Ebner², Rainer Bader², and Ursula van Rienen¹

¹ Institute of General Electrical Engineering, University of Rostock, Albert-Einstein-Str. 2, 18059 Rostock, Germany.
ulf.zimmermann@uni-rostock.de, ursula.van-rienen@uni-rostock.de

² Department of Orthopaedics, University Medicine Rostock, Doberaner-Str. 142, 18057 Rostock, Germany.
catherine.ebner@med.uni-rostock.de, rainer.bader@med.uni-rostock.de

Summary. Electrosimulative systems are used to improve bone regeneration after fractures and during certain bone diseases. To accelerate the bone regeneration after surgery electrostimulation is implemented in a Total Hip Replacement (THR). In this study a new multi-electrode setting for the computational model of an electrostimulative hip stem is compared to an optimized single-electrode setting. The goal is to investigate the benefit of several electrodes providing sufficient stimulation fields without decreasing the mechanical stability of the hip stem.

1 Introduction

The activating effect of electromagnetic fields on the growth of bone cells is known since 1974 [1]. Numerous stimulation techniques have been investigated, which use high- and low-frequency electromagnetic fields to enhance the regeneration of necrotic and fractured bones [2]. At the University of Rostock, a low-frequency electrostimulative hip revision system is being developed to improve the mechanical stability as well as the durability of the implant in the bone. The system consists of two parts: the acetabular part, which is placed in the pelvic bone and the femoral part, which is placed in the thigh bone.

In former studies, design optimization of an electrostimulative acetabular cup has been done using numerical simulation [3] [4]. Promising results in first validation tests have also shown potential to transfer electrostimulation to the hip stem. Here the basic idea is to modify a conventional uncemented straight hip stem (Ti6Al4V) by milling a notch into both, the anterior and posterior, sides. The notch is filled with a biocompatible insulator (e.g. ZrO₂) and a thin stimulating wire (Ti6Al4V) as first electrode. The hip stem itself acts as second electrode. Thus, an electric field is provided, which stimulates the growth of bone tissue and thereby strengthen the osseous anchorage.

According to the method of Kraus, the electric field lies within 5 and 70 V/m at a frequency of 20 Hz [5]. Emanating from the first electrode the electric field on the electrically conducting hip stem decreases rapidly with increasing distance. The insulator cannot be arbitrarily enlarged, since bone tissue does not connect well to the insulator and the mechanical stability of the hip stem should not be neglected. Hence, the dimensions of the insulator and the first electrode have

to be optimized. In the present work, the electric field distribution of a multi-electrode setting is investigated and compared to an optimized single-electrode setting.

2 Methods

For the simulation, the CAD model of a small (size 2), straight hip stem was modified. The first model for the single-electrode setting included a notch with insulator and a stimulative wire, while the second model for the multi-electrode setting was designed with two stimulative wires parallel positioned (Fig. 1). These models were inserted into the CAD model of a porcine femur, which has been reconstructed from CT scans. To stimulate electric fields distribution, the Finite Integration Technnique program CST EM Studio[®] is used. The electrical properties of the biological tissues were taken form literature [6]. Due to the substantially higher conductivity of the electrodes compared to the biological tissue, it is approximated by a perfect electric conductor (PEC) to minimize the computational effort. For the same reason, the insulator is approximated by an ideal electric insulator (Vacuum).

Furthermore, the stationary current solver of CST EM Studio[®] is used to solve Laplace's equation. Prior tests showed that the error of this solver is below 0.5 % compared to a quasistatic solution at a frequency of 20 Hz, while the computation time is reduced substantially. A hexahedral mesh has been chosen to benefit from CST EM Studio[®]'s Enhanced Fast Perfect Boundary Approximation. It is refined in close proximity to the stimulation electrodes as well as the implant-bone interface. The mesh was improved by an additional adaptive mesh refinement, which was used during the first simulations. The final mesh for the multi-electrode setting and the single-electrode setting consisted of 10.47 and 9.55 million hexahedral mesh cells, respectively.

Using a single-electrode setting, the implant itself acts as electrode (0 V) while in the multi-electrode setting it is assigned with a floating potential. The electric fields on the implant-bone interface strongly depend on the potential and the dimensions of insulator and electrodes as well as the distance be-

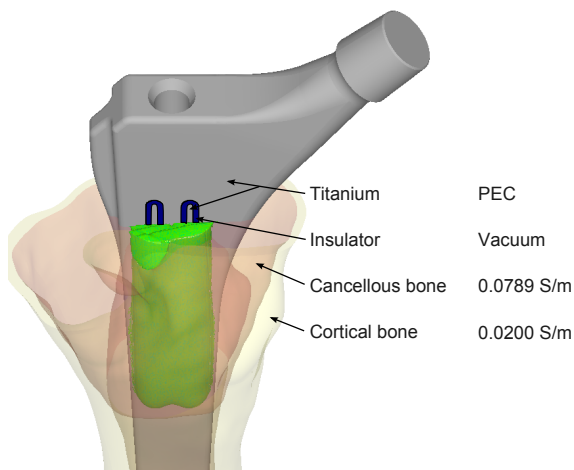


Fig. 1. Isosurface of the electric field at 5 V/m for the electrostimulative hip stem with a multi-electrode setting.

tween the two electrodes of the multi-electrode setting. The first optimization was performed with a single-electrode setting using the internal optimizer of CST EM Studio[®]. The optimization goals were to keep the electric field at previously defined points of interests above 5 V/m and below 70 V/m while keeping the width of the insulator as small as possible. During the optimization process of the single-electrode setting, the stimulation distance between the isosurface at 70 V/m, which includes the overstimulated area, and the isosurface at 5 V/m, which includes the stimulated area, was used to compare different configurations.

3 Results and Discussion

The final result of the single-electrode setting includes a wire and an insulator, which exhibits a width of 1.45 mm and 1.40 mm, respectively. The stimulation potential has been set to 0.17 V, which lead to a stimulation distance of 4.83 mm. Compared to the initial configuration with a potential of 0.2 V and a width of 1 mm for both, the insulator and the electrode, this is an improvement of 25 % while the general overstimulation has been reduced substantially. In contrast to this setting, the multi-electrode setting produces a more planar electric field. This can be seen in Fig. 1, where the isosurface of the electric field at 5 V/m is shown. However comparing the measurement points above the implant-bone interface it becomes obvious, that even without optimization nearly the same area is as well stimulated as with the optimized single electrode. Though the stimulation field of the multi-electrode setting does not radiate into the bone as deep as the electric field of one big electrode which is assigned with a potential nearly twice as high as one electrode of the multi-electrode setting, overstimulation has been further reduced.

For this proof of concept each stimulation electrode as well as the insulator has a width of 1 mm. The distance between both electrodes is 5 mm and

the stimulation potential is at 0.1 V and -0.1 V, respectively. Compared to the single-electrode setting the overall size of the insulator has been increased to 4 mm instead of 2.8 mm. Because this is the area where bone tissue does not attach to the hip stem, the multi-electrode setup cannot be recommended without further optimization. Nevertheless especially for bigger revision hip stems this will be necessary to cover the whole anterior and posterior sides of the implant with a sufficient electric field.

Another issue is the mechanical stability. The small hip stem passed a numerical static strength analysis for fatigue failure with a notch of 3 mm width. The optimized single-electrode setting requires a notch with a width of 4.25 mm, while the multi-electrode arrangement even requires two notches. All settings have to be approved by further fatigue analysis. If the improved implant fails, the optimization has to be repeated with an increased weight at the optimization goal to reduce the size of the insulator. For this reason the next step is to optimize the multi-electrode setting using a multidimensional approach to find a Pareto amount of configurations as it has been done in [4]. In this way it would be possible to directly select optimal electrode configurations by focusing on the width of the insulator.

Acknowledgement. This work was supported by the Deutsche Forschungsgemeinschaft (DFG: RI 814 / 17-2).

References

1. C.A.L. Bassett, R.J. Pawluk, and A.A. Pilla. Acceleration of fracture repair by electromagnetic fields. A surgically noninvasive method. *Ann. NY Acad. Sci.*, 238:242–262, 1974.
2. W. Latham, and J.T.C. Lau. Bone Stimulation. A Review of Its Use as an Adjunct. *Techniques in Orthopaedics*, 26:14–21, 2011.
3. C. Potratz, D. Kluess, H. Ewald, and U. van Rienen. Multiobjective Optimization of an Electrostimulative Acetabular Revision System. *IEEE Trans. Bio. Eng.*, 57:460–468, 2010.
4. U. Zimmermann, and U. van Rienen. An Automatic Pareto Classifier for the Multiobjective Optimization of an Electrostimulative Acetabular Revision System. *IEEE Trans. Magnetics*, 50, 2014.
5. W. Kraus. Magnetfeldtherapie und magnetisch induzierte Elektrostimulation in der Orthopädie. *Orthopädie*, 13:78–92, 1984.
6. C. Gabriel, A. Peyman, and E.H. Grant. Electrical conductivity of tissue at frequencies below 1 MHz. *Phys. Med. Biol.*, 54:4863–4878, 2009.

Uncertainty Quantification for Permanent Magnet Synchronous Machines with an Inclined Rotor Shaft

Zeger Bontinck^{1,2}, Herbert De Gersem³, and Sebastian Schöps^{1,2}

¹ Technische Universität Darmstadt, Graduate School for Computational Engineering, Dolivostr. 15, Darmstadt, Germany

² Technische Universität Darmstadt, Institut für Theorie Elektromagnetischer Felder, Schlossgartenstr. 8, Darmstadt, Germany bontinck@gsc.tu-darmstadt.de, schoeps@gsc.tu-darmstadt.de

³ KU Leuven-Kulak, Etienne Sabbelaan 53, 8500 Kortrijk, Belgium Herbert.DeGersem@kuleuven-kulak.be

Summary. The influence of an inclined rotor mounting of a synchronous machine on the electromotive force is studied. The 3D structure of the rotor is divided into 2D slices. The positions of the bearings are stochastic parameters and determine the position of the centre of the rotor in each slice. The stochastic moments of the electromotive force are efficiently determined by evaluating a spline interpolation of these quantities by using 2D finite element simulations.

1 Introduction

During the production of permanent magnet synchronous machines (PMSMs), manufacturing tolerance may lead to a (not necessarily equal) eccentric mounting of both bearings. This causes a static, inclined eccentricity of the rotor shaft (Fig. 1). A straightforward simulation would involve a stochastic 3D model, which would be prohibitively expensive for this application. Even a so-called quasi-2D model [1] considering a number of slices distributed along the axis, each with a rotor position depending on the uncertain mounting of both bearings and the axial position of the slice, would be computationally inefficient. The main idea of this paper is to precompute machine performance parameters as a function of an uncertain rotor position and upscale the stochastic results in order to come to a prediction of the machine's performance for an eccentric, possibly inclined rotor mounting.

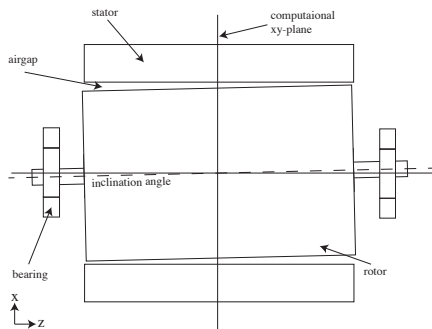


Fig. 1. Inclination due to imperfections of bearings

The considered PMSM has six poles and surface mounted magnets [2]. A 2D finite-element (FE) model is built such that a topologically identical mesh

is maintained for each stochastic rotor position. The FE solution for the magnetic vector position is post-processed for the electromotive force (EMF) induced in the stator windings and the total harmonic distortion (THD).

2 Uncertain, Inclined Rotor Model

The uncertainty handled here are the positions of the two bearings supporting the rotor. The eccentricity of each bearing is expressed in polar coordinates with respect to the coordinate system attached to the nominal position of the rotor, i.e. the centre of the stator. The radii R_1, R_2 and the azimuths θ_1, θ_2 , with the technical assumption that $R(\omega), \theta(\omega) \in L^2(\Theta, \Sigma, P)$, are independent random variables on the probability space (Θ, Σ, P) . Engineering expertise suggests that R has a gaussian distribution and θ a uniform distribution,

$$R_1, R_2 \sim \mathcal{N}(0, \sigma^2) \quad \text{and} \quad \theta_1, \theta_2 \sim \mathcal{U}(0, \frac{\pi}{3}), \quad (1)$$

where the standard deviation $\sigma = 0.067$ mm has been chosen such that 3σ corresponds to 0.2 mm. During the post-processing the symmetry of the model is exploited to reduce the random space.

3 Description

PMSMs are sufficiently described by the magneto-static formulation of the Maxwell's equations. This means that eddy and displacement currents can be omitted. One obtains the elliptical PDE

$$\nabla \times (\nu(\omega) \nabla \times \mathbf{A}(\omega)) = \mathbf{J}_{\text{src}} - \nabla \times \mathbf{H}_{\text{pm}}, \quad (2)$$

with Dirichlet boundary conditions and where ω denotes the dependency on the stochastic parameters. \mathbf{A} is the magnetic vector potential, ν the reluctivity of the material, \mathbf{J}_{src} is the source current density and \mathbf{H}_{pm} is the coercivity of the permanent magnets.

Discretizing with edge shape functions and using the Galerkin approach one retrieves the system of equations of the form $\mathbf{K}_\nu(\omega) \mathbf{u}(\omega) = \mathbf{j}_{\text{src}} + \mathbf{j}_{\text{pm}}$ where the respective terms follow from discretizing the corresponding terms of (2), e.g. [3, 4]. Here, $\mathbf{u}(\omega)$ represents the discrete degrees of freedom of \mathbf{A} .

To determine the induced voltage the loading method is used [5]. In this method the d - and q -components of the magnetic flux are calculated by performing a Fourier analysis of \mathbf{A} on a contour located in the air-gap.

4 Uncertainty Quantification

A 17×13 tensor grid of the $[R, \theta]$ space is constructed to enable a spline-interpolation over the full domain (the black points in Fig. 2). This means that a 2D simulation is only performed on each grid node. By using a Monte Carlo approach the positions of the two bearings are determined (respectively the green and the red point in Fig. 2). The inclined rotor axis is computed to integrate the EMF along that axis. Along a path over the interpolated surface (blue points in Fig. 2), the EMF is calculated by integrating the corresponding path. In total 1000 paths are generated by the inbuilt tools of MATLAB[®] and analysed in this way.

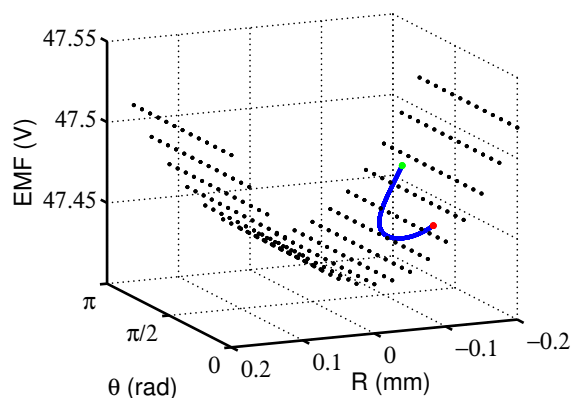


Fig. 2. The black points show the grid used for the interpolation. The blue points is the path along which the EMF is evaluated. The green point depicts the starting point (position of the frontal bearing) and the red point depicts the endpoint (position of the bearing at the back).

The same principle is applied to determine the THD of the inclined rotor. By obtaining the harmonic spectrum of the model for each gridpoint, the THD can be calculated in each point by

$$\text{THD}(\omega) = \frac{\sum_{p=2}^{\infty} |E_p(\omega)|^2}{|E_1(\omega)|^2}, \quad (3)$$

where p represents the order and E_p the EMFs.

5 Results

The computed expectation values for the EMF and THD are respectively 47,439 V and $3,884 \cdot 10^{-3} \%$. The standard deviations are respectively 0,006 V and $5 \cdot 10^{-6} \%$.

The expectation values are in good agreement with previous Monte Carlo results in which the influence of a common eccentric rotor position for every slice is studied [6]. The standard deviations for both quantities are however smaller. The former model corresponds to more pessimistic scenarios. These are rather unlikely in the model discussed in this paper, due to the gaussian distribution of the mounting of the bearings.

6 Conclusion and Prospects

By using standard numerical techniques (spline interpolation and Monte Carlo simulations) the influence of an inclined rotor position on the electromotive force and the total harmonic distortion is studied. The 3D model is reduced to a set of 2D models by dividing the rotor in a set slices on which the calculations are then performed.

Future work will contain a comparison to real 3D calculations and dynamic eccentricity. Also the influence on the force and torque exerted on the rotor will be studied.

Acknowledgement. This work is supported by the German BMBF in the context of the SIMUROM project (grant number 05M13RDA), by the Excellence Initiative of the German Federal and State Governments and the Graduate School of Computational Engineering at TU Darmstadt.

References

1. B. Boualem and F. Piriou Numerical models for rotor cage induction machines using finite element method. *IEEE Trans. Magn.* 34:3202–3205, 1998.
2. S. Henneberger, U. Pahner, K. Hameyer and R. Belmans. Computation of a highly saturated permanent magnet synchronous motor for a hybrid electric vehicle. *IEEE Trans. Magn.*, 33:4086–4088, 1997.
3. S.J. Salon. Finite Element Analysis of Electrical Machines, Kluwer, 1995.
4. P. Monk. Finite Element Methods for Maxwells Equations, Oxford University Press, 2003.
5. M. Rahman, M. Azizur and P. Zhou. Determination of saturated parameters of PM motors using loading magnetic fields. *IEEE Trans. Magn.*, 27:3947–3950, 1991.
6. Z. Bontinck, H. De Gersem and S. Schöps. Uncertainty quantification of the eccentricity of permanent magnetic synchronous machines. *EPNC Conference, Pilsen, Czech Rep.*, Submitted, 2014.

Robust topology optimization of a Permanent Magnet synchronous machine using level set and stochastic collocation methods

Piotr Putek^{1,3}, Kai Gausling¹, Andreas Bartel¹, Konstanty M. Gawrylczyk², Jan ter Maten¹, Roland Pulch³, and Michael Günther¹

¹ Bergische Universität Wuppertal, Chair of Applied Mathematics and Numerical Analysis, Germany, {putek, gausling, bartel, termaten, guenther}@math.uni-wuppertal.de,

² West Pomeranian University of Technology, Department of Electrotechnology and Diagnostic, Szczecin, Poland, Konstanty.Gawrylczyk@zut.edu.pl

³ Ernst-Moritz-Arndt-Universität Greifswald, Germany, pulchr@uni-greifswald.de

Summary. The aim of this paper is to incorporate the stochastic collocation method (SCM) into a topology optimization for a permanent magnet (PM) synchronous machine with material uncertainties. The variations of the non-linear material characteristics are modeled by the Polynomial Chaos Expansion (PCE) method. During the iterative optimization process, the shapes of rotor poles, represented by zero-level sets, are simultaneously optimized by redistributing the iron and magnet material over the design domain. The gradient directions of the multi-objective function with constraints, composed of the mean and the standard deviation, is evaluated by utilizing the continuous sensitivity equation approach and the SCM. The stochastic collocation method with the PCE combined with the level set method yields designs by using already existing deterministic solvers. Finally, a two-dimensional numerical result demonstrates that the proposed method is robust and effective.

1 Introduction

Nowadays, permanent-magnet (PM) machines have become more popular due to their attractive features such as a high performance, efficiency, and power density. Therefore, they have found a broad use in industrial applications such as robotics, computer peripherals, industrial drivers or automotive industry. However, the torque ripple that comes mainly from the motor design, results in mechanical vibrations, acoustic noise and problems with the speed control in drive systems [1]. Thus, such an undesired cogging torque (CT) needs to be minimized.

In this paper, we focus on designing a PM machine, as the machine topology itself is a major contributor to the electromagnetic torque fluctuation. Because the result of the design procedure is strongly affected by the unknown material characteristics [2], the uncertainties in modeling the soft ferromagnetic material are taken into account. In some applications [3], especially the relative permeability of the magnetic material itself should be accounted to model more accurately the magnetic flux density of permanent magnets. This parameter is also in our model assumed as uncertain.

The novel aspect of the proposed method is the incorporation of stochastic modeling into the topology optimization method for the low cogging torque (CT) design of an electric controlled permanent mag-

net excited synchronous machine (ECPSM), shown in Fig. 1.

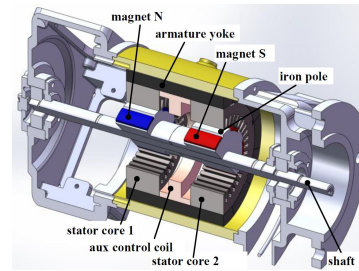


Fig. 1. Cross-section of ECPSM with the surface-mounted PM rotor and stator structure exhibiting the three-phase windings with the fixed excitation control auxiliary coil [1].

2 Stochastic forward problem

Let $\mathbf{v} : \Omega \rightarrow \Pi \subseteq \mathbb{R}^q$ denotes the random reluctivity $\mathbf{v}(\xi) = (v_1(\xi), \dots, v_q(\xi))$ defined on some probabilistic space $(\Omega, \mathcal{F}, \mathbb{P})$, where v_i are independent. The direct problem is governed by the stochastic PDF on $\Omega \subset \mathbb{R}^2$ with the periodic BC:

$$\nabla \cdot (\mathbf{v}(\mathbf{x}, |\nabla A|^2, \xi) \nabla A - \mathbf{v}_{PM}(\xi) \mathbf{B}_r) = J.$$

Here, A and \mathbf{B}_r denote the vector potential and the remanent flux density of the PM, while J is the forced current density. We express A in the truncated PCE as $A(t, \mathbf{v}) = \sum_{i=0}^K v_i(t) \varphi_i(\mathbf{v})$ with the unknown a priori coefficients v_i and the polynomial basis $(\varphi_k)_{k \in \mathbb{N}}$. In order to calculate v_i the SCM is used [4], where the solution of the deterministic problem is computed at each quadrature grid point \mathbf{v}^k , $k = 0, \dots, K$. Then, the PCE of A are computed by using a multi-dimensional quadrature rule with corresponding weights w_k :

$$v_i(t) := \langle A(t, \mathbf{v}), \varphi_i(\mathbf{v}) \rangle \approx \sum_{k=0}^K w_k A(t, \mathbf{v}^k), \varphi_i(\mathbf{v}^k).$$

Then, the first moments are given as:

$$\mathbb{E}[A(t, \mathbf{v})] = v_0(t), \quad \text{Var}[A(t, \mathbf{v})] = \sum_{k=1}^K |v_k(t)|^2.$$

3 Robust topology optimization

The problem of the low CT design of the ECPSM is solved using the modified level set method with total

variation regularization (TV) [1, 5]. Let $\phi(\mathbf{x})$ signifies the signed distance functions, which describes the interfaces Γ_j ($j=1,2$) between different regions.¹ Then, the following cost functional is minimized:

$$F(\mathbf{v}(\phi, \xi)) = \int_{\Omega} h(\nabla A(\mathbf{v}(\phi, \xi))) dx + \int_{\Omega} |\nabla \mathbf{v}(\phi, \xi)| dx, \quad (1)$$

which is subjected to the constraint

$$G(\mathbf{v}(\phi, \xi)) = \int_{\Omega} g(A(\mathbf{v}(\phi, \xi))) dx. \quad (2)$$

Here, the first term of (1) represents the CT, while the second one refers to the TV regularization. The function $G(\mathbf{v}(\phi, \xi))$ describes the back electromotive force (the back-EMF). To calculate the total derivative of (1) and (2), at least two dual systems should be defined:

$$\nabla \cdot (\mathbf{v}(\mathbf{x}, |\nabla A|^2, \xi) \nabla A - \mathbf{v}_{PM}(\xi) \mathbf{B}_r) = \Upsilon_{F/G}^*(A),$$

where $\Upsilon_F^*(A)$ and $\Upsilon_G^*(A)$ denote the associated linear operators [6]. Using the expectation and variance, the stochastic optimization problem defined by (1) and (2) can be approximated by:

$$\begin{aligned} \min_{\mathbf{v}} : & \mathbb{E}[F(\mathbf{v})] + \kappa_1 \sqrt{\text{Var}[F(\mathbf{v})]} \\ \text{s.t.} : & \mathbf{K}(\mathbf{v}^k) \mathbf{A}^k = \mathbf{f}^k, \quad k = 0, \dots, K, \\ & \mathbb{E}[G(\mathbf{v})] + \kappa_2 \sqrt{\text{Var}[G(\mathbf{v})]} < \tau, \\ & \mathbf{v}_{\max j} \leq \mathbf{v}_j \leq \mathbf{v}_{\min j}, \quad j = 1, 2, \end{aligned} \quad (3)$$

where κ_1 , κ_2 and τ are prescribed parameters and \mathbf{K} denotes stiffness matrix.

4 Preliminary results

The initial configuration of the ECPS machine is depicted in Fig 2. The quantities that are taken subject

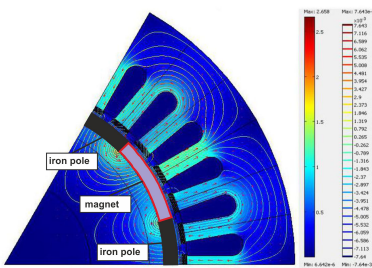


Fig. 2. Initial topology of the ECPSM.

to variations are the reluctivity of the iron pole and the PM pole both with the variation 10%. Also the permeability of the air-gap is assumed to be uncertain (10%). The random parameters are modeled by uniform distributions. For stochastic modeling the PCE with Legendre basis and the Stroud 5 formula in the SCM are used. The optimized rotor poles are shown in Fig. 3. For the optimal configuration the CT is calculated over a half of the period to assess the stator teeth interaction with the rotor poles, shown in Fig. 4.

¹ $v_j(\mathbf{x}, \xi) = H(\phi(\mathbf{x})) v_{j,1}(\xi) + [1 - H(\phi(\mathbf{x}))](\xi) v_{j,2}$

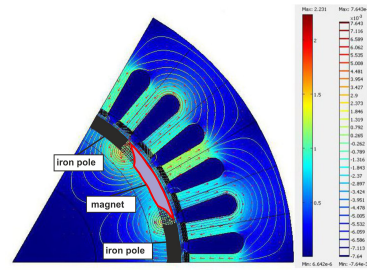


Fig. 3. Optimal topology of the ECPSM.

The applied methodology allows to reduce efficiently the CT about 60%, and improve the back-EMF waveform. This paper also highlights the unique design challenges of the proposed methodology.

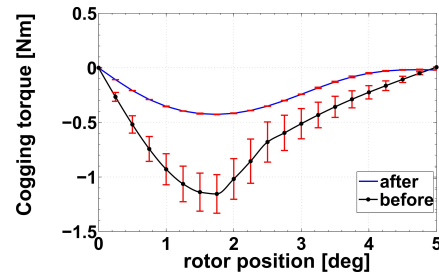


Fig. 4. The mean and the standard deviation of the CT before and after optimization.

Acknowledgement. The project nanoCOPS (Nanoelectronic COupled Problems Solutions) is supported by the European Union in the FP7-ICT-2013-11 Program under the grant agreement number 619166.

References

1. P. Putek, P. Paplicki, and R. Palka. Low Cogging Torque Design of Permanent Magnet Machine Using Modified Multi-Level Set Method With Total Variation Regularization. *IEEE Trans.Magn.*, 50:657–660, 2014.
2. P. Sergeant, G. Crevecoeur, L. Dupre and A. van den Bossche. Characterization and optimization of a permanent magnet synchronous machine. *COMPEL*, 28:272–284, 2008.
3. J. M. M. Rovers, J. W. Jansen, and E. A. Lomonova. Modeling of Relative Permeability of Permanent Magnet Material Using Magnetic Surface Charges *IEEE Trans.Magn.*, 49:2013–2919, 2013.
4. D. Xiu. Efficient Collocational Approach for Parametric Uncertainty Analysis. *Commun. in Comput. Phys.*, 2:293–309, 2007.
5. P. Putek, P. Paplicki, and R. Palka. Topology optimization of rotor poles in a permanent-magnet machine using level set method and continuum design sensitivity analysis. *COMPEL*, 66:1-21, 2014.
6. J. Conway *A Course in Functional Analysis*. Springer, New York, 1997.

Solution of Nonlinear Eigenmode Formulations for Externally Coupled Cavities

Bastian Bandlow and Rolf Schuhmann

FG Theoretische Elektrotechnik, EN 2, Technische Universität Berlin, Einsteinufer 17, D-10587 Berlin, Germany
bandlow@tet.tu-berlin.de, schuhmann@tet.tu-berlin.de

Summary. A recently proposed eigensolver for nonlinear eigenvalue problems is tested. The formulation arises from electromagnetic cavities which are externally coupled to hollow waveguides. The solver is capable to find all eigenmodes within a certain region of the complex spectrum.

1 Introduction

Within the area of computational electrodynamics, nonlinear eigenvalue problems may occur with several setups: Resonators containing dispersive (i.e. frequency dependent) materials [1], lossy periodic structures [2] and setups with transparent boundary conditions [3, 4]. One common way to deal with nonlinear eigenvalue problems of large-sparse matrix dimensions is the linearization near an educated guess of the target eigenvalue [4]. Alternatively, Jacobi-Davidson algorithms can be applied to the polynomial eigenproblem, where again a linearization is used to solve the low-dimensional projected eigenvalue problem [1, 5].

An integral eigenvalue solver for the nonlinear eigenvalue problem was recently proposed which is capable to compute a few eigenvalues from sparse matrices with large dimension [6]. Making use of the theorem of Keldysh the proposed algorithm allows for the computation of all eigenvalues which lie inside a predefined contour in the complex plane. The advantage is that no linearization is necessary, and the completeness of the set of eigenvalues in certain region of the complex plane can be guaranteed.

2 Eigenvalue Formulation with Waveguide Ports

The discrete Maxwell's eigenvalue problem is set up in the framework of the finite integration technique (FIT). The Maxwell grid equations can be written in frequency domain for possibly dispersive materials, neglecting currents, as

$$\mathbf{C}\hat{\mathbf{e}} = -i\omega\mathbf{M}_\mu(\omega)\hat{\mathbf{h}}, \quad \mathbf{C}^T\hat{\mathbf{h}} = i\omega\mathbf{M}_\varepsilon(\omega)\hat{\mathbf{e}}, \quad (1)$$

where $\mathbf{C} \in \mathbb{R}^{N \times N}$ is the topological curl-operator consisting of entries with $\{-1; 0; 1\}$. For the basics and notation of FIT see [7].

The eigenvalue formulation which allows for modeling of outgoing waves through waveguide ports can be derived as

$$(-\omega^2\mathbf{M}_\varepsilon + i\omega\mathbf{B}\mathbf{P}(\omega)\mathbf{B}^T + \mathbf{C}^T\mathbf{M}_{\mu^{-1}}\mathbf{C})\hat{\mathbf{e}} = 0. \quad (2)$$

The expression $\mathbf{B}\mathbf{P}(\omega)\mathbf{B}^T$ models the coupling to external waveguides: The column matrix \mathbf{B} contains the modal field pattern in the waveguides' cross-section at the boundary of the computational domain, and the diagonal matrix \mathbf{P} contains normalization coefficients for the generalized impedances [3, 8]. There is one column in \mathbf{B} and one entry in \mathbf{P} for each mode (index m) in each of the ports. Exemplarily, for TE modes the entries of \mathbf{P} read

$$p_{m,m}(\omega) = \sqrt{\omega^2 - \omega_{c,m}^2} / \omega \sqrt{1 - (\omega_{c,m}/\omega_{0,m})^2} \quad (3)$$

where $\omega_{c,m}$ is the cutoff frequency and $\omega_{0,m}$ is the reference frequency. While the neglect of waveguide ports in (2) would lead to a linear eigenvalue problem, the consideration of those ports renders the eigenvalue problem nonlinear. A similar formulation is reported for an FE approach in [9].

The nonlinear eigenvalue solver proposed in [6] is implemented in Matlab straight forwardly. The most important parameter besides the size and location of the closed contour Γ in the complex plane is the sampling by N parts of the contour for the numerical integration. For each of these N parts a linear system of full dimension has to be solved for a number of d right hand side vectors, where d is the dimension of a test subspace. This defines the major computational effort of the algorithm.

3 Numerical Example

The numerical test example is a simple rectangular waveguide with a dielectric inset, dividing the longitudinal direction in three parts. It supports trapped modes with radiation through the port apertures. The discretized problem by means of the finite integration technique leads to 31840 unknowns. The dimensions as well as the parameters of the waveguide port and the computational mesh can be found in Table 1.

Table 1. Data of the test example.

Waveguide	1st Mode	Computational Mesh
$22.86 \times 10.16 \text{ mm}^2$	TE	$21 \times 10 \times 64$ lines
length 100 mm	$f_c = 6.5 \text{ GHz}$	$2 \times$ symmetry
8.5 mm slab, $\epsilon_r = 12$		2 ports

4 Results

Figure 1 shows the user-chosen closed contour Γ around some mid-point (\times) and computed eigenvalues (*). Trapped eigenmodes can be identified in the complex ω -plane by a very low imaginary part corresponding to a very high quality factor. For the highest resolution Γ was sampled by $N = 170$ points in order to integrate by means of the trapezoidal rule [6]. Five eigenvalues appear within Γ and Fig. 2 shows that the residual norm is below 10^{-10} for $N = 170$. Moreover, for low sampling resolutions of Γ some

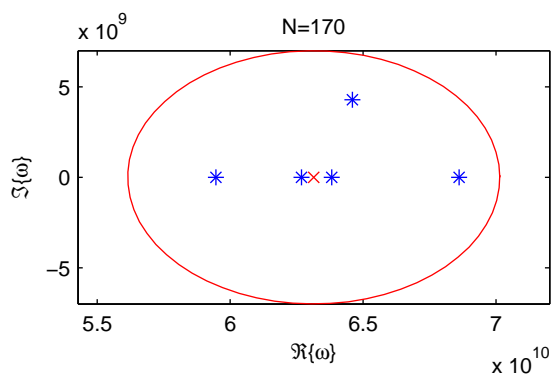


Fig. 1. Closed contour Γ around mid point (\times ,red) in the complex plane. Five eigenvalues (*) can be calculated when Γ is integrated with 170 samples.

additional eigenvalues may appear, which are not inside Γ (seven eigenvalues for sampling rates $N = 40$ to $N = 110$). Of course, these can easily be dropped by a simple a posteriori check. For very coarse samplings the residuals increase by some orders of magnitudes. The drawback of the finer resolution of Γ is an increased computation time as the diagram in Fig. 3 suggests.

5 Conclusions

The results from first numerical experiments with the integral nonlinear eigenvalue solver look promising: All expected eigenvalues can be computed, however the computational effort is high. Further improvements could be achieved by various modifications of the basic algorithm such as preconditioning or a smart control of residual errors.

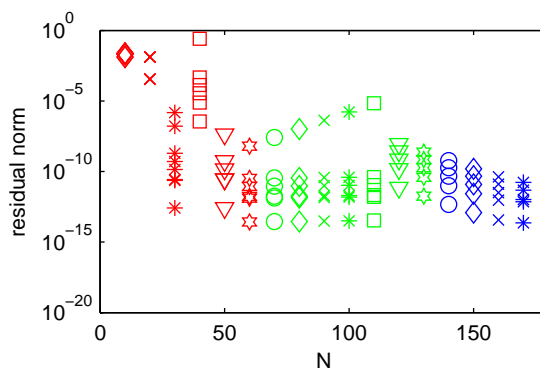


Fig. 2. Residual norm of the computed eigenvalues with increasing resolution of the integration path Γ .

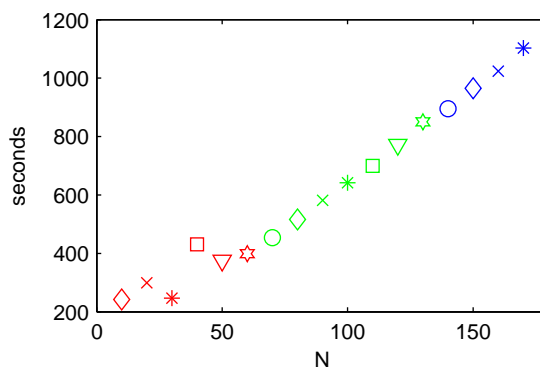


Fig. 3. Computation times for different N .

References

1. B. Bandlow and R. Schuhmann. Computation of eigenmodes in dispersive materials. In *SCEE 2008*, volume 14, pages 61–68. Springer, 1st edition, 2010.
2. B. Bandlow. PhD thesis, University of Paderborn, 2011.
3. T. Wittig, R. Schuhmann, and T. Weiland. Model order reduction for large systems in computational electromagnetics. *Linear Algebra and its Applications*, 415(2–3):499 – 530, 2006.
4. B. Bandlow and R. Schuhmann. Electromagnetic eigenmode characterization by sensitivity analysis. In *SCEE 2012, 11. - 14. September*, Zurich, Switzerland, 2012.
5. G. L. G. Sleijpen and H. A. Van der Vorst. A Jacobi-Davidson iteration method for linear eigenvalue problems. *SIAM J. Matrix Anal. Appl.*, 17(2):401–425, 1996.
6. W.-J. Beyn. An integral method for solving nonlinear eigenvalue problems. *Linear Algebra and its Applications*, 436(10):3839 – 3863, 2012.
7. T. Weiland. Time domain electromagnetic field computation with finite difference methods. *International Journal of Numerical Modelling: Electronic Networks, Devices and Fields*, 9(4):295–319, 1996.
8. O. Farle, M. Löscher, and R. Dyczij-Edlinger. Efficient fast frequency sweep without nonphysical resonances. *Electromagnetics*, 30(1-2):51–68, 2010.
9. W. Ackermann and T. Weiland. High precision cavity simulations. In *Proceedings of the 11th International Computational Accelerator Physics Conference*, pages 43 – 47, 2012.

On several Green's function methods for fast Poisson solver in free space

Dawei Zheng, Gisela Pöplau, and Ursula van Rienen

Universität Rostock dawei.zheng@uni-rostock.de, gisela.poeplau@uni-rostock.de,
ursula.van-rienen@uni-rostock.de

Summary. We summarize four closely related numerical methods for Poisson's equation in free space: Green's function method, integrated Green's function method, reduced integrated Green's function method, and cutting integrated Green's function method. A new and final routine called cutting reduced Green's function method is carried out recently as well. These methods can be used for different practical problems to accelerate the calculation. Numerical test results are also given to compare.

1 Introduction

Poisson's equation is broadly used in many areas, such as electrostatics, mechanical engineering and theoretical physics - for instance in beam dynamics simulations in particle accelerators. The Poisson's equation in free space plays a very important role in the calculation of space charge effects. The common way to solve this equation is to use the convolution of the density of charged particles and Green's function in free space, known as Green's function method. However, the numerical calculation may suffer from errors in some cases such as a very long cigar-shape or short pancake-shape bunch. Integrated Green's function is especially invented for such issue, that deals with analytical integration rather than a numerical integration. However, the computation is involved and time-consuming so that parallel computers are needed for efficiency.

We present some appropriate methods as accurate as the IGF method yet costing less CPU time for different practical problems. In general, the reduced integrated Green's function (RIGF) method, which is suitable in all problems calculating by IGF - for instance the near-bunch field calculation. While the cutting (integrated) Green's function (CIGF) method, which benefits far-bunch field calculation efficiently. A further new method, cutting reduced integrated Green's function (CRIGF) method can accelerate the calculations even more. This routine can also be used in other Poisson solver code to improve efficiency.

2 Green's function type methods

Regard Poisson's equation:

$$-\Delta\varphi(x,y,z) = \frac{\rho(x,y,z)}{\epsilon_0}, \text{ in } \Omega \subset \mathbb{R}^3, \quad (1)$$

with the Laplace operator Δ , the electric potential φ , the charge density ρ , the permittivity in vacuum ϵ_0 and the considered domain Ω .

The solution in free space [2] reads as:

$$\varphi(x,y,z) = \frac{1}{4\pi\epsilon_0} \cdot \iiint \rho(x',y',z')G(x,x',y,y',z,z')dx'dy'dz', \quad (2)$$

with Green's function

$$G(x,x',y,y',z,z') = \frac{1}{\sqrt{(x-x')^2 + (y-y')^2 + (z-z')^2}}. \quad (3)$$

The different Green's function methods discretize the integral Eq.(2) in different ways.

2.1 Green's function (GF) method

GF integral: With the well-known midpoint rule for the numerical integral in Eq.(2), the discretized GF formula [1] is given by

$$\varphi(x_i,y_j,z_k) \approx \frac{h_x h_y h_z}{4\pi\epsilon_0} \cdot \sum_{i'=1}^{N_x} \sum_{j'=1}^{N_y} \sum_{k'=1}^{N_z} \rho(x_{i'},y_{j'},z_{k'})G(x_i,x_{i'},y_j,y_{j'},z_k,z_{k'}). \quad (4)$$

However, this often used Green's function method is not accurate enough in some cases [2]. Therefore new numerical integrals are studied as:

$$\varphi(x_i,y_j,z_k) \approx \frac{1}{4\pi\epsilon_0} \cdot \sum_{i'=1}^{N_x} \sum_{j'=1}^{N_y} \sum_{k'=1}^{N_z} \rho(x_{i'},y_{j'},z_{k'})\tilde{G}(x_i,x_{i'},y_j,y_{j'},z_k,z_{k'}), \quad (5)$$

where the $\tilde{G}(x_i,x_{i'},y_j,y_{j'},z_k,z_{k'})$ will be introduced in the following subsections.

2.2 Integrated Green's function (IGF) method

IGF integral: With the summation of integrals for Green's function over each grid cell $[x_i - \frac{h_x}{2}, x_i + \frac{h_x}{2}] \times [y_j - \frac{h_y}{2}, y_j + \frac{h_y}{2}] \times [z_k - \frac{h_z}{2}, z_k + \frac{h_z}{2}]$, the IGF integral formula is calculated from the Green's function in Eq.(3) like :

$$\tilde{G}_I(x_i, x_{i'}, y_j, y_{j'}, z_k, z_{k'}) = \int_{x_{i'}-h_x/2}^{x_{i'}+h_x/2} \int_{y_{j'}-h_y/2}^{y_{j'}+h_y/2} \int_{z_{k'}-h_z/2}^{z_{k'}+h_z/2} G(x_i, x', y_j, y', z_k, z') dx' dy' dz'. \quad (6)$$

This integral can be calculated from the primitive function (antiderivative) of Eq.(3) derived by MATHEMATICA, its formal expression can be found in [3].

However, the calculation of the IGF integral is very involved and time consuming. Therefore the other type Green's function integrals are introduced for different purposes.

2.3 Reduced integrated Green's function (RIGF) method

If the required field domain just covers the charged bunch, the RIGF integral [4] is recommended for high efficiency.

RIGF integral:

$$\tilde{G}_R(x_i, y_j, z_k) = \begin{cases} \tilde{G}_I(x_i, y_j, z_k), & (1, 1, 1) \leq (i, j, k) \leq (R_x, R_y, R_z); \\ h_x h_y h_z G(x_i, y_j, z_k), & \text{otherwise;} \end{cases}$$

where (R_x, R_y, R_z) should be determined firstly.

A very long cigar-shape uniform ellipsoidal beam is taken as the test example. The result shown as Table(1), where, the $\hat{\eta}_\varphi$ and $\hat{\eta}_E$ stand for the relative er-

Table 1. Comparison of IGF and RIGF

N	$\hat{\eta}_\varphi$	$\hat{\eta}_E$	IGF Time	$\hat{\eta}_\varphi$	$\hat{\eta}_E$	RIGF Time
32	0.0239	0.0500	2.7158 s	0.0242	0.0501	0.3525 s
64	0.0032	0.0212	18.0722 s	0.0031	0.0212	2.2570 s
128	0.0012	0.0140	77.7485 s	0.0013	0.0140	15.6330 s

rors of potential and norm of the corresponding electric field, respectively. In principle, the RIGF integral is a mixed GF and IGF integrals.

2.4 Cutting integrated Green's function (CIGF) method

If the required field domain is much larger than the charged bunch, the CIGF integral [5] is recommended for high efficiency.

CIGF integral:

$$\tilde{G}_C(x_i, y_j, z_k) = \begin{cases} \tilde{G}_I(x_i, y_j, z_k), & (1, 1, 1) \leq (i, j, k) \leq (C_x, C_y, C_z); \\ 0, & \text{otherwise;} \end{cases}$$

where (C_x, C_y, C_z) is determined by the domain-bunch ratio. The large area with zero charge density guarantees the CIGF exactitude.

Table 2. Comparison between IGF and CIGF

N	$\hat{\eta}_\varphi$	$\hat{\eta}_E$	IGF Time	CIGF Time
32	0.0587	0.0619	1.5175 s	0.6233 s
64	0.0130	0.0334	10.1015 s	3.6115 s
128	0.0045	0.0290	78.5222 s	27.6219 s

An ideal uniform ellipsoidal beam is taken as the test example. The results are shown in Table(2). In principle, the CIGF integral is equal to IGF integrals, when the field domain is much larger than the charged domain.

3 Cutting reduced integrated Green's function (CRIGF) method

Furthermore, the combination of RIGF and CIGF as the CRIGF should be more efficient than pure CIGF for the same problem.

$$\tilde{G}_{CR}(x_i, y_j, z_k) =$$

$$\begin{cases} \tilde{G}_I(x_i, y_j, z_k), & (1, 1, 1) \leq (i, j, k) \leq (R_x, R_y, R_z); \\ h_x h_y h_z G(x_i, y_j, z_k), & (R_x, R_y, R_z) \leq (i, j, k) \leq (C_x, C_y, C_z); \\ 0, & \text{otherwise;} \end{cases}$$

where (C_x, C_y, C_z) and (R_x, R_y, R_z) are chosen as above.

For the same example as CIGF method, the results are shown in Table(3).

Table 3. Comparison of CIGF and RCIGF

N	$\hat{\eta}_\varphi$	$\hat{\eta}_E$	CIGF Time	$\hat{\eta}_\varphi$	$\hat{\eta}_E$	CRIGF Time
32	0.0587	0.0619	0.6233 s	0.0587	0.0619	0.2231 s
64	0.0130	0.0334	3.6115 s	0.0130	0.0334	0.6857 s
128	0.0045	0.0290	27.6219 s	0.0044	0.0292	5.8347 s

In all, the CRIGF method can be chosen as a routine for any Poisson solver code for various practical problems coming from different disciplines.

References

1. R.W. Hockney and J. W. Eastwood. Computer Simulation Using Particles. Institut of Physics Publishing, Bristol, (1992).
2. J. Qiang, S. Lidia, R.D. Ryne, and C. Limborg-Deprey, Phys. Rev. ST Accel. Beams, vol 9, 044204 (2006).
3. J.Qiang, S. Lidia, R.D. Ryne, and C. Limborg-Deprey, Phys. Rev. ST Accel. Beams, vol 10, 129901 (2007).
4. D. Zheng, G. Pöplau, U. van Rienen, Reduced integrated Green's function method for fast Poisson solver in beam dynamics simulation. submitted to Phys. Rev. ST Accel. Beams.
5. D. Zheng, A. Markovič, G. Pöplau, U. van Rienen, Study of a fast convolution method for solving the space charge fields of charged particle bunches. IPAC (2014).

Turning points in nonlinear circuits

Ignacio García de la Vega¹ and Ricardo Rianza²

¹ Departamento de Matemática Aplicada a las Tecnologías de la Información
Escuela Técnica Superior de Ingenieros de Telecomunicación
Universidad Politécnica de Madrid
Ciudad Universitaria s/n. 28040 - Madrid, Spain
ignacio.garciadelavega@gmail.com (corresponding author)

² Departamento de Matemática Aplicada a las Tecnologías de la Información
Escuela Técnica Superior de Ingenieros de Telecomunicación
Universidad Politécnica de Madrid
Ciudad Universitaria s/n. 28040 - Madrid, Spain
ricardo.riaza@upm.es

Summary. This work addresses bifurcation phenomena in nonlinear circuits. Our analysis is focused on quadratic turning points, which, in certain circumstances, yield saddle-node bifurcations. Algebraic conditions guaranteeing the existence of this kind of points are well-known in the context of explicit ODEs [3, 7, 8]. We firstly adequate these conditions to semiexplicit DAEs, which naturally accommodate nonlinear circuit models. Afterwards, we analyze these reformulated conditions in terms of the circuit topology and the devices' characteristics.

1 Introduction

Bifurcation theory plays a key role in the qualitative analysis of dynamical systems. In nonlinear circuit theory, bifurcations of equilibria describe qualitative changes in the local phase portrait near an operating point, and are important from both an analytical and a numerical point of view. In this work we address a systematic characterization of local bifurcations in circuit-theoretic terms; specifically, we analyze quadratic turning points, eventually yielding saddle-node bifurcations under additional conditions. Our goal is to arrive at a description of the algebraic conditions characterizing these turning points in terms of the underlying circuit digraph and the devices' characteristics.

2 Quadratic turning points

Consider the system of differential equations

$$x' = f(x, \mu) \quad (1)$$

with $x \in \mathbb{R}^n$, f sufficiently smooth and depending on a parameter $\mu \in \mathbb{R}$. Provided that $f(x^*, \mu^*) = 0$, (x^*, μ^*) is called a *quadratic turning point* of (1) if the conditions 1-3 below are satisfied [3]. We denote by v (resp. w) a non-vanishing right (resp. left) eigenvector of the matrix of partial derivatives $D_x f(x^*, \mu^*)$.

1. $\text{rk } D_x f(x^*, \mu^*) = n - 1$;
2. $w D_\mu f(x^*, \mu^*) \neq 0$;
3. $w D_{xx} f(x^*, \mu^*)(v, v) \neq 0$.

With terminological abuse, we will often use the expression “turning point” to mean a “quadratic turning point”.

If, additionally,

- 4 the algebraic multiplicity of the null eigenvalue of $D_x f(x^*, \mu^*)$ is one; and
- 5 the remaining eigenvalues of $D_x f(x^*, \mu^*)$ have non-zero real parts,

then (x^*, μ^*) is called a *saddle-node bifurcation point*, because the system undergoes a saddle-node bifurcation as μ crosses μ^* [4, 5, 7, 8].

Our purpose in this work is to provide a circuit-theoretic analysis guaranteeing that conditions 1-3 above are satisfied. Condition 1 means that $D_x f(x^*, \mu^*)$ has a zero eigenvalue with geometric multiplicity one. Condition 2 can be equivalently written as

$$D_\mu f(x^*, \mu^*) \notin \text{im } D_x f(x^*, \mu^*)$$

and also as

$$\text{rk } Df(x^*, \mu^*) = n, \quad (2)$$

where Df is the full matrix of partial derivatives of f , that is, $Df = (D_x f \ D_\mu f)$. Equation (2) implies that $f(x, \mu) = 0$ describes a curve of equilibria locally around (x^*, μ^*) ; it is not difficult to check that this curve is tangent to the hyperplane $\mu = \mu^*$. Finally, condition 3 can be recast as

$$D_{xx} f(x^*, \mu^*)(v, v) \notin \text{im } D_x f(x^*, \mu^*) \quad (3)$$

and in turn this expresses a transversality condition (in the hyperplane $\mu = \mu^*$) between the so-called singular manifold, defined by $\det D_x f(x, \mu^*) = 0$, and the space $\ker D_x f(x, \mu^*)$.

3 Semiexplicit DAEs and circuit models

Characterizing in circuit-theoretic terms conditions 1-3 above is a two-fold purpose. First, one has to reformulate such conditions in terms of a differential-algebraic equation (DAE), which is the feasible form available in practice for a nonlinear circuit model. Second, the conditions must be reformulated in terms of the underlying digraph and the devices' characteristics.

The natural form of a circuit model is a semiexplicit DAE, namely

$$x' = g(x, y, \mu) \quad (4)$$

$$0 = h(x, y, \mu) \quad (5)$$

with $x \in \mathbb{R}^n$, $y \in \mathbb{R}^m$, $\mu \in \mathbb{R}^l$; g and h are sufficiently smooth. We will only consider systems with a scalar parameter ($l = 1$). It will be assumed that (x^*, y^*, μ^*) is an equilibrium point, and the first requirement we will impose on this system is the nonsingularity of $D_y h(x^*, y^*, \mu^*)$. This (index-one) condition [2] makes it easier to reformulate the turning point conditions in DAE terms.

Our analysis will be based on the use of branch-oriented circuit models [6], defined by

$$C(v_c)v_c' = i_c \quad (6)$$

$$L(i_l)i_l' = v_l \quad (7)$$

$$0 = B_c v_c + B_l v_l + B_g v_g + B_r v_r + B_u v_u + B_j v_j \quad (8)$$

$$0 = A_c i_c + A_l i_l + A_g i_g + A_r i_r + A_u i_u + A_j i_j \quad (9)$$

$$0 = i_g - \gamma(v_g) \quad (10)$$

$$0 = v_r - \eta(i_r), \quad (11)$$

where we denote the branch voltages by v , the currents by i , and use the subscripts c , l , g , r , u and j to reference capacitors, inductors, voltage-controlled resistors, current-controlled resistors, voltage sources and current sources, respectively. The attention is restricted to autonomous problems and therefore v_u and i_j are assumed to take on constant values defined by DC sources.

Kirchhoff laws, corresponding to equations (8) and (9), are expressed in terms of the incidence matrix A and a reduced loop matrix B of the underlying digraph (cf. e.g. [1]). Each column in matrices A and B is linked with a branch in the circuit. The rank of certain submatrices of A and B depends on the presence or absence of certain topological structures (loops and cutsets) in the indexed branches; therefore, the imposition of the algebraic conditions discussed in Section 2 entails certain configurations of the circuit devices. The attention in a first step will be focused on problems in which a given nonlinear resistor (e.g. a diode) enters a locally-active region (for instance because of a tunneling effect), assuming that the remaining devices are strictly locally passive. This setting makes it possible to characterize conditions 1-3 of Section 2 in circuit-theoretic terms.

The results are of potential interest in numerical continuation techniques directed to nonlinear circuit

dynamics. They should also pave the way for a future analysis of other bifurcation phenomena, involving not only saddle-node points but also for instance Hopf or Takens-Bogdanov bifurcations.

Acknowledgements

Research supported by Project MTM2010-15102 of Ministerio de Ciencia e Innovación, Spain.

References

1. B. Bollobás, *Modern Graph Theory*. Springer-Verlag, New York, 1998.
2. K. E. Brenan, S. L. Campbell and L. R. Petzold. *Numerical Solution of Initial-Value Problems in Differential Algebraic Equations*. SIAM, Philadelphia, 1996.
3. W. J. F. Govaerts. *Numerical Methods for Bifurcations of Dynamical Equilibria*. SIAM, Philadelphia, 2000.
4. J. Guckenheimer and P. Holmes. *Nonlinear Oscillations, Dynamical Systems, and Bifurcations of Vector Fields*. Springer-Verlag, New York, 1983.
5. L. Perko. *Differential Equations and Dynamical Systems*. Springer-Verlag, New York, 1991.
6. R. Riaza, *Differential-Algebraic Systems*. World Scientific, Singapore, 2008.
7. J. Sotomayor. Structural stability and bifurcation theory. In *Dynamical Systems*, M. M. Peixoto (ed.). Academic Press, New York, 549–560, 1973.
8. J. Sotomayor. Generic bifurcations of dynamical systems. In *Dynamical Systems*, M. M. Peixoto (ed.). Academic Press, New York, 561–582, 1973.

Boundary Integral Formulation for the Electrical Response of an Axon to an Extracellular Stimulation

Fernando Henríquez¹, Carlos Jerez-Hanckes¹, and Fernando Altermatt²

¹ Department of Electrical Engineering, Escuela de Ingeniería, Pontificia Universidad Católica de Chile, Santiago, Chile
fjhenriq@uc.cl, cjerez@ing.puc.cl

² Department of Anesthesiology, Escuela de Medicina, Pontificia Universidad Católica de Chile, Santiago, Chile.
fernando.altermatt@gmail.com

Summary. We present a two-dimensional boundary integral formulation coupled with a second-order time evolution scheme to model Hodgkin-Huxley nerve impulse time propagation.

1 Introduction

Stimulation of nerve fibers through external electrodes is widely used in several clinical procedures, hence the interest in modeling such phenomena. Boundary integral-based formulations such as the one proposed by Leon *et al.* [1] couple the Hodgkin–Huxley (H–H) model [2] to a membrane potential assumed to be constant. Ying *et al.* [3] propose a FEM formulation in which a non-zero thickness nerve is considered with external stimuli set as constant electric fields. The proposed FEM is decoupled from the time evolution equations allowing to solve both sub-problems independently. This reduces stability and requires small time steps with huge computational requirements for a single axon. Nonetheless, the authors show that time response around the surface of the axon changes, thus discarding Leon *et al.*'s hypothesis.

We aim at reducing computational effort for systems by using the so-called *Multiple Traces Formulation* (MTF) [4], coupled to the H–H model through a second order accuracy time stepping method allow us to obtain an excellent overall performance with a much reduced number of unknowns.

2 Single axon formulation

Consider a trasverse cut of an axon, denoted by Ω_i , with cellular membrane Γ and extracellular space $\Omega_e := \mathbb{R}^2 \setminus \bar{\Omega}_i$, with conductivities σ_i and σ_e , respectively. The membrane is modeled as a zero-thickness interface. Set ϕ_e as an electrical potential defined in the extracellular space such that $\Delta\phi_e = 0$ over Ω_e . The potential ϕ_e plays the role of the extracellular excitation. Define u_i and u_e over Ω_i and Ω_e such that

$$u_i := u \quad \text{in } \Omega_i, \quad (1)$$

$$u_e := u - \phi_e \quad \text{in } \Omega_e \text{ and} \quad (2)$$

$$|u_e| \sim \|\mathbf{x}\|^{-1} \quad \text{as } \|\mathbf{x}\| \rightarrow \infty \quad (3)$$

The volume problem is to seek u_i and u_e satisfying

$$\Delta u_\alpha = 0 \quad \text{in } \Omega_\alpha, \quad \alpha \in \{i, e\} \quad (4)$$

$$u_i - u_e = v + \phi_e \quad \text{on } \Gamma \quad (5)$$

$$\begin{aligned} \mathbf{n}_i \cdot (\sigma_i \nabla u_i) + \mathbf{n}_e \cdot (\sigma_e \nabla u_e) = \\ -\mathbf{n}_e \cdot (\sigma_e \nabla \phi_e) \quad \text{on } \Gamma \end{aligned} \quad (6)$$

wherein \mathbf{n}_i and \mathbf{n}_e denote inner and outer normals to Γ . Transmembrane current $i = -\mathbf{n}_i \cdot (\sigma_i \nabla u_i)$ and voltage v evolve in time following H–H equations. Let $i_{\text{ion}}(v, \mathbf{q})$ be the ionic current flowing across Γ , c_m the membrane capacitance per unit area, and \mathbf{q} a vector of state variables. Then, the H–H system can be written as

$$c_m \frac{\partial v}{\partial t} = i - i_{\text{ion}}(v, \mathbf{q}) \quad \text{on } \Gamma \text{ and } t > 0, \quad (7)$$

$$\frac{\partial \mathbf{q}}{\partial t} = \mathcal{M}(v, \mathbf{q}) \quad \text{on } \Gamma \text{ and } t > 0. \quad (8)$$

$$v(0) = v_0 \quad \text{on } \Gamma \quad (9)$$

$$\mathbf{q}(0) = \mathbf{q}_0 \quad \text{on } \Gamma \quad (10)$$

The overall problem is to find v over Γ and as a function of the time variable t satisfying equations (4)–(6) and (7)–(10).

2.1 Multiple Traces Formulation

For a given v , (4)–(6) can be rewritten in terms of Boundary Integral Operators (BIOs) over Γ . Functions u_α , $\alpha \in \{e, i\}$, satisfy the interior Calderón projector identities

$$\begin{pmatrix} u_\alpha \\ \partial_\alpha u_\alpha \end{pmatrix} = \begin{pmatrix} \frac{1}{2}\mathbf{I} - \mathbf{K}_\alpha & \mathbf{V}_\alpha \\ \mathbf{D}_\alpha & \frac{1}{2}\mathbf{I} + \mathbf{K}'_\alpha \end{pmatrix} \begin{pmatrix} u_\alpha \\ \partial_\alpha u_\alpha \end{pmatrix} \quad \text{on } \Gamma,$$

where $\partial_\alpha u_\alpha = \mathbf{n}_\alpha \cdot \nabla u_\alpha$. Set $\Pi_\alpha := (u_\alpha|_\Gamma, \partial_\alpha u_\alpha)^\top$, $\Lambda := (v, 0)^\top$, and

$$\mathbb{A}_\alpha := \begin{pmatrix} -\mathbf{K}_\alpha & \mathbf{V}_\alpha \\ \mathbf{D}_\alpha & \mathbf{K}'_\alpha \end{pmatrix}, \quad \mathbb{X}_\sigma := \begin{pmatrix} \text{Id} & 0 \\ 0 & -\frac{\sigma_e}{\sigma_i} \text{Id} \end{pmatrix}.$$

Following the MTF, (4)–(6) can be rewritten as

$$\begin{pmatrix} \mathbb{A}_e & -\frac{1}{2}\mathbb{X}_\sigma^{-1} \\ -\frac{1}{2}\mathbb{X}_\sigma & \mathbb{A}_i \end{pmatrix} \begin{pmatrix} \Pi_e \\ \Pi_i \end{pmatrix} = \frac{1}{2} \begin{pmatrix} -(\Phi + \Lambda) \\ \mathbb{X}_\sigma(\Phi + \Lambda) \end{pmatrix} \quad (11)$$

2.2 Time stepping method

For $N^t \in \mathbb{N}$, let $\Pi^t = \{t_n\}_{n=0}^{N^t}$ be a uniform partition of $[0, T]$ such that $t_n = n\tau$, where $\tau = T/N^t$. Also, we define $t_{n+1/2} = t_n + \tau/2$. For a given time-dependent quantity ϕ , define $\phi_n = \phi(t_n)$ and $\hat{\phi}^{n+1/2} = \frac{3\phi^n - \phi^{n-1}}{2}$. Following Ganesh & Mustapha [5], the time-discrete representation of (11) and (7)–(10) is

$$\begin{pmatrix} \mathbb{A}_e & -\frac{1}{2}\mathbb{X}_\sigma^{-1} & (1/4, 0)^\top \\ -\frac{1}{2}\mathbb{X}_\sigma & \mathbb{A}_i & (-1/4, 0)^\top \\ (0, 0) & (0, \sigma_i) & \frac{c_m}{\tau} \end{pmatrix} \begin{pmatrix} \Pi_e \\ \Pi_i \\ v^{n+1} \end{pmatrix} = \begin{pmatrix} -\frac{1}{2}(\Phi + \frac{1}{2}\Lambda^n) \\ \frac{1}{2}\mathbb{X}_\sigma(\Phi + \frac{1}{2}\Lambda^n) \\ \frac{c_m}{\tau}v^n - i_{\text{ion}}(\hat{v}^{n+1/2}, \hat{\mathbf{q}}^{n+1/2}) \end{pmatrix}$$

for $n = 1 \dots N^t - 1$, (12)

where $\Lambda^n = (v^n, 0)^\top$, along with

$$\mathbf{q}^{n+1} = \mathbf{q}^1 + \tau \mathcal{M}(\hat{v}^{n+1/2}, \hat{\mathbf{q}}^{n+1/2}),$$

for $n = 1 \dots N^t - 1$. (13)

Inputs values for v^0 and \mathbf{q}^0 , given by the initial conditions, and for v^1 and \mathbf{q}^1 that must be computed, for example, using a predictor–corrector method [5].

The presented time stepping method has a rate of convergence τ^2 . Since low order discretization of the integral equations leads to $\mathcal{O}(h^2)$ -convergence (h : mesh size) for smooth solutions, it can be showed that the fully discrete problem has a rate of convergence equal to $h^2 + \tau^2$. Choosing $h \propto \tau$ it is possible to recover a rate of convergence equal to two for the fully discrete problem [5].

3 Results

We ran simulations assuming a two dimensional circular axon and the external excitation equal to $\phi_e = -\mathbf{E} \cdot \mathbf{x}$, where \mathbf{E} is an constant electric field pointing to $+\mathbf{x}$, as defined in Figure 1 and \mathbf{x} is vector position measured from the axon's center. Table 1 shows convergence results for a linear behavior assumption of the membrane, i.e. $i_{\text{ion}} \propto v$ [6], using norms

$$\|\phi\|_2 = \left(\int_0^T \|\phi(t)\|_{L^2(\Gamma)} dt \right)^{1/2}$$

$$\|\phi\|_\infty = \sup_{t \in [0, T]} \|\phi(t)\|_{L^2(\Gamma)}$$

and for equal numbers of spatial dofs and time steps. Figure 2 shows the results for the positions defined in Figure 1 for the full H–H system.

Acknowledgement. This work was funded by VRI Interdisciplina 11/2011 by Pontificia Universidad Católica de Chile and FONDECYT Iniciación 11121166.

Table 1. Error order of convergence values for $i_{\text{ion}} \propto v$.

N	$\ u - U^n\ _2$	e.o.c	$\ u - U^n\ _\infty$	e.o.c
10	1.49×10^{-2}	–	4.72×10^{-1}	–
50	5.79×10^{-4}	-2.01	1.90×10^{-2}	-1.99
100	1.44×10^{-4}	-2.00	4.76×10^{-3}	-2.00
500	5.84×10^{-6}	-1.99	1.93×10^{-4}	-1.98

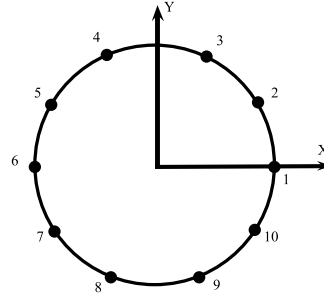


Fig. 1. Transmembrane potential calculation points.

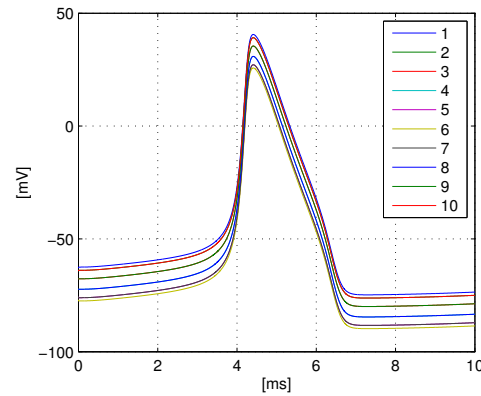


Fig. 2. Results for full H–H at points according to Fig. 1

References

1. L. J. Leon and F. A. Roberge. A new cable model formulation based on Green's theorem. *Annals of Biomedical Engineering*, 18:1–17, 1990.
2. A.L. Hodgkin and A.F. Huxley. A quantitative description of membrane current and its application to conduction and excitation in nerve. *The Journal of Physiology*, 18:1–17, 1990.
3. W. Ying and C. S. Henriquez. Hybrid Finite Element Method for Describing the Electrical Response of Biological Cells to Applied Fields. *IEEE Transactions on Biological Engineering*, 117:500–544, 1962.
4. R. Hiptmair and C. Jerez–Hanckes. Multiple traces boundary integral formulation for Helmholtz transmission problems. *Advances in Computational Mathematics*, 37:39–91, 2012.
5. M. Ganesh and K. Mustapha. A fully discrete H^1 -Galerkin method with quadrature for nonlinear advection–diffusion–reaction equations. *Numerical Algorithms*, 43:355–383, 2006.
6. W. Krassowska and J. C. Neu, Response of a single cell to an external electric field *Biophysics Journal*, 66:1768–1776, 1994.

Multi-GPU Acceleration of Algebraic Multigrid Preconditioners

Christian Richter¹, Sebastian Schöps², and Markus Clemens¹

¹ Bergische Universität Wuppertal, Chair of Electromagnetic Theory, 42119 Wuppertal, Germany
christian.richter@uni-wuppertal.de, clemens@uni-wuppertal.de

² Technische Universität Darmstadt, Graduate School of Computational Engineering Institut für Theorie Elektromagnetischer Felder, 64285 Darmstadt, Germany *schoeps@gsc.ce.tu-darmstadt.de*

Summary. Solving discrete poisson problems, as they can be found in the finite element analysis of electrostatic problems, can be accelerated by the usage of GPUs. To overcome the limitations in memory and speed, multi-GPU implementations are needed. In this paper a multi-GPU code is presented that is based on the CUSP library and especially its algebraic multigrid preconditioner. The computational efficiency is underlined by an application example.

1 Introduction

Accuracy requirements and thus problem sizes of finite element simulations in computational electromagnetics, e.g. for the insulator as shown in Fig. 1, have been increasing over the years. Recently, the computer architecture has begun to change too: single threaded codes do not benefit from the increasing computational power as before. Thus the usage of parallel codes and in particular graphics processor units (GPUs) have become an important field of research. The CUSP library [2] provides state-of-the-art linear algebra operations and solvers for GPUs, e.g. the conjugate Gradients Method (CG) with Algebraic Multigrid (AMG) Preconditioner using smoothed aggregation [1, 3].

However some features are missing. For example, even though global memory increases with each GPU generation, it remains a critical limitation and various approaches for memory reductions have been discussed [4]. One possibility to accelerate calculation speed as well as reducing memory demand is a mixed precision approach. When using a single precision preconditioner in a double precision outer CG loop, this does typically not significantly influence the number of iterations [5]. However, due to reduction, data can be transferred faster and this leads also to an increased calculation speed. An implementation based on CUSP has been presented recently in [6].

Using multiple GPUs is another promising approach for increasing the available memory and calculation speed at the same time. However, there is a trade-off between acceleration and memory consumption: at best acceleration and memory scale linearly with the number of used GPUs. However, communication overhead reduces the gain in practice. This can be overcome when data redundancy is accepted, i.e. complete vectors for the sparse matrix-vector multiplication (SpMV) are exchanged.

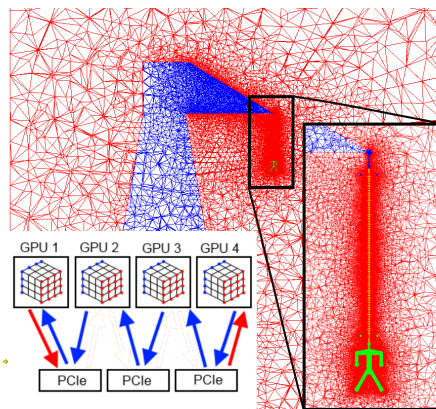


Fig. 1. Mesh-grid of the numerical example and parallel data exchange between multiple GPUs

2 Multiple GPUs in CUSP

To ensure future compatibility with the ongoing development of CUSP, the multi-GPU environment has been realized as an independent add-on. It contains classes that hold the distributed vectors, matrices and the AMG-preconditioner. Additional routines manage communications and the parallel BLAS operations on the GPUs.

The matrix class holds pointers to the matrix parts that are distributed row by row across the GPUs, see Fig. 2. This ensures a fast distribution without complex partitioning algorithms and a good load balancing across all GPUs. The vector class holds a copy of the whole vector and a view for the corresponding rows resulting from a given matrix class.

Vectors can be copied to all GPUs (*copy-1n*), gathered from all GPUs (*gather-n1*), scattered across the GPUs (*scatter-1n*) and combined on all GPUs from parts that are distributed across all GPUs (*gather-nn*). By using the streams called *instruction pipelines* in CUDA, data exchange between all GPUs takes place simultaneously, utilizing the PCIe's 6 GB/s up- and download for every GPU at a time as shown in Fig. 1. Especially the time-consuming process of copying a vector to all GPUs (*copy-1n*) and gathering a distributed vector (*gather-nn*) can be realized almost independently from the number of GPUs used. The AMG class stores the distributed matrices and vectors of all levels. It supports basic operations to distribute the CUSP AMG preconditioner across the

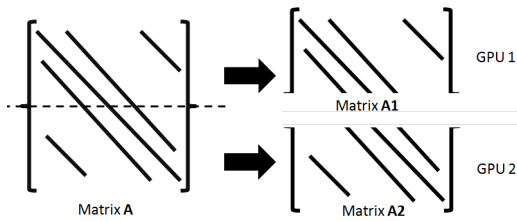


Fig. 2. Distribution of a matrix across multiple GPUs

GPUs and solve the preconditioner on multiple GPUs. These operations enable the execution of a CG solver with AMG preconditioner on multiple GPUs from a single host.

3 Numerical Example

As real-world example the finite element simulation of the high voltage isolator from [7] is presented, Fig. 1. The discrete model has 1.5e6 degrees of freedom (DoF) with a linear system matrix consisting of 21e6 nonzero entries. The problem is solved up to a relative residual of 1e-12. All calculations are performed on the same compute server running CentOS 6.5: the host is equipped with an Intel Xeon E5-2670, 128 GB RAM. Four NVIDIA Tesla K20Xm GPU accelerators are attached to the host. To ensure data consistency the error-correcting code (ECC) is enabled. This reduces the effective bandwidth of all GPUs by 20% from 250 GB/s to 200 GB/s each. The code is compiled using OpenMP for host parallelization and architecture model 3.5 on the device. We use CUDA 5.0, Thrust 1.8.0 and CUSP 0.4.

Fig. 3 shows the computational time for basic operations executed on one to four GPUs, respectively. Table 1 shows the memory requirements of the system matrix for the linear system including the matrix and two vectors. For comparison the problem was solved in [4] using several libraries: on the host Petsc with AMG preconditioner (20.178 s), Trilinos ML (17.291 s), CUSP's host (16.642 s) and GPU implementation (4.754 s) are benchmarked. The host computations had access to all cores via OpenMP or MPI. Nonetheless, CUSP on a single GPU outperforms all host implementations. The operations of the new multi-GPU code are again about 3 times faster, see Fig. 3. However, the overall solver performance is reduced by communication processes.

4 Conclusion

It has been shown that multiple GPUs allow to solve larger problems and to reduce calculation time. As

Table 1. Memory usage per GPU for the linear system of 1.5e6 DoF

	1 GPU	2 GPU	4 GPUs
Matrix	256 MB	131 MB	66 MB
LinSys	278 MB	154 MB	88 MB

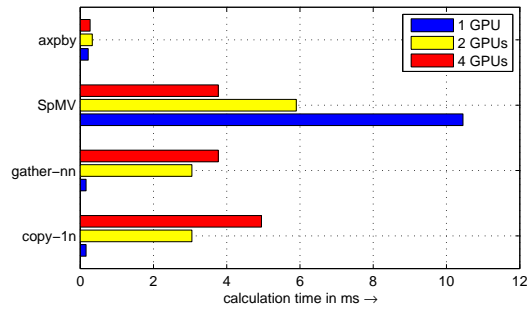


Fig. 3. Computational time for basic operations

there is a large gap between the PCIe and the GPUs intern bandwidth effective communication routines were developed. Communication was hidden behind other calculation. Speedups up to a factor of 3× could be obtained when using four GPUs. The memory consumption has been reduced to a factor of 0.5 for a sparse matrix vector operation. In the full paper, these results will be presented in context with the AMG-CG implementation.

Acknowledgement. This research is supported by the 'Excellence Initiative' of the German Federal and State Government and the Graduate School CE at the TU Darmstadt. The authors would like to thank NVIDIA for donating a Tesla K20 to the CUDA Research Center at the BU Wuppertal and C. Schmitt for his HPC support at TU Darmstadt.

References

1. K. Stüben, Algebraic multigrid (AMG): An introduction with applications," GMD, Report 53, Mar. 1999.
2. N. Bell and M. Garland, "CUSP: Generic parallel algorithms for sparse matrix and graph computations," 2012, version 0.3.0. [Online].
3. N. Bell, S. Dalton, and L. N. Olson, "Exposing fine-grained parallelism in algebraic multigrid methods," *SIAM J. Sci. Comput.*, vol. 34, no. 4, 2012.
4. C. Richter, S. Schöps, and M. Clemens, GPU-Acceleration of Algebraic Multigrid Preconditioners for Discrete Elliptic Field Problems," *IEEE Trans. Magn.*, vol. 50, no. 2, pp. 461 – 464, 2 2014.
5. D. Göddeke., "Fast and accurate finite-element multigrid solvers for PDE simulations on GPU clusters," *Berlin, Logos-Verlag*, 2011.
6. C. Richter, S. Schöps, and M. Clemens, GPU-Accelerated Mixed Precision Algebraic Multigrid Preconditioners for Discrete Elliptic Field Problems," *Ninth International Conference on the Computation in Electromagnetics (CEM 2014)*.
7. H. Ye, M. Clemens, and J. Seifert, "Electro-quasistatic field simulation for the layout optimization of outdoor insulation using microvaristor material," (*IEEE Trans. Magn.*), vol. 49, no. 5, pp. 1709 – 1712, 5 2013.

Multirate GARK schemes for multiphysics problems

Andreas Bartel¹, Michael Günther¹, Christoph Hachtel¹, and Adrian Sandu²

¹ Bergische Universität Wuppertal, Institute of Mathematical Modelling, Analysis and Computational Mathematics (IMACM), Gaußstraße 20, D-42119 Wuppertal, Germany

[bartel, guenther, hachtel]@math.uni-wuppertal.de

² Virginia Polytechnic Institute and State University, Computational Science Laboratory, Department of Computer Science, 2202 Kraft Drive, Blacksburg, VA 22060, USA asandu@cs.vt.edu

Summary. Multirate GARK schemes define a multirate extension of GARK schemes, generalized additive Runge-Kutta schemes. These allow for exploiting multirate behaviour in both the right-hand sides and in the components in a rather general setting, and are thus especially useful for coupled problems in a multiphysics setting.

We apply MGARK schemes to a benchmark example from thermal-electrical coupling, characterized by a slow and fast part with a stiff and non-stiff characteristic, resp. We test two MGARK schemes: an IMEX method, which makes fully use of the different dynamics and stability properties of the coupled system; and a fully implicit schemes, which inherits the stability properties from both underlying schemes without any coupling constraint.

1 Multirate GARK schemes

We consider a two-way partitioned system

$$y' = f(y) = f^{\{s\}}(y) + f^{\{f\}}, \quad y(t_0) = y_0, \quad (1)$$

with one slow component $\{s\}$, and one active (fast) component $\{f\}$. Note that this setting contains component-wise splitting

$$y = \begin{pmatrix} y_s \\ y_f \end{pmatrix}, \quad f^s = \begin{pmatrix} f_s \\ 0 \end{pmatrix}, \quad f^f = \begin{pmatrix} 0 \\ f_f \end{pmatrix}$$

as a special case.

The slow component is solved with a large step H , and the fast one with small steps $h = H/M$. We will consider the multirate generalization of GARK schemes [3] with M micro steps $h = H/M$, as given in the following

Definition 1 (Multirate GARK method [4]). *One macro-step of a generalized additive multirate Runge-Kutta method with M equal micro-steps reads*

$$\begin{aligned} Y_i^{\{s\}} &= y_n + H \sum_{j=1}^{s\{s\}} a_{i,j}^{\{s,s\}} f^{\{s\}}(Y_j^{\{s\}}) + \\ &\quad + h \sum_{\lambda=1}^M \sum_{j=1}^{s\{f\}} a_{i,j}^{\{s,f,\lambda\}} f^{\{f\}}(Y_j^{\{f,\lambda\}}), \\ Y_i^{\{f,\lambda\}} &= y_n + h \sum_{l=1}^{\lambda-1} \sum_{j=1}^{s\{f\}} b_j^{\{f\}} f^{\{f\}}(Y_j^{\{f,l\}}) + \\ &\quad + H \sum_{j=1}^{s\{s\}} a_{i,j}^{\{f,s,\lambda\}} f^{\{s\}}(Y_j^{\{s\}}) + \end{aligned}$$

$$+ h \sum_{j=1}^{s\{f\}} a_{i,j}^{\{f,f\}} f^{\{f\}}(Y_j^{\{f,\lambda\}}),$$

$$\lambda = 1, \dots, M,$$

$$y_{n+1} = y_n + h \sum_{\lambda=1}^M \sum_{i=1}^{s\{f\}} b_i^{\{f\}} f^{\{f\}}(Y_i^{\{f,\lambda\}}) +$$

$$+ H \sum_{j=1}^{s\{s\}} b_j^{\{s\}} f^{\{s\}}(Y_j^{\{s\}}).$$

The base schemes are Runge-Kutta methods, $(A^{\{f,f\}}, b^{\{f\}})$ for the slow component and $(A^{\{s,s\}}, b^{\{s\}})$ for the fast component. The coefficients $A^{\{s,f,\lambda\}}$, $A^{\{f,s,\lambda\}}$ realize the coupling between the two components.

1.1 Order conditions

The MGARK scheme can be written as a GARK scheme [3] over the macro-step H with the fast stage vectors $Y^{\{f\}} := [Y^{\{f,1\}T}, \dots, Y^{\{f,M\}T}]^T$. The corresponding Butcher tableau reads

$\frac{1}{M}A^{\{f,f\}}$	0	...	0	$A^{\{f,s,1\}}$
$\frac{1}{M}\mathbf{1}b^{\{f\}T}$	$\frac{1}{M}A^{\{f,f\}}$...	0	$A^{\{f,s,2\}}$
\vdots	\ddots	\ddots	\ddots	\vdots
$\frac{1}{M}\mathbf{1}b^{\{f\}T}$	$\frac{1}{M}\mathbf{1}b^{\{f\}T}$...	$\frac{1}{M}A^{\{f,f\}}$	$A^{\{f,s,M\}}$
$\frac{1}{M}A^{\{s,f,1\}}$	$\frac{1}{M}A^{\{s,f,2\}}$...	$\frac{1}{M}A^{\{s,f,M\}}$	$A^{\{s,s\}}$
$\frac{1}{M}b^{\{f\}T}$	$\frac{1}{M}b^{\{f\}T}$...	$\frac{1}{M}b^{\{f\}T}$	$b^{\{s\}T}$

Therefore the order conditions for MGARK schemes can be derived from the corresponding ones for GARK schemes. Up to order two the order conditions given in Table 1 have to be fulfilled.

1.2 Stability

We consider systems (1) where each of the component functions is dispersive (with constants $\nu^{\{s\}} < 0$, $\nu^{\{f\}} < 0$):

$$\langle f^{\{s\}}(y) - f^{\{s\}}(z), y - z \rangle \leq \nu^{\{s\}} \|y - z\|^2,$$

$$\langle f^{\{f\}}(y) - f^{\{f\}}(z), y - z \rangle \leq \nu^{\{f\}} \|y - z\|^2,$$

p	order condition
1	$b^{\{s\}T} \mathbf{1} = 1$ $b^{\{f\}T} \mathbf{1} = 1$
2	$b^{\{s\}T} A^{\{s,s\}} \mathbf{1} = \frac{1}{2}$ $b^{\{s\}T} \left(\sum_{\lambda=1}^M A^{\{s,f,\lambda\}} \right) \mathbf{1} = \frac{M}{2}$ $b^{\{f\}T} A^{\{f,f\}} \mathbf{1} = \frac{1}{2}$ $b^{\{f\}T} \left(\sum_{\lambda=1}^M A^{\{f,s,\lambda\}} \right) \mathbf{1} = \frac{M}{2}$

Table 1. Order conditions for MGARK schemes.

with respect to the same scalar product $\langle \cdot, \cdot \rangle$. As for two solutions $y(t)$ and $\tilde{y}(t)$ of (1), each starting from a different initial condition, the norm of the solution difference $\Delta y(t) = \tilde{y}(t) - y(t)$ is non-increasing, we demand a similar property from the numerical approximations: the MGARK scheme is said to be nonlinearly stable, if the inequality

$$\|y_{n+1} - \tilde{y}_{n+1}\| \leq \|y_n - \tilde{y}_n\|$$

holds for any two numerical approximations y_{n+1} and \tilde{y}_{n+1} obtained by applying the scheme to the ODE (1) with dispersive functions and with initial values y_n and \tilde{y}_n .

As a consequence of stability theory for GARK schemes, an MGARK scheme applied to a component-wise partitioned right-hand side is nonlinearly stable, if both base schemes are algebraically stable.

1.3 Two simple MGARK schemes for multiphysics application

In general, one is interested in a rough approximation of coupled multiphysics problems, which reflect the impact of the couplings of both systems. Hence we restrict to MGARK schemes of order 2:

- MGARK-IMEX-2: The implicit-explicit version solves the fast, stiff part with an implicit base scheme, and the slow, non-stiff part with an explicit one. The coefficients are given by

$$b^{\{s\}} = \left(\frac{1}{2} \quad \frac{1}{2} \right), \quad A^{\{s,s\}} = \begin{pmatrix} 0 & 0 \\ 1 & 0 \end{pmatrix},$$

$$A^{\{s,f,1\}} = \begin{pmatrix} 0 \\ M \end{pmatrix},$$

$$A^{\{s,f,\lambda\}} = \begin{pmatrix} 0 \\ 0 \end{pmatrix} \quad \forall \lambda = 2, \dots, M,$$

$$b^{\{f\}} = 1, \quad A^{\{f,f\}} = \frac{1}{2},$$

$$A^{\{f,s,\lambda\}} = \begin{pmatrix} \frac{1}{2} & 0 \end{pmatrix} \quad \forall \lambda = 1, \dots, M.$$

Note that only the fast part is algebraically stable, but neither the slow part and the joint system.

- MGARK-IMIM-2: To get an overall stable scheme, both parts are solved by an implicit base scheme. The coefficients are given by

$$b^{\{s\}} = (0 \ 1), \quad A^{\{s,s\}} = \begin{pmatrix} 0 & 0 \\ 0 & \frac{1}{2} \end{pmatrix},$$

$$A^{\{s,f,1\}} = \begin{pmatrix} 0 \\ \frac{M}{2} \end{pmatrix},$$

$$A^{\{s,f,\lambda\}} = \begin{pmatrix} 0 \\ 0 \end{pmatrix} \quad \forall \lambda = 2, \dots, M,$$

$$b^{\{f\}} = 1, \quad A^{\{f,f\}} = \frac{1}{2},$$

$$A^{\{f,s,\lambda\}} = \begin{pmatrix} \frac{1}{2} & 0 \end{pmatrix} \quad \forall \lambda = 1, \dots, M.$$

As both base schemes are algebraically stable, the MGARK method inherits this property for a component-wise partitioning.

2 Benchmark example

We will test both MGARK implementations for the electrical-thermal multiphysics system introduced in [1] with the specifications discussed in [2]. The thermal component defines the slow (and non-stiff) part, the electrical component the fast (and stiff) part of the system.

Acknowledgement. The work of A. Sandu has been supported in part by NSF through awards NSF OCI-8670904397, NSF CCF-0916493, NSF DMS-0915047, NSF CMMI-1130667, NSF CCF-1218454, AFOSR FA9550-12-1-0293-DEF, AFOSR 12-2640-06, and by the Computational Science Laboratory at Virginia Tech.

The work of M. Günther and Ch. Hachtel has been supported in part by BMBF through grant 05M13PXA (BMBF Verbundprojekt KoSMOS) and by the EU through grant 619166 (FP7-STREP nanoCOPS).

References

1. A. Bartel, M. Günther and M. Schultz. Modeling and discretization of a thermal-electric test circuit. In: K. Antreich, R. Bulirsch, A. Gilg, P. Rentrop (eds.): *Modeling, simulation and optimization of integrated circuits*. Int. Series of Numerical Mathematics 146, pp. 187–201.
2. Ch. Hachtel, A. Bartel and M. Günther. Efficient simulation for electrical-thermal systems via Multirate-Mor. Abstract SCEE 2014.
3. A. Sandu and M. Günther. A class of generalized-structure additive Runge-Kutta methods. *Submitted for publication*.
4. M. Günther and A. Sandu. Multirate generalized additive Runge Kutta methods. *Submitted for publication*.

Different views on model order reduction for the electronics industry

Joost Rommes

Mentor Graphics

Summary. Model order reduction has become a key ingredient for the simulation of electric circuits and semiconductor structures. The benefits are often clear, but it is not always clear how one can apply model order reduction in the most effective way: to understand this, one has to carefully define when a model can be called reduced. In this presentation we will discuss various applications of model order reduction in the electronics industry. With practical examples, we will show that not only different methods, and different definitions of reduced, may be needed for different applications, but also that for one application one may have to combine various methods.

An a posteriori error bound for reduced order modeling of micro- and nano-electrical(-mechanical) systems

Lihong Feng¹, Peter Benner¹, and Athanasios C. Antoulas²

¹ Max Planck Institute for Dynamics of Complex Technical Systems, Germany feng@mpi-magdeburg.mpg.de, benner@mpi-magdeburg.mpg.de

² Department of Electrical and Computer Engineering, Rice University, USA aca@rice.edu

Summary. We propose an a posteriori output error bound for reduced order models of micro- and nano-electrical(-mechanical) systems. The error bound enables automatic generation of the reduced models computed by parametric model reduction methods based on approximation (interpolation) of the transfer function, e.g. Krylov subspace based methods. Although established for parametrized systems, the error bound is also well-grounded for linear time invariant (LTI) systems without parameters, since it considers the non-parametric LTI systems as a special case.

1 Introduction

Parametric model order reduction (PMOR) is an advanced model order reduction (MOR) technique for reduced order modelling of parametrized systems, e.g. micro- and nano-electrical(-mechanical) systems with geometrical, physical variations; and also coupled electro-thermal problems, where the coupling terms are treated as parameters. A linear parametrized system can be written as,

$$\begin{aligned} E(\tilde{\mu}) \frac{dx}{dt} &= A(\tilde{\mu})x + Bu(t), \\ y(t, \tilde{\mu}) &= Cx, \end{aligned} \quad (1)$$

where, $x \in \mathbb{R}^n$ is the vector of unknowns, $u(t) \in \mathbb{R}^{m_1}$ is the input signal and $y(t, \tilde{\mu}) \in \mathbb{R}^{m_2}$ is the output response. $E \in \mathbb{R}^{n \times n}$, $A \in \mathbb{R}^{n \times n}$, $B \in \mathbb{R}^{n \times m_1}$, $C \in \mathbb{R}^{m_2 \times n}$ are the system matrices. $\tilde{\mu} \in \mathbb{R}^p$ is a vector of parameters. The number of degrees of freedom n is usually very large. Through PMOR, a reduced order model is obtained as

$$\begin{aligned} \hat{E}(\tilde{\mu}) \frac{dz}{dt} &= \hat{A}(\tilde{\mu})z + \hat{B}u(t), \\ \hat{y}(t, \tilde{\mu}) &= \hat{C}z, \end{aligned} \quad (2)$$

where $\hat{E} = W^T E V$, $\hat{A} = W^T A V$, $\hat{B} = W^T B$, $\hat{C} = C V$, and $z \in \mathbb{R}^r$, with $r \ll n$. PMOR methods aim to preserve the parameters as symbolic quantities in the reduced models, such that a single reduced model is accurate for all possible variations of the parameters.

In recent years, some PMOR methods, e.g. the Krylov subspace based PMOR methods [3], the interpolation based PMOR methods [1], and the reduced basis methods [2, 4] have been developed. PMOR methods based on Krylov subspaces are highly efficient in computing reduced order models due to the effective use of well-known techniques from Numerical Linear Algebra, and are pursued in circuit and

MEMS simulation. Among these methods, only for the reduced basis method a posteriori error bounds are known. These enable automatic generation of a reliable reduced parametrized model.

We propose an a posteriori output error bound for reduced order models of linear parametrized systems. The error bound is a bound for the difference between the transfer functions of the original system and the reduced model, and is applicable to any PMOR methods based on approximation (interpolation) of the transfer function. The main theoretical contributions are firstly, the error bound is independent of the discretization method (finite difference, finite element, finite volume) applied to the original PDEs. Secondly, the error bound can be directly used in the discretized vector space, without going back to the PDEs, and especially to the bilinear form (weak formulation) associated with the finite element discretization, which must be known a priori for deriving/using the error bound for the reduced basis method [2]. This is typically useful when only discretized systems of ODEs/DAEs are available, for example the system of DAEs established based on modified nodal analysis in circuit simulation.

Technically, the proposed output error bound provides a way of automatically generating reliable reduced models computed by the Krylov subspace based PMOR methods, which is desired in design automation for circuits and MEMS. Although Krylov subspace based MOR methods have been integrated into some simulation tools [5], the reduced model cannot be guaranteed to satisfy the required accuracy due to the lack of a robust error bound. We are making the design automation reliable by proposing an a posteriori output error bound valid for both parametric linear systems and non-parametric LTI systems.

2 Error Bound for Linear Parametrized Systems

In order to derive the error bound for the transfer function $\hat{H}(\mu)$ of the reduced model (2), we need the primal system and the dual system defined in the frequency domain. The primal system is defined as

$$\begin{aligned} G(\mu)x(\mu) &= B, \\ y(\mu) &= Cx(\mu). \end{aligned} \quad (3)$$

It can be obtained by applying the Laplace transform to the original system, and taking the input $u(t)$ as the impulse input. For the system in (1), $G(\mu) = sE(\tilde{\mu}) - A(\tilde{\mu})$. The newly defined vector μ includes both the Laplace variable s and $\tilde{\mu}$. The output $y(\mu)$ is exactly the transfer function $H(\mu)$ of the original system in (1). For non-parametric systems, $\mu = s$, and $G(\mu) = G(s) = sE - A$. The dual system is defined as

$$\begin{aligned} G^*(\mu)x^{du}(\mu) &= -C^T, \\ y^{du}(\mu) &= B^T x^{du}(\mu). \end{aligned} \quad (4)$$

Here, $G^*(\mu)$ is the conjugate transpose of $G(\mu)$. We also need the residuals caused by the reduced models for the primal and the dual systems. The reduced model of the primal system is obtained by the pair W , V used in (2).

$$\begin{aligned} W^T G(\mu) V z(\mu) &= W^T B, \\ \hat{y}(\mu) &= C V z(\mu), \end{aligned} \quad (5)$$

where $\hat{x}(\mu) = V z(\mu)$ approximates $x(\mu)$. It can be easily seen that $\hat{H}(\mu) = \hat{y}(\mu)$. The reduced model of the dual system is

$$\begin{aligned} (W^{du})^T G^*(\mu) V^{du} z^{du}(\mu) &= -(W^{du})^T C^T, \\ \hat{y}^{du}(\mu) &= B^T V^{du} z^{du}(\mu), \end{aligned} \quad (6)$$

where $\hat{x}^{du}(\mu) = V^{du} z^{du}(\mu)$ is the approximation of $x^{du}(\mu)$. The two residuals are $r^{pr}(\mu) = B - G(\mu)\hat{x}(\mu)$ and $r^{du}(\mu) = -C^T - G^*(\mu)\hat{x}^{du}(\mu)$.

Defining two new variables $e(\mu) = (\hat{x}^{du}(\mu))^* r^{pr}(\mu)$ and $\tilde{y}(\mu) = \hat{y}(\mu) - e(\mu)$ and assuming that $G(\mu)$ satisfies

$$\inf_{\substack{w \in \mathbb{C}^n \\ w \neq 0}} \sup_{\substack{v \in \mathbb{C}^n \\ v \neq 0}} \frac{w^* G(\mu) v}{\|w\|_2 \|v\|_2} = \beta(\mu) > 0, \quad (7)$$

we have the following theorem.

Theorem 1. *For a SISO linear parametrized system in (1), if $G(\mu)$ satisfies (7), then $|y(\mu) - \tilde{y}(\mu)| \leq \tilde{\Delta}_p(\mu)$, $\tilde{\Delta}_p(\mu) := \frac{\|r^{du}(\mu)\|_2 \|r^{pr}(\mu)\|_2}{\beta(\mu)}$. As a result,*

$$|H(\mu) - \hat{H}(\mu)| = |y(\mu) - \hat{y}(\mu)| \leq \Delta_p(\mu),$$

where $\Delta_p(\mu) := \tilde{\Delta}_p(\mu) + |e(\mu)|$.

Remark. Extension to multiple-input multiple-output (MIMO) system is straight forward.

Remark. By simple derivation, it can be seen that $\beta(\mu)$ is the smallest singular value of $G(\mu)$, so that the error bound $\Delta_p(\mu)$ is computable. By combing the greedy algorithm proposed for the reduced basis method [4] with the Krylov subspace based PMOR algorithm in [3], one can use the error bound to adaptively select the parameters, so as to automatically construct the reduced model. We call the combined algorithm PMMGreedy. Due to space limitation, the algorithm is not presented, but is detailed in [6].

3 Results

We use a second order parametrized system for a MEMS model: Gyroscope¹ as an example. There are 4 parameters in the systems.

After 36 iterations of PMMGreedy, a reduced model with size $r = 201$ is obtained, satisfying the absolute error tolerance $tol = 10^{-7}$. In the table, $\Delta_p(\mu^{final})$ is the value of the error bound $\Delta_p(\mu)$ at the parameter μ^{final} selected by the algorithm at the final iteration step, which is the error bound for the reduced model. The true error ϵ_{true} of the reduced model is very close to but below $\Delta(\mu^{final})$, showing that the error bound is both rigorous and sharp. To simulate the reduced model over 2500 samples of μ , only 29 seconds are spent, while one needs over three hours to simulate the original system.

Table 1. The reduced model obtained by PMMGreedy

ROM size	$\Delta_p(\mu^{final})$	ϵ_{true}	iterations	run time
210	7.1×10^{-8}	1.4×10^{-9}	36	29s

Acknowledgement. This work is supported by the collaborative project nanoCOPS, Nanoelectronic COupled Problems Solutions, supported by the European Union in the FP7-ICT-2013-11 Program under Grant Agreement Number 619166.

References

1. U. Baur, P. Benner, C. Beattie, S. Gugercin. Interpolatory projection methods for parameterized model reduction. *SIAM J. Sci. Comput.*, 33:2489-2518, 2011.
2. S. Boyabal. Mathematical modelling and numerical simulation in materials science. *PhD thesis*, Université Paris Est, 2009.
3. P. Benner and L. Feng. A robust algorithm for parametric model order reduction based on implicit moment matching. *Reduced Order Methods for modeling and computational reduction, MS & A series*, 9:159-186. (A. Quarteroni, G. Rozza, Editors), Springer 2014.
4. A. T. Patera and G. Rozza. Reduced Basis Approximation and A Posteriori Error Estimation for Parameterized Partial Differential Equations. *Version 1.0, Copyright MIT 2006*. Available at URL <http://augustine.mit.edu>.
5. E. B. Rudnyi and J. G. Korvink. Model Order Reduction for Large Scale Engineering Models Developed in ANSYS. *Lecture Notes in Computer Science*, 3732:349-356, 2006.
6. L. Feng, P. Benner and A. C. Antoulas. Some a posteriori error bounds for reduced order modelling of (non-)parametrized linear systems. *In preparation*.

¹ benchmark available at www.modelreduction.org

Reduction of index-2 electrical networks using the Implicit-IMOR method

N. Banagaaya¹, G. Ali², and W. H. A. Schilders¹

¹ Dept. of Mathematics and Computer Science, Technische Universiteit Eindhoven, The Netherlands
n.banagaaya@tue.nl, w.h.a.schilders@tue.nl

² Dept. of Mathematics, University of Calabria, and INFN-Gruppo c. Cosenza, Arcavacata di Rende (Cosenza), Italy
giuseppe.ali@unical.it

Summary. Using modified nodal analysis to model electrical networks, these models lead to a differential algebraic equation if the network involves a resistor elements and these networks are always very large. Reduction of index-2 electrical networks using the conventional MOR methods is always difficult especially with index greater one. The IMOR method was proposed to overcome this problem but it is computationally expensive since it involves matrix inversions. We present the implicit-IMOR (IIMOR) method which is computationally cheaper than the IMOR method.

1 Introduction

Modeling of electrical networks using Modified nodal analysis leads to control problem of the form

$$\mathbf{E}\mathbf{x}'(t) = \mathbf{A}\mathbf{x}(t) + \mathbf{B}\mathbf{u}(t), \quad \mathbf{x}(0) = \mathbf{x}_0, \quad (1a)$$

$$\mathbf{y}(t) = \mathbf{C}^T\mathbf{x}(t), \quad (1b)$$

where $\mathbf{E}, \mathbf{A} \in \mathbb{R}^{n,n}$, $\mathbf{B} \in \mathbb{R}^{n,m}$ and $\mathbf{C} \in \mathbb{R}^{n,\ell}$. $\mathbf{x}(t) \in \mathbb{R}^n$ is the state vector, $\mathbf{u}(t) \in \mathbb{R}^m$ is the input vector and $\mathbf{y}(t) \in \mathbb{R}^\ell$ is the desired output vector. If \mathbf{E} is nonsingular, (1a) is a system of ordinary differential equations (ODEs), otherwise it is a system of differential algebraic equations (DAEs). If an electrical network involves a combination of resistors and other electrical elements, we always obtain a DAE. If we assume (1a) is a DAE then \mathbf{x}_0 must be a consistent initial condition and the polynomial $\det(\lambda\mathbf{E} - \mathbf{A})$ must not vanish identically for some $\lambda \in \mathbb{C}$. In practice dimension of the DAE n is far larger than the number of input and outputs m and ℓ , respectively and it can be computationally expensive due to much storage requirement. This is an attractive feature for model order reduction (MOR). Thus (1) can be replaced by a much smaller reduced-order model given by

$$\mathbf{E}_r\mathbf{x}'_r(t) = \mathbf{A}_r\mathbf{x}_r(t) + \mathbf{B}_r\mathbf{u}(t), \quad \mathbf{x}_r(0) = \mathbf{x}_{r0}, \quad (2a)$$

$$\mathbf{y}_r(t) = \mathbf{C}_r^T\mathbf{x}_r(t), \quad (2b)$$

where $\mathbf{E}_r, \mathbf{A}_r \in \mathbb{R}^{r,r}$, $\mathbf{B}_r \in \mathbb{R}^{r,m}$ and $\mathbf{C}_r \in \mathbb{R}^{r,\ell}$. $\mathbf{x}_r(t) \in \mathbb{R}^r$ is the reduced state vector, $\mathbf{y}_r(t) \in \mathbb{R}^\ell$ is the approximated desired output vector and $r \ll n$ is the order of the reduced model. Most of the conventional MOR methods, they always assume that $\mathbf{x}_0 = 0$ which leads to transfer function $\mathbf{H}(s) = \mathbf{C}^T(s\mathbf{E} - \mathbf{A})^{-1}\mathbf{B}$ after taking the Laplace transform of (1). The transfer

function of the reduced-order model (2) is also given by $\mathbf{H}_r(s) = \mathbf{C}_r^T(s\mathbf{E}_r - \mathbf{A}_r)^{-1}\mathbf{B}_r$. Then the acceptable reduced-order model must have a small approximation error of $\|\mathbf{H} - \mathbf{H}_r\|$ and $\|\mathbf{y} - \mathbf{y}_r\|$ in a suitable norm. For the case of electrical networks, the reduced-order models must also preserve passivity and stability. The reduced-order model (2) can be obtained via projection. If we use the Galerkin projection, we need to first construct a $n \times r$ matrix \mathbf{V} so that $\mathbf{V}^T\mathbf{V} = \mathbf{I}$, then we can approximate $\mathbf{x}(t)$ by $\mathbf{V}\mathbf{x}_r(t)$. As a result, we obtain the reduced-order model (2) with the system matrices $\mathbf{E}_r = \mathbf{V}^T\mathbf{E}\mathbf{V}$, $\mathbf{A}_r = \mathbf{V}^T\mathbf{A}\mathbf{V}$, $\mathbf{B}_r = \mathbf{V}^T\mathbf{B}$ and $\mathbf{C}_r = \mathbf{V}^T\mathbf{C}$. The projection matrix \mathbf{V} determines the subspace of interest and can be computed in many different ways. In circuit community, the most common used method to compute \mathbf{V} is the Aenoldi process which is as known as the PRIMA method [2] because of its passivity preservation property. However in [1], they showed that conventional MOR methods which use that assumption that that $\mathbf{x}_0 = 0$ tend to lead to inaccurate reduced-order models or reduced-order models which are very difficult to solve when applied to DAEs especially with index greater than one. This motivated [1], to introduced the index-aware MOR (IMOR) method which involves first decoupling the DAE into differential and algebraic parts using special bases and projectors. Then reduce the differential and algebraic parts separately, for the differential part, they used the conventional MOR methods while they had to develop new reduction methods for the algebraic part. This approach strongly lies on the März decoupling procedure proposed in [3] since it is numerically feasible. The IMOR method leads to simple and accurate reduced-order models even for electrical networks [4]. However the IMOR method can be computationally expensive, thus impractical for large-scale problems since its decoupling procedure involves matrix inversion. In [5], they proposed the implicit version of the IMOR method which do not involve matrix inversion, which they call Implicit-IMOR (IIMOR) method. The IIMOR method is computationally cheaper than IMOR method. However the IMOR method is more accurate than the IIMOR method, thus one has to trade off between accuracy and complexity. In this paper, we apply the IIMOR

method on index-2 electrical networks. In Sec. 2, we briefly discuss the IIMOR method.

2 Implicit-IMOR method

If we assume that the finite spectrum the matrix pencil (\mathbf{E}, \mathbf{A}) has at least one finite eigenvalue then system (1) can decoupled in to the form [5]:

$$\mathbf{E}_p \xi_p' = \mathbf{A}_p \xi_p + \mathbf{B}_p \mathbf{u} \quad (3a)$$

$$-\mathbf{L} \xi_q' = \mathbf{A}_q \xi_q - \mathbf{L}_q \xi_q + \mathbf{B}_q \mathbf{u}, \quad (3b)$$

$$\mathbf{y} = \mathbf{C}_p^T \xi_p + \mathbf{C}_q^T \xi_q, \quad (3c)$$

where $\mathbf{E}_p \in \mathbb{R}^{n_p, n_p}$ is nonsingular, $\mathbf{A}_p \in \mathbb{R}^{n_p, n_p}$, $\mathbf{B}_p \in \mathbb{R}^{n_p, m}$, $\mathbf{A}_q \in \mathbb{R}^{n_q, n_q}$, $\mathbf{B}_q \in \mathbb{R}^{n_q, m}$, $\mathbf{C}_p \in \mathbb{R}^{n_p, \ell}$ and $\mathbf{C}_q \in \mathbb{R}^{n_q, \ell}$. $\mathbf{L} \in \mathbb{R}^{n_q, n_q}$ is a nilpotent matrix of index μ and $\mathbf{L}_q \in \mathbb{R}^{n_q, n_q}$ is a non-singular lower block-triangular matrix, for $\mu > 1$. We note that also μ is a tractability index of the DAE and $n = n_p + n_q$ is the dimension of the DAE (1). In order to derive the IIMOR reduced-order model, we first strictly separate (3) into differential and algebraic subsystems [5]. We then, reduce the differential and algebraic parts separately. The conventional MOR method such as PRIMA method, is used to reduce the differential part as follows. Choose an expansion point $s_0 \in \mathbb{C} \setminus \sigma(\mathbf{E}_p, \mathbf{A}_p)$ and then construct an order- r Krylov subspace generated by \mathbf{M}_p and \mathbf{R}_p given by: $\mathcal{V}_p := \mathcal{K}_r(\mathbf{M}_p, \mathbf{R}_p) = \text{span}\{\mathbf{R}_p, \mathbf{M}_p \mathbf{R}_p, \dots, \mathbf{M}_p^{r-1} \mathbf{R}_p\}$, $r \leq n_p$, where $\mathbf{M}_p := (s_0 \mathbf{E}_p - \mathbf{A}_p)^{-1} \mathbf{E}_p$, $\mathbf{R}_p := (s_0 \mathbf{E}_p - \mathbf{A}_p)^{-1} \mathbf{B}_p$. Then, $\mathbf{V}_p \in \mathbb{R}^{n_p, r}$ denotes the orthonormal basis matrix of subspace \mathcal{V}_p , so that $\mathbf{V}_p^T \mathbf{V}_p = \mathbf{I}$. The reduced-order subsystem is obtained by using the approximation $\xi_p = \mathbf{V}_p \hat{\xi}_p$, leading to a reduced-order subsystem with system matrices $\hat{\mathbf{E}}_p = \mathbf{V}_p^T \mathbf{E}_p \mathbf{V}_p$, $\hat{\mathbf{A}}_p = \mathbf{V}_p^T \mathbf{A}_p \mathbf{V}_p \in \mathbb{R}^{r \times r}$, $\hat{\mathbf{B}}_p = \mathbf{V}_p^T \mathbf{B}_p \in \mathbb{R}^{r \times m}$ and $\hat{\mathbf{C}}_p = \mathbf{V}_p^T \mathbf{C}_p \in \mathbb{R}^{r \times \ell}$. $\hat{\xi}_p \in \mathbb{R}^r$ is the reduced-order differential variable. Thus the dimension of the differential part is reduced to $r \ll n_p$.

Using the fact that the reduction of the differential part confines ξ_p to the subspace \mathcal{V}_p , spanned by \mathbf{V}_p , then it can be proved that ξ_q lies in the subspace \mathcal{V}_q given by $\xi_q \in \mathcal{V}_q = \mathcal{K}_\mu(\mathbf{L}_q^{-1} \mathbf{L}, \mathbf{L}_q^{-1} \mathbf{R}_q)$, where $\mathbf{R}_q = (\mathbf{A}_q \mathbf{V}_p \mathbf{B}_q) \in \mathbb{R}^{n_q, r+m}$. We denote by \mathbf{V}_q an orthonormal basis of \mathcal{V}_q , so that $\mathbf{V}_q^T \mathbf{V}_q = \mathbf{I}$, and we write $\xi_q = \mathbf{V}_q \hat{\xi}_q$. Then, the reduced-order algebraic subsystem has the system matrices given by $\hat{\mathbf{L}}_q = \mathbf{V}_q^T \mathbf{L}_q \mathbf{V}_q$, $\hat{\mathbf{L}} = \mathbf{V}_q^T \mathbf{L} \mathbf{V}_q$, $\hat{\mathbf{A}}_q = \mathbf{V}_q^T \mathbf{A}_q \mathbf{V}_p$, $\hat{\mathbf{B}}_q = \mathbf{V}_q^T \mathbf{B}_q$ and $\hat{\mathbf{C}}_q = \mathbf{V}_q^T \mathbf{C}_q$. We note that the IIMOR method inherits all the properties of the IMOR method, thus it also preserves the goal of model order reduction.

3 Numerical results

In this section, we consider a MNA model that originates from [6], it is an index-2 system of dimension

$n = 10913$ with $m = \ell = 9$ inputs and outputs. We are able to decoupled this system into $n_p = 10790$ and $n_q = 123$, differential and algebraic equations, respectively. We used both the IMOR and IIMOR methods for comparison. In both methods we used the PRIMA method to reduced the differential part. The IMOR method lead to reduced-order model with 900 differential and 35 algebraic equations, while the IIMOR method lead to a reduced-order model with 900 differential and 99 algebraic equations. We can observe that the IIMOR reduced-order model is much larger. The IIMOR and IMOR method took 443 and 9662 seconds, respectively. Thus, the IIMOR method is computationally cheaper than the IMOR method. Both methods approximate the magnitude and phase of transfer function as shown in Fig. 1.

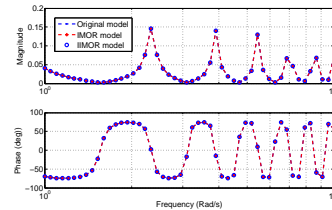


Fig. 1. Magnitude and phase of the transfer functions.

Acknowledgement. This work was supported by The Netherlands Organisation for Scientific Research (NWO).

References

1. G. Alí, N. Banagaya, W. H. A. Schilders and C. Tischendorf. Index-aware model order reduction for linear index-2 differential-algebraic equations with constant coefficients. *SIAM J. SCI. COMPUT.*, 25:A1487–A1510, 2013.
2. A. Odabasioglu and M. Celik. PRIMA: passive reduced-order interconnect macromodeling algorithm. *IEEE Trans. Computer-Aided Design*, 17:645–654, 1998.
3. R. März, Canonical Projectors for Linear Differential Algebraic Equations. *Computers Math. Applic.*, 31:121–135, 1996.
4. G. Alí, N. Banagaya, W. H. A. Schilders and C. Tischendorf. Index-aware Model Order Reduction: LTI DAEs in electric networks. *Meeting Abstract : Scientific Computing in Electrical Engineering (SCEE 2012), September 11-14, 2012, Zurich, Switzerland*, (pp. 75-76).
5. G. Alí, N. Banagaya and W. H. A. Schilders. Implicit-IMOR method for index-1 and index-2 linear constant DAEs. (*External Report, CASA Report, No. 14-10*). Eindhoven: Technische Universiteit Eindhoven, 28 pp., 2014.
6. Y. Chahlaoui. *Benchmark Examples for Model Reduction of Linear Time Invariant Dynamical Systems*, <http://www.icm.tu-bs.de/NICONET/benchmodred.html>

Model Reduction for Maxwell Equations using Subspace Recycling

André Bodendiek¹ and Matthias Bollhöfer²

¹ Formerly TU Braunschweig, Germany

² TU Braunschweig, Institute for Computational Mathematics, Germany m.bollhoefer@tu-bs.de

Summary. We present an efficient model order reduction method for 3D Maxwell equations based on moment matching. This method repeatedly applies a rational Arnoldi-type method but bypasses solving several shifted systems by reusing the orthonormal basis from a previous call. When solving a sequence of shifted systems we only factorize one selected system while the remaining sequence of systems is solved by a QMR method with subspace recycling.

1 Introduction

Model order reduction (MOR) [2] has become of great importance whenever the efficient simulation of a dynamical system is infeasible due to the dimension of the underlying model problem (as is the case for Maxwell equations), see [2]. In computational electromagnetics the discretization of Maxwell's equations of first order yields a dynamical system of type

$$\begin{aligned} M_\varepsilon \dot{E} &= -M_\sigma E + CH + B_E u, \\ M_\mu \dot{H} &= -C^T E + B_H u, \\ y &= G_E E + G_H H, \end{aligned} \quad (1)$$

with spd mass matrices M_* , a discretized curl operator C , and the input-output behavior is described by B_* , G_* . The objective of MOR is to compute a reduced order model such that the input-output behavior of the original model problem will be preserved within a given accuracy. To do so, we compute an orthonormal subspace $V = \text{diag}(V_E, V_H)$ such that $V_E, V_H \in \mathbb{R}^{n,r}$ with $r \ll n$. Then system (1) is reduced by applying the Galerkin projection $\Pi = VV^T$.

2 Recycling Moment Matching Methods

For MOR methods we will focus on moment matching methods to compute the subspace V for the reduced-order model, i.e., for a given sequence of shifts $\mathcal{S} = \{s_1, \dots, s_l\} \subset \mathbb{R}$ we will match the leading moments of the transfer function $\mathcal{H}(i\omega) = \mathcal{G}(i\omega \mathcal{M} - \mathcal{A})^{-1} \mathcal{B}$ at selected expansion points $\omega \in \mathcal{S}$, where

$$\mathcal{M} = \begin{pmatrix} M_\varepsilon & 0 \\ 0 & M_\mu \end{pmatrix}, \quad \mathcal{A} = \begin{pmatrix} M_\sigma & C \\ -C^T & 0 \end{pmatrix}$$

and $\mathcal{G} = (G_E, G_H)$, $\mathcal{B} = \begin{pmatrix} B_E \\ B_H \end{pmatrix}$. We will therefore employ an Arnoldi-type method called adaptive-order rational Arnoldi (AORA) [5] which allows to adaptively select the expansion point $s \in \mathcal{S}$ according to

locally minimize the error of the output moments. This yields an orthonormal matrix V such that

$$\text{span} V = \mathcal{K}_{j_1}(s_1) + \dots + \mathcal{K}_{j_l}(s_l), \quad (2)$$

where each $\mathcal{K}_{j_i}(s_i)$ is a Krylov subspace,

$$\mathcal{K}_j(s) = \text{span}\{\mathcal{B}_s, \mathcal{A}_s \mathcal{B}_s, \dots, \mathcal{A}_s^{j-1} \mathcal{B}_s\},$$

$$\mathcal{A}_s = (s\mathcal{M} - \mathcal{A})^{-1} \mathcal{M}, \quad \mathcal{B}_s = (s\mathcal{M} - \mathcal{A})^{-1} \mathcal{B}.$$

After each call of the rational Arnoldi method we use a greedy-type approach for determining an additional expansion point s_{l+1} to improve the accuracy of the reduced order model [3]. Then the rational Arnoldi method is restarted with $\mathcal{S} \cup \{s_{l+1}\}$ until eventually our estimate predicts a sufficiently accurate reduced-order model.

When calling the rational Arnoldi method repeatedly, we have to solve sequences of shifted systems

$$(is_p \mathcal{M} - \mathcal{A})x = b^{(q)} \quad (3)$$

with varying shifts s_p and varying right hand sides $b^{(q)}$ in order to rebuild and to adapt the sum of Krylov subspaces (2). We can dramatically reduce the number of system solves by re-using the orthonormal basis V from a previous call. This is done using a restricted shift selection strategy. Instead of freely selecting the shift $s \in \mathcal{S} \cup \{s_{l+1}\}$ we can either select the new shift s_{l+1} or an old shift from \mathcal{S} , but in order of appearance from the last call. This in turn requires to solve a system of type (3) only when the new additional shift s_{l+1} is chosen. Besides, the rational Arnoldi process only requires the Gram-Schmidt reorthogonalization leading to a significantly accelerated method which we will refer to as modified AORA method.

3 Solving Sequences of Shifted Systems

The (repeated) use of the rational Arnoldi method requires solving sequences of shifted systems (3). Moreover, switching the sign of the second block row, the system matrix $i\omega \mathcal{M} - \mathcal{A}$ becomes complex-symmetric and is highly indefinite since it can be regarded as a first-order time-harmonic Maxwell operator. This makes it hard to use preconditioned iterative solvers. Here we propose to compute one single LU decomposition of $is_* \mathcal{M} - \mathcal{A}$ using a representative shift s_* . The shift s_* is chosen as geometric mean of

the boundaries of the interval from which the shifts s_1, s_2, \dots are selected. This in turn enables us to use a preconditioned Krylov subspace method for solving (3) whenever $s \neq s_*$. Since the preconditioner and the matrix are both complex-symmetric, we use the simplified QMR method (SQMR) [4] to exploit symmetry. As there several systems to solve, we supplement the SQMR method with subspace recycling following the rBiCG method from [1]. When solving $Ax = b$, in addition to the normal Krylov subspace acceleration, we add a search space U (and its dual space \tilde{U}). The initial solution x_0 is replaced by $x_1 = x_0 + Uz$ such that its associated residual $r_1 = b - Ax_1$ is orthogonal with respect to $\tilde{C} = A^T \tilde{U}$. After that the Krylov method essentially uses the projected matrix $(I - C(\tilde{C}^T C)^{-1} \tilde{C}^T)A$ rather than A . The search space U is typically constructed using approximate eigenvectors associated with eigenvalues of small modulus and is obtained as a by-product of the Krylov subspace method. The simplified QMR method allows for skipping the dual search space \tilde{U} .

4 Numerical Results

We will demonstrate the effectiveness of our approach for a PCB circuit of dimension $N = 226'458$ in the frequency range $f \in [7.5, 10.0]$ GHz, discretized with Finite Integration Technique [6].

We analyze the accuracy of the original AORA method compared with the modified AORA method by computing the relative error

$$\varepsilon_{\text{rel}}(\omega) = \frac{|\mathcal{H}(i\omega) - \tilde{\mathcal{H}}(i\omega)|}{|\mathcal{H}(i\omega)|}$$

between the transfer functions \mathcal{H} , $\tilde{\mathcal{H}}$ of the original model and the reduced-order model. From Fig. 1 we see that both reduced models are of similar accuracy.

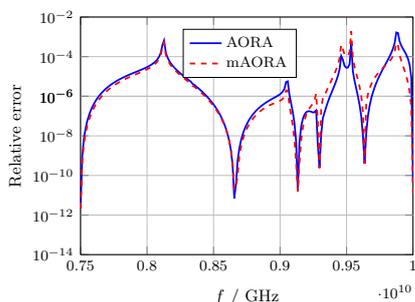


Fig. 1. $\varepsilon_{\text{rel}}(\omega)$ for both rational Arnoldi methods.

Examining the savings using recycling, Fig. 2 demonstrates that recycling the Arnoldi basis from a previous call significantly accelerates the overall method.

Finally, Fig. 3 clearly illustrates the reduced number of iteration steps using subspace recycling in the SQMR method, particularly when the shift s significantly differs from s_* .

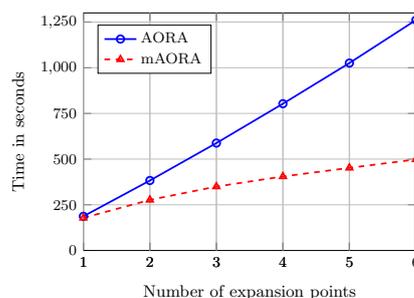


Fig. 2. Computation time AORA versus (modified) AORA.

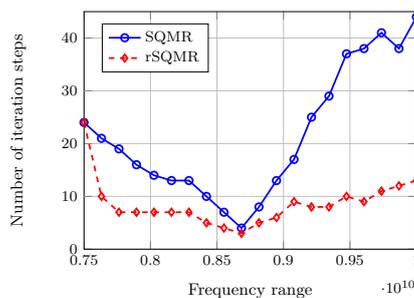


Fig. 3. Iteration steps SQMR versus recycling SQMR.

Acknowledgement. This work was supported by the research network MoreSim4Nano funded by the German Federal Ministry of Education and Science (BMBF) with grant no. 05M10MBA.

References

1. K. Ahuja, E. de Sturler, S. Gugercin, and E. Chang. Recycling BiCG with an application to model reduction. *SIAM Journal on Scientific Computing*, 34(4):A1925–A1949, 2012.
2. A. C. Antoulas. *Approximation of Large-Scale Dynamical Systems*. SIAM Publications, 2005.
3. A. Bodendiek and M. Bollhöfer. Adaptive-order rational Arnoldi-type methods in computational electromagnetism. Technical report, TU Braunschweig, Institut Computational Mathematics, 2012.
4. R. W. Freund and N. M. Nachtigal. Software for simplified Lanczos and QMR algorithms. *Applied Numerical Mathematics*, 19(3):319 – 341, 1995.
5. H.-J. Lee, C.-C. Chu, and W.-S. Feng. An adaptive-order rational Arnoldi method for model-order reductions of linear time-invariant systems. *Linear Algebra Appl.*, 415:235 – 261, 2006.
6. T. Weiland. A discretization method for the solution of Maxwell’s equations for six-component fields. *Electronics and Communications*, 31(3):116–120, 1977.

Reduction of Stochastic Circuit Models for Uncertainty Quantification

Roland Pulch

Institut für Mathematik und Informatik, Ernst-Moritz-Arndt-Universität Greifswald, Walther-Rathenau-Str. 47, D-17487 Greifswald, Germany. roland.pulch@uni-greifswald.de

Summary. In models of electric circuits, uncertainties with respect to physical parameters are quantified by the introduction of random variables. We construct a large dynamical system based on an arbitrary sampling technique, where subsystems are coupled by the definition of the outputs only. Consequently, model order reduction can be applied efficiently to the stochastic formulation. We investigate the performance of the reduction and present numerical results.

1 Stochastic modelling

We consider the linear dynamical system

$$\begin{aligned} E(\mathbf{p})\dot{\mathbf{x}}(t, \mathbf{p}) &= A(\mathbf{p})\mathbf{x}(t, \mathbf{p}) + B(\mathbf{p})\mathbf{u}(t) \\ \mathbf{y}(t, \mathbf{p}) &= C\mathbf{x}(t, \mathbf{p}) \end{aligned} \quad (1)$$

with the state variables $\mathbf{x} \in \mathbb{R}^n$, the output variables $\mathbf{y} \in \mathbb{R}^q$ and matrices $A, E \in \mathbb{R}^{n \times n}$, $B \in \mathbb{R}^{n \times k}$, $C \in \mathbb{R}^{q \times n}$. The matrices A, B, E include the physical parameters $\mathbf{p} \in \Pi \subseteq \mathbb{R}^p$. Thus both the states and the outputs depend on time as well as the parameters. The dimension n can be small or large in the following.

We assume that the selected parameters exhibit uncertainties. For example, imperfections of an industrial production cause variations of the parameters due to miniaturisation. To quantify the uncertainties, the parameters are replaced by independent random variables. Let $\rho : \Pi \rightarrow \mathbb{R}$ be their joint density function. We obtain an associated Hilbert space $L^2(\Pi, \rho)$ for functions depending on the random parameters. Now the aim is to determine statistics of the outputs like the expected value and the variance, for example, or more sophisticated quantities.

To compute probabilistic integrals approximately, a sampling technique or a quadrature formula yields nodes $\{\mathbf{p}_1, \dots, \mathbf{p}_s\} \subset \Pi$ and weights $w_1, \dots, w_s \in \mathbb{R}$. Consequently, the dynamical systems

$$E(\mathbf{p}_j)\dot{\mathbf{x}}(t, \mathbf{p}_j) = A(\mathbf{p}_j)\mathbf{x}(t, \mathbf{p}_j) + B(\mathbf{p}_j)\mathbf{u}(t) \quad (2)$$

have to be resolved for $j = 1, \dots, s$.

Let an orthonormal basis $\{\Phi_1(\mathbf{p}), \dots, \Phi_m(\mathbf{p})\}$ be given for a subspace in $L^2(\Pi, \rho)$. Typically, orthogonal polynomials are chosen following the concept of the polynomial chaos, see [5]. An expansion of the outputs with respect to the basis reads as

$$\begin{aligned} \mathbf{v}_i(t) &:= \int_{\Pi} \mathbf{y}(t, \mathbf{p}) \Phi_i(\mathbf{p}) \rho(\mathbf{p}) \, d\mathbf{p} \\ &\doteq \sum_{j=1}^s w_j \Phi_i(\mathbf{p}_j) C\mathbf{x}(t, \mathbf{p}_j) \end{aligned} \quad (3)$$

for $i = 1, \dots, m$, where the integration is done component-wise. Our aim is to compute the coefficients \mathbf{v}_i , since they produce an approximation of the original outputs \mathbf{y} in $L^2(\Pi, \rho)$. Moreover, the expected value and the variance are reproduced approximately.

Let $\hat{\mathbf{x}}(t) := (\mathbf{x}(t, \mathbf{p}_1), \dots, \mathbf{x}(t, \mathbf{p}_s)) \in \mathbb{R}^{ns}$. We consider the outputs $\hat{\mathbf{y}}(t) := (\mathbf{v}_1(t), \dots, \mathbf{v}_m(t)) \in \mathbb{R}^{qm}$. Using (2) for $j = 1, \dots, s$ and (3) for $i = 1, \dots, m$, we define the larger system

$$\begin{aligned} \hat{E}\dot{\hat{\mathbf{x}}}(t) &= \hat{A}\hat{\mathbf{x}}(t) + \hat{B}\mathbf{u}(t) \\ \hat{\mathbf{y}}(t) &= \hat{C}\hat{\mathbf{x}}(t). \end{aligned} \quad (4)$$

The system (4) consists of s separate subsystems (2), which are coupled only by the definition of the outputs. Hence the matrices $\hat{A}, \hat{E} \in \mathbb{R}^{ns \times ns}$ exhibit a block diagonal structure. It holds that $\hat{B} \in \mathbb{R}^{ns \times k}$. The formula (3) yields the matrix $\hat{C} \in \mathbb{R}^{qm \times ns}$.

In contrast, the stochastic Galerkin approach generates a large system of the form (4) with dimension nm , which is fully coupled, cf. [3, 4]. Moreover, the Galerkin system sometimes loses the stability, although all systems (1) are stable. Obviously, the system (4) inherits the stability of the systems (1).

2 Model order reduction

Methods of model order reduction (MOR) can be applied efficiently, if the numbers of both inputs and outputs are relatively small in comparison to the dimension of the state space, i.e., $q, k \ll n$ in (1). Typically, a sampling method or a quadrature scheme involves a large number s of nodes. The number of input signals in the coupled system (4) and in the original system (1) coincide. The number of output signals in (4) depends on the number m of used basis functions. A relatively small subspace of $L^2(\Pi, \rho)$ may yield a sufficiently accurate approximation and thus we suppose $m \leq s$. Consequently, the assumption $qm \ll ns$ is reasonable and a high potential for reduction appears in the case of the system (4). This assumption is also satisfied for systems (1) of a small dimension n provided that $m \ll s$.

We reduce the stochastic model (4) using MOR methods for linear dynamical systems like moment matching techniques or balanced truncation, for example, see [1, 2]. Once a reduced order model is constructed, a transient simulation directly yields an approximation of the coefficient functions (3) and thus we obtain the desired random process $\mathbf{y}(t, \mathbf{p})$.

This strategy can be seen as an alternative to parametric MOR. In a parametric MOR, the system (1) is reduced in a first step, while preserving the dependence on all $\mathbf{p} \in \Pi$. In a second step, the probabilistic integrations are applied to the reduced system.

In the previous work [4], MOR has been applied successfully to the coupled system of the stochastic Galerkin approach. However, a large computational effort is required for the reduction, since the moment matching technique asks for an LU -decomposition of a huge matrix without a band structure.

3 Simulation of a test example

We apply the band pass filter depicted in Fig. 1, which represents a circuit with single input and single output. A mathematical modelling yields a system of the form (1) with dimension $n = 6$ and $q = k = 1$. All capacitances, inductances and resistances are chosen as random variables, where independent uniform distributions with 20% variation around the mean values are used. Thus $p = 11$ random parameters appear. As quadrature scheme, we apply the Stroud formula of order 5 involving $s = 243$ nodes.

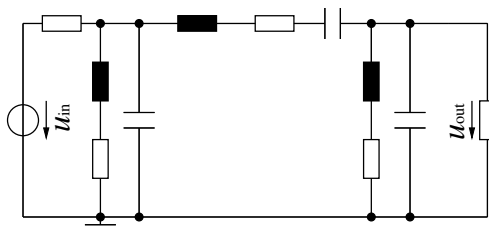


Fig. 1. Circuit of a band pass filter.

For the output of the stochastic model, we select an orthonormal basis using all multivariate Legendre polynomials up to degree two. Thus $m = 78$ basis functions are involved. Now the system (4) exhibits the dimension $ns = 1458$ of the state space and the number of outputs becomes $qm = 78$. To illustrate the dynamics of the system (4), Fig. 2 shows the eigenvalues of the matrix \hat{A} . In particular, the system is stable.

Based on the controllability Gramian and the observability Gramian, we determine the Hankel singular values of the system (4). Fig. 3 illustrates the 100 largest singular values. We recognise that less than 90 singular values are above the machine precision. Hence the order 1458 of the system (4) can be reduced efficiently by the technique of balanced truncation, because the reduced system can have a dimension much less than 100. Moreover, the Hankel singular values imply an error estimate for the transfer functions as well as the transient simulations, which allows for a control of the reduction error, see [1].

Acknowledgement. This research is a part of the project nanoCOPS (Nanoelectronic Coupled Problems Solutions) funded by the European Union in FP7-ICT.

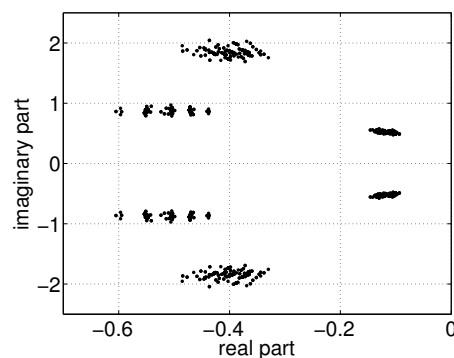


Fig. 2. Eigenvalues of the matrix \hat{A} in the system (4).

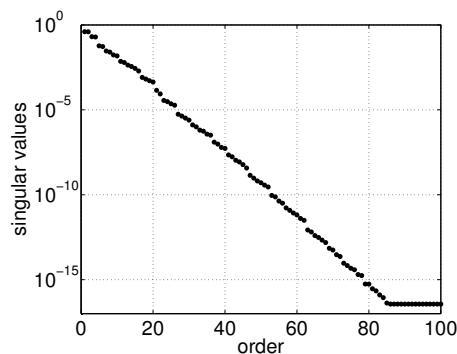


Fig. 3. Dominant Hankel singular values of the system (4).

References

1. A.C. Antoulas. *Approximation of Large-Scale Dynamical Systems*. SIAM, Philadelphia, 2005.
2. P. Benner, V. Mehrmann, and D.C. Sorensen. *Dimension Reduction of Large-Scale Systems*. Springer, Berlin, 2005.
3. R. Pulch. Polynomial chaos for linear differential algebraic equations with random parameters. *Int. J. Uncertainty Quantification* 1:223–240, 2011.
4. R. Pulch and E.J.W. ter Maten. Stochastic Galerkin methods and model order reduction for linear dynamical systems. Preprint, Bergische Universität Wuppertal, 2013.
5. D. Xiu. *Numerical Methods for Stochastic Computations: A Spectral Method Approach*. Princeton University Press, 2010.

Reduced Basis Modeling for Uncertainty Quantification of Electromagnetic Problems in Stochastically Varying Domains

Peter Benner and Martin W. Hess

Max Planck Institute for Dynamics of Complex Technical Systems, Sandtorstr. 1, 39106 Magdeburg, Germany
benner@mpi-magdeburg.mpg.de, hessm@mpi-magdeburg.mpg.de

Summary. The reduced basis method (RBM) is a model order reduction technique for parametrized partial differential equations (PDEs) which enables fast and reliable evaluation of the transfer behavior in many-query and real-time settings. We use the RBM to generate a low order model of an electromagnetic system governed by time-harmonic Maxwell's equations. The reduced order model then makes it feasible to analyze the uncertainty by a Monte Carlo simulation. Stochastic collocation is employed as a second technique to estimate the statistics.

1 Introduction

As the simulation of integrated circuits requires a significant amount of computational power, the simulation of large-scale models benefits greatly from using model order reduction (MOR) techniques. The original system size is typically reduced to a dimension of less than 100, which allows to examine the frequency response of parametrized systems using the reduced model.

Of particular interest are small random variations in geometry, which are given by random variables of given distribution. Inaccuracies in the production process can lead to variations in the geometry, which influence the overall behavior of the model. The influence of the geometric variations on quantities of interest is measured in the form of expectation and variance of output functionals. This is summarized under the term Uncertainty Quantification (UQ).

As a sample application we consider a coplanar waveguide, which is governed by Maxwell's equations. The parametric model reduction technique we use is the reduced basis method (RBM). The RBM generates low order models to parametrized partial differential equations (PDEs) and the approximation tolerance is certified with rigorous error estimators.

2 Reduced Basis Model Order Reduction for Maxwell's Equations

The coplanar waveguide (see [2]) is bounded by a shielded box with perfect electric conducting (PEC) boundary. The system is excited by discrete ports used to model input and output currents/voltages.

We are interested in parameter studies of the input-output behavior of electromagnetic models. There-

fore, we need to compute the electromagnetic field induced by the applied current. We simulate Maxwell's equations in the second order time-harmonic formulation

$$\nabla \times \mu^{-1} \nabla \times E + j\omega\sigma E - \omega^2 \epsilon E = -j\omega J,$$

subject to zero boundary conditions

$$E \times n = 0 \quad \text{on } \Gamma_{\text{PEC}},$$

which is solved for the discretized electric field E . The equation is discretized with Nédélec finite elements (see [1]) over the entire shielded box as the computational domain. The parameter vector is denoted by $\mathbf{v} \in \mathcal{D} \subset \mathbb{R}^p$, such that $E(\mathbf{v})$ is the parameter-dependent electric field solution.

MOR allows to significantly reduce the computational time required for parameter studies. It substitutes the large-scale model by a model of low order, which approximates the transfer behavior. The aim of the RBM is to determine a low order space X_N of dimension N , which approximates the parametric manifold $M^{\mathbf{v}} = \{E(\mathbf{v}) | \mathbf{v} \in \mathcal{D}\}$ well. Assuming sufficient smoothness of $M^{\mathbf{v}}$, a space X_N can be determined, such that projecting the variational form onto X_N gives good approximations $E_N(\mathbf{v})$ to $E(\mathbf{v})$. The space X_N is spanned by snapshots of the field solutions for a discrete set of parameter realizations. The snapshot locations are chosen in a greedy process using a rigorous error estimator. The error estimators $\Delta_N(\mathbf{v})$, which give rigorous bounds on the approximation error in the $H(\text{curl})$ norm:

$$\|E(\mathbf{v}) - E_N(\mathbf{v})\|_{H(\text{curl})} \leq \Delta_N(\mathbf{v}),$$

are used to certify the accuracy of the reduced order model. See [2] for more details.

As in UQ, we are interested in the expected value, standard deviation or k - σ values of particular quantities of interest. As these quantities of interest are given by functionals $I(E)$ of the field solution, the accuracy of the reduced order model w.r.t. $I(E)$ can be further enhanced by using a primal-dual error estimation framework. Here, the adjoint system equation is solved as well and the output error estimator $\Delta_N^o(\mathbf{v})$ is given by

$$\Delta_N^o(\mathbf{v}) = \frac{\|r^{pr}(\cdot; \mathbf{v})\|_{X'} \|r^{du}(\cdot; \mathbf{v})\|_{X'}}{\beta_N(\mathbf{v})},$$

where r^{pr} is the primal, r^{du} the dual residuum and β_N an estimator for the inf-sup stability constant. The dual space of the full order finite element space is denoted by X' , see [2] for more details.

3 Uncertainty Quantification

Let $(\Omega, \mathcal{F}, \mathcal{P})$ denote a probability space. Given is a square integrable random variable $Y : \Omega \rightarrow \mathbb{R}$ with probability density function f and a function $g : \Gamma \rightarrow \mathbb{R}^d$, corresponding to a mapping of realizations of a random variable to the output of the electromagnetic system.

Stochastic collocation computes statistical quantities like the mean by a quadrature rule

$$\mathbb{E}(g(Y)) = \int_{\Gamma} g(x) f(x) dx \approx \sum_{i=1}^n g(\xi_i) w_i,$$

where the realizations ξ_i are the sample points, n denotes the sample size and the weights w_i are determined using the probability density function f . See [3] for more details.

In statistical analysis the expectation and variance of quantities of interest like the response surface w.r.t. uncertain parameters is computed.

Monte Carlo simulations use equally weighted samples, which have been generated using the underlying distribution. A drawback of the Monte Carlo simulation is its slow convergence rate of $1/\sqrt{n}$. Additionally, the stochastic collocation is employed.

We use stochastic collocation in sparse grids of the Stroud- or Hermite-type. Anisotropic sparse grids can give additional computational advantages over isotropic grids, see [5]. To further enhance the computation speed of statistical quantities, stochastic collocation is combined with reduced basis model order reduction. This allows to quantify models of a much larger complexity.

4 Modeling Stochastically Varying Domains

For all $\omega \in \Omega$, let $D(\omega)$ denote the random domain with boundary $\partial D(\omega)$. We employ a mapping to a deterministic domain \bar{D} such that we can assemble the system matrices for the domain \bar{D} and use affine transformations to map to a particular realization $D(\omega)$. In [6] the affine transformations are shown for a deterministic parameter. For our analysis, we quantize the geometry into subsections and allow stochastic variations on each subsection. The affine transformation is then applied to each subsection.

5 Numerical Experiments

Using the RBM on parametric systems with deterministic parameters shows exponential convergence rates,

see Fig. 1. Similarly to [4], we aim to extend this to stochastic parameters using the primal-dual error estimation framework but we focus on the particular application to Maxwell's equations. The talk will cover numerical results when applying the RBM in combination with Monte Carlo simulation and stochastic collocation.

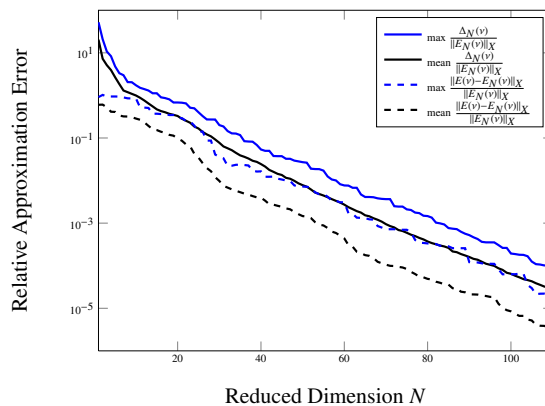


Fig. 1. Convergence of the RBM on the coplanar waveguide with two parameters. The full model contains 52'134 degrees of freedom.

References

1. R. Hiptmair. Finite Elements in computational electromagnetism. *Acta Numerica*, 237–339, 2002.
2. M.W. Hess and P. Benner. Fast Evaluation of Time Harmonic Maxwell's Equations Using the Reduced Basis Method. *IEEE Transactions on Microwave Theory and Techniques*, 61:2265–2274, 2013.
3. P. Benner and J. Schneider. Uncertainty Quantification for Maxwell's Equations Using Stochastic Collocation and Model Order Reduction. Preprint: MPIMD/13-19, Max Planck Institute for Dynamics of Complex Technical Systems, 2013.
4. B. Haasdonk, K. Urban and B. Wieland. Reduced Basis Methods for Parametrized Partial Differential Equations with Stochastic Influences using the Karhunen-Loève Expansion. *SIAM Journal on Uncertainty Quantification*, 1:79-105, 2013.
5. P. Chen, A. Quarteroni and G. Rozza. Comparison Between Reduced Basis and Stochastic Collocation Methods for Elliptic Problems. *Journal of Scientific Computing*, 59:187–216, 2014.
6. M.W. Hess and P. Benner. Reduced Basis Modeling for Time-Harmonic Maxwell's Equations. *COMPEL*, 33, no. 4, 2014.

Multipoint Model Order Reduction using Reflective Exploration

Elizabeth Rita Samuel¹, Francesco Ferranti¹, Luc Knockaert¹, and Tom Dhaene¹

Ghent University - iMinds, Gaston Crommenlaan 8 Bus 201, B-9050 Gent, Belgium {elizabeth.ritasamuel, francesco.ferranti, luc.knockaert, tom.dhaene}@ugent.be.

Summary. Reduced order models obtained by model order reduction methods must be accurate over the whole frequency range of interest. Multipoint reduction algorithms allow to generate accurate reduced models. In this paper, we propose the use of reflective exploration technique for obtaining the expansion points adaptively for the reduction algorithm. At each expansion point the corresponding projection matrix is computed. Then, the projection matrices are merged and truncated based on their singular values to obtain a compact reduced order model.

1 Introduction

Electromagnetic (EM) methods are used for the analysis of complex high-speed systems and usually generate very large systems of equations. Therefore, model order reduction (MOR) techniques are crucial to reduce the complexity of large scale models and the computational cost of the simulations, while retaining the important physical features of the original system [1–3]. Multipoint MOR methods have been developed over the years [1,4,5], which allows to generate accurate reduced models over the whole frequency range of interest. In this paper, the expansion points are selected adaptively using a reflective exploration technique. It is a selective sampling algorithm, where the model is improved incrementally using the best possible data at each iteration, allowing it to propose candidate exploration points [6]. An error-based exploration is performed to find the expansion points. After obtaining the expansion points, the corresponding projection matrices are computed using any of the Krylov based MOR techniques. The projection matrices are then merged and truncated based on their singular values to obtain a compact reduced order model. Then the reduced order models are obtained by congruence transformation using the truncated projection matrix. The technique is validated using a multiconductor transmission line example.

2 Projection Matrix

For this paper, the PRIMA algorithm [3] has been used for obtaining the projection matrices at the expansion points.

For n expansion points we obtain the corresponding projection matrices V_{q_i} for $i = 1, 2, \dots, n$, then the common projection matrix is defined as:

$$V_{comm} = [V_{q_1} V_{q_2} \dots V_{q_n}]. \quad (1)$$

The common projection matrix is not truncated using its singular values during the iterative procedure of the adaptive reflective exploration. It is truncated after all the expansion points have been adaptively chosen using reflective exploration.

3 Reflective Exploration

The reflective exploration requires a reflective function to select the expansion points. The reflective function used for the proposed algorithm is the root mean square (RMS) (2) error between the obtained best models:

$$Err_{est}^{(I)} = \sqrt{\frac{\sum_{k=1}^{K_s} \sum_{i=1}^{P_{in}} \sum_{j=1}^{P_{out}} \frac{|H_{I,(ij)}(s_k) - H_{I-1,(ij)}(s_k)|^2}{|H_{I,(ij)}(s_k)|^2}}{P_{in} P_{out} K_s}} \quad (2)$$

where, K_s , P_{in} and P_{out} are the number of frequency samples considered on a dense grid, input and output ports of the system, respectively. The exploration consists of an adaptive modeling loop and an adaptive sampling loop.

1. Adaptive Modeling Loop: The algorithm starts with two expansion points selected at $[\omega_{min}, \omega_{max}]$ of the frequency range of interest. The reduced order q at these points is equal to the number of ports of the system. Then with a common projection matrix as explained in Section 2, the reduced model is obtained. Then in the next iteration again the projection matrix is computed for a reduced order equal to two times the port of the system. If the RMS error between the two best models (i.e., the model obtained in the I^{th} and the $(I-1)^{th}$ iteration) exceeds a certain threshold, then the reduced order q is again increased by the number of ports for the respective expansion points.
2. Adaptive Sampling Loop: When the difference in RMS error between the I^{th} and $(I-1)^{th}$, is less than 10%, a new expansion point is selected. For selecting the new expansion point the error per frequency is computed by taking the norm L1, of the frequency response of the best model (H_I) and the original model (H_{act}):

$$Err_{s_k} = norm(H_{act,(ij)}(s_k) - H_{I,(ij)}(s_k)); \quad k = 1, \dots, K_s, \quad (3)$$

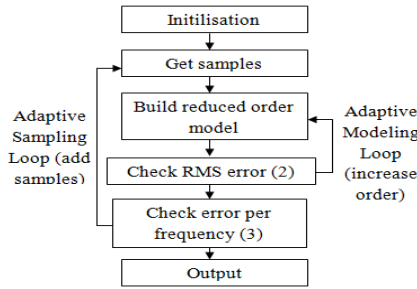


Fig. 1. Flowchart 1: Reflective Exploration.

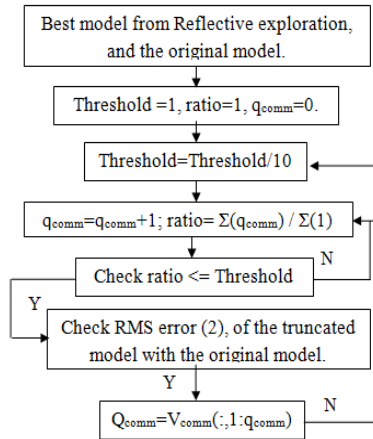


Fig. 2. Flowchart 2: Truncation of the projection matrix.

and the frequency at which Err_{s_k} is maximum is considered as the new expansion point.

This process is iteratively repeated until the RMS error between the original frequency response and the reduced model is 0.001. Figure 1 shows the reflective exploration algorithm.

4 Model compacting

After obtaining the best reduced order model from the iterative procedure, it might be possible to further compact the model with the information obtained from the singular values Σ of V_{comm} (1). Figure 2 shows the flowchart for the truncation of the singular values. The projection matrix Q_{comm} with congruence transformation gives the reduced state-space matrices of order q_{comm} .

5 Numerical Results

A multiconductor transmission line described by an original state-space of order 1202 and 4 ports is considered. As described in Section 3, 4 expansion points are chosen adaptively. Table 1 gives the dimension of the reduced models. The reduced model after truncation has an RMS error of $4.128e - 4$ when evaluated over a dense grid of $K_s = 200$ frequency samples as shown in Figure 3.

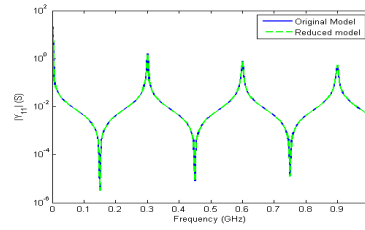
Fig. 3. Magnitude of Y_{11} .

Table 1. Dimension of the Original and Reduced Model.

Models	Dimension
Original	1202
Model after reflective exploration	64
Model after compacting	42

Acknowledgement. This work was supported by the Research Foundation Flanders (FWO-Vlaanderen) and by the Interuniversity Attraction Poles Programme BESTCOM initiated by the Belgian Science Policy Office. Francesco Ferranti is a post-doctoral research fellow of FWO-Vlaanderen.

References

1. K. Gallivan, E. Grimme, and P. V. Dooren. A rational Lanczos algorithm for model reduction. *Numerical Algorithms* vol. 12, no. 1, pp. 3363, Mar. 1996.
2. L. Knockaert and D. De Zutter. Laguerre-SVD reduced-order modeling. *IEEE Transactions on Microwave Theory and Techniques* vol. 48, no. 9, pp. 1469-1475, Sept. 2000.
3. A. Odabasioglu, M. Celik, and L. Pileggi. PRIMA: passive reduced order interconnect macromodeling algorithm. *IEEE Transactions on Computer-Aided Design of Integrated Circuits and Systems* vol. 17, no. 8, pp. 645-654, Aug. 1998.
4. F. Ferranti, M. Nakhla, G. Antonini, T. Dhaene, L. Knockaert, and A. E. Ruehli. Multipoint Full-Wave Model Order Reduction for Delayed PEEC Models with Large Delays. *IEEE Transaction on Electromagnetic Compatibility* vol. 53, no. 4, pp. 959-967, Nov. 2011.
5. G. J. Burke, E. K. Miller, S. Chakrabarti and K. Demarest. Using Model-Based Parameter Estimation to Increase the Efficiency of Computing Electromagnetic Transfer Functions. *IEEE Transactions on Magnetics* vol. 25, no. 4, pp. 2807-2809, 1989.
6. U. Beyer and U. B. Frank. Data Exploration with Reflective Adaptive Models. *Computational Statistics & Data Analysis* vol. 22, no. 2, pp. 193-211, 1996.

Efficient Simulation for Electrical-Thermal Systems via Multirate-MOR

Christoph Hachtel, Michael Günther, and Andreas Bartel

Lehrstuhl für Angewandte Mathematik und Numerische Analysis, Fachbereich C Mathematik und Naturwissenschaften, Bergische Universität Wuppertal, Gaußstr. 20, 42119 Wuppertal, Germany, hachtel@math.uni-wuppertal.de, guenther@math.uni-wuppertal.de, bartel@math.uni-wuppertal.de

Summary. The presented Multirate-MOR scheme exploits the structure of a coupled circuit-thermal system to increase the efficiency of the numerical simulation. The simultaneous use of different step sizes allows the algorithm to adapt to differing dynamical behaviour of the components. We combine this with a model order reduction to obtain smaller subsystems. We will give first numerical results and discuss aspects to be considered in this context.

1 Introduction

We consider an electrical circuit which includes thermal effects. That is, heat is dissipated by certain devices and electrical parameters are temperature dependent. By regularisation of the circuit and semi-discretisation of the thermal part we can achieve a coupled system of ODEs. Here we have to deal with a very different dynamical behaviour of the components of the system: electrical components are changing very fast while components that describe the thermal behaviour change rather slowly. Demanding a high accuracy of the thermal behaviour a fine discretisation of space is needed and we get a large part system with slow dynamic behaviour. To exploit this special structure, we will apply a model order reduction to the thermal part and solve the remaining system of ODEs with a multirate integration scheme.

2 Mathematical Tools

Before modeling the electric-thermal system we introduce the mathematical methods applied in this work.

Mixed-Multirate. Given a system of ODEs with initial values for the unknown \mathbf{y} , we partition the system with respect to the dynamic behaviour of the components. For simplicity of notation we assume to identify two part systems with different dynamical behaviour (active: A , and inactive/slow: L):

$$\dot{\mathbf{y}}_A = \mathbf{f}_A(\mathbf{y}_A, \mathbf{y}_L) \quad \mathbf{y}_A(t_0) = \mathbf{y}_{A,0} \quad (1)$$

$$\dot{\mathbf{y}}_L = \mathbf{f}_L(\mathbf{y}_A, \mathbf{y}_L) \quad \mathbf{y}_L(t_0) = \mathbf{y}_{L,0}. \quad (2)$$

In fact, this can generalised to more than two subsystems. The red terms indicate the respective coupling. Now, multirate methods integrate the slow components with large step sizes H and the active components with a much smaller one h while $h \ll H$.

The crucial part is how to realise the coupling between the active and the slow part. We are following the idea of [1]: The mixed-multirate compound-step method. Here the coupling is realized by computing the macro-step and the first micro-step coupled manner. For the remaining micro-steps one can either interpolate the slow part or use a dense-output formula. What makes mixed-multirate schemes so interesting is that we can use different integrators for the compound-step and the remaining micro-steps. The underlying ODE integration schemes are given by a linear implicit 2(3)-ROW-method for the compound-step and a 3(4)-ROW-scheme for the remaining micro-steps. So we can handle at least moderately stiff ODEs. A set of coefficients can be found in [1].

MOR with Balanced Truncation. If we deal with a high dimensional slow part a model order reduction (MOR) will help to improve efficiency of the time integration. We limit ourselves to linear MOR so starting point is a linear dynamical system. In the multirate context of (2) this reads

$$\begin{aligned} \dot{\mathbf{y}}_L &= \mathbf{A}\mathbf{y}_L + \mathbf{B}\mathbf{y}_A, & \mathbf{y}_L(t_0) &= \mathbf{y}_{L,0}, \\ \mathbf{y}_L &= \mathbf{C}\mathbf{y}_L, & \dim(\mathbf{y}_L) &= n \quad (\mathbf{C} = \mathbf{Id}). \end{aligned}$$

In a MOR method, rectangular biorthogonal projection matrices \mathbf{V}_r , \mathbf{W}_r are computed, such that the dimension r of reduced system matrices $\mathbf{W}_r^T \mathbf{A} \mathbf{V}_r$, $\mathbf{W}_r^T \mathbf{B}$, $\mathbf{C} \mathbf{V}_r$ is significantly smaller than the dimension of the original system ($r \ll n$). While the output of the reduced system $\mathbf{y}_{r,L}$ shall approximate the original output as good as possible. The idea of balanced truncation is now to keep all important states and truncate all states which need a large amount of energy to be reached and to be observed. Truncating states that are difficult to reach and to observe become equivalent if the system is balanced. One gets such a balanced system by solving Lyapunov-Equations and construct a suitable transformation matrix. Balanced truncation offers good and reliable error-bounds (cf. [2]) but can be computationally expensive for very large systems.

3 Modeling and Simulation

We apply the multirate-MOR approach the electric circuit shown in Fig. 1 with thermal dependent and thermal active devices. The example was taken from [3] with some modifications.

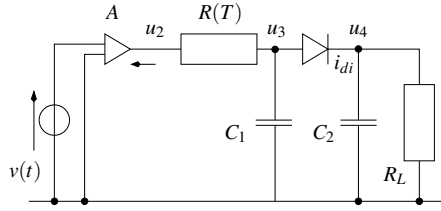


Fig. 1. Circuit Diagram.

Modeling. The resistor $R(T)$ in our example circuit (Fig. 1) is modeled as thermal dependent and thermal active device. On the one hand the resistance is dependent to the temperature and on the other hand the resistor gets heated by the current running through. The diode is modeled as temperature dependent passive element. The circuit is provided by a sinusoidal voltage source for some small time interval. An ODE description of the circuit's voltages can be achieved by nodal analysis using Kirchhoff's law of current for nodes three and four; Joule's law gives the dissipated power at the resistor. In total that reads:

$$C_1 \dot{u}_3 = (u_2 - u_3)/R(T) - i_{di}(u_3 - u_4, T_{di}) \quad (3)$$

$$C_2 \dot{u}_4 = i_{di}(u_3 - u_4, T_{di}) - u_4/R_L \quad (4)$$

$$\dot{e} = (u_2 - u_1)i_R = (u_2 - u_3)^2/R(T). \quad (5)$$

The thermal behaviour of the resistor is modeled by a 1D-heat equation with terms for heat conduction, heating due to electric current (Joule's law) and Newton Cooling. To get an ODE description we discretise the spatial variable in the PDE by method of lines and use a finite volume approach. For the inner cells in an equidistant grid we end up with

$$M'_{W,i} \dot{T}_i = \frac{\Lambda}{h^2} (T_{i+1} - 2T_i + T_{i-1}) + P'_{W,i} - \gamma S'_{W,i} (T_i - T_{env}).$$

The boundary cells are similar. The coupling electric to thermal is realised in (5). The other way round we take the solution of the thermal \mathbf{T} part and compute the total resistance $R(\mathbf{T})$. We interpret the temperature of the last cell to be the diode's temperature.

Simulation and Results. To apply the presented multirate-MOR scheme we set the equations of the system of ODEs stemming from the electric behaviour to be the active part and the semi-discretised heat equation to be the slow part. This is a quite natural choice. The description of the thermal behaviour is a priori not linear. To be able to apply a linear MOR method we linearise the thermal part first. To apply a balanced truncation MOR the system has to be complete observable and reachable (cf. [2]) unfortunately the thermal part is not complete reachable. Here we follow an idea of [2] and consider only the reachable subsystem. We also applied a modal order reduction to compare the MOR schemes. In Fig. 2 the relative error to the full system is shown. As expected we get better results by using the balanced truncation.

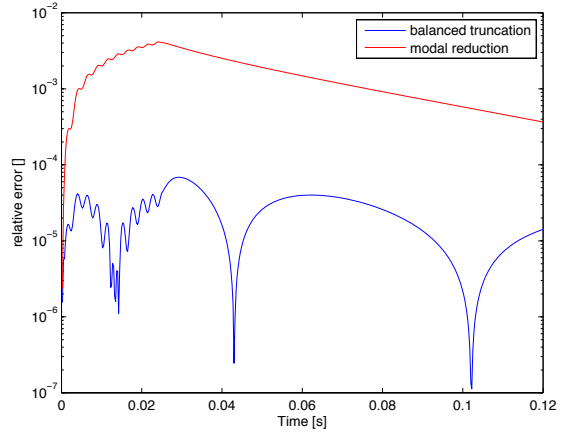


Fig. 2. Relative Error of the Diode's Temperature with different MOR Techniques.

4 Outlook

The applied MOR reduction in a pre-processing step before solving the system with a multirate integrator can only be useful if on the one hand the error due to the MOR is small and on the other hand the computation time decreases significantly. For the first aspect we have to look how sensitive the whole system is with respect to errors in the slow to active interface. For the other aspect we have to consider among others the dimension of the interface. We will present first ideas how to approach to these problems.

Acknowledgement. This work was supported by the Research Network KoSMos: *Model Reduction Based Simulation of coupled PDAE Systems* funded by the German Federal Ministry of Education and Science (BMBF), grant no. 05M13PXA. Responsibility for the contents of this publication rests with the authors.

References

1. Bartel, A.: Multirate ROW Methods of Mixed Type for Circuit Simulation. U. van Rienen, M. Günther, D. Hecht: *Scientific Computing in Electrical Engineering, Lecture Notes in Computational Science and Engineering*, Springer 2001.
2. Antoulas, A.: *Approximation of Large-scale Dynamical Systems*. SIAM (2005)
3. Bartel, A., Günther, M., Schulz, M.: Modeling and Discretization of a Thermal-Electric Test Circuit. K. Antreich, R. Bulirsch, A. Gilg, P. Rentrop (eds.): *Modeling, Simulation and Optimization of Integrated Circuits*, Int. Series of Numerical Mathematics, 146, pp. 187–201.

Tuesday	July 22	Wednesday	July 23	Thursday	July 24	Friday	July 25
08:00-09:10	Registration					08:30-09:20	MOR (Inv.) Rommes
09:10-09:25	Conference opening	09:00-09:50	Meth. (Inv.) Frommer	09:00-09:50	Circ. (Inv.) Klaggess	09:20-09:45	MOR Feng
09:25-10:15	CM (Inv.) Clenet	09:50-10:40	Meth. (Inv.) Alotto	09:50-10:40	Circ. (Inv.) Pistauer	09:45-10:10	MOR Banagaaya
10:15-10:40	CM Kirsch					10:10-10:35	MOR Bollhöfer
10:40-11:10	Coffee break	10:40-11:10	Coffee break	10:40-11:10	Coffee break	10:35-11:10	Coffee break
11:10-11:35	CM Casagrande	11:10-11:35	Meth. Gruber	11:10-11:35	Circ. Bittner	11:10-11:35	MOR Pulch
11:35-12:00	CM Farle	11:35-12:00	Meth. Jerez-Hanckes	11:35-12:00	Circ. Romano	11:35-12:00	MOR Hess
12:00-12:25	CM Banova	12:00-12:25	Meth. Hollaus	12:00-12:25	Circ. Gausling	12:00-12:25	MOR Samuel
Lunch break							
14:15-15:05	CP (Inv.) Schöps			14:15-15:05	Circ (Inv.) LaMagna		
15:05-15:30	CP Liu			15:05-15:30	CM Gangl		
15:30-15:55	CP Tischendorf			15:30-15:55	Intro Poster P-2		
15:55-16:20	Intro Poster P-1			15:55-17:00	Coffee break & P-2		
16:20-17:25	Coffee break & P-1						
17:25-17:50	CP Jüttner			17:00-17:25	Meth. Ali		
17:50-18:15	CP Kerler			17:25-17:50	Meth. Jansen		
SOCIAL EVENT (until ~23:00)							
Closing							



**BERGISCHE
UNIVERSITÄT
WUPPERTAL**